UiO : University of Oslo

Helene B. Erlandsen

Perturbing and constraining Norway's surface water and energy balance

Thesis submitted for the degree of Philosophiae Doctor

Department of Geosciences
Faculty of Mathematics and Natural Sciences

The Norwegian Water Resources and Energy Directorate
The Norwegian Meteorological Institute

2021

Series of dissertations submitted to the
Faculty of Mathematics and Natural Sciences, University of Oslo
No. 2442

ISSN 1501-7710

Cover: Hanne Baadsgaard Utigard.
Print production: Reprosentralen, University of Oslo.

Acknowledgements

"*[..] all clocks are clouds;*
or in other words,
that only clouds exist,
though clouds of very different degrees of cloudiness"
Popper on Pierce (Popper 1972)

The work presented here is a project of the Norwegian Water Resources and Energy Directorate (NVE), which has its basis within both meteorology and hydrology. Supervision has been shared between the Norwegian Water Resources and Energy Directorate, The University of Oslo (UiO), and the Norwegian Meteorological Institute. At UiO, the work has contributed to the Land ATmosphere Interactions in Cold Environments (LATICE) project.

Lena M. Tallaksen, Ingjerd Haddeland, Jørn Kristiansen and Hege Hisdal have guided me through the work on this thesis. Thank you for your ideas, patience, constructive comments, and enthusiasm; without you there would be no papers and no thesis. Additionally, thank you Stein Beldring, Stephanie Eisner, and Shaochun Huang, for sharing of your knowledge and applying your time to what has become the final paper of the thesis. I would also like to thank my current employer, the Norwegian Meteorological Institute, for allowing me time to finalize this work.

Thanks for all the interesting discussions on land surface modeling and on university life, Irene, Johanne, and Kjetil. Irene, I am looking forward to finalizing the work on diagnosing land-atmosphere coupling during summer in South Norway sometime soon, when we all have more time available.

Thank you Gunn, Inge, John, Bjarte, Marit-Lise for your support, and for being fantastic grand parents. Thank you Ole, for encouraging and supporting me and this work in these hectic, but joyful years. You have contributed with time and patience as I have pursued this PhD. During this time, we have also moved houses several times and have become parents to two little sons, Peter and Finn. Finally, thank you Peter and Finn for being wonderful.

"*The outcome of any serious research*
can only be to make two questions grow
where only one grew before."
Thorstein Veblen

Helene B. Erlandsen
Oslo, August 2021

Abstract

The main objective of this work is to better our understanding of the surface water and energy balance in Norway in the context of climate change and land cover change. From a meteorological point of view, the land surface is a set of surface boundary conditions for a set of differential equations, which together may be discretized on a numerical grid to, e.g. provide a weather forecast. From a hydrological point of view, the land surface is an incompletely mapped layer (something with depth), with a more completely mapped atmospheric forcing, for which a combination of physically based equations and data-driven methods may provide an early flood warning, or water resource guidance.

The land surface is thus placed at the physical boundary between the two disciplines meteorology and hydrology. From a research modeler's perspective, the land surface may be explored in a setting coupled with an atmospheric model, or offline, as a stand-alone land surface model driven by atmospheric data. The two methods compliment each other. Coupled model studies capture the connectedness of land-atmosphere processes, such as land-atmosphere coupling and feedback. Stand-alone land surface models demand much less computational resources, allowing longer and higher resolution studies, and benefit from the additional constraint of being forced by observational atmospheric variables, since modeled atmospheric variables often contain biases.

Norway is located at the receiving end of storms that have passed over the North Atlantic. This results in a particular interest in weather and numerical weather prediction, and has further facilitated Norway becoming the largest hydroelectric producer in Europe. In this thesis, the Norwegian land surface water balance and its drivers and feedback mechanisms are investigated by combining numerical model experiments and new observational data, while keeping the problem of climate change and land cover change in mind.

The atmosphere's sensitivity to changes in land surface conditions has been explored using regional, high resolution runs of the Weather Research and Forecasting (WRF) model, perturbing either the forest extent, snow cover, or sea surface temperature (SST), revealing a considerable sensitivity of annual runoff to both vegetation and SST changes. In a second study, a method for producing high-resolution data-sets of near-surface humidity and incident radiation was developed; variables integral to assessing the surface energy balance, needed to estimate evaporation and snow melt. A third study utilized data developed using the method of the second study, and modified a conceptual hydrological model covering mainland Norway on a 1x1 km grid to respond to changes in humidity and incident radiation. More than three decades of model integration showed that the altered model produced equally good or better results than the previous model versions, despite containing fewer calibrated parameters. In addition to daily discharge, its ability to simulate snow water equivalent, potential evaporation, and discharge trends, was scrutinized - to evaluate its suitability for applications under climate change. The water balance produced

showed lower mean annual evaporation than previous estimates for Norway. Future observational and modeling studies are needed to further constrain and enhance the estimated surface water balance in Norway.

List of papers

Paper I

Erlandsen, H. B., I. Haddeland, L. M. Tallaksen, and Kristiansen, J. 'The Sensitivity of the Terrestrial Surface Energy and Water Balance Estimates in the WRF Model to Lower Surface Boundary Representations: A South Norway Case Study.' In: *Journal of Hydrometeorology*, **18**, (2017), pp. 265–284, DOI: 10.1175/JHM-D-15-0146.1

Paper II

Erlandsen, H. B. L. M. Tallaksen, and Kristiansen, J. 'Merits of novel high-resolution estimates and existing long-term estimates of humidity and incident radiation in a complex domain'. In: *Earth System Science Data*, **11**, (2019), pp. 797–821, DOI: 10.5194/essd-11-797-2019

Paper III

Erlandsen, H. B., Beldring S., Eisner S., Hisdal H., Huang S., and Tallaksen L. M. 'Constraining the HBV model for robust water balance assessments in a cold climate' In: *Hydrology Research*, **nh2021132**, (2021), DOI: 10.2166/nh.2021.132

Papers undertaken as part of this PhD not included in this thesis

Nilsen, I.B, **Erlandsen, H. B.**, Stordal, F., Xu C-Y., and Tallaksen L. M. 'Diagnosing land-atmosphere coupling in a seasonally snow-covered region (South Norway)'. (n.d.) The manuscript is currently being restructured.

Contents

1. Introduction

How can we better understand the inter-dependency between land-surface and atmospheric characteristics? In particular, how can we understand the impact of changes in land surface characteristics on atmospheric variables such as near-surface temperature, humidity, and precipitation? Further, how can we better our understanding and simulations of the response of terrestrial variables such as snow cover, surface temperature, evaporation and runoff to changes in atmospheric characteristics?

For more than 1000 years the inter-dependencies between land-surface and atmospheric characteristics has been discussed and analyzed, both to better understand our environment, but also driven by necessity, as severe weather events producing droughts and floods impact human life, health, infrastructure and food resources. Understanding these inter-dependencies is also rewarding, as land water resources may be managed to provide e.g. irrigation for agriculture, or electricity from hydro-power plants, and infrastructure may be adapted to local flood risk. At least for the last 50 years researchers have been unraveling the effect of land use and land cover on atmospheric characteristics, providing information relevant for regulating forestry and agriculture. The interplay between observations, scientific understanding, modeling, validation, prediction, and societal benefits was recently nicely illustrated in a schematic in Stith et al. (2018) which is reproduced in Fig. 1.1.

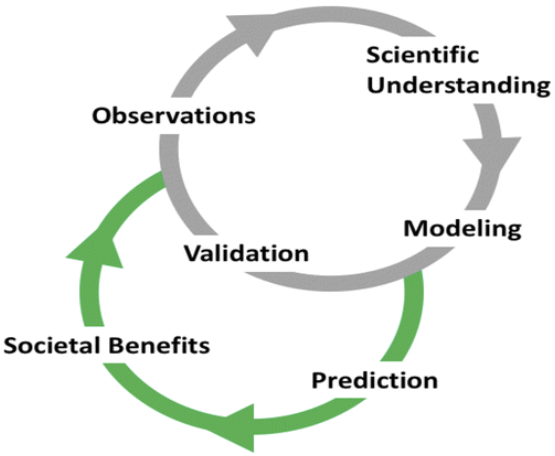

Figure 1.1: Schematic of science serving society. Reprint of Figure 2-7 of Jeffrey L. Stith et al. (Jan. 2018). "100 Years of Progress in Atmospheric Observing Systems". In: *Meteorological Monographs* 59, pp. 1–2. ISSN: 0065-9401. DOI: 10.1175/amsmonographs-d-18-0006.1, ©American Meteorological Society; used with permission.

For at least 100 years these inter-dependencies have been modeled. Computerized numerical models have catalyzed new model applications and insights since the 1950s. Land-atmosphere coupling is central to both meteorology and hydrology. These two disciplines have traditionally relied on (slightly) different models. From a meteorological point of view, the land surface is a set of surface boundary conditions for a set of differential equations, which together may be discretized on a numerical grid to, e.g. provide a weather forecast. From a hydrological point of view, the land surface is an incompletely mapped layer (something with depth), with a more completely mapped atmospheric forcing, for which a combination of physically based equations and data-driven methods may provide an early flood warning, or water resource guidance.

The land surface is thus placed at the physical boundary between the two disciplines meteorology and hydrology. This PhD-thesis is inspired by both academic traditions. My aim is to show that the two disciplines may fruitfully complement each other. Using data from Norway, we have investigated the Norwegian land-surface water and energy balance by perturbing it and applying constraints to it.

Norway is located at the receiving end of storms that have passed over the North Atlantic. These climatic conditions can explain why meteorology have a strong academic tradition in Norway, reflecting a particular interest in weather and numerical weather predictions. The same climatic conditions has facilitated the interest in hydrology, and Norway becoming the largest hydroelectric producer in Europe. Therefore, Norway is an interesting case for studying the inter-dependency between land-surface and atmospheric characteristics. Presently, the boundary conditions for the surface water and energy balance are shifting due to climate change and land use and land cover change. This results in a heightened societal need to better quantify and understand the present surface water and energy balance, and how it responds to perturbations.

1.1 Objectives

The main objective of this work has been to advance our understanding of the surface water and energy balance in Norway in the context of climate change and land cover change. These topics are investigated in three papers, which are linked together to form a whole. The three studies address the scientific and societal needs of improving our understanding of the land surface's impact on atmospheric variables in Norway, and getting a clearer picture of Norway's surface water and energy balance.

Main objective (O): To better our understanding of the surface water and energy balance in Norway in the context of climate change and land cover change.

The secondary objectives are:

- **O1: To identify the surface water and energy balance's sensitivity to changes in the boreal tree line, snow cover, and SST in a state-of-the-art regional climate model.**
- **02: To quantify, compare, and possibly enhance the quality of long-term datasets with atmospheric variables necessary to integrate the surface water and energy balance in an offline model.**
- **O3: To utilize high-quality forcing data and additional physical constraints to provide enhanced long-term estimates of the surface water balance.**

The secondary objective O1 contributes to the main objective by perturbing features impacting the surface water and energy balance in Norway. Secondary objectives O2 and O3 contributes to the main objective by constraining the surface water and energy balance in Norway.

The first study, Paper I, considers the secondary objective O1. In a state-of-the-art regional climate model it considers three research questions (RQ): what is the sensitivity of the surface water and energy balance in South Norway

- (RQ1.1) to a boreal tree line perturbation; and
- (RQ1.2) to snow cover changes and
- (RQ1.3) to a SST perturbation.

The study is ambitious in terms of constructing numerical model experiments perturbing surface compounds in a regional climate model. It is titled "The sensitivity of the terrestrial surface energy and water balance estimates in the WRF model to lower surface boundary representations: A South Norway case study". We explored the sensitivity of the South Norway surface water and energy balance, by constructing experimental runs in a high resolution (3.7 km) regional climate model. Three surface compounds: vegetation, snow, and sea surface temperature (SST), were perturbed in model simulations covering two hydrological years, i.e. 12 consecutive months starting at a time with minimum snow storage. In the first hydrological year, 2009/10, a persistent negative phase of the North Atlantic Oscillation resulted in winter drought and a relative dry year, while the second year, 2010/11, was relatively warm and wet.

The perturbations consisted of 1) increasing the boreal forest line, 2) increasing ground snow by altering the snow/rain criterion in the land surface scheme, and 3) perturbing SST. The three experiments shed light on the regional importance of each of these surface features within South Norway, while keeping the limitations of a single model study in mind. The study further provides information on expected sensitivities in similar regional weather and climate models. The results are summarized in Sec. 5.3.1, and the full article is provided (see Paper I).

The subsequent study, Paper II: "Merits of novel high-resolution estimates and existing long-term estimates of humidity and incident radiation in a complex domain" considers the secondary objective 02: to quantify, compare, and possibly enhance the quality of long-term datasets with atmospheric variables necessary to integrate the surface water and energy balance in offline models. It follows up on concerns regarding our ability to accurately model the surface energy balance and the hydrologic variables sensitive to near-surface humidity and incident radiation, e.g. snow and evaporation, and thus runoff. Quality controlled estimates of incident radiation and humidity are also valuable for assessing the quality the same variables simulated within weather and climate models, such as those simulated by the regional climate model used in Paper I.

At the time, few quality controlled time-series of observed incident shortwave radiation were available in Norway. Further, little information existed on the quality of estimates of near-surface humidity and incident radiation, particularly longwave radiation, from reanalysis datasets[1] for Norway. In addition to reanalysis datasets, estimates of these variables were also available from reanalysis datasets post-processed using additional sources of observational data. We also evaluated the estimates provided by two existing methods, commonly applied within hydrology, which use empirical algorithms relating humidity and incident radiation to two more readily observed variables, precipitation and near-surface temperature. In the process of the study it became evident that we could provide enhanced post-processed reanalysis-based estimates by making use of reanalysis data and national, gridded, observation-based estimates of temperature and precipitation. The second study produced both a scientific article and a dataset. Two major hypotheses were investigated in Paper II:

1. ($\mathcal{H}_a$) There are vertical gradients in near-surface humidity and incident radiation in our domain.

2. ($\mathcal{H}_a$) The added value of the high horizontal resolution of the more empirically based estimates outweighs the added value of relying on estimates from coarser-resolution numerical weather prediction reanalyses.

Paper III considers O3: To utilize high-quality forcing data and additional physical constraints to provide enhanced long-term estimates of the surface water balance. The study further aimed to produce a more robust and more physically based hydrological model suitable for studies of changes in water balance elements

[1] see Chapter 4 for a description of reanalysis datasets

in a non-stationary climate. The study is titled: "Constraining the HBV model for robust water balance assessments in a cold climate". The method outlined in Paper II for constructing high resolution estimates of near-surface humidity and incident radiation was applied to generate a new version of driving data for a gridded hydrological model covering mainland Norway with a resolution of 1x1 km. The method was applied using the most recent input data available, the Era5 reanalysis (Hersbach et al. 2020) and novel versions of the national, gridded SeNorge precipitation and temperature datasets (Lussana et al. 2019). Following Paper II the new dataset was published (dois: 10.5281/zenodo.3351430, 10.5281/zenodo.3516560), and evaluated by comparison to surface observations and other available datasets.

After the new dataset was compiled and prepared a gridded version of the HBV model (Beldring 2008) was updated with model structural changes allowing it to respond to changes in additional atmospheric variables than precipitation and temperature. The structural changes included (i) introducing enhancements to a physically-based evaporation parameterization recently implemented (Huang et al. 2019), (ii) a net radiation-restricted degree-day factor for snow-melt, and (iii) a diagnostic precipitation phase threshold based on temperature and humidity. Although model complexity was increased in some aspects it was also reduced in others. The degree-day factor was restricted in range and made region-specific instead of vegetation-type specific. The number of soil classes was reduced, and the traditional, lognormal SWE-based grid cell tiling was replaced with a simple sigmoidal tanh-function representing grid cell snow cover fraction. The model alterations allowed a reduction in the number of calibrated model parameters.

The model was calibrated and validated making use of observations from more than 100 discharge stations. Both independent discharge observations and time-periods were included in the discharge evaluation. Additionally the model was evaluated in terms of its emulated snow and potential evaporation, and the long-term (1985-2014) monthly emulated discharge trends were compared to those observed. Finally, the estimated 1980-2014 mean annual water balance was compared to previous estimates of mainland Norway's annual water balance, highlighting where considerable uncertainty still is present. The major findings are presented in Sec. 5.3.4, and the full study is provided, see Paper III.

These studies address the scientific and societal needs of improving our general understanding of the land surface's impact on atmospheric variables and vice versa, and getting a clearer picture of the surface water and energy balance. In particular, the Norwegian land surface water balance and its drivers are investigated by combining numerical model experiments and new observational data, while keeping the problem of climate change and land cover change in mind.

The rest of this thesis is structured as follows. To reveal the academic superstructure within which the papers are located, I present in some length the historical and institutional contexts of the surface water and energy balance (Chapter 2). Chapter 3 presents numerical models, i.e. weather forecasting and climate models, land surface models, and hydrological models. An overview of meteorological and hydrological observational data is provided in Chapter 4.

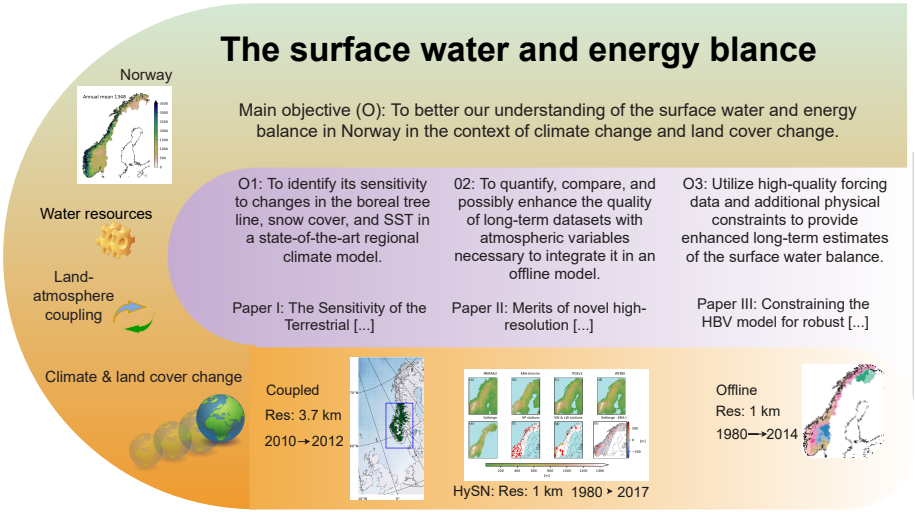

Figure 1.2: Schematic of the study. The main objective (O): To better our understanding of the surface water and energy balance in Norway in the context of climate change and land cover change is met in three secondary objectives, where each of them comprise a paper within this thesis. Themes that are central to the thesis are: Norway - with ample water resources, land-atmosphere coupling, and climate and land cover change. The objectives O1 provides information on the land surface water and energy balance by exploring its sensitivity to changes in surface compounds, while O2 and O3 provide information to better constrain the surface water and energy balance in Norway.

These chapters not only reveal how the questions and conclusions of previous research has developed over time, but also show how and why development of models and improvements in data gathering has facilitated improved understandings and empirical predictions. Third, I present a synthesis of the thesis, including a description of the study area (Sec. 5.1), and summaries of the methods and numerical models applied (Sec. 5.2) and the major findings of each of the three papers - also showing studies' placement in historical and institutional context (Sec. 5.3), and, finally, a summery and outlook based on the findings of all three papers (Sec. 5.4). The interconnections between the thesis' overall topic of investigation and the three papers should be clear: each of the studies touch upon related, but slightly different issues within hydrology and land-surface modeling, using Norway as a case. Fig. 1.2 illustrates the objectives of the thesis investigated in three papers.

2. The surface water and energy balance

Water is present in our current climate, in our atmosphere, hydrosphere and lithosphere, in three aggregation states, commonly known as ice (or snow), liquid water, and water vapor. The concentration of water in each state varies according to the surrounding temperature and pressure, and its physical and radiative properties varies according to state, pressure, and temperature. Subjected to changing pressure and temperature water moves about the hydrological cycle, affecting the short wave and longwave radiation balance and changes state and thus heat with the environment (see Fig. 2.1). Water vapor and clouds stand for around two thirds of the atmospheric greenhouse effect in our current climate.

In a changing climate, with changing atmospheric temperature or pressure, water in the atmosphere responds rapidly by evaporating, condensing and precipitating, thus changing the concentration and location of water, and the global and local energy balance. Water vapor and clouds are consequently identified as fast feedback processes of the climate system. This sensitivity causes large local and seasonal variations in their distribution and concentration. Typical resident time for water vapor in the atmosphere and within plants is in the order of ten days. Convective (microscale) weather processes can occur on spatial scales less than one kilometer and with temporal scales of less than an hour, while mesoscale weather systems occur on spatial scales typically between five and 200 km and within a day. Changes in seasonal snow cover and significant changes in soil moisture over areas with a spatial scale of 100 km generally occurs over

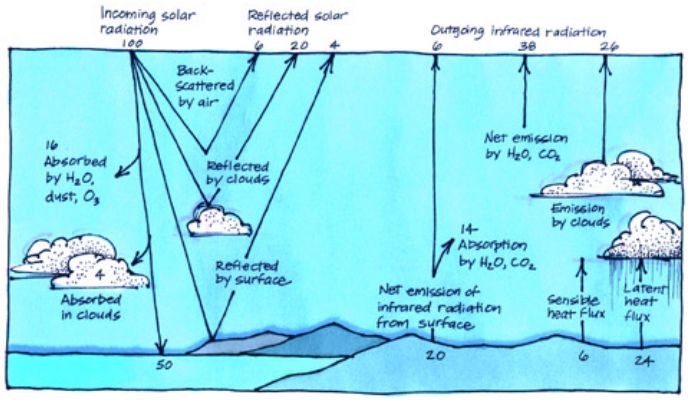

Figure 2.1: The global energy balance is inherently connected to the global water balance. The fluxes are describe as percentages of the average incoming flux of solar radiation $[Wm^{-2}]$ at the top of the atmosphere. Figure from NOAA ESRL website (2020)

months. (National Research Council 1991)

There is substantial uncertainty in the globally averaged terrestrial water balance (Haddeland et al. 2011; Wild 2017), and evidence of slight changes in it (Trenberth et al. 2005; Stephens et al. 2012). Estimates indicate that average terrestrial precipitation is about 30% of precipitation over the oceans, and evapotranspiration over land is about 17% of ocean evaporation. Of terrestrial precipitation it is estimated that 65% originates from terrestrial evaporation, while the remaining part is ocean evaporation advected to land (Trenberth et al. 2011). The following section provides a brief overview of the scientific findings contributing to our current understanding of the surface water and energy balance.

2.1 da Vinci to Stefan-Boltzmann

McMahon et al. (2016) and Duffy (2017) provide overviews of the history of estimating evaporation and the terrestrial hydrological cycle, respectively, while Ohmura (2014) gives an account of the development of energy balance climatology. The start of scientific hydrology in western science has been placed to 1674, with Perrault's publication of 'De l'origine des fontaines' (On the origin of springs), describing that there was enough rainfall draining into the Sein to account for the flow of the Sein (McMahon et al. 2016). Perrault is also credited with making the first measurment of evaporation, by measuring sublimation from a block of ice (McMahon et al. 2016). Before this time, most western scientists believed that underground networks provided the water for springs, providing water all the way up to the highest summits (Duffy 2017); as illustrated in Kircher (1678) (see Fig. 2.2). Even Leonardo da Vinci (1452-1519) at some time stated that, similarly to blood circulating in the body, underground veins connected the sea with the highest mountains providing water for rivers, but, at least within the last decade of his life, his notes showed that he re-assessed his views[1] (Isaacson 2017).

About a decade after Perrault's publication the English astronomer-mathematician Edmond Halley put forward a study (Halley 1686) where he measured the amount of water loss of a heated pan, and stated that evaporation was driven by the heating of water atoms, leaving them lighter than air so that they rise, and, conversely, that the cooling of them might result in precipitation. During the latter part of the 18th century Joseph Black coined the term latent heat to describe a heat transfer that caused a volume change in a substance while its temperature was constant. Latent heat describes energy in a hidden form, which is needed or extracted for a substance to change phase state from or to solid, liquid, or gas form. As water evaporates from a surface to the air, the air increases its latent (or hidden) heat content due to the energy which might be released from the

[1] In the Codex Leicester he noted: "The origin of the sea is contrary to the origin of the blood ....[because] all the rivers are caused solely by the water vapors raised up into the air." (Isaacson 2017)

Figure 2.2: The philosopher Athanasius Kircher illustrated in his work Mundus Subterraneus, in the chapter *The origin of rivers* (Kircher 1678), how, supposedly, tides pump seawater into hidden, underground channels, before the water arrives at outlets feeding rivers.

water vapor if it later condenses. A similar amount of energy as is transferred to the atmosphere is spent on the surface as the water is vaporized.

In 1802 Dalton conducted a series of pan experiments concluding that the evaporation rate from the pan of water is proportional with the temperature of the water, diminishes with increasing humidity, and increases with wind speed (McMahon et al. 2016). Following Dalton's experiments various empirical equations were derived in the 19th century concerning evaporation over water (McMahon et al. 2016), which could be expressed as:

$$E = (e_s - e_d)f(u), \tag{2.1}$$

where E is evaporation, e is vapor pressure (needed at two levels, both the evaporating surface and at some height (d) in the atmosphere above), while $f(u)$ is a function of horizontal wind speed.

The field of thermodynamics also further developed in the 19th century, with experiments and theoretical development leading to the identification of the ideal gas law, and a scientific consensus regarding the conservation of energy in various forms. The term sensible heat was known at the time, and were as "an energy that was indicated by the thermometer". Within thermodynamics sensible heat contrasts latent heat, and is associated with an energy transfer resulting in a temperature change.

Hydrology was further developed in the 19th century with experiments resulting in the 1856 publication of Darcy's law for laminar flow though a

porous media (Duffy 2017). The law was based on the work of the French engineer Henry Darcy, who had previously worked on building a pressurized water distribution system in Dijon, and was published during the last years of his life where he dedicated his work to theoretical development based on sand column experiments. Notable historical development for energy balance climatology are given in Ohmura (2014); e.g. in 1838 the solar constant and atmospheric emissivity were likely measured for the very first time in Paris, Stefan-Boltzmann's law of radiation was first derived in 1884, while the first quantitative description of the energy balance of the climate system was likely provided in Heinirch Hertz's inaugural lecture at the University of Karlsruhe in 1885 (presented in Mulligan and Hertz (1997)).

2.2 Planck to Bowen

In 1900 Max Planck published results on black body emission, authenticating the Stephan-Boltzmann equation and ultimately leading to improved radiometers, i.e. instruments for measuring radiation (Ohmura 2014). The following decades the surface heat (or energy) balance became a topic of increased research, in part due to its potential to optimize agricultural development, and measurement instruments were developed and refined, which made way for new discoveries.

It was known at the time, that heat could be transferred in the atmosphere via radiation, conduction and convection, and that the heat balance of the surface could be estimated more or less as we may state it today[2] :

$$R_{net} = SW\downarrow(1-\alpha_s) + LW\downarrow(\epsilon_s) - \epsilon_s\sigma T_s^4 = G + SH + LH, \tag{2.2}$$

where R_{net} is net incident surface radiation, $SW\downarrow$ is incident shortwave (or solar) radiation, α_s the surface's albedo, $LW\downarrow$ the incident longwave (or thermal) radiation, ϵ_s the surface emissivity or absorbtivity, σ is the Stefan-Boltzmann constant, T_s the surface temperature, G the heat stored in the surface layer, SH is sensible heat, and LH is latent heat. The two latter components, SH and LH, are often referred to as the turbulent fluxes. The latent heat term is commonly defined as heat required to convert ice or water to vapor, while sensible heat is commonly defined as heat transferred to and from the surface and atmosphere via conduction and convection.

During the same period the theory regarding turbulent transfer in the near-surface atmosphere was developed. Fluid mechanical theory for momentum transfer was applied for the turbulent vertical transport of heat in the atmosphere, i.e. eddy motion in the atmosphere Taylor (1915). The topic of near-surface thermal stratification was advanced by the British scientist Lewis Fry Richardson; he expressed atmospheric stability as the ratio of buoyancy forces to shear forces (the Richardson number) (Richardson 1920).

[2] there are additional terms which sometimes are included and defined explicitly in the surface energy balance, such as heat used to melt, but not vaporize, ice or snow, heat released by deposition (water vapor condensing on the surface), heat input via precipitation with a warmer temperature than the surface, heat released by precipitation freezing on or in the surface, etc.

"We realize thus that: big whirls have little whirls that feed on their velocity, and little whirls have lesser whirls and so on to viscosity – in the molecular sense."

Lewis. F. Richardson, 1922 (p. 66, Richardson ([1922]2007))

Richardson also introduced the concept describing the turbulent heat fluxes in an electrical analogue form, where the flux is described by the potential difference between two layers and a resistance between these layers (Richardson ([1922]2007), Randall et al. (2018)):

$$\text{flux} = \frac{\text{potential difference}}{\text{resistance (r)}}. \tag{2.3}$$

An elegant method for estimating the surface fluxes without calculating turbulent exchange coefficients was later provided by Bowen (1926). If the heat (C_{SH}) and water vapor (C_{LE}) turbulent exchange coefficients are equal, the Bowen ratio (β), in current notation, is:

$$\beta = \frac{SH}{LE} = \frac{c_p \rho C_{SH} u (T_s - T_a)}{\lambda \rho C_{LE} u \varepsilon / P_s (e_s - e_a)} = \gamma \frac{T_s - T_a}{e_s - e_a}, \tag{2.4}$$

where λ is the latent heat of vaporization, ε is the ratio of the molecular weight of water vapor to dry air, 0.622, c_p is the specific heat capacity of air, T_s is the temperature of the evaporating surface, T_a the atmospheric temperature, e_s the vapor pressure at the evaporating surface, e_a the atmospheric vapor pressure, and $\gamma = (c_p P_s)/(\lambda \varepsilon)$ is the psychometric constant[3]. Monteith (1981) describes γ by considering an air mass with a temperature T and humidity e. Under certain conditions changes (δ) in these variables may be related by γ:

$$\frac{\delta e}{\text{change in latent heat}} = \frac{\gamma \delta T}{\text{change in sensible heat}} \tag{2.5}$$

If the turbulent exchange coefficients differ the Bowen ratio may be expressed as:

$$\beta = \frac{SH}{LE} = \gamma \frac{C_{SH}(T_s - T_a)}{C_{LE}(e_s - e_a)} = \gamma \frac{r_{LE}(T_s - T_a)}{r_{SH}(e_s - e_a)}, \tag{2.6}$$

where r_{SH} is the resistance to turbulent exchange of heat, $r_{SH} = 1/(uC_{SH})$, and r_{LE} is the resistance to turbulent exchange of moisture, $r_{LE} = 1/(uC_{LE})$.

[3]It should be noted that this 'constant' is only approximately a constant. Further, it is used in conjunction with variables of various units, and has in those cases a different form. E.g. for a Bowen ratio expression where humidity is provided as specific humidity ($q \simeq \varepsilon e / P_s$), and the turbulent exchange coefficents are considered equal: $\beta = \frac{SH}{LE} = \frac{c_p \rho C_{SH} u (T_s - T_a)}{\lambda \rho C_{LE} u (q_s - q_a)} = \gamma \frac{T_s - T_a}{q_s - q_a}$, where γ will be: $\gamma = c_p / \lambda$.

2.3 Budyko

In Europe, North America, and Soviet Russia meteorological and hydro-meteorological monitoring systems expanded. Theoretical advances and new observational instruments paved way for the Soviet climatologist Mikhail I. Budyko's monograph "Heat balance at the earth's surface", containing methods for calculating the climatological components of the surface heat (energy) balance. The monograph was translated into English (Budyko 1958) and thus had an impact on research outside Soviet Russia. Budyko (1958) also provided a scheme for estimating evaporation in two stages (Eq. 92-96). The first stage considers cases where there is ample soil water (w) available, defined as levels exceeding the critical soil moisture threshold (w_K), denoted as at least 70-80% of field capacity. Field capacity is a practical measure of soil water-holding capacity defined as the amount of water the soil can store after excess water has drained away. Above the critical soil moisture threshold evaporation is equal to its maximum potential, E_0, which is independent of soil moisture and depends only on the meteorological conditions:

$$E = E_0,\ w \geq w_K. \tag{2.7}$$

The second stage for estimating evaporation considers cases where soil moisture is below the critical threshold. In this case evaporation decreases linearly with increasing soil water deficit:

$$E = E_0 \frac{w}{w_K};\ w < w_K. \tag{2.8}$$

Published ideas of natural zonality in vegetation, governed by climatic conditions, dates back to late 18th century Russian scientific literature, and to Alexander von Humboldt's 1807 Tableau Physique (Humboldt 1807). von Humboldt put forward the idea that climate is an organizing principle of life, shaping the distinct communities of plants and animals found at different altitudes and latitudes (see Figure 2.3) (Appenzeller 2019). Budyko's monograph (Budyko 1958) highlights how empirical relationships derived in the early 1900, which related long-term evaporation to the greatest possible evaporation and precipitation, were validated by, at the time, novel observations. With this he put forward the usefulness of of considering the long-term hydrological equilibrium limits as boundary conditions for geographic zonality and ecosystem biomes.

The relationship between annual evaporation, annual precipitation and net surface radiation is illustrated in Budyko (1958), replicated in Figure 2.4. If the received surface radiation (here: R), converted by division with the latent heat of fusion (here: L) to possible evaporation (E), is equal to or larger than annual precipitation (here: r); i.e. $R/Lr \geq 1.0$ on the x-axis, there is enough energy for evaporation to equal precipitation ($E/r = 1.0$, as indicated from point A in Fig. 2.4). Over time (without a long-term water source nearby, such as melting glacier) evaporation cannot exceed precipitation, and evaporation is thus water (supply) limited. If the radiative energy provided is less than that needed to evaporate the received precipitation - the fraction of evaporation to precipitation

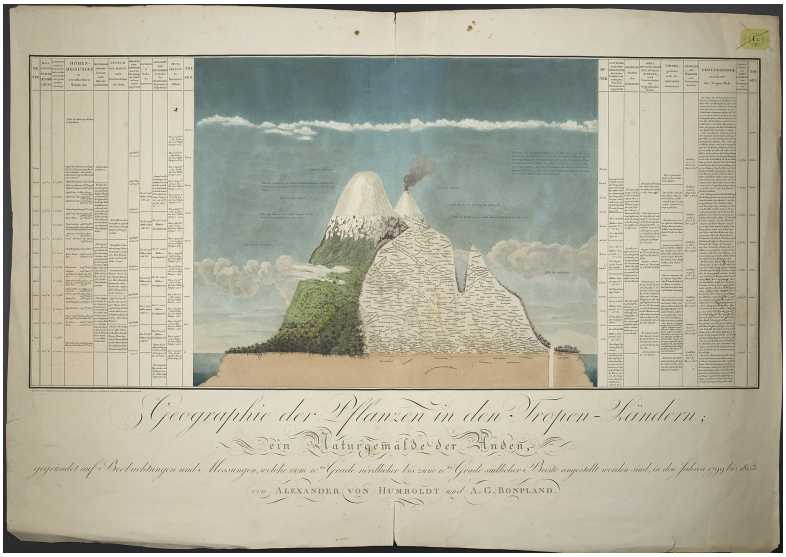

Figure 2.3: Alexander von Humboldt's 1807 Tableau Physique was an innovative diagram depicting a cross-section of equatorial Andes mountains, showing how plant communities changed with elevation and climate (Humboldt 1807). Figure source WIKIMEDIA COMMONS

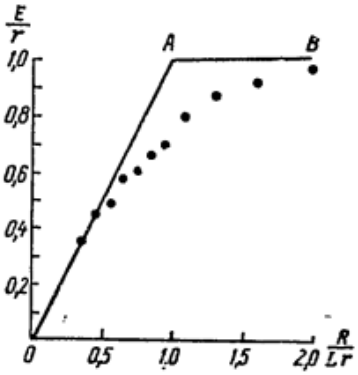

Figure 2.4: The relationship between annual climatological evaporation (E) to precipitation (here: r), according to the ratio of received surface radiation (R) divided by the latent heat of fusion (here: L) and precipitation. Reprinted with permission, original Fig. from M I Budyko (1958). *The heat balance of the earth's surface.* Teplovoĭ balans zemnoĭ poverkhnosti.English. Washington: U.S. Dept. of Commerce, Weather Bureau, 259 p. ©Taylor & Francis.

will decrease proportionally. In this case evaporation is limited by a lack of energy input.

Budyko (1958) further included renditions of the first global (from 70°N to 60°S, excluding high mountain areas) energy balance charts including estimates of latent and sensible heat. The surface radiation charts were based on 1050 observation sites on land and 350 ocean sites, while charts with estimates of latent and sensible heat, and heat advection by the ocean were based on observations from 650 ocean sites and 650 land sites.

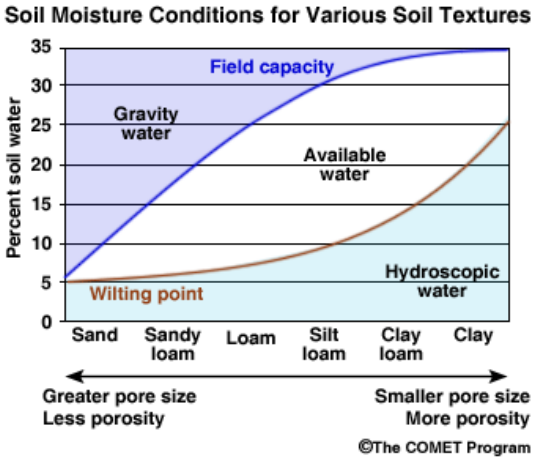

Figure 2.5: Schematic showing how soil water conditions vary with soil textures of various degrees of porosity. The source of this material is the COMET®Website at http://meted.ucar.edu/ of the University Corporation for Atmospheric Research (UCAR), sponsored in part through cooperative agreement(s) with the National Oceanic and Atmospheric Administration (NOAA), U.S. Department of Commerce (DOC). ©1997-2017 University Corporation for Atmospheric Research. All Rights Reserved.

2.4 Green and Ampt, Richards, Horton

A number of advances within the field of soil hydrology occurred within the first half of the 20th century. The publication Green and Ampt (1911) advanced the work of Darcy regarding water and soil permeability in soil. Green and Ampt (1911) made the following observation "*We may regard a porous soil as composed-of a bundle of capillary tubes, irregular in area, length, direction and shape, but sufficiently minute to reduce the velocity of flow of air or water*". A more complete description of vertical flow of water through soil arrived with the publication "Capillary conduction of liquids through porous mediums" (Richards 1931); by combining the expression for soil water diffusion based on Darcy's law and the continuity equation (for water):

$$\frac{\partial \theta}{\partial t} = \frac{\partial}{\partial z}[K(\theta)(\frac{\partial h}{\partial x} + 1)] \tag{2.9}$$

where K is hydraulic conductivity, h is the matric head, z is elevation, θ is the volumetric water content, and t is time. This equation (Eq. 2.9) is commonly referred to as Richard's equation after Richards (1931), however, the previously mentioned British scientist Lewis F. Richardson included a similar equation in his visionary book *Weather Prediction by Numerical Process* (Richardson ([1922]2007) published nine years earlier (see Sec. 3).

Richard's equation is non-linear and was difficult to apply in practice at the time. American civil engineer and soil scientist Robert E. Horton provided an empirical equation for rainfall infiltration into soil, simplifying Darcy's law. In 1931 he also summarized "The field, scope, and status of the science of hydrology" (Horton 1931). Here he defined hydrology: "*As a pure science, hydrology deals with the natural occurrence, distribution, and circulation of water on, in, and over the surface of the Earth.*". In Horton (1933) the rate at which rain enters the soil was related to maximum infiltration capacity, a term describing the maximum rate which rain can be absorbed by soil in a given condition. Rainfall at rates exceeding the infiltration capacity would instead be diverted to overland flow. He further reserved the expression percolation to refer to free downward flow by gravity of water below the soil surface, above the water table. Infiltration capacity and field capacity were further discussed in terms of soil texture (e.g. clay, gravel), and Horton (1933) stated that the two soil properties scale oppositely with soil texture. For finer scale soil such as clay, infiltration capacity is low while the field capacity is high, while for coarse scale soil such as gravel the infiltration capacity is high while the field capacity is low. A medium soil texture was thus regarded as most advantageous for plants (disregarding groundwater supply). Figure 2.5 provides a modern depiction of the relationship between field capacity, soil water availability, and soil texture.

2.5 Penman and Monteith

Another advancement was the approach for estimating evaporation, suggested in Penman (1948). While ocean evaporation could be estimated by measuring sea surface temperature, land evaporation was more difficult to estimate, in part due to the difficulty of measuring a surface temperature, especially for vegetation covered surfaces. The British soil physicist Howard L. Penman's provided a method for calculating evaporation from a saturated surface by combining two existing approaches for estimating evaporation, the energy balance approach and the sink strength approach, essentially the then more than a century old Eq. 2.1. He further made use of Bowen's ratio (Eq.2.4), and calculated evaporation for two near-surface layers, and replaced $(T_s - T_a)/(e_s - e_a)$ with the slope of the saturation vapor pressure - temperature curve (the $e_s : T$ - curve[4]), Δ. He arrived at, using modern day notation:

[4]Similarly to γ, the units of Δ vary according to the humidity variable used.

$$\lambda E = \frac{\Delta R_n + \gamma \lambda E_a}{\Delta + \gamma} \tag{2.10}$$

where R_n is the surface net radiation, Ea is given according to Dalton, Eq. 2.1, but with the first term, the saturation vapor pressure of the evaporating surface - replaced with the saturation vapor pressure at air temperature (T): $E_a = (es(T) - e(T))f(u)$. The expression is thus the product of the atmospheric the vapor pressure deficit (the difference between saturation vapor pressure at ambient temperature ($e_s(T)$) and saturation vapor pressure at dew point temperature ($e_s(T_d)$), or, similarly, the actual vapor pressure ($e(T)$)) and a wind speed function.

Penman's original formula was in non-standard units, and thus less accessible for researchers outside the U.S.A. Further, the formula did not explicitly consider plant transpiration (the formula was "*restricted to consideration of the early stages that would arise after thorough wetting of the soil by rain or irrigation, when soil type, crop type and root range are of little importance.*" (Penman 1948)). The concept of capillary rise and plant transpiration had been studied at least since the 1700s. Plants transpire water from within the leaf through opening of pores (stomata) on the leafs, regulating gas exchange for photosynthesis. Plants' root systems give access to soil moisture at considerable depths below the surface, further plants extend vertically from the surface in complex forms altering surface roughness and the height of surface atmosphere exchange. Further, plant transpiration is largely constricted to the daytime, when photosynthesis occur, and plants impact surface albedo as sunlight which is not useful for photosynthesis, e.g. the green part of the color spectrum of visible light and the longer wavelengths referred to as near infrared light, are reflected.

"*I believe that the nature and distribution of life on our planet depends just as much on the value of Δ/γ as on the magnitude of the Solar Constant and other prestigious parameters of geophysics.*"

Monteith (p. 24, Monteith 1981)

A more explicit treatment of surface resistance for plant communities, or canopies, based on measurements, became well known with the publication of Monteith (1965). John Monteith worked under Penman at the Rothamsted Experimental Station outside London (Ong and Black 2012). His publication built on a similar description of single leaf evaporation deduced by Penman in 1953 (Monteith 1965). Monteith (1965) highlighted that Eq. 2.10 is not valid for a surface which is not necessarily saturated, such as at the surface of a leaf, or a canopy. Monteith (1965) further argued: "*The path for the diffusion of water vapour from leaf cells into the free atmosphere is divided into two parts, one determined primarily with the size and distribution of stomata, and the other by wind speed and the aerodynamic properties of the plant surface. Diffusive*

resistances for single leaves and for plant communities are established from measurements in the laboratory and in the field [...]".

For these surfaces Monteith (1965) modified the Penman equation (Eq. 2.10) to consider a resistance to latent heat transfer (r_{LE}) different from the resistance for sensible heat transfer (r_{SH}) (see equation 2.3 and 2.6). A modified psychometric constant (γ) is defined: $\gamma^* == \gamma(r_{LE}/r_{SH})$. The Penman-Monteith equation for plant potential evaporation stated below. Its derivation following Snyder and Paw U (2002), using the energy-balance approach, is provided in Appendix I.

$$LE = \frac{\frac{\rho c_p}{\gamma^* r_{SH}}(e_s(T) - e(T)) + \frac{\Delta}{\gamma^*}R_n}{\frac{\gamma^*+\Delta}{\gamma^*}} = \frac{\Delta R_n + \frac{\rho c_p}{r_{SH}}(e_s(T) - e(T))}{\gamma^* + \Delta} \tag{2.11}$$

The above equation is often formulated with r_{LE}, the resistance to vapor transfer, replaced with two resistances, one component describing the plant specific resistance to vapor exchange from the plant to some level above the canopy surface (r_s), and another component describing the aerodynamic resistance (r_a) from that level and on wards: $r_{LE} = r_s + r_a$. If one further assumes that the aerodynamic resistance for heat and vapor transfer is the same ($r_{SH} = r_a$), $\gamma^* = \gamma(r_{LE}/r_{SH}) = \gamma((r_s + r_{SH})/r_{SH}) = \gamma(r_s/r_a + 1)$, the Penman-Monteith expression for canopy evaporation is:

$$LE = \frac{\Delta R_n + \frac{\rho c_p}{r_a}(e_s(T) - e(T))}{\Delta + \gamma(1 + \frac{r_s}{r_a})} \tag{2.12}$$

Equation 2.11 and 2.12 are usually referred to as the Penman-Monteith equation, although Monteith himself underscored that he did not derive the equation (Monteith 1981). The two component resistance to canopy vapor exchange is further referred to as the "big-leaf" approximation. The big-leaf approximation is the assumption that the canopy can mathematically be condensed to a single plane, and treated as one big leaf (Sinclair et al. 1976). Monteith (1965) included examples of maximum rates of transpiration for different crops and climates, and crop surface resistances based on field measurements.

2.6 Nomenclature related to evaporation

Horton (1931) stated that "*there is a simple basic fact involved in the hydrologic cycle*

Rainfall = Evaporation + Runoff

There are different processes contributing to evaporation, which may be given distinct names." Horton (1931) noted that: "*Inasmuch as most persons think of evaporation in a more restricted sense, it is better to define runoff as equal to rainfall minus water-losses. Water-losses are of three kinds, all evaporative in their natures (a) Interception; (b) transpiration; (c) direct evaporation from soils*

and water-surfaces.)". Interception (a) is the difference between the precipitation input towards the surface and the amount of which reaches the bare ground (throughfall). Transpiration (b) is evaporation taking place inside the vegetation before it is transported to the surrounding air. Direct evaporation from soils (c) occur due to vapor diffusion and capillary rise in the soil. Direct evaporation from water surfaces (also c), e.g. from ocean, fjords, and lakes, swamps, rice paddies, and other water covered surfaces, is a type of evaporation where surface resistance is zero while aerodynamic resistance is present. This type of evaporation also occurs from surfaces which are intermittently water covered, such as foliage or rocks after precipitation, and is thus related to (a).

Additionally, during winter, in many regions, sublimation, the transfer of water from solid (ice or snow) to gas state, is a source of water flux to the atmosphere. Further, when accounting for water fluxes at the surface-atmosphere interface, in certain conditions, one also might consider additional moisture flux sources than precipitation to the surface; the relatively small fluxes due to dew formation (vapor condensing on the surface), and deposition (water changing from vapor to a solid state) on surface material. One might also consider latent heat exchange due to water freezing and melting on the ground.Although the surface latent heat flux does not equate to evaporation, evaporation is by far largest component of the surface latent heat flux, and the term evaporation is often used interchangeably when assessing large scale, global, or annual surface latent heat flux.

Evaporation on land is further described using a range of terms. Many use the term evapotranspiration, abbreviated ET, to describe either the combination of soil evaporation and transpiration, or the combination of soil evaporation, transpiration, and evaporation from intercepted precipitation (see e.g. Miralles et al. 2020, for references), while others prefer the term evaporation when referring to compound sources (e.g. Horton 1931; Monteith 1985; Lhomme 1997; Kay et al. 2013; McMahon et al. 2016; Miralles et al. 2020). Further, the term actual evaporation (AE or AET) is sometimes used to differentiate evaporation from potential evaporation, however, if the term 'potential' always is used when referring to potential evaporation, the term 'actual evaporation' should not be necessary to use. In this text the term evaporation is used when referring to evaporation in general, or evaporation from compound sources, while potential evaporation is used to refer to that calculated using e.g. the Penman-Monteith equation. It is further interesting to note that incident radiation, both longwave and shortwave radiation, provide energy for many evaporative processes on land, such as water evaporating from intercepted precipitation, dew covered vegetation, sublimation,and soil evaporation, while plants use distinct parts of incident shortwave radiation for transpiration. A further complicating matter is the rather complex transfer of radiation within plant canopies, a topic which will not be discussed here.

2.7 Use and lack of use of the Penman-Monteith algorithm

The Penman-Monteith algorithm relies on input data (forcing data), such as near-surface humidity and surface net radiation, variables which were not, and still are not regularly observed in most areas. Monteith (1981) stated that: "*The Penman formula was soon adopted by hydrologists and irrigation engineers, meteorologists were more cautious [...] they were also critical of the relatively large number of empirical constants which were needed to determine net radiation, for example, in the days before instruments were available to measure this quantity*". More empirically based evaporation expressions requiring less input data were, and are still, often used instead of the Penman-Monteith equation. A range of equations express evaporation as forced only by atmospheric mean temperature, or temperature and dew point temperature, or e.g. temperature and potential extra-terrestrial solar incident radiation (see e.g. Xu and Singh 2001, for an overview). It should be noted that the different equations are suitable for distinct purposes; certain equations are only valid to calculate crop transpiration, and it is often unclear whether these estimates are valid for vegetation in regions where evaporation of intercepted precipitation is common, such as in Norway. Further, the aggregation of the distinct physical processes controlling evaporation into one or a few observation-calibrated parameters provides equations which are strictly only at least valid at the time and place where the model was calibrated.

While some have developed algorithms for evaporation which rely on forcing data more readily available, others summarized guidelines and/or developed methods for estimating unknown forcing variables from known forcing variables. Examples and guidelines for estimating dew point temperature, incident shortwave, and incident longwave radiation are provided e.g. in "Crop evapotranspiration: Guidelines for computing crop requirements" (Allen et al. 1998), also referred to as FAO-56; and are also listed in the supplemental material of McMahon et al. (2016). Further, software such as MTCLIM (Bristow and Campbell 1984; Thornton and Running 1999; Bohn et al. 2013) is available to estimate unknown forcing variables from known variables, taking into account elevation differences as well. Examples of common approximations are that humidity, in the form of dew point temperature, is given by daily minimum temperature, incident shortwave radiation is approximated making use of the astronomical extra-terrestrial solar radiation, and longwave radiation is estimated using 2-meter temperature, and, perhaps, the previously estimated humidity; further, in some cases, the incident radiation is modulated using precipitation and the diurnal temperature range as proxies for cloud-cover.

The Penman-Monteith equation for evaporation would later be applied in land surface models included in numerical weather prediction and global climate models, where the availability of forcing data is not a problem, since the models were developed for that specific purpose, to model atmospheric variables.

3. Numerical models

3.1 The advent of numerical weather and climate prediction models

At the turn of the 20th century - the then common method for weather forecasting: finding historical similar weather charts, was proposed replaced a two-step approach. The method's first step consisted of analysis of the initial state of the atmosphere using observations, while a second, prognostic step consisted of applying the physical laws of motion, to calculate how the initial state changes over time. The approach was suggested in Bjerknes (1904) (translated in e.g. Bjerknes (2009)), by Norwegian mathematician who had diverted his attention to meteorology, with the ambition "*to make meteorology an exact science, a true physics of the atmosphere*" (Randall et al. 2018).

Almost 100 years ago, in 1922, the same mathematician who gave name to the Richardson number for thermal stability published a ground breaking book called "Weather Prediction by Numerical Processes", outlining a scheme for numerical weather prediction. His work was based on the publications of Bjerknes. Richardson took note from the physically based astronomical forecasts available at the time in nautical almanacs, and stated in the book's preface that "*Perhaps some day in the dim future it will be possible to advance the computations faster than the weather advances and at a cost less than the saving to mankind due to the information gained. But that is a dream.*" (Richardson ([1922]2007). In the book he lay the foundations for a gridded solution to set of equations Bjerknes had proposed.[1] He noted the observations needed to conduct the first step of the method, the analysis, were lacking, and thus laid out a plan outlining where variables would be observed to be most useful for the gridded approach. The possibilities of treating land and ocean purely as a surface boundary condition to the atmosphere, or, instead, attempting concurrent forecasts of land and sea states together with the atmosphere were discussed. Richardson vouched for the latter approach, since forecasts of land and sea states were of independent value, e.g. for agriculture. For numerical schemes evolving land state he proposed using two equations, one for the conduction of heat, and one for the transfer of water. He further proposed discretizing soil in levels of varying depth, with a thin layer close to the surface, and thicker layers further down. He also included a separate section of the book on vegetation, describing their effect on the atmosphere trough transpiration, interception, and modulating surface roughness. He proposed a scheme for transpiration, and noted that transpiration would become limited if soil moisture became lower than a soil type specific threshold (akin to Budyko's later proposed critical soil moisture threshold), citing literature providing critical values based on field research, e.g. 0.02 for coarse sandy soil, and 0.1 for sandy loam.

[1] a finite differences approach on a staggered grid

Richardson estimated that 64 000 people were needed to numerically solve the differential equations to provide a weather forecast. Later studies have found the estimate to be a vast underestimation (Randall et al. 2018). Richardson attempted himself to manually compute a weather hindecast. He used an idealized pressure field to initialize his scheme. The idealized pressure field happened to be closely related to one of two solutions for the set of equations he used, the solution for rapidly traveling gravity-inertia waves. It was the second solution, low frequency waves linked to Earth's rotation, which would have provided more realistic initial conditions for his numerical weather prediction model (Lynch 1992). Richardson's numerical scheme was also not numerically stable[2] using the model time step (3 hours) he had chosen (Lynch 1992). His attempt of compiling a weather forecast thus failed. In the years that followed both theoretical, technical and observational advances paved way for the fulfillment of Richardson's dream. From 1927 radiosondes started providing upper air observations, and an increase in aviation during and after the second world war provided further upper air observations.

The first numerical weather forecast produced using an electronic computer is described in Charney et al. (1950). The computations were performed using the Electronic Numerical Integrator and Computer (ENIAC), and care had been made to ensure numerical stability and to avoid the presence of the high-frequency waves which had caused problems for Richardson. A simplified version of the dynamical equations known to describe atmospheric flow, the quasi-geostrophic approximation with constant static stability resulting in a barotropic state[3], was used for several reasons. The first reason was to start of numerical weather computations considering the solutions to a simpler problem first. The second reason was practical; the scheme was possible to solve numerically, using the ENIAC computer, within reasonable time. The model consisted of 15x18 grid cells, and covered an area over and around North America with a horizontal resolution of about 736 km. The model's integration time step was increased to three hours, however, the total integration time for providing a 24-hour forecast was about 24-hours. Thus, this first attempt of numerical weather prediction (NWP) using an electronic computer nearly fulfilled Richardson's dream of a weather forecast advancing faster than the weather.

In the 1950s observational studies provided more information on the global atmospheric general circulation. Concurrently, several nations initialized operational, regional NWP prediction systems. These initial regional NWP systems first showed best results using simple, one-level, barotropic models (Lynch 2008). It wasn't until the 1960s and 1970s that smart solutions allowing stable numerical schemes using less simplified equations and more atmospheric layers evolved (Lynch 2008).

[2] meaning that the numerical error of the finite difference scheme grows in time

[3] where pressure is a function of density alone, so that temperature gradients does not vary across pressure gradients.

3.2 Development of general circulation models with parameterized processes

The first study including a longer term numerical integration of the quasi-geostrophic equations was published in Phillips (1956). It included a month long integration of a model with two atmospheric (vertical) levels. The Phillips (1956) experiment was inspired by simple laboratory dish-pan experiments, where monitions developed within the fluid of a dish-pan subjected to heating around its edges and cooling in the center. In Phillips (1956) one hemisphere was represented by a cylinder 17 cells high with a 16 cell circumference, with heating in one end.

His model also included "*empirical elements in that the representation of certain physical effects is based on meteorological experience with the actual atmosphere, rather than being predicted from the fundamental laws of physics.*" (Phillips 1956). These elements are what we now refer to as parameterized processes. The term "parameterized processes" is often used for all processes within a NWP model except for the scheme describing atmospheric motion (now usually referred to as the model's dynamical core). Parameterized processes thus include all processes not (fully) represented or resolved in the dynamical core, such as radiation, precipitation, unresolved turbulence, phase changes of water, and so on. When aiming to understand the large scale general circulation these processes are more important to include. Phillips (1956) aimed to replicate basic known features of the atmospheric general circulation such as surface zonal wind, the existence of the jet stream, pole-ward energy transport, the mean latitudinal temperature gradient, and to a large extent he succeeded in doing so.

3.3 Land surface models

During the 1960s a team within the Geophysical Fluid Dynamics Laboratory (GFDL) of the National Oceanic and Atmospheric Administration (NOAA) dedicated their work to understanding the atmospheric global circulation using computers. The models were developed iteratively, each advancing the description of unresolved processes, including e.g. for the first time a radiation parameterization, a cumulus parameterization, and, later on, the first land surface model (Randall et al. 2018).

What is commonly referred to as the first land surface model (e.g. Pitman 2003; Randall et al. 2018) was the "Budyko bucket model"-hydrology implemented in the general circulation model described in Manabe (1969). Manabe (1969) aimed to construct "*a mathematical model of the joint ocean-atmosphere system and to investigate the problem of ocean-atmosphere interaction*", and with this "*to simulate the hydrologic cycle in the atmosphere and to find how the hydrology of the earth's surface interacts with the general circulation of the atmosphere*". The model was run without representation of seasonal or diurnal variations, with a horizontal grid resolution of about 475 km, and a symmetric distribution of ocean and continents across the equator. Surface hydrology was represented

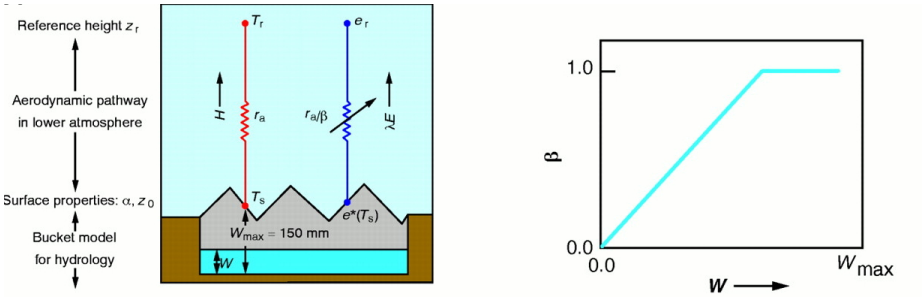

Figure 3.1: Schematic of the Manabe (1969) first generation land surface model, using a bulk aerodynamic formulation and "Budyko bucket model"-hydrology. Latent heat flux was parameterized following Eq. 2.7 and Eq. 2.8. β describes the reduction of evaporation when soil moisture is below the critical level (here Eq. 2.8 is $E = E_0 w/w_K = E_0\beta$). (Left) The sensible (here: H) and latent (λE) heat fluxes flow from the surface to the atmosphere, and both have an aerodynamic resistance r_a. (Right) The latent heat flux is regulated by the level of moisture (W) in the bucket through the moisture availability function β. Reproduced with permission, Figure 2A ("Schematic the "bucket model" hydrology implemented in Manabe (1969)") from P. J. Sellers (Jan. 1997). "Modeling the Exchanges of Energy, Water, and Carbon Between Continents and the Atmosphere". In: *Science* 275.5299, pp. 502–509. ISSN: 00368075. DOI: 10.1126/science.275.5299.502; reprinted with permission from AAAS.

based on Budyko (1958). It was assumed that the land surface was covered with 1 m deep soil boxes. All boxes had a field capacity of 150 mm of water, so that any water input which would result in more than 150 mm of soil water was converted to runoff. Surface albedo was prescribed, except for in areas with snow cover, where it was adjusted to 0.7. Surface hydrology was added to simulate both a sensible and a latent heat flux, where latent heat flux was parameterized following Budyko (1958) (using Eq. 2.7 and Eq. 2.8), linearly reducing evaporation for soil moisture values below 75% of the field capacity. Potential evaporation was calculated using a bulk aerodynamic resistance. Thus, the surface resistance of plant communities to transpiration (canopy resistance), as e.g. had recently been described in Monteith (1965), was not included. Figure 3.1 provides a schematic of the "Budyko bucket model" hydrology implemented in Manabe (1969).

Land surface models similar to the description above are now referred to as first-generation land surface models (Sellers 1997). Second generation land surface models evolved from the late 1970s and during the 1980s. In Deardorff (1978) the Penman-Monteith type evaporation formula and the inclusion of a foliage layer near the ground was described and tested. Intercepted water, or precipitation retained on foliage, was also considered. The new scheme increased computational time, but this was argued as justified as Deardorff found errors of up to a factor of 2 in evaporation estimates without the new treatment of

vegetation. Lack of computational resources also impacted the treatment of soil temperature in the land surface models. Although it was known that soil temperature could be dealt with by solving the diffusion equation for soil heat transfer, this scheme required as many horizontal layers in the soil as the global circulation models at the time included for the atmosphere; and was hence not implemented. The simplest models assumed that the soil had no heat capacity, and thus needed to omit the diurnal variation in solar radiation in order to avoid exaggerated amplitudes in surface temperature. Deardorff (1978) showed that good results could be achieved using an efficient method for calculating soil temperature and soil moisture involving only two slab-layers of soil, using the force-restore method.

Deardorff's schemes were partly incorporated into the National Center for Atmospheric Research (NCAR) third generation general circulation model (Washington et al. 1980). It was acknowledged that to some extent weather forecasts could include very simple parameterizations of surface processes without detrimental effects to the rather short term and low resolution forecasts developed at the time. The implementation of more realistic and complex land surface process in global circulation models was actively discussed, and e.g. Manabe (1982) recommended to develop a hierarchy of hydrological parameterizations with a varying degree of complexity and to evaluate how the simulated climate was altered by each added increment in complexity. Indeed, Monteith himself stated that "*the specification of surface wetness for atmospheric models is not likely to improve rapidly and there is no immediate hope of replacing the rather arbitrary empirical expressions in current use by more fundamental relationships. I therefore see little point in constructing physically elaborate but morphologically unrealistic models of vegetation as proposed in Deardorff (1978).*" (Monteith 1981).

3.4 Anthropogenic land use and climate change emerges as scientific topics of interest

Since the late 19th century spectroscopic measurements had become advanced enough to detect the most important electromagnetic absorption bands of water vapor and carbon dioxide, identifying carbon dioxide as a greenhouse gas (Ohmura 2014). It was suspected that CO_2 was increasing due to the use of coal, oil, and gas; however, the measurements to support the suspicion were lacking. With the funding and support of the first International Geophysical Year, which commenced in 1957, measurements of atmospheric near-surface CO_2 concentrations started at several locations (Keeling et al. 2011).

While the topic of human's influence on climate via emissions of carbon dioxide was gaining traction, early studies conducted with global circulation models were mostly academical, with no immediate applications considered (Randall et al. 2018). The impact of the presence of greenhouse gases such as water vapor, carbon dioxide, and ozone was first studied in the simplified single

column[4] model described in Manabe and Strickler (1964). About ten years later "*The Effects of Doubling the CO2 Concentration on the climate of a General Circulation Model*" was published in Manabe and Wetherald (1975). The study used a simplified general circulation model without any seasonal or diurnal variation. Though the model was rather simple, major findings of the study included a polar amplification of the surface temperature response due to the ultimately positive temperature-snow-albedo-temperature feedback mechanism[5], and an intensification of the hydrologic cycle.

Global circulation models were also used to study present day land-atmosphere interactions, e.g. the impact of land use change. "*Anthropogenic Albedo Changes and the Earth's Climate*" by Sagan et al. (1979) summarized topics of concern regarding how humans had influenced climate by modifying the land surface e.g. by agriculture and the use of forest for energy. Of particular concern was the recent desertification of the Sahel region of Africa, which was shown could have been exacerbated by albedo changes due to deforestation (Charney et al. 1975). Other studies, e.g. Shukla and Mintz (1982) and Yeh et al. (1984), found that in the general circulation model used at the time precipitation showed sensitivity to soil moisture variation.

3.5 Second generation land surface models

Likely, the increase in computational resources with time, and the interest in understanding land-atmosphere processes paved way for additional development and complexity in the description of the land surface (e.g. Dickinson 1984). While the group of parameterizations used to described the land surface in the late 1960s and 1970s are now referred to as first generation land surface models, it was not until the mid-1980s that the group of parameterizations used to describe land surface processes were given proper names.

Two early examples of named land surface models are the Biosphere Atmosphere Transfer Scheme (BATS) (Dickinson et al. 1986) and the Simple Biosphere Model (SiB, Sellers et al. (1986). According to Pitman (2003) two models built philosophically on Deardorff (1978) and implemented the now commonly used Jarvis-type surface evaporation resistance formula (Jarvis 1976). Jarvis (1976) showed that by using non-linear least square regression they could independently relate the different components of vegetation surface resistance (r_s) to vapor pressure deficit, photosynthetic active radiation (PAR), temperature, and leaf water potential, giving the total resistance as the product of each of the latter components.

BATS was first developed to be used with the general circulation model of NCAR, and later implemented in NCAR's global, spectrally discretized Community Climate Model (CCM). CCM was intended for use for both global circulation studies and long-term weather forecasts, and was further intended

[4] that it a model including just one horizontal cell, but several cells in the vertical dimension

[5] an increase in temperature reduces snow cover, which then lowers the mean albedo which increases absorbed sunlight, which increases surface temperature

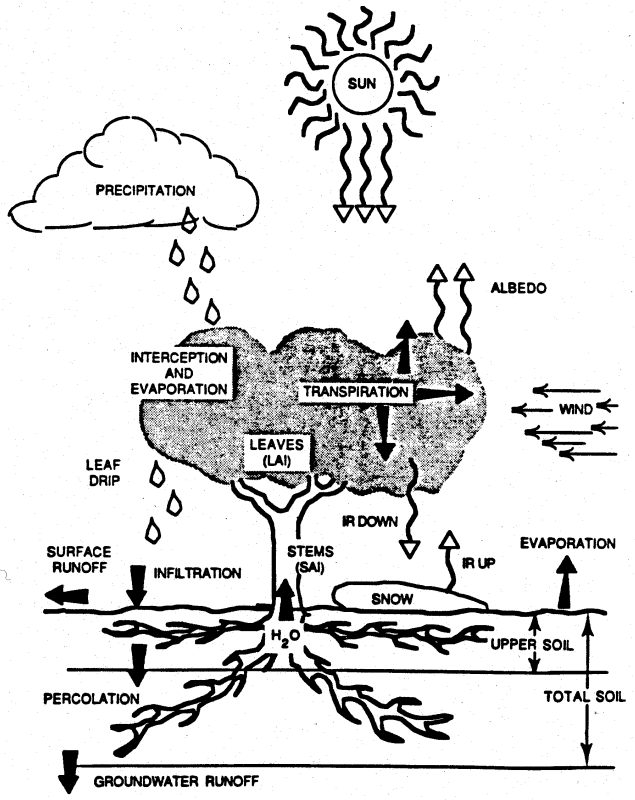

Figure 3.2: Schematic of an early version of the land surface model BATS. Reprint of Figure 2 "*Schematic diagram illustrating the features included in the land surface parameterization scheme used here"* of Dickinson et al. (1986) (CC BY-NC 4.0)

to be used and developed by a larger community, including universities. Its code was thus freely available and documented. Freely and openly sharing code and technical documentation of numerical weather prediction models and global circulation models became widespread, and would continue until the present day.

The early version of BATS, described in Dickinson et al. (1986), consisted of about 3000 lines of code. It was developed with the possibility to run the model coupled to a global climate model, or in a stand-alone, offline version, i.e. driven by previously derived near-surface atmospheric variables, with no coupling from the soil to these atmospheric variables. Instead of relying on near uniform prescriptions of surface parameters, each model grid square was assigned a land cover type and with soil information. Data from various ground based surveys were assessed and aggregated to provide gridded land cover and soil information. The land cover classification was reduced to 18 vegetation/land

Parameter	Land Cover/Vegetation Type*																	
	1	2	3	4	5	6	7	8	9	10	11	12	13	14	15	16	17	18
Maximum fractional vegetation cover	0.85	0.80	0.80	0.80	0.80	0.90	0.80	0.0	0.60	0.80	0.10	0.0	0.80	0.0	0.0	0.80	0.80	0.80
Difference between maximum fractional vegetation cover and cover at temperature of 269 K	0.6	0.1	0.1	0.3	0.3	0.5	0.3	0.0	0.2	0.6	0.1	0.0	0.4	0.0	0.0	0.2	0.3	0.2
Roughness length (m)	0.06	0.02	1.0	1.0	0.8	2.0	0.1	0.05	0.04	0.06	0.1	0.01	0.03	0.0024	0.0024	0.1	0.1	0.8
Depth of the total soil layer (m)**	1.0	1.0	1.5	1.5	2.0	1.5	1.0	1.0	0.5	1.0	1.0	1.0	1.0	1.0	1.0	1.0	1.0	2.0
Depth of the upper soil layer (m)**	0.1	0.1	0.1	0.1	0.1	0.1	0.1	0.1	0.1	0.1	0.1	0.1	0.1	0.1	0.1	0.1	0.1	0.1
Rooting ratio (upper to total soil layers)	3	8	10	10	10	12	8	9	4	3	8	5	5	5	5	5	5	10
) Vegetation albedo for wavelengths <0.7μm	0.10	0.10	0.05	0.05	0.08	0.04	0.08	0.20	0.09	0.08	0.17	0.80	0.06	0.07	0.07	0.05	0.08	0.06
) Vegetation albedo for wavelengths >0.7μm	0.30	0.30	0.23	0.23	0.28	0.20	0.30	0.40	0.26	0.28	0.34	0.60	0.18	0.20	0.20	0.23	0.28	0.24
) Minimum stomatal resistance ($s\ m^{-1}$)	150	250	250	250	250	250	250	250	250	250	250	250	250	250	250	250	250	250
) Maximum LAI	6	2	6	6	6	6	6	0	6	6	6	0	6	0	0	6	6	6
) Minimum LAI	0.5	0.5	5.0	1.0	1.0	5.0	0.5	0.0	0.5	0.5	0.5	0.0	0.5	0.0	0.0	5.0	1.0	3.0
) Stem (& dead matter) area index	0.5	4.0	2.0	2.0	2.0	2.0	2.0	0.5	0.5	2.0	2.0	2.0	2.0	2.0	2.0	2.0	2.0	2.0
) Inverse square root of leaf dimension ($m^{-1/2}$)	10	5	5	5	5	5	5	5	5	5	5	5	5	5	5	5	5	5
) Light sensitivity factor ($m^2\ W^{-1}$)	0.01	0.01	0.03	0.03	0.03	0.03	0.01	0.01	0.01	0.01	0.01	0.01	0.01	0.01	0.01	0.01	0.01	0.03

*See definitions in Table 1.

**Soil depths in code are in mm as are all water storages to make the conversion factor 1.0 between water amounts and SI energy fluxes.

Figure 3.3: Table 2 (p. 17) of Dickinson et al. (1986) (CC BY-NC 4.0), listing vegetation/land cover parameters for each of 18 vegetation/land cover classes defined.

cover types. Parameters associated with the land cover and soil classes, such as albedo, minimum stomatal resistance, soil porosity, were taken from a range of literature sources, and listed in tables (see Figure 3.3 and 3.4), which were read by the model during model integration. In contrast to most land surface model these days, the model included a varying depth of the total active soil layer, which varied between 0.5 to 2 m according to the grid cell land cover type (see 3.3).

The Simple Biosphere Model, SiB, is described as a biosphere model, designed for use with global circulation models, intended to be both as physically and biologically realistic as possible (Sellers et al. 1986). Plant soil moisture potential was calculated by summing up soil moisture from the surface to the vegetation type's given root depth (i.e. the number of soil layers the plant has access to). Also SiB had the possibility to be run offline, to be tested and evaluated when driven by measured near-surface variables. Sellers et al. (1986) notes the atmospheric variables necessary for driving SiB in an offline mode: grid area average values of near-surface temperature, humidity, wind speed, and incident shortwave and longwave radiation, partitioned into five sources. A lack of high quality field data available for testing the land surface model was, however, also noted in Sellers et al. (1986).

Sellers et al. (1986) stated a long-term goal of producing a fully interactive

TABLE 3. SOIL PARAMETERS

FUNCTIONS OF TEXTURE

Parameter	Texture Class (from sand (1) to clay (12))											
	1	2	3	4	5	6	7	8	9	10	11	12
Porosity (volume of voids to volume of soil)	0.33	0.36	0.39	0.42	0.45	0.48	0.51	0.54	0.57	0.60	0.63	0.66
Maximum soil suction (m)	0.03	0.03	0.03	0.2	0.2	0.2	0.2	0.2	0.2	0.2	0.2	0.2
Saturated hydraulic conductivity (mm s^{-1})	0.2	0.08	0.032	0.013	8.9×10^{-3}	6.3×10^{-3}	4.5×10^{-3}	3.2×10^{-3}	2.2×10^{-3}	1.6×10^{-3}	1.1×10^{-3}	0.8×10^{-3}
Ratio of saturated thermal conductivity to that of loam	1.7	1.5	1.3	1.2	1.1	1.0	0.95	0.90	0.85	0.80	0.75	0.70
Exponent "B" defined in Clapp & Hornberger (1978)	3.5	4.0	4.5	5.0	5.5	6.0	6.8	7.6	8.4	9.2	10.0	10.8
Moisture content relative to saturation at which transpiration ceases	0.095	0.128	0.161	0.266	0.300	0.332	0.378	0.419	0.455	0.487	0.516	0.542

/FUNCTIONS OF COLOR

Parameter	Color (from light (1) to dark (8))							
	1	2	3	4	5	6	7	8
Dry soil albedo								
< 0.7 μm	0.23	0.22	0.20	0.18	0.16	0.14	0.12	0.10
⩾ 0.7 μm	0.46	0.44	0.40	0.36	0.32	0.28	0.24	0.20
Saturated soil albedo								
< 0.7 μm	0.12	0.11	0.10	0.09	0.08	0.07	0.06	0.05
⩾ 0.7 μm	0.24	0.22	0.20	0.18	0.16	0.14	0.12	0.10

Figure 3.4: Table 3 (p. 22) of Dickinson et al. (1986) (©CC BY-NC 4.0), listing soil parameters for each of six soil classes defined.

biosphere-atmosphere model yielding predictions over decades or longer, with vegetation responding to increasing CO_2. Land surface model which include a vegetation actively responding to and interacting with carbon and nitrogen via photosynthesis are now referred referred to as a third generation land surface model (e.g. Pitman (2003)). These third generation models are sometimes used together with global climate models which simulate a biogeochemically and radiatively coupled carbon–climate system with time-varying greenhouse gases. Some of these models have to option to include dynamic vegetation, which allows shifts in vegetation species due to changing climate conditions (Randall et al. 2018). Third generation land surface models will not be further discussed here as they are not used in the studies conducted within this thesis. Third generation land surface models are most relevant when greenhouse gas budget and cycling is considered, for simulations of vegetation and atmosphere interaction over periods where observations of vegetation is not available, and/or during long climate simulations (several decades or more). The added complexity of these third generation land surface models further implies larger possibilities for ill-posed model set-ups resulting in unwanted or unrealistic results (see e.g. Rosero et al. (2010) and other examples given in Randall et al. (2018)).

Also underground processes were better described in second generation land surface models, e.g. vertical flow of water through soil. Dickinson (1984) stated that "*soil moisture determines the demand rate at which occurs the switch over from demand limited to supply-limited evapotranspiration*" and outlined in

detail a numerical scheme for soil water diffusion based on Darcy's law and the continuity equation (the Richards equation, see Eq. 2.9).

The initial versions of BATS and SiB included fairly simplified descriptions of snow cover. For thermal processes snow was parameterized as part of the upper soil layer, while for hydrological processes snow was parameterized separately (Pitman 2003). Multi-layer snow models were not implemented in land surface models until the 1990s (Pitman 2003). Surface albedo was given attention, perhaps inspired by the work in Hansen (1983), where a early version of a global climate model was found to have an improper snow masking depth for vegetation resulting in a surface albedo of 0.6-0.7 in forested parts of Canada and Siberia, while observations indicated an albedo of 0.35-0.55. In BATS (Dickinson et al. 1986) surface snow cover fraction and surface roughness were modulated by the presence of vegetation protruding from snow, which was estimated by scaling up the vegetation's assigned roughness length (see row c) of Table 3.3. The surface albedo values (listed for different vegetation types in Table 3.3) were mostly based ground measurements by Monteith, but publications including satellite derived albedo values were also considered in their derivation.

3.6 Physiographic fields in land surface models

Dickinson (1983) lamented that: "*One of the primary obstacles to improving model descriptions of surface processes over the earth is the great heterogeneity in surface structure over most land areas. The minimum horizontal spatial elements of global climate models are generally rectangular surfaces with sides at least several hundred kilometers in dimension. Over such a surface, there can be thousands of individual land elements as characterized by particular vegetative cover, soil type, and terrain. The question as how to properly characterize averages over these individual elements within a model grid square is still largely unresolved. Before such complexities are addressed, it is perhaps important to first better establish the sensitivity of different climate parameters to various aspects of simplified but still somewhat realistic average descriptions of land surfaces.*". He also noted in a subsequent publication, Dickinson (1984), that, concerning the Richard's equation, "*the largest source of error in applying the parameterization will come from difficulties in specifying the soil hydraulic properties due to their vertical and horizontal variability*".

Since the mid 1980s the increase in computational resources have facilitated land surface modeling at a much higher resolution; however, uncertainty surrounding the physiograhic fields which map out soil and vegetation types, and the parameter values assigned to these soil and vegetation types, such as soil porosity, vegetation rooting depth, and minimum stomatal resistance, particularly when scale issues are considered, are still seen as main challenges within land surface modeling (Mendoza et al. 2015; Cuntz et al. 2016; Samaniego et al. 2017; Dai et al. 2019).

3.6.1 Physiographic fields - land cover

The land cover classes included in the BATS (Dickinson 1983) were based on work summarized in Wilson and Henderson-Sellers (1985) and Matthews (1983, 1984). Wilson and Henderson-Sellers (1985) digitized 53 land cover classes based on global and national atlases. Matthews (1983) produced a 1°x1°data-base of land cover using the UNESCO vegetation classification system (UNESCO 1973), drawing upon more than 100 global and national sources, and used satellite imagery to complement the ground based sources. The satellite data used was NASA Landsat images, which were used to find fingerprints of human land use among natural vegetation. In Matthews (1984) the land cover classification of Matthews (1983) was altered to provide input to the Goddard Institute for Space Studies General Circulation Model II (GISS Model II), reducing the total number of classes to eight.

Satellites had been monitoring the weather since the 1960s, and observations from satellites were consulted in e.g. Hansen (1983) and Dickinson et al. (1986) when determining sea-ice and surface albedo. Matthews (1983) stated that "*neither the specifics of vegetation type nor of crop combinations can be determined from visual interpretation of these images [...]*", referring to the satellite images from Landsat. The Landsat program launched in 1972, with what is now referred to as Landsat 1, the first satellite with a dedicated purpose of studying and monitoring landmasses. With time information from satellites would provide a range of information on land cover and land use, first making use of vegetation's differing reflection in parts of the visible and near infrared electromagnetic spectrum, as quantified in the normalized difference vegetation index (NDVI). In 1994 the first satellite derived global land cover dataset was published, with a 1° resolution, based on data from the Advanced Very High Resolution Radiometer (AVHRR) (see further references within Friedl et al. 2002).

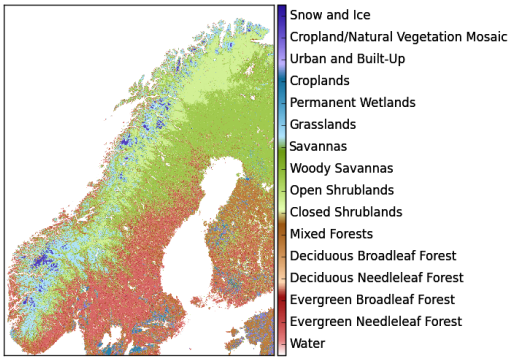

Figure 3.5: Land cover types in and around Norway according to Broxton et al. (2014b)

The range of information possible to retrieve from satellites on land cover and land use was, and is still, used to better emulate land surface processes within numerical models. The sheer mass of rather high quality products satellites can retrieve on vegetation has likely fueled land surface model development. Example of more recent satellite derived products are e.g. more robust global, high resolution products providing land cover type classification (Broxton et al. 2014b) (see Fig. 3.5 depicting the land cover classification in and around Norway), maximum green vegetation fraction (Broxton et al. 2014a); and regionally refined products, such as forest albedo values for Norway, Sweden, and Finland (Bright et al. 2018). These products are not without uncertainty, and ground and near-ground based surveys are still of importance, both for refining retrieval algorithms and their post-processing (e.g. Majasalmi et al. 2018).

3.6.2 Physiographic fields - soil

Early offline modeling results using BATS showed that surface temperature had comparable sensitivity to the specified soil texture as to specified vegetation characteristics (Wilson et al. 1987a). Different soil textures are linked to different soil water conditions, as seen in Fig. 2.5. The soil data used in the early version of BATS (Dickinson et al. 1986) was based on the FAO Soil Map of the World (FAO/UNESCO 1974). This soil map was the product of a 20-year project starting in 1961, with the aim to map out the soil types of the world, while at the same time producing trans-national communities of soil experts, and harmonizing soil mapping and labeling (Selcer 2015). According to Dai et al. (2019) the FAO Soil Map of the World "*was made based on soil surveys conducted between the 1930s and 1970s and technology that was available in the 1960s*". The derived soil map consisted of 18 76x110 cm sheets including 5000 different map units, and thus resulted in a product which was not easily accessible for non-experts. Due to the coarse scale of the map (1: 5 000 000, about 50 km), only three textural classes, sand, clay, and silt were included (FAO/UNESCO 1974).

The schematic of the texture classes displayed in FAO/UNESCO (1974) is reproduced in Fig. 3.6. In Wilson and Henderson-Sellers (1985)'s "A global archive of land cover and soils data for use in general circulation climate models" the dataset was digitized with a 1°x 1°resolution, and prepared for use in numerical models. Prior to this there was, at the time, according to Wilson and Henderson-Sellers (1985), "*no global soils data in digital form*". For the BATS-implementation the data was upscaled to BATS coarser grid (about 4.5°latitude x 7.5°longitude), and with this the three texture classes were increased to twelve classes (see the table of BATS soil properties, Fig. 3.4).

Later on different digitized version of the FAO Soil Map of the Wold were constructed, e.g. the 1°x 1°version of Zobler (1999). Figure 3.7 shows the soil types in and around Norway according to Zobler (1999). Though it is outdated in many regions, the FAO Soil Map of the World has been widely used up until today (see e.g. a recent overview in Table 1 in Dai et al. 2019). It served up until very recently as the only soil map available for regions outside the conterminous

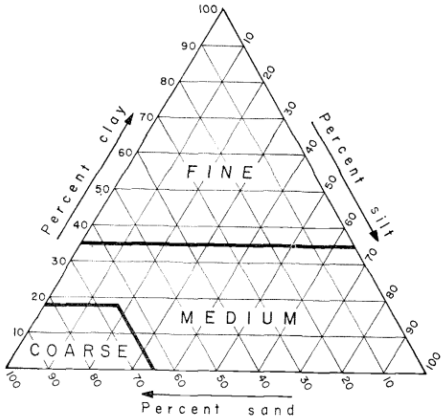

Figure 3.6: Schematic of the texture classes used in FAO/UNESCO (1974) on the basis of the upper 30 cm soil composition of clay, silt, and sand. The schematic is from FAO/UNESCO (1974).

United States for the state-of-the-art Weather Research and Forecasting (WRF) model (Skamarock et al. 2008)[6] (see also Dy and Fung 2016).

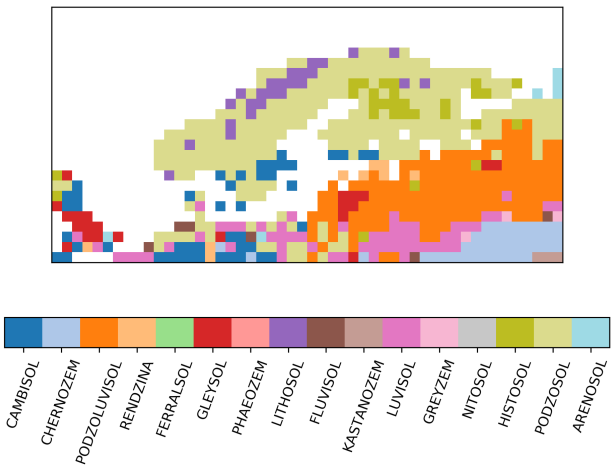

Figure 3.7: Soil types in and around Norway according to a digitized, 1°x1°resolution, version of the FAO Soil Map of the Wold by Zobler (1999).

Figure 3.8 depicts the default soil texture classes for a model domain covering areas in and around Norway and Great Britain. The dominant soil texture

[6] until April 2017, with the release of WRF ARW WPS version 3.9, see https://www2.mmm.ucar.edu/wrf/users/wpsv3.9/updates-3.9.html

category for the whole soil column is categorized as the soil texture of the top soil layer (Lin and Cheng 2016). Limited emphasis on soil texture has also been evident in other numerical weather prediction models. The global numerical weather forecasting model of the European Centre for Medium-Range Weather Forecasts (ECMWF), the Integrated Forecast System (IFS), was run with a globally uniform soil texture until the modifications described in Balsamo et al. (2009) were implemented.

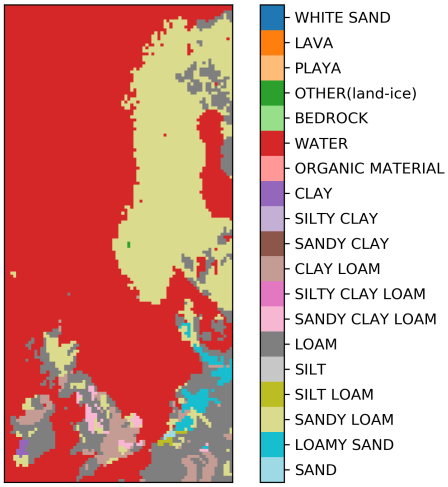

Figure 3.8: Soil texture in and around Norway and Great Britain as categorized using WRF 3.5.1 (the soil map is from the file initializing a WRF run (wrfinput) using the Noah land surface model).

Recently, more updated global soil maps have been derived, e.g. Batjes (2016). Most climate and weather forecasting models ingest global physiographic fields. For soil information in particular, the quality of these fields hinge on that information from regional and national surveys is made available; however, data on soil type and texture from Norway was only very recently added to the World Soil Information Service (WoSIS) (Batjes et al. 2020).

Another relevant physiographic field for land surface modeling, which is even less well mapped than soil type and texture, is depth to bedrock. Depth to bedrock or depth of soil (and unconsolidated material) is linked to land surface model soil variables and parameters, since these usually are given in volumetric form (see e.g. Deardorff 1978). In the land parameterization of Hansen (1983) outlined for GISS Model I and II optimum soil depths were chosen to minimize the error in the daily surface temperature for the upper soil layer, and the annual amplitude of surface temperature for the lowest soil layer. Hansen (1983) found that optimum levels were 10 cm for the upper layer and 4 m for the lower layer, and further noted that that these depths are close to the typical 1/e damping

depths for daily and annual thermal waves. Today many land surface models (LSMs) have a uniform soil depth between two or three meters.

3.7 Parameters and model complexity

The physiographic fields determining vegetation type and soil type are sometimes referred to as primary parameters, while their associated qualities, such as roughness length, soil porosity, etc. may be referred to as secondary parameters (see e.g. Yang 2004). Land surface models differ in whether parameters are treated as primary or secondary fields. As an example, when configuring the WRF model one has the option to treat maximum albedo in the presence of snow as a physiographic field, ingesting a gridded dataset based on satellite observations, or to treat it as a secondary parameter associated with local vegetation type.

Secondary soil parameter values such as soil hydraulic and thermal parameters are usually estimated by pedotransfer functions, often based on soil texture (see e.g. Dai et al. 2019). Many early land surface models used the results from Clapp and Hornberger (1978), which based their results on soil samples from 34 locations with the United States. Clapp and Hornberger (1978) cautioned that the average values they presented had not been verified and that there was considerable variability in their derived values also within soil texture types.

Different land surface models have been produced tailored for different applications. The SiB model intended to realistically simulate controlling biophysical processes (Xue et al. 1991); however, it was criticized for describing above ground processed in a complex way, while below ground processes were more simply described (Pitman 2003). Its large number of estimated parameters was found to make model sensitivity studies and validation difficult (Xue et al. 1991). Xue et al. (1991) described a simplified version of SiB model (SSiB), where the number of input parameters were reduced from 54 to 26, by describing vegetation in one layer instead of two, and simplifying other parameterized processes. The simplification about halved the computational cost of running the model.

Wood et al. (1992) questioned whether the versions of BATS and SiB, at the time, were of an appropriate level of complexity when confronted by lack of micrometeorological data to calibrate or validate the models, and when considering that a more simple model could be run with a higher resolution demanding the same computational resources. In the same Paper It was demonstrated that a three parameter, calibrated version of the variable infiltration capacity (VIC) water balance model, sometimes been referred to as the Nanjing model, driven with precipitation, potential evapotranspiration, temperature from a general circulation model, could reproduce observed flow with higher skill than a bucket model.

The large number of land surface models and their complexity, led to project such as the Project for Intercomparison of Land-Surface Parameterization Schemes (PILPS) (e.g. Henderson-Sellers et al. 1993). Findings from PILPS, presented in Chen et al. (1997), evaluated the capacity of 23 land surface

models for simulating surface fluxes, surface net radiation, upward longwave radiation, and ground heat flux for a full year at an observation site in the Netherlands. Second generation models generally outperformed first generation land surface models. Particularly, the lack of stomatal resistance under non-water-stressed conditions limited the first generation schemes.

In Koster et al. (1999) annual runoff produced by nine different land surface models run offline at a 1°x1°resolution were aggregated within catchments to river discharge and compared to observations. Their skill was additionally benchmarked by comparison to the annual discharge derived from a climatological relation provided in Budyko (1958). At an annual time-scale the models did not perform significantly better than the simple Budyko-relationship. Not much later Milly and Shmakin (2002) tested the added value of increasing model complexity in various sub-processes, a study in line with the suggestion by Manabe (1982) of evaluating added complexity incrementally (see Sec. 3.3). Particularly, the use of globally variable land parameters over uniform parameter values were tested, and, following Koster et al. (1999), the modeled annual discharge was benchmarked against that provided by the simple semi-empirical Budyko (1958)-relationship. Unlike Koster et al. (1999), Milly and Shmakin (2002) found that their model provided significantly better estimates than the Budyko (1958)-relationship, and speculated that the poor results found in Koster et al. (1999) partly was attributed to errors in the precipitation forcing data. Milly and Shmakin (2002) further found that introducing globally variable land parameters significant enhanced the capability of the model to simulate the annual runoff ratio.

As of 2001 there existed 30 different land surface models (Bastidas et al. 2001). Efforts were undertaken to bound parameter values via calibration to observational data. Bastidas et al. (2001) found that optimization state variables in a version of BATS by calibrating parameters to fit observations deteriorated BATS fluxes, and vice versa; and hypothesized a deficiency in the BATS model structure. Duan et al. (2001) stated that the secondary parameters, those tied to soil and vegetation classes, had not been fully validated using retrospective forcing data and corresponding data on land surface characteristics.

Duan et al. (2001) listed several arguments against the a priori definition of land surface parameter values. One was that tuning of various land surface models had resulted in different optimal parameter values for different land surface models and configurations. Another argument was scale dependency, as previous studies (e.g. Koren et al. 1999) had showed that models run with forcing data of differing spatial and temporal resolution resulted in different output. The latter had in part to do with the coarse scale forcing data at the time, which provided a mean precipitation flux for grid cell covering perhaps 3000 km^2, while real world precipitation includes local areas of high intensity precipitation and other areas with no precipitation. The parameterization of rainfall infiltration to soil, or, oppositely, rainfall exceeding the maximum infiltration capacity diverted to overland flow (Hortonian flow), is, unsurprisingly, sensitive to the averaging out of rainfall in time or space.

Results from the Model Parameter Estimation Experiment (MOPEX) was presented in Duan et al. (2006). Their finding included that calibration has huge

potential for improvement parameter estimation, and that hydrological processes were differently represented in different models, and that all of the models were (are) imperfect. A contributing cause to the differing parameter sets found after calibration or tuning of various land surface models is the complexity of the land surface and land surface models. The large number of included parameters in land surface models leads to a high degree of freedom in the models. This means that in a calibration or tuning exercise of model parameters, different parameter sets may result in the same model output.

According to Beven and Freer (2001): "*Given current levels of understanding and measurement technologies, it may be endemic to mechanistic modelling of complex environmental systems that there are many different model structures and many different parameter sets within a chosen model structure that may be behavioural or acceptable in reproducing the observed behaviour of that system.*". This may be referred to as the equifinality concept, and is used where " *[...] there should be sufficient interactions among the components of a system that, unless the detailed characteristics of these components can be specified independently, many representations maybe equally acceptable*".

While the original version of BATS (Dickinson et al. 1986) was described by four authors using 79 equations and 69 pages, a third generation land surface model, the Community Land Model version 4.5 (CLM4.5 Oleson et al. 2010), needed 26 authors, 1093 equations and 420 pages, and additional technical notes (Bonan 2019). Bonan (2019) notes that while an increase in process richness and thus complexity may increase realism, it likely reduces robustness and reliability. This is due to the general increase in model flexibility with model complexity, as depicted in Fig. 3.9. If validation is limited, it is possible that a model produces right results for the wrong reasons, i.e. that parts of the model which are not validated includes unrealistic parameterizations, inappropriate parameter values, or unrealistic values for state variables. Models may also be tuned to produce realistic output for certain variables, even while ingesting incorrect meteorologic forcing data.

Physically based models are necessary to construct model experiments altering physical boundary conditions in order to learn something about the real world. Any physically based model which includes one or more parameters which are poorly constrained by observations must be considered partly empirical (Abramowitz 2012). A high number of processes included in a model, which in part rely on parameter values which are unmeasured or impossible to measure, increases a model's degree of freedom and decreases parameter transferability (e.g. Newman et al. 2017). A large number of poorly constrained calibrated or tuned parameters may ultimately produce what Kirchner (2006) termed "*mathematical marionettes*", i.e. models which are overfitted and likely will provide poor results when confronted with out-of-sample validation data.

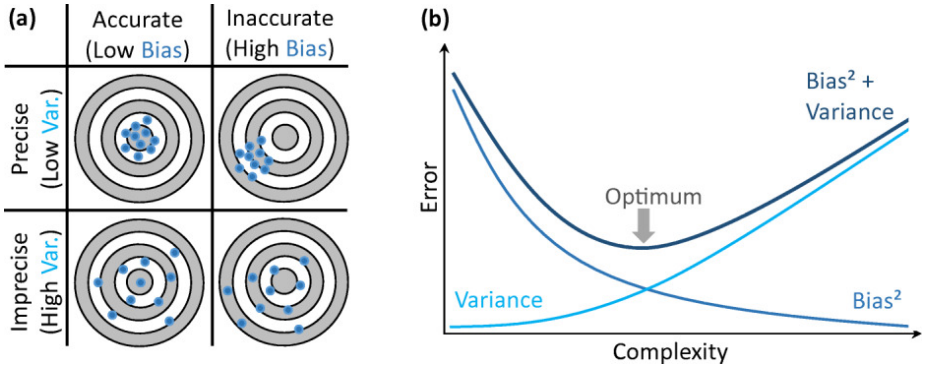

Figure 3.9: The figure, reproduced from Höge et al. (2018) visualize concepts and effects of bias and variance: "*(a) Accuracy and precision visualized as bias and variance of shots on a target. Bias is the distance between the target center and the average position of shots. Variance is the spread of shots around their average. (b) Decomposition of total squared error into squared bias and variance (after e.g., Friedman et al. (2001)). Bias is supposed to decrease and variance is supposed to grow with increasing model complexity, both due to growing model flexibility. Their superposition forms a minimum that marks optimal model complexity.*" Reprint of Fig. 1 in Marvin Höge et al. (Mar. 2018). "A Primer for Model Selection: The Decisive Role of Model Complexity". In: *Water Resources Research* 54.3, pp. 1688–1715. ISSN: 19447973. DOI: 10.1002/2017WR021902, reused with permission, ©2018 American Geophysical Union

3.8 Conceptual hydrological models

Early general circulation models were built with the purpose to replicate general features of the climate system by modulating and refining the early, physically based models developed for numerical weather prediction (see Sec. 3 and 3.2). Hydrology is the study of the land component of the hydrological cycle (Peel and McMahon 2020). Early hydrological models varied in structure and philosophy, but have generally been developed to aid in managing, understanding, and making predictions for water resources. Hydrologic models used for watershed modeling, as will be discussed here, have been approached from both the perspective of an engineer and that of a earth scientist (see Fig. 3.10). According to Dooge (1986) the engineer uses observations to check predictions made with the purpose of controlling materials and forces of nature for the use and benefit of man, while a scientist uses observations to validate and compare predictions from models built on a theoretical system of various hypotheses in order to understand nature. Similarly to Dickinson (1984) (see Sec. 3.6), Dooge (1986) lamented that "*hydrologic processes can be analyzed on the basis of the equations of hydraulics and soil physics, but the high degree of spatial variability in a catchment of any size poses serious problems of parameter specification*"; and that "*the linking of the hydraulic conductivity which is a macroparameter to the microparameters*

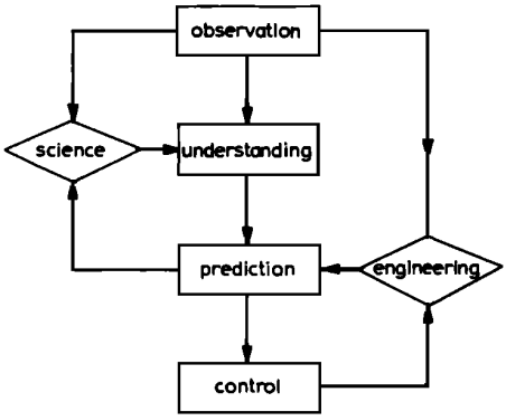

Figure 3.10: Dooge (1986) illustrated that hydrology, as one of the earth sciences and as the basis of water resources development, has been approached both from the perspective and motivation of an earth scientist, and from the perspective and motivation of an engineer. Reprint of Fig. 1 in James C. I. Dooge (Aug. 1986). "Looking for hydrologic laws". In: *Water Resources Research* 22.9S, 46S–58S. ISSN: 00431397. DOI: 10.1029/WR022i09Sp0046S, reused with permission ©1986 American Geophysical Union

of the porous media structure has been tackled using both deterministic and probabilistic models but remains a daunting problem".

This problem, and that hydrological modeling has often been approached from an engineering point of view, has resulted in models which range from black-box regression type models, where it is hard to derive a physical meaning from model parameters, to more physically based models, akin to land surface models. The models that fall in between these two categories are sometimes referred to as conceptual models. All of the modeling approaches, however, are subjected to the fact that "*The physical laws governing water movement at small scales have been understood for decades. What we still don't understand well enough is how to apply these physical laws to systems that are complex, heterogeneous on all scales, and often poorly characterized by direct measurement.*"(Kirchner 2006). Further, as put forward in Clarke (1973): "*[...] models originally formulated without reference to physical processes may have parameters for which some physical interpretation can be found, whilst models apparently firmly based in physics may contain obviously empirical components*".

An example of a model parameterization often used in conceptual hydrologic models is the degree-day method for computing snow-melt. It usually relates daily snow-melt to near-surface temperature on days where the temperature is above zero, and may be presented as:

$$M = max(C_{temp}(T2 - T2_{melt}), 0); \tag{3.1}$$

where M is snow melt, C_{temp} is an empirical parameter, $T2$ is the near-surface temperature, $T2_{melt}$ is the near-surface temperature associated with snow melt.

The degree-day method for snow melt known to be old; a version is e.g. provided in Horton (1915) : "*The writer's experiments indicate that the melting constant is about 0.04 to 0.06 inch depth of water per 24 hours per degree of temperature above 33°F.* ". Different snow-melt index-based algorithms were reviewed and tested in *Snow hydrology; summary report of the snow investigations.* (United States Army Corps of Engineers 1956). The engineers or scientists at the time were knowledgeable of the physical processes governing snow melt; however, the snow report summarized: "*Temperature indexes of snow-melt have been widely used to estimate runoff from snow-melt for areas where it's contribution to total runoff warranted consideration. Temperature was used because it was generally thought to be the best index of the heat transfer processes associated with snow-melt and because it was (and in many cases will continue to be) the only reliable and regularly available meteorological variable.*"(United States Army Corps of Engineers 1956). Indeed, a more recent study (Ohmura 2001) found that incident longwave radiation flux was the major source of snow- and ice-melt in several observational datasets from glaciers, and that the near-surface temperature was, in most cases, closely connected with the incident longwave radiation. The lack of information on below-ground features and the reliance as much as possible on reliable and regularly available meteorological variables partly explain why many of the hydrological models developed were something in-between black-box regression models and physically-based models.

3.9 Numerical hydrological models

During the late 1950s and early 1960s the availability of rapid computational resources and long-term records of both precipitation and runoff laid the foundation for the for the development of computer-based hydrologic models. In 1967, current advances and issues were summarized in "Digital Computer Simulation in Hydrology" (Dawdy and Thompson 1967). The usefulness of using digital computers for modeling was highlighted by referring to Folse (1929), where it is stated that the computation of an early model for the hydrologic cycle involved 41 people, 16 years, and over 34000 man-hours to complete.

The earliest well documented and successful attempt of a rainfall-runoff modeling on a digital computer is perhaps "Computation of a synthetic streamflow record on a digital computer" (Linsley and Crawford 1960). A water-accounting procedure was programmed for a solution on an IBM 650 computer to synthesize daily streamflow when rainfall records were available. It is noted that the work was not based on scientific research, but rather a project of necessity, resulting from a request for advice from the university (Stanford University) on increasing the capacity of the one of their water supply reservoirs. The treatment of potential evaporation in the model was discussed at length, as it was parameterized in a rather simple manner, in part due to lack of observational data. The model was further developed and later given the name the Stanford

Watershed Model (see references within Crawford and Linsley 1963; Crawford and Burges 2004).

An early application of the Stanford Watershed Model is described in *Application of Stanford watershed model concepts to predict flood peaks for small drainage areas* (Clarke 1968). The model was applied to a small catchment in Kentucky. The purpose of the study was to "*equate total rainfall to total runoff and losses throughout a span of years, and, if all significant hydrological parameters may be deduced; then through direct measurements of some essential input descriptors and indirect estimates of others, the water-balance concept may be applied to other basins.*" (Clarke 1968).

The model was what is now referred to as a lumped model, meaning that the entire catchment was treated as a single numerical unit which is integrated in time. The most important model input, precipitation data, was retrieved from a nearby precipitation gauge. The model included 23 parameters, some which could be derived from watershed characteristics, some by analysis of measured discharge, and some by trial and error (i.e. tuning or calibration).

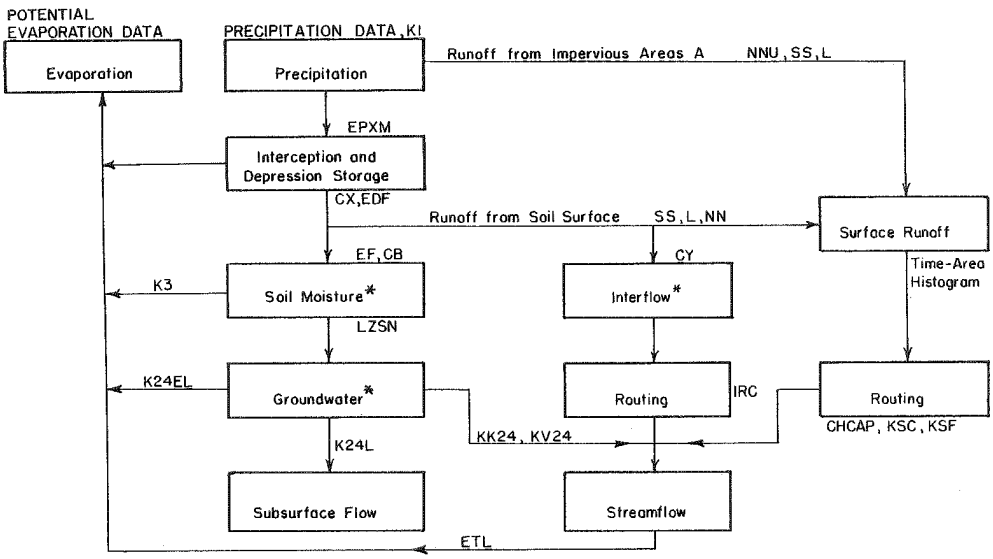

Figure 3.11: Reproduction of Fig. 28 in K. D. Clarke (1968). *Application of Stanford watershed model concepts to predict flood peaks for small drainage areas.* Tech. rep. Division of Research Department of Highways Commonwealth of Kentucky, "*Fig. 25. Moisture Accounting in Stanford Watershed Model* ".

Parameters which could be derived based on watershed characteristics included the ratio of average rainfall on the catchment to the average rainfall at the rain gauge, a parameter representing the catchment vegetation's interception rate of precipitation, and a parameter representing rate of loss through evaporation. The latter two could be taken from vegetation dependent tabular values. Two

recession rate parameters for base-flow and interflow could be estimated using graphical techniques analyzing observed flood events. Parameters defined by tuning or calibration included e.g. indices defining within and above soil storage capacity and infiltration capacities. Evaporation was scaled to potential evaporation data fed into the model, since "*Flood peaks are not sensitive to evaporation rates*" (Clarke 1968). Further, in order to simplify the computational process, and since "*snow-melt does not produce extreme flood events on small Kentucky watersheds*" (Clarke 1968) all precipitation was treated as rain. By ingesting estimates of potential evaporation and not representing snow, the model did not need temperature data input. The Stanford Watershed Model had at the time other versions including snow processes (see e.g. Anderson 1968). Just a few years later the version IV of the Stanford Watershed Model was selected for use in the operational U. S. National Weather Service river forecast system (Staff Hydrologic Research Laboratory 1972)

Another early hydrological model was the Streamflow Synthesis and Reservoir Regulation (SSARR) model. Similarly to the Stanford Watershed Model, SSARR was also developed first for the Pacific coast of the U.S.. While the model was first developed in 1957 for an IBM 650 computer for synthesizing streamflow in the Columbia River Basin, it was later applied various places, e.g. as described in *Application of Streamflow Synthesis and Reservoir Regulation-" SSARR"-Program to the Lower Mekong River* (Rockwood 1968).

A myriad of different computer-based hydrological models were developed from the 1960s and on-wards, see e.g. Table S1 in Peel and McMahon (2020). With time, distinct versions of existing models were developed. An example is the HBV model (Bergström and Forsman 1973), developed at the Swedish Meteorological and Hydrological Institute, which now exits in a range of forms, e.g. also in a gridded version modified and further developed by Norwegian researchers (Beldring 2008). The first distributed or gridded hydrological model was presented in Huggins and Monke (1968). The principles of a physically based hydrological model was outlined in Freeze and Harlan (1969). A model which was both distributed and physically based, implementing e.g. the Richards equation for capillary flow (Eq. 2.9), did not come about until around the same time as second generation land surface models were developed (see Sec. 3.5), with the Système Hydrologique Europeén (SHE) model (Abbott et al. 1986). Unlike the second generation land surface models, many hydrological models are not freely and openly distributed; and some have been developed as commercial software (e.g. the MIKE SHE model, see Refsgaard et al. 2010).

The numerical hydrological modeling community has also been concerned with what is known as the inverse problem, that is establishing model parameter values from more or less well known model input and output values (e.g. Moradkhani and Sorooshian 2008). This is referred to as an ill-posed problem due to the non-uniqueness of the problem's solutions (see also Sec. 3.7 on equifinality). The first step of numerical weather prediction, analysis of the initial state of the atmosphere, is also usually tackled as an inverse problem (see e.g. Bauer et al. 2015).

Establishing model parameter values which are not available from observations

were first done based on expert knowledge or tuning. With time model calibration procedures were refined, and various methods and software have been developed to assist in objective parameter calibration (e.g. Bastidas et al. 2001; Duan et al. 2001; Wang et al. 2019). An highly influential publication was "River flow forecasting through conceptual models part I - A discussion of principles" (Nash and Sutcliffe 1970), where an a dimensionless goddness-of-fit index for use in objective optimization was suggested; now known as the Nash-Sutcliffe efficiency score.

The different approaches and philosophies hydrological models are based on are still debated. Physically based models akin to land surface models might be better suited for "what-if"-studies, exploring e.g. the effect of vegetation change; however, several studies have found lumped and more conceptually-based hydrological models preform well in model inter-comparison studies evaluating runoff in the form of catchment discharge (e.g. Newman et al. (2017)). The simpler models usually demand less forcing data. They are also more computationally efficient, which is important considering that hydrological models rely on model calibration.

Since the first conceptual models were developed there has been some emphasis on reducing the number of calibrated parameters to counter over-fitting (see e.g. Fig. 3.9) and thus make the models more robust (Peel and McMahon 2020). At the same time there has been an emphasis to include a realistic description of the fundamental physics, particularly as this can be useful for the purpose of transferring calibrated parameters to ungauged catchments (i.e. for parameter transferability). The simplified description of some processes, relying on calibrated parameters for e.g. evaporation, have also been criticized as less than optimal for certain applications, e.g. climate change studies, since the parameter values might not be valid in other climates than that considered in the model calibration and validation (see e.g. Milly and Dunne 2011a; Arsenault et al. 2018). The possibility of achieving robust calibrated values hinges on long time-series of high-quality observational data. Further, the implementation of e.g. a physically-based evaporation scheme requires similarly long-term, high quality estimates of additional meteorological variables than precipitation and evaporation, namely incident radiation, and near-surface humidity, and wind. As discussed in Sec. 2.7, a myriad of approaches has been developed to implement more physically based evaporation algorithms, often relying on empirical estimates of the unobserved meteorological variables.

4. Meteorological and hydrological observational data

Observational data are at the center point of land modeling, whether or not the models are mainly data driven or more physically-based. Further, the theories which form the basis of the models have been developed and refined in confrontation with observations (see Fig. 1.1). Milly and Shmakin (2002) divided error sources of model variables into intrinsic model errors, forcing errors, and parameter errors, and stated that, at the time, they believed that insufficient characterization and control of forcing data errors, particularly precipitation, is the main limiting factor when land models are tested, since large forcing data errors likely mask model improvement.

An early example of this issue is documented in "Investigation of the sensitivity of the land-surface parameterization of the NCAR Community Climate Model in regions of tundra vegetation" (Wilson et al. 1987b), where the climate model's high temperature bias in the arctic tundra was sought redeemed by altering land surface parameterizations. However, unrepresentative observational data (due to majority of observation stations located on or very near the coast) and biases in the model's estimated incident radiation (July net radiation was likely around 50% too high in places[1]) made model development more difficult. A newer example is "Global evaluation of runoff from 10 state-of-the-art hydrological models" (Beck et al. 2017a) where precipitation biases is found to likely be the cause of discharge biases, particularly peak-discharge in snow-dominated areas. The study further speculates that poorer performance of the land surface models compared to global hydrological models in snow-dominated regions may be due to a reliance on sub-optimal forcing data.

Offline runs of land surface models and hydrological models rely on atmospheric data input. The minimal input for a rainfall-runoff model is rainfall (see Sec. 3.8). Near-surface temperature is a necessary input if evaporation is included with a minimum level of sophistication, or if snow processes are represented. Further, more physically based processes-descriptions require additional inputs which drive the surface energy balance, such as near-surface humidity, incident shortwave and longwave radiation, and wind information. Land surface models developed for use coupled with atmospheric models need similar atmospheric variables, usually with a sub-daily temporal resolution, and often require more detailed information on the frequency distribution of received radiation. Soil moisture, snow cover, snow depth, and snow water equivalent observations are relevant for model initialization and validation. The inverse problem of rainfall-runoff modeling rely on river discharge observations. Validation of evaporation estimates in both land surface models and hydrological models require evaporation observations, while validation and development of

[1] "[...] presumably because of poor estimation of cloud cover and properties" (Wilson et al. 1987b)

models solving the surface energy balance also require observations of the two turbulent fluxes, received, reflected and emitted radiation, and ground heat flux.

The availability of various observational data vary wildly according to variable. Precipitation and temperature are and have been measured for a considerable time. According to Dooge (1988) both rain gauges and stream gauges were first likely deployed for societal purposes. The first stream gauges were deployed four thousand years ago to relate the level of the Nile to the level of taxation. Similarly, the first record of a rain gauge a thousand years ago in India was also used to estimate taxation. Temperature is a variable which required sensor development to measure. Discontinued, early measurements were at least retrieved along side instrument development from the 17th century (e.g. Camuffo and Bertolin 2012). Around the same time early versions of the barometer, measuring pressure, and hygrometers, measuring humidity, were also developed. From the middle of the 19th century more systematized national networks of weather observation were established with standardized thermometer shelters, and the invention of the telegraph provided a means for data communication. The number of weather stations increased greatly in the 20th century, particularly with the development of automated weather stations; however, to this day many regions are poorly sampled, particular locations away from population centers, such as in the mountains. Further, a number of sources of measurement errors exist in present time, e.g. the underestimation of precipitation in the form of snow due to wind effects (e.g. Wolff et al. 2015).

The measurement of incident radiation required both theoretical and instrument development (see Sec. 2.1 and Ohmura (2014)). While instruments measuring radiation existed from the last decade of the 19th century, dome-covered (all-weather) instruments were not developed until the 1950s (Ohmura 2001). Not long after satellite measurements became useful for climatology, particularly the quantification of the top of the atmosphere (TOA) energy balance. Satellite-based quantification of surface radiative fluxes require, due to changing effects of the atmosphere in between, and a limited number of surface observations to inform calibration, additional input data and additional empirical or physical algorithms. As a result higher uncertainty is associated with satellite estimates of surface radiative fluxes than those from the TOA (Wild 2017).

Radiation sensors are more costly than e.g. temperature sensors, and also require more in terms of maintenance. The Baseline Surface Radiation Network (BSRN) was proposed established by the World Meteorological Organization (WMO) in 1988, to collect and archive freely available, high-quality ground-based radiation measurements (Driemel et al. 2018). When it commenced in 1992 data from just 9 stations met the standards. Today the network includes around 64 stations (see Fig. 4.1 and BRSN Webiste (2016)). Measurements of shortwave radiation are generally more available than longwave radiation, and the latter is lacking to a point where it hinders both model development and validation (e.g. Carrer et al. 2012; Erlandsen et al. 2019). For comparison, for the recent years, temperature and precipitation data are available from around 16000 and 40000 observation station, respectively, in the data archive GHCN-Daily (Jaffrés 2019) (see also Fig. 4.2 depicting surface meteorological data ingested by a weather

forecasting model).

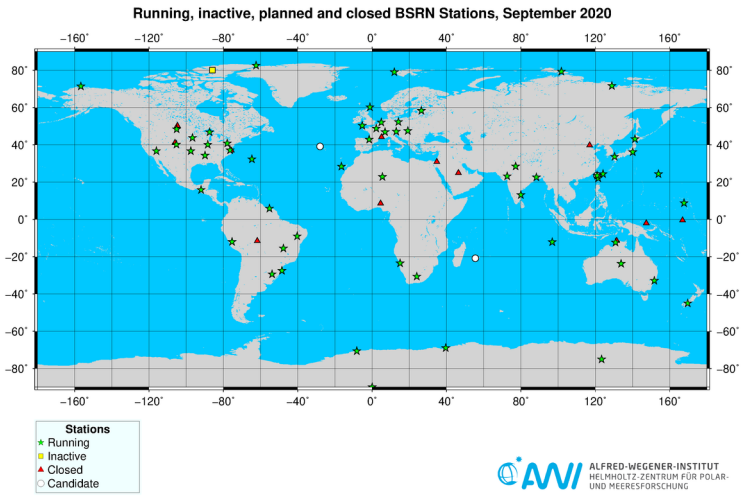

Figure 4.1: Stations included in the Baseline Surface Radiation Network. Figure retrieved from the BRSN Webiste (2016).

Over time, the first of the two-step procedure for numerical weather prediction, outlined by Richardson, has been refined. Present day models ingest a vast amount of data, not only from weather stations on land, but also oceanic observations, e.g. from ships, buoys, and oil platforms, and upper-air observations from e.g. weather balloon-soundings, air crafts, and satellites. The increase in data availability, better methods to ingest the data, model development, and techniques to work with uncertainty in initial conditions by running several streams of the same forecast based on slightly different initial conditions (ensemble forecasting), has led to *The quiet revolution of numerical weather prediction* (Bauer et al. 2015). The skill in predicting large scale features, such as the height of the 500hPa pressure level (geopotential height) 3 to 10 days in advance has increased with about one day per decade (Bauer et al. 2015).

Data from numerical weather prediction models may act as a surrogate for observational data, and have the quality of coverage and a high number of output variables; some which are prognostic, e.g. surface temperature and incident radiation, while others are diagnostic, e.g. 2-meter temperature, and snowfall. The development of global weather reanalysis projects, which are based on combining a numerical weather prediction model, kept at a frozen model development state for consistency, advanced data assimilation techniques, and vast amounts of observational data, particularly data not readily available in time to be used in operational weather forecasting, have become essential for atmospheric science research (Randall et al. 2018). The first global reanalysis product (see Kalnay et al. 1996) was developed in the mid-1990s, with a horizontal resolution of around 210 km. The available variables from the reanalysis were

ranked from A to C according to their reliability, largely based on whether they were heavily constrained by observational data (e.g. upper-air temperature and wind) or derived solely from the model fields (e.g. precipitation).

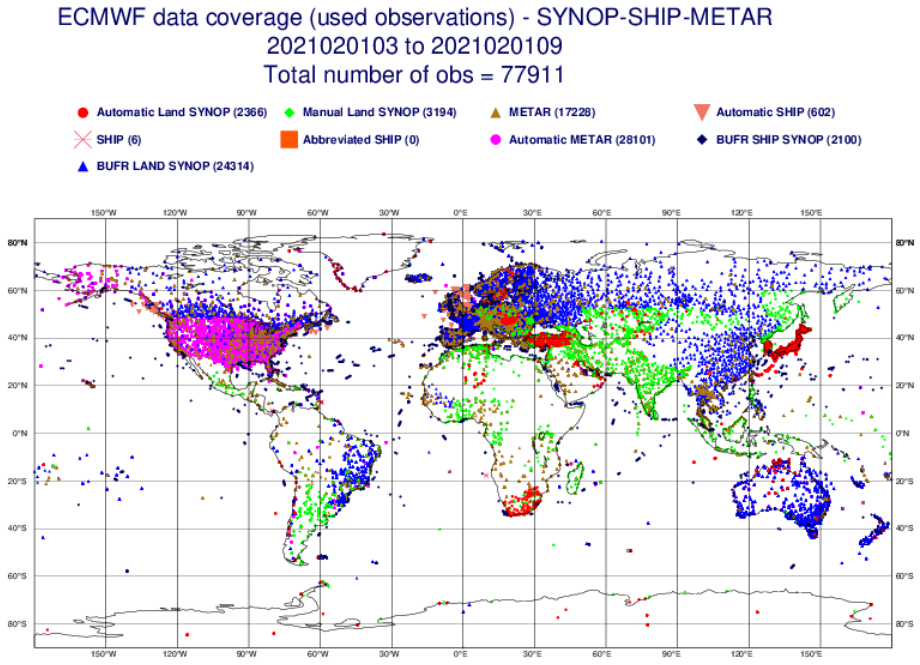

Figure 4.2: Geographical data coverage ECMWF website (n.d.).

While the use of the exact same numerical weather predictions model in a reanalysis system is a source of consistency, the ingested observational data vary with time. Time-varying observational input is usually a caveat of gridded observational datasets as well. Additionally, the very process of data assimilation, and the many different short forecasts the reanalysis prognostic fields are a product of, means that the surface water and energy balance is not closed over time in these products (e.g. Kauffeldt et al. 2015; Hersbach et al. 2020). Reanalysis datasets may further have considerable biases in variables which are less constrained by observations (e.g. Balsamo et al. 2015). One may speculate that some variables, might have benefited less from development within numerical weather prediction if their errors did not significantly degrade the quality of regularly reported output of short-term weather forecasts. An additional aspect concerning the output of global reanalysis datasets are issues regarding spatial scale. At the perhaps 1-km resolution of a regional hydrological model, output from a global reanalysis might not be representative.

The representativeness of a variable at a given scale is in part related to the variable's spatial auto-correlation. At a given instance atmospheric temperature has a smoother spatial field than e.g. precipitation. Near the land surface

temperature is closely connected to topography. The first law of thermodynamics, the hydrostatic equation, and the ideal gas law provide some information to adjust temperature valid for one elevation to another elevation. These type of physical relationships are used in hydrological and land surface model frameworks to adjust temperature from forcing data with one mean grid cell elevation to the grid cell elevation of the model to be run. Elevation adjustment does not resolve biases unrelated to altitude. Further, the presence of ground snow, dense vegetation, water bodies, and orographic features such as sheltered valleys and ridge tops may cause vertical gradients deviating from those assumed under standard elevation adjustment procedures (e.g. Daly et al. 2010). At a higher horizontal resolution these "problematic" features need to be addressed. Thus, with land surface models run at resolutions of one kilometer or less: "*High-resolution meteorological datasets of sufficient accuracy are thus greatly needed.*" (Bierkens et al. 2015).

Surface latent heat flux, or evaporation, is a variable produced by both hydrological models and land surface models. This essential variable for determining the surface water and energy balance is particularly hard to measure (see e.g. Sec. 2.6 and 2.7, Fisher et al. (2017), Allen et al. (2020)). A variety satellite-derived evaporation estimates exist. Since evaporation is not possible for the satellites to measure directly algorithms are used to produce satellite-based evaporation products. The algorithms used are "*almost indistinguishable from land surface hydrology models, such that it is questionable that this qualifies as "observation".*" (Fekete et al. 2015). Depending on the choice of input data, particularly the choice of incident radiation data, the algorithms arrive at drastically different estimates of global terrestrial evaporation (Badgley et al. 2015). Surface or near-surface measurements are thus still essential data sources regarding evaporation. Since around 1997 surface measurements based on eddy covariance methods have routinely been measured in a global network, called FLUXNET, with more than 140 long-term measurement sites (in 2001) (Baldocchi et al. 2001), and more today.

The monitoring of river discharge near the outlet of a river is beneficial, not only because of its application for flood and engineering design, but also because it is constitutes a spatial aggregate of the catchment water balance. It thus holds information from considerable areas, which can help constrain and correct e.g. precipitation estimates based on scattered rain gauges which routinely under-catch snowfall (e.g. Beck et al. 2017b). Without the presence of a dam or a glacier the catchment annual discharge may not exceed catchment annual precipitation. However, in order to constrain precipitation further a sensible minimum and maximum range of evaporation must be estimated. In Beck et al. (2017b) a similar formula as the Budyko-relationship depicted in Fig. 2.4 was used to estimate long-term catchment evaporation.

Similarly to the difference in code sharing policies between hydrological and meteorological numerical model developers, there is also a difference in the availability of e.g. stream gauge and rain gauge observations. Budgetary constraints and political instabilities hinder the collection and sharing of in-situ streamflow measurements (Hannah et al. 2011). In some cases streamflow

observations are measured by privater companies, e.g. hydro-power companies, with little incentive for sharing data. According to Fekete and Vörösmarty (2007) 50% of continental land mass were at some point considered monitored by streamflow gauges, however, it was emphasized that the data coverage in the global archive, the WMO Global Runoff Data Centre (GRDC), has decreased rather than increased in the recent decades. The lack of data availability and homogenization of streamflow measurements have likely contributed to their under-utilization in climate studies. Hopefully, the continued emphasis on streamflow data value and the general global push towards FAIR (Findability, Accessibility, Interoperability, and Reusability) guiding principles for scientific data management and stewardship (Wilkinson et al. 2016) will contribute to an increase in freely available data from in-situ streamflow monitoring in the future.

5. Thesis synthesis

The previous chapters (Chapter 2, 3, and 4) have outlined the historical and international context of the studies undertaken as a part of this thesis, and should illustrate the connectivity of the objectives, methods and models used, and the research questions and hypotheses investigated (see Sec. 1.1). Each of the studies touch upon related, but slightly different issues within hydrological and land surface modeling in Norway. The following part of this thesis presents the study region, Norway. Thereafter a brief overview of the numerical models and methods used is presented (Sec. 5.2), before each study and their major findings are presented (Sec. 5.3). Finally, a summery and outlook is offered (Sec. 5.4).

5.1 Placement - Norway

Norway is a country located in the north-west corner of continental Europe. Mainland Norway boarders on the eastern side mostly to Sweden, however, the northern regions also border to Finland and Russia. While its land boarder is about 2500 km long, and its baseline coastline is of similar length, the coastline including bays and fjords is about ten times longer. Mainland Norway stretches several latitudes, from 58° North across the polar circle to 71° North.

Inland the Scandinavian Mountains divide the Norway's western and eastern regions. The combination of the Scandinavian Mountains and Norway's location on the eastern end of the North Atlantic, with prevailing westerly winds, results in high annual precipitation on Norway's western coast. The eastern regions leeward of the mountain range receive distinctly lower precipitation rates. Mean annual precipitation received mainland Norway is likely around 1300 to 1400 mm (e.g. Erlandsen et al. 2021). The mean temperature (1971–2000) varies from -4°C in the mountains to about 7°C near the coast. The 2-meter temperature increased by 0.5°C per decade between 1976 and 2014 (Hanssen-Bauer et al. 2017). At least a third of precipitation falls as snow. The length of the snow season varies from a few days to 300 days a year, depending on latitude, elevation, and distance from the coast.

About 38% of the land area is forest covered, while elsewhere the land surface is dominated by bare rock and shallow deposits (see e.g. Fig. 4.1). Relatively shallow soils with a low water storage capacity in large parts of the country make way for a rapid runoff response to precipitation (Beldring 2002), but also for moisture stressed conditions in periods of meteorological drought (e.g. Buckland et al. 1997). The annual evaporation is not well constrained by observations. In Erlandsen et al. (2021) evaporation was estimated in a hydrological model to be on average around one-sixth of the received precipitation; however, in regions of South-East Norway it was more than 40% of received precipitation.

The larger amounts of precipitation received has facilitated a large hydro-power industry within Norway. The first hydro-power plants were established

in the latter decades of the 1800s to provide energy for industry development. In the 1930s around 3000 hydro-power plants were established in Norway, and electricity was available to more than 70% of the population (Fladen et al. 2017). Today more than 90% of Norway's produced electricity is from hydro-power. Norway has been referred to as the 'green battery' of Europe, as the largest hydroelectric producer in Europe, also with the largest installed hydro-power generation capacity (Askeland et al. 2019).

The surface water balance in Norway is interesting to understand in order to provide information for the public. This can be done through flood and drought forecasting, weather forecasting, and climate projections. A range of sectors rely and benefit from this type of information, e.g. the hydro-power industry, the agricultural and forestry industry, insurance companies, and the public and governmental sector which provide land use plans, zoning plans and municipal plans.

The three studies conducted in this thesis improve upon a range of unresolved issues relevant for land surface modeling within Norway. The first study uses a regional numerical climate model to investigate the atmospheric sensitivity to perturbations in surface compounds. The second study compares the quality of various estimates of near-surface humidity and incident radiation, i.e. atmospheric drivers of the land surface, and provides a new method for providing estimates of these variables suitable for kilometer-scale land surface modeling in Norway. The third study utilizes the dataset developed in the second study, and implements structural changes in a gridded hydrological model covering mainland Norway to allow sensitivity to near-surface humidity and incident radiation. The augmented hydrological model is then run over several decades to shed light on mainland Norway's surface water balance.

5.2 Models and methods

The work presented in this thesis has involved the use of several numerical models. In Paper I a version of a regional climate model commonly used for research and weather forecasting, the Weather Research and Forecasting (WRF) model, specifically the Advanced Research WRF, version 3.5.1 (Skamarock et al. 2008) was used. The model version used is presented in further detail in Paper I. Validation of the two-year control run of the model was performed by comparing the model output to gridded observational data and station observations using methods developed in Python, and using a version of the MET software (Brown et al. 2009), ingesting surface and upper-air observations of temperature and humidity in Binary Universal Form for the Representation (BUFR) format (see Fig. 5.1). Some general aspects of the WRF model framework are discussed in Sec. 5.3.2), and an example of the numerical components of the model is provided in Table 5.1.

WRF model structure and parameters depend on model configuration, since a wide range of options are available to the user. For each physics region of the model (land surface, surface layer, planetary boundary layer, shortwave

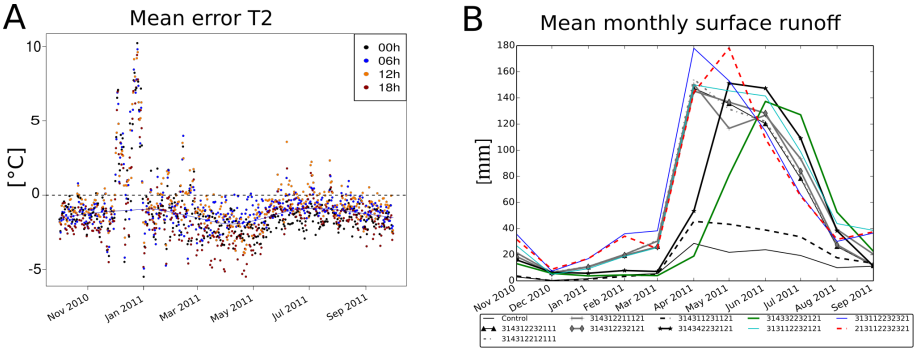

Figure 5.1: The panels provides examples of the model validation and experiments conducted for the study region defined in Paper I. **A** displays output from MET software; the mean error of the control run's diagnosed 2-meter temperature compared to surface observations at different hours of the day (marker color) between October 1st 2010 and September 30th 2011. **B** displays the monthly areal mean surface runoff from offline, experimental runs (October 1st 2010 - September 30th 2011) of the community Noah land surface model with multiparameterization options [Noah-MP] (e.g. Niu et al. 2011). The offline runs were conducted with output from the control run of Paper I as forcing, utilizing an option within the WRF-Hydro framework (Gochis et al. 2013).

radiation, longwave radiation, micro-physics, cumulus), a hand-full to a dozen scheme options are available. In addition to the scheme options used in Paper I, a few additional scheme options were tested, such as the use of a parameterization providing a diurnal variation in SST for daily SST (see Fig. 5.2). The effect of varying the model's physical scheme options was further investigated for a subset of the model integration time. The model was restarted around the start of the melting season of 2011 (April through June) with different scheme options. Options tested were different variants of the land surface scheme, a different set of radiation and cloud microphysics schemes, and exclusion of the cumulus scheme (see Fig. 5.3).

The land surface model used in Paper I is the Noah land surface model (see e.g. Mitchell 2001, and references therein) with alterations in the snow parameterizations described in Wang et al. (2010). Noah is an open source, community model. It builds upon the Oregon State University (OSU) model. OSU was chosen in the 1990s to be further developed for use in the National Centers for Environmental Prediction (NCEP) operational weather and climate prediction based on existing familiarity with the model, and fair performance in the PILPS (see Sec. 3.7, Mitchell (2001)). The OSU model was developed to be used in NWP and thus to be computationally efficient (Mahrt and Pan 1984; Ek et al. 2003). It shares several similarities with the first second generation land surface models, BATS and SiB, described in Sec. 3.5, e.g. that soil and vegetation secondary parameters are read from table values. An example of

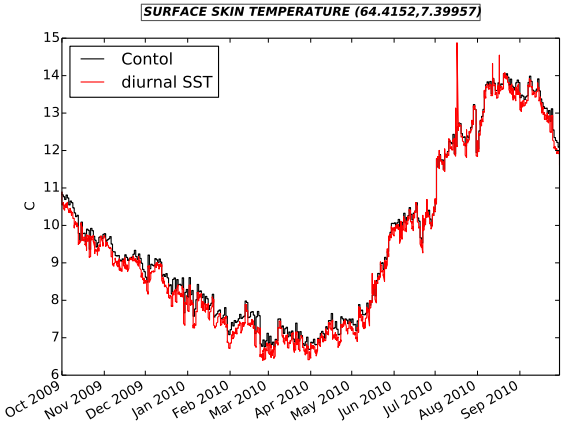

Figure 5.2: A WRF option tested, but not used in Paper I was the inclusion of a diurnal SST parameterization (Zeng and Beljaars 2005), as it was found to slightly reduce the daily average SST throughout most of the year. The parameterization reduced SST with about 0.5°C and in summer produced, in many locations, temperature spikes which look spurious.

the numerical components of the model is provided in Table 5.1. More details regarding the Noah land surface model are provided in Paper I.

Since atmospheric coupling to land (and ocean) was investigated in detail in paper I, the model was not initialized with land surface and soil fields from the reanalysis providing lateral boundary conditions for the model, as is commonly done. Instead, a framework (the HRLDAS software, Chen et al. (2007)) for running the land surface model Noah offline, was implemented to provide soil and surface variables. This is due to fact that soil, also as represented in the land surface model, has a significant capacity for storing heat and moisture over days, months, or longer, depending on the ground characteristics and soil depth. The energy and water received and exchanged by the land surface is related to elevation, i.e. the orography of the model. Additionally, different land surface model schemes have different structures which means soil values from one model (in this case the land surface model used in Era-Interim) is not necessarily suitable for another model (e.g. Kristiansen et al. 2012). To spin-up the soil and surface fields Noah was run looping over the hydrological year preceding the staring point of Paper I ten times, using data from the reanalysis Era-Interim as forcing data. Fig. 5.4 shows the initial soil moisture in the third soil layer of Noah without spin-up and after 1-year of spin-up using HRLDAS.

For Paper II the libRadtran software package version 1.7 for radiative transfer calculations (Mayer and Kylling 2005) was used to provide surface incident clear-sky shortwave radiation to be used to quality control the observations of incident shortwave radiation. Paper II developed a method to generate high resolution

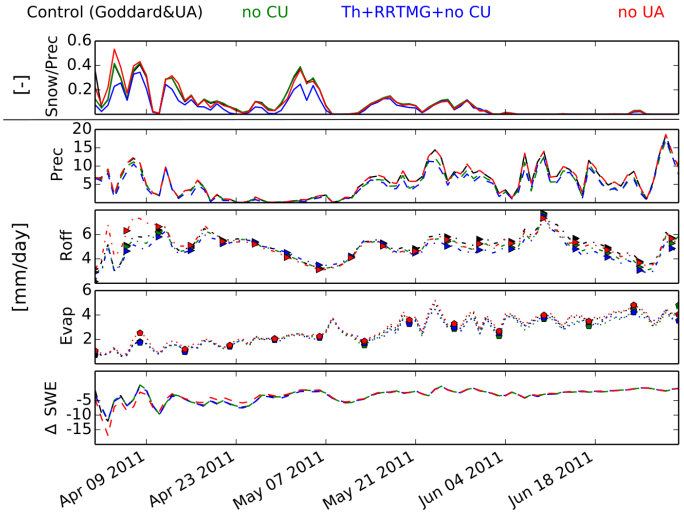

Figure 5.3: Time-series of daily emulated fraction of precipitation diagnosed as snowfall (Snow/Prec), precipitation (Prec), runoff (Roff), surface evaporation (Evap), and day to day changes in snow cover (Δ SWE) when the model configuration options in Paper I were altered. Data from the control run is marked in black, a model version run without the cumulus scheme is marked in green, a model version run without the cumulus scheme and further with different schemes representing microphysics and radiation is marked in blue, and a model version where a different version of the land surface model is used is marked in red.

estimates of incident radiation and near-surface humidity estimates, which also was published. The software was written in Python (doi: 10.5281/zenodo.1435010), making particular use of the package xarray (Hoyer and Hamman 2017) for data handling in general, xesmf (Zhuang 2020) for regridding and reprojecting the data, and Dask (Dask Development Team (2016), a flexible library for parallel computing in Python). This was first applied to the Era-Interim reanalysis and two versions of the SeNorge dataset. For paper III the method was applied to the Era5 reanalysis and a recently updated version of the SeNorge dataset. The new dataset is stored at Zenodo: doi: 10.5281/zenodo.3351430), and the code used to compile it is provided in Appendix II.

For Paper III a conceptually based, gridded version of the hydrological model HBV, described in Beldring et al. (2003), was used. Versions of the HBV model has been used by the Norwegian Water and Energy Resources Directorate for decades for research and operational flood forecasting. The HBV model was first developed in Sweden in the early 1970s (e.g. Bergström and Forsman 1973), and shares similarities with the Stanford Watershed Model and the SSARR

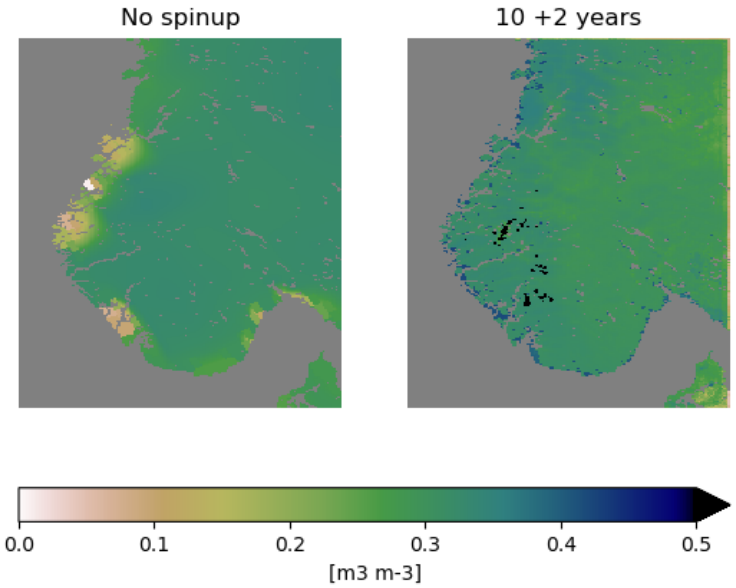

Figure 5.4: The panels depict soil moisture in Noah's lowest soil layer (from 1 to 2 m depth) at October 1st. The left panel displays the soil moisture field from Era-interim interpolated by the WRF model pre-processor to the inner domain of Paper I (see Fig. 5.5). The right panel shows soil moisture after a 10-year offline spin-up and two additional years where the land surface model is run in a coupled mode within the WRF model. The areas with the highest amounts of soil moisture are in and around glaciers.

model described in Sec. 3.9. HBV was developed to be a model of reasonable complexity, requiring input data readily available in Swedish catchments. The Beldring et al. (2003) version of the HBV model is further described in Sec. 5.3.4 and paper III. Paper III also involved calibrating the HBV model, implemented with a 1-by-km resolution for mainland Norway. This involved using the PEST: Model-Independent Parameter Estimation and Uncertainty Analysis (Doherty 2015) software, calibrating model parameters for each of five regions defined.

The components of the WRF model, the Noah land surface model, and the HBV model are listed and compared in Table 5.1. It is evident that the three models have features in common, such as the reliance on surface physiographic fields. The Noah land surface model may be integrated in the WRF model or in stand-alone mode using the e.g. HRLDAS or WRF-Hydro software. The models differ in their complexity; WRF is by far the most complex "model", while the HBV model is the least complex. The computational cost of running

the WRF model is much greater than running the Noah land surface model offline or running the HBV model.

Table 5.1: Schematic defining numerical model components and presenting examples of these from a land surface model (Noah), a regional weather forecasting and research model (WRF), and a distributed hydrological model (HBV). The table is adapted from Williams et al. (2009)

Numerical model components	Definition	Example Noah-LSM (Paper I)	Example WRF (Paper I)	Example HBV (Paper III)
System boundary	Limits of the physical domain where processes are integrated	South-Norway's surface incl. vegetation to soil 2 m below ground	10°W-20°E, 57-59°N, surface or 2 m below ground to TOA[1] (50 hPa)	Norway's land land surface incl. vegetation and soil
State variables	Variables which may be computed by their previous state in time (prognostic variables)	Surface and soil moisture and temperature, SWE, snow albedo (α_s)	Atmospheric, surface, and soil temperature and moisture, SWE, α_s	Upper and lower reservoir water level, SWE
Forcing input	Variables needed at system's spatial boundary to evolve the state variables	Near-surface sub-daily T, wind, RH, incident radiation, precipitation	Atmospheric T, humidity pressure wind	Near-surface daily T, precipitation, incident radiation, wind, RH
Initial conditions	State variables at initial time	As for state variables	As for state variables	As for state variables
Model structure	Numerical discretization of variables; their evolution and interaction	Interception capacity, aerodynamic, & soil water diff. resistance α_s decay, snow melt	Conservation of momentum, moisture, & mass Eq. of state, Penman-Ep, snow melt, interception	Conservation of mass, soil water resistance, to diffusion, snow melt
Parameters	May be global gridded, primary, secondary, unit-less, uncertain scale-dependent, determined by calibration	Orography, gravitational constant, soil and veg. types, Zilitinkevich thermal roughness length, beta (β), soil conductivity	Orography, gravitational constant, soil and veg. types, ozone climatology, Zilitinkevich thermal roughness length, beta (β), orographic drag, soil conductivity	Orography, gravitational constant, soil and veg. types, degree-day snow-melt factor, snow-fall under-catch correction factor, beta (β), field capacity
Model output	State variables and diagnostic variables	Runoff, surface outgoing longwave radiation, snow depth, surface evaporation, sensible heatflux	Runoff, surface outgoing longwave radiation precipitation, cloud cover, 2-meter temperature and humidity	Runoff, SWE, soil moisture deficit, groundwater table depth, surface evaporation

5.3 The papers and their major findings

5.3.1 Paper I : Sensitivity of the Terrestrial Surface Energy and Water Balance Estimates in the WRF Model to Lower Surface Boundary Representations: A South Norway Case Study

The first study (Paper I) investigates, in a regional numerical climate model, how perturbations in three surface compounds impose changes in the surface water and energy balance in South Norway. Changes were implemented in a version of the WRF model covering South Norway with a horizontal resolution of 3.7 km. The model domain is depicted in Fig. 5.5. The experiments were implemented for both a relatively cold and dry hydrological year (2009/10) and a relatively warm and wet hydrological year (2010/11).

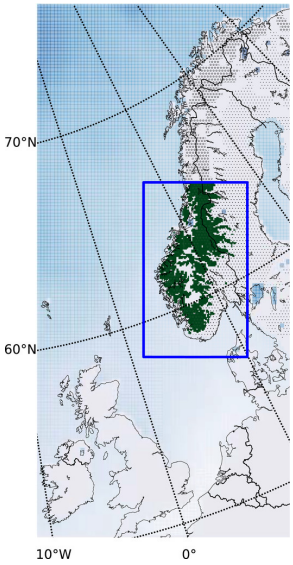

Figure 5.5: Image reproduced from Erlandsen et al. (2017) Journal of Hydrometeorology 18, 1; 10.1175/JHM-D-15-0146.1. The outer area of the figure depicts the outer model integration domain. The inner domain, or study area, is within the blue rectangle. Areas originally covered with evergreen needleleaf are marked with dots. Areas where mixed or wooded tundra are replaced by an evergreen needleleaf forest in the Veg experiment are marked with a dark green color (stars) in the inner (outer) domain.

Paper I is thus a sensitivity study of a numerical weather forecasting model. These types of studies are as old as numerical weather forecasting models are. Sensitivity studies have been conducted to better understand our numerical models, to discover possible errors in them, and, if the models are fair, sensitivity studies can further our understanding of real world sensitivity to various pertur-

bations. This latter precaution also holds for impact studies in general. Early examples of sensitivity studies have been discussed in Sec. 3.4, e.g. Charney et al. (1975), Shukla and Mintz (1982), Hansen (1983), and Yeh et al. (1984), and also includes the early sensitivity studies of the BATS land surface scheme published in Wilson et al. (1987a,b), discussed in Sec. 3.6 and Chapter 4.

The study resonates with the suggestion provided in Dickinson (1983), stated in Sec. 3.6. Segments of the text are repeated also here, since the concern is still valid today. While today's numerical models may be run with a horizontal resolution of a few kilometers, parts of the physiographic data which the numerical models build on are poorly sampled to this day (see e.g. Sec. 3.6 and Fig. 3.8). Dickinson (1983) stated "*One of the primary obstacles to improving model descriptions of surface processes over the earth is the great heterogeneity in surface structure over most land areas. [...] The question as how to properly characterize averages over these individual elements within a model grid square is still largely unresolved. Before such complexities are addressed, it is perhaps important to first better establish the sensitivity of different climate parameters to various aspects of simplified but still somewhat realistic average descriptions of land surfaces.*".

Studies comparing the sensitivity of terrestrial atmospheric variables to land-cover change and SST anomalies in other regions have found they produce impacts of a similar magnitude (Findell et al. 2009; De Noblet-Ducoudré et al. 2012). In Paper I we evaluated and compared the role of feedbacks exerted from changes in the land cover to the remote effects of a perturbation in SST, using a regional climate model. The purpose of the experiments was to learn more about the sensitivity of the surface water and energy balance in South Norway to changes in each of these compounds; reflecting on possible effects of an improper description of these compounds and the effects which might be expected if these compounds change, e.g. due to climate change.

Three surface compounds were perturbed, the height of the boreal forest line (the *Veg*-experiment), ground snow cover (the *Snow*-experiment), and SST (the *SST*-experiment). The current context of each experiment and the research questions RQ1.1, RQ1.2, and RQ1.3 (see Sec. 1.1) are listed in the following:

- (RQ1.1) *Veg*: There is a considerable uncertainty regarding historical and future land-cover distribution (see e.g. Sec. 3.6 and e.g. Meiyappan and Jain (2012). A recent study using a dynamic global vegetation model (a third generation LSM, see Sec. 3.5) found that it produced large over-estimations of boreal forest in Norway (Horvath et al. 2021). Agricultural abandonment, grazing pressure, tree planting campaigns, and climate warming influence the density and extent of the Norwegian forests (Bryn 2008; De Wit et al. 2014). In many regions forest lines have expanded to higher altitudes. However, because of historic and current land-use practices, in certain areas the forest line can be as much as 200 m below its present potential (Wehn et al. 2012). *To shed light on this model experimental runs were conducted where mixed and barren tundra below*

1150 m were replaced with evergreen needleleaf forest, increasing the forest line by about 200 m (see Fig. 5.5).

- (RQ1.2) *Snow*: Studies dating back to Yeh et al. (1983) have looked at how anomalies in ground snow may influence weather the following seasons by initializing experimental runs with added or removed snow. Numerical weather forecasting models and even reanalyses regularly show biases in snow cover (e.g. Slater et al. 2007; Balsamo et al. 2015; Broxton et al. 2017). *In Erlandsen et al. (2017) we introduced a novel approach for perturbing the ground snow without initializing the model with added water, which would have confounded the analysis. We altered the discrimination of precipitation phase to more often determine snowfall. Precipitation was treated as snow if the near-surface temperature was below 2.5°C. This increased ground snow cover with one to two weeks on average.*

- (RQ1.3) *SST*: Biased SST may preclude a hindcast, weather forecast, or climate projection; e.g. in historical runs CMIP5 models generally show colder than observed SST in the extra-tropical North Atlantic (Wang et al. 2014). Further, SST in the North Atlantic has increased with about 0.29°C per decade between 1978–2007 (Cattiaux et al. 2011), and this warming has contributed to warming terrestrial Europe in the same period. *To shed light on the effect of a SST perturbation a uniform SST increase of 0.4° C was implemented in both model domains (see Fig. 5.5).*

5.3.1.1 Major findings

The differences in ground snow cover, surface temperature, net radiation, sensible heat, latent heat, evaporation, precipitation, and runoff produced by the model experimental runs were analyzed. In general the sensitivity was found was mostly similar in the relatively cold and dry 2009/10 and the warmer and wetter 2010/11. Fig. 5.6 (b-d) shows the fall (SON), winter (DJF), spring (MAM), and summer (JJA) runoff response of each of the three experiments in 2010/-11.

Major findings of each of the experiments (and research questions) are listed here:

- (RQ1.1) *Veg*: Increasing the boreal tree line led to an increase in annual evaporation in the study area of 8%. Snow-melt generally started earlier, shifting a fraction of runoff from summer to spring (see Fig. 5.6). Annual runoff was not much affected, as precipitation increased by nearly the same amount.

  - Future model studies and ideally observational studies are are needed to explore this finding further. The mechanisms triggering precipitation could be studied in greater detail by e.g. perturbing one and one secondary vegetation related parameter, using a variety of model structures (e.g. a different physical schemes), and also varying soil settings. If the finding holds true it means that vegetation changes

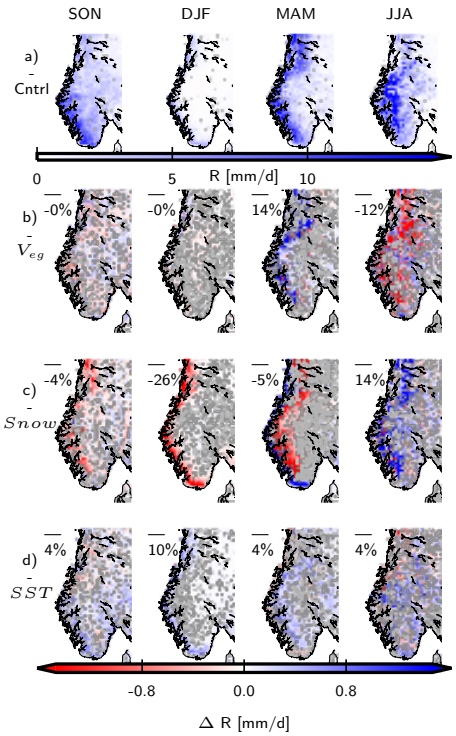

Figure 5.6: a) depicts mean daily runoff in the control run during the 2010/-11 fall (SON), winter (DJF), spring (MAM), and summer (JJA). b)-d) show significant changes in seasonal mean daily temperature from the control run, for b): the forest line heightening experiment (*Veg*), c): the snow cover experiment (*Snow*), and d): the $0.4\,°C$ SST increase experiment (*SST*); with the mean change in the areas of significant change denoted in the upper left corner. Areas of no significant change are marked in gray. Figure reproduced from Erlandsen et al. (2017) Journal of Hydrometeorology 18, 1; 10.1175/JHM-D-15-0146.1.

modeled in offline land surface or hydrological models will neglect this balancing effect of water recycling.

Significant increases in annual net radiation and surface temperature were found. Temperature increased in all seasons except summer, when evaporative cooling dominated. In areas of significant change, the magnitude of the average annual warming was about 0.2°C. The findings regarding the temperature response were similar to results found in both modeling and observational studies (see Paper I).

- (RQ1.2) *Snow*: The experiment changing ground snow cover by altering the amount of received precipitation treated as snow had the smallest

effect on annual precipitation and runoff. Large changes in seasonal runoff occurred (see Fig. 5.6): peak runoff was on average delayed with more than one month, and showed a higher amplitude. Slight reductions in precipitation were seen, predominantly in late spring and early summer; however, in scattered inland areas, slight precipitation increases were seen. Surface temperature was on average reduced with 0.2°C.

  - As with the experiment altering vegetation, these finding regarding how snow anomalies influence atmospheric variables might be in part model specific. Future observational and modeling studies are needed to confirm these findings. Later, we have become aware that the WRF model most likely has a too high field capacity within most of Norway. In principle, this exaggerated field capacity might hinder the soil shifting into water-stressed conditions, which would impact the ratio of latent to sensible heat flux, surface and two meter temperature, and possibly also precipitation.

- (RQ1.3) *SST*: Of the three experiments the 0.4°C SST perturbation resulted in the smallest change in net radiation and turbulent fluxes within South Norway. Incoming and outgoing longwave radiation increased with similar amounts. Significant changes in annual surface temperature were found in most of the study area. Land surface temperature increased on average with 0.2°C, half of the SST increase. The temperature increase was largest in the colder seasons. The SST perturbation further induced the largest change in annual runoff over South Norway. This was due to an increase in moisture transportation from the ocean increasing precipitation, and smaller overall increases in evaporation. Also for precipitation the largest change was seen in winter. The larger response in temperature and precipitation in winter is consistent with findings in Cattiaux et al. (2011) and Køltzow et al. (2011).

We believe there is some uncertainty regarding whether the findings are representative of real world sensitivity; especially those regarding the sensitivity to changes in snow and vegetation cover. This is elaborated on below and in Sec. 5.4.

5.3.2 Use of the WRF model in Paper I

The WRF model software consists of a framework allowing users to build a model based on various assumptions, or schemes, describing physical processes relevant for a numerical weather prediction model, e.g. the parameterization of the land-surface, radiation, and the planetary boundary layer. In general, in regional weather and climate prediction models choices of parameterization schemes, domain location and size (see e.g. Køltzow et al. 2011), initialization of soil moisture, soil temperature and snow, horizontal, vertical and temporal resolution, surface parametric fields, configuration of lateral boundary conditions, drag and diffusivity options, nesting, nudging, etc. (see e.g. Køltzow et al.

2011; Warner 2011) influence model results. The combination of these choices ant the frequent updates of the model's numerical code results in the WRF model versions results in considerably different model output (e.g. Katragkou et al. 2015a). Since 2017 the specification of distinct suites of physical schemes which are known to perform well for certain configurations and domains have received more attention (Powers et al. 2017). The consequence of this flexibility is uncertainty regarding the quality of the model, and that in order to distill robust and relevant information from the studies undertaken parts of the model output must at minimum be validated. A literature survey, personal communication with researchers at the University of Oslo, and some experimental model runs formed the basis for the scheme options selected for the study. The set of physics choices used are listen in Table 1 in Paper I.

A control run and the model experiments were run for two hydrological years, with lateral boundary conditions and SST from Era-Interim. To provide higher confidence in that the model also reflected real world sensitivity a rather rigorous validation of several variables of the control run output was implemented. An evaluation of 2-meter temperature, precipitation, specific humidity, wind speed, and snow depth showed that the model mostly performed well, but had a temperature bias of -0.9° on average, and slightly to high specific humidity (4% higher than the observations). The quality of the estimated precipitation is more uncertain since precipitation has a lower spatial auto-correlation than e.g. temperature, and the observation-based, gridded precipitation dataset used for validation (SeNorge) also contain uncertainties (see Sec. 4). In terms of snow cover the model showed fair values; however, snow cover was underestimated in some coastal areas while it was slightly overestimated many inland regions of eastern Norway.

While a subset of the model's output was rater rigorously validated, demonstrating that the model was fairly skillful in emulating these variables, a lack of quality controlled surface radiation observations hindered the validation of these variables. Given the research's roots within both meteorology and hydrology, we wanted to further study catchment hydrology. Input from experts within hydro-meteorological modeling during a research stay at the National Center for Atmospheric Research (NCAR), and consultation with hydrologists at NVE made it clear that the possible analysis of catchment hydrology was in part hindered by a lack of validation data; since any errors in the variables feeding the land surface scheme would percolate into the land surface scheme output (i.e. garbage in, garbage out). The complexity of a regional climate model also made it clear that any land surface model development would more easily be conducted in an offline modeling setting. Paper II considers estimates of near surface humidity and incident radiation, variables integrated in the surface water and energy balance, which, at the time, were inadequately evaluated within Norway.

5.3.3 Paper II : Merits of novel high-resolution estimates and existing long-term estimates of humidity and incident radiation in a complex domain

As discussed throughout Chapter 2 and 4, observational data are at the center point of land modeling, whether or not models are mainly data driven or more physically-based. Snow-melt has a non-linear sensitivity to air-temperature (see e.g. Sec. 3.8), and evaporation is governed by a range of atmospheric and surface variables (see Sec. 2.5, 2.7 and Eq. 2.11).

There exists long-term, high-resolution (1-by-1 km) national, gridded, observation-based estimates of precipitation and near-surface temperature for Norway in the SeNorge datasets (see e.g. Lussana et al. 2019). Additionally, a near-surface wind speed dataset had been developed by researchers at the Norwegian Meteorological Institute. Meanwhile, at the time, we could not find any information on the merits and caveats of existing long-term estimates of of near-surface humidity and incident shortwave (SW↓) and longwave (LW↓) radiation available for Norway. Establishing this was the purpose of Paper II.

In the process we discovered that we could modify an existing approach where reanalysis estimates are post-processed with gridded observation-based data by using the national SeNorge dataset instead of coarser, global datasets. In particular, Norway's complex topography and coastline (see Sec. 5.1) made us suspect that standard atmospheric lapse rates regularly used during altitude adjustment of forcing variables to the resolution and orography of numerical models might be unreasonable (see e.g. Sec. 4 or e.g. Daly et al. (2010), Kotlarski et al. (2010), and Mizukami et al. (2014)). Using a finer-scale gridded observational dataset we hoped to further enhance the post-processing of reanalysis-based estimates of humidity and incident radiation. The method for producing the dataset is described briefly in the article (Paper II), and more fully in the article's supplement. The code used to develop the data is available at GitHub (https://doi.org/10.5281/zenodo.1435555). The new dataset, named HySN, covers 1979 to 2017 with a daily resolution, and was made available through the research data archive Zenodo (https://doi.org/10.5281/zenodo.1970170).

Paper II addressed the sources of uncertainty concerning commonly used estimates of humidity, SW↓, and LW↓ available for long-term land surface modeling in the region through the following processes.

- The construction of an original dataset, HySN.
- Gathering long-term gridded datasets of humidity (either in the form of dew point temperature (T_d) or vapor pressure (VP)) and incident radiation:
  - from two global reanalysis datasets
    - Era-Interim, developed by ECMWF, available from 1979 to August 2019 with a horizontal resolution ($\Delta_{x,y}$) of about 0.66° x 0.66° (Dee et al. 2011);
    - MERRA 2, developed by NASA, available from 1980 until the present, $\Delta_{x,y} \simeq 0.5°$ x 0.625° (Bosilovich et al. 2015);

  - two post-processed reanalysis datasets:
    - PGMFDv2: An updated version (see Schmied et al. 2016) of the 0.5° x 0.5° Princeton global meteorological forcing dataset (Sheffield et al. 2006):
    - WFDEI, the WATCH forcing data methodology to ERA-Interim reanalysis data, described in Weedon et al. (2014);
    - HySN, post-processing ERA-Interim with SeNorge data; developed and described in the same study;
  - and two versions of empirically based estimates compiled for continental Norway:
    - VFDv1, 1 x 1 km VIC (see e.g Wood et al. (e.g. 1992) and Sec. 3.7) type forcing data (VFD) version 1, with estimates of humidity and incident shortwave radiation based on the MTCLIM algorithms (see Sec. 2.7)
    - VFDv2, as for VFDv1, however, based on slightly different algorithms and input data.

    The orography and land mask of the datasets are displayed in panel (a)-(e) in Fig. 5.7.

- Surface observations from between 1982 and 1999 were gathered from variety of providers. Humidity measurements from 84 stations were used, and, by employing quality control routines and including agricultural stations, SW↓ observations from 10 stations were made available. Meanwhile, only two stations had observations of LW↓. The location of the observation stations are shown in Fig. 5.7 (f) and (g). Lacking observations of incident radiation, particularly longwave radiation is a common problem, hindering both model development and model evaluation (see Sec. 4).

- Multiple linear regression models were constructed to provide vertical gradients in both the observations and the model estimates in order to adjust the estimates to the altitude of the observations before their differences were assessed.

- The correlation of model estimates with observations were compared on a daily timescale by compiling anomaly correlation coefficients.

- Further, the cumulative distributions; sensitivity to weather types, continentality, and latitude; and decadal trends were compared.

We also investigated two hypotheses: $\mathcal{H}_a$ that there are vertical gradients in near-surface humidity and incident radiation in our domain, and $\mathcal{H}_b$ – that the added value of the high horizontal resolution of the more empirically based estimates outweighs the added value of relying on estimates from coarser-resolution numerical weather prediction reanalyses.

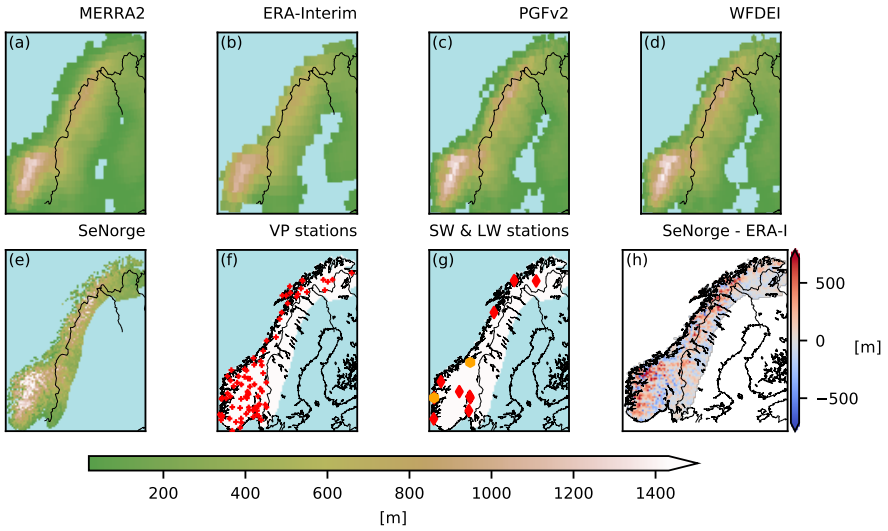

Figure 5.7: The orography and land mask of MERRA2 (a), ERA-Interim (b), PGMFDv2 (c), WFDEI (d), and SeNorge (c) are visualized on the SeNorge grid with a green–brown color scheme. For reference, national borders and the coastline derived from a high-resolution dataset are delineated in black. Locations of the 84 VP stations used in the model comparison are denoted with red crosses in (f). In panel (g) the stations where SW↓ measurements were retrieved are marked with red, and those where LW↓ were retrieved are marked with orange. The last map (h) displays the difference in meters between the SeNorge and ERA-Interim orography in common land areas. Higher elevations in SeNorge are indicated with red, while blue indicates higher elevations in ERA-Interim. The figure is reproduced from Erlandsen et al. (2019).

5.3.3.1 Major findings

The number of stations with observations of humidity and SW↓ allowed deriving vertical gradients for the variables for the observations and model estimates. To derive dependencies for SW↓ the data were first converted to clearness index (CI), which describes the daily incident shortwave radiation fraction of the potential extraterrestrial radiation at the local position and time. For LW↓ the vertical gradients were found by fitting regression models to a well performing dataset, Era-Interim.

($\mathcal{H}_a$) Paper II showed that altitude is a significant predictor of humidity, SW↓, and LW↓ in the domain:

- The vertical gradient in humidity in the observations considered is similar to the moist adiabatic lapse rate, but varies with season and distance to the coast. Vapor pressure vertical gradients were on average -0.25 hPa per

100 m in winter and -0.34 hPa per 100 m in summer (see Fig. 5.8 a). The summer gradient is similar to what was found in the Alps in summer in Marty (2000) (-0.35 hPa per 100m). The gradient found in winter was larger than that found in Marty (2000).

- Observed SW↓ was shown to increase with altitude in all seasons. Vertical gradients in SW↓, translated to CI, were 0.020 per 100 m in winter, 0.013 100 m in spring, 0.005 100 m in summer and 0.003 100 m in fall (see Fig. 5.8 b). The vertical gradients found were larger than the clear-sky type gradient of 0.00295 per 100 m used in the implementation of the Bristow and Campbell (1984) in versions of MTCLIM. Converted back to SW↓ the vertical gradients amount to about 0.3 Wm^{-2} per 100 m in fall and winter, 1.6 Wm^{-2} per 100 m in spring, and 1.2 Wm^{-2} per 100 m in summer. The seasonality of the gradients were different than those found in Marty (2000), which might be explained by differences in the cloud and snow cover climatology or the received extraterrestrial radiation.

- Average vertical gradients in LW↓ were analyzed in Era-Interim and were found to be -4.5 Wm^{-2} per 100 m in winter and -1.8 Wm^{-2} per 100 m in summer. The gradients have a opposite sign than those in SW↓, and show a similar magnitude to those in SW↓ in summer, but a considerably higher magnitude in winter. The gradient was larger than what the clear-sky adjustment implemented in HySN and similar post-processing methods provide. The range in the vertical gradients was similar to that found in Marty (2000).

($\mathcal{H}_b$) The second hypotheses investigated was rejected. The added value of the high horizontal resolution of the more empirically based estimates did not outweigh the added value of relying on estimates from coarser-resolution numerical weather prediction reanalyses. For all variables the estimates based on newer reanalysis data showed a higher daily temporal correlation (ACC) with the observations than the empirically based VIC type forcing data. Several of the reanalysis-based products (ERA, WFDEI, HySN) also showed a lower mean absolute station bias than the VIC type forcing data.

- (Vapor pressure): The new estimates, HySN, based on reanlysis data, provided humidity estimates with the overall highest quality given for the metrics considered in Paper II. VFDv1 and VFDv2 showed a 60% stronger decrease in humidity with distance from the coast than the observations (see Fig 5.8 a).

- (SW↓): The HySN estimates further outperformed the empirically based VIC type forcing data and the MERRA2 estimates of SW↓. It was unclear whether the HySN estimates had much added value compared to ERA-Interim and WFDEI. The VIC type forcing data showed an exaggerated latitudinal gradient in SW↓, likely a result of using diurnal temperature range as a proxy for cloud cover, which is perhaps not appropriate in coastal environments or at high latitudes.

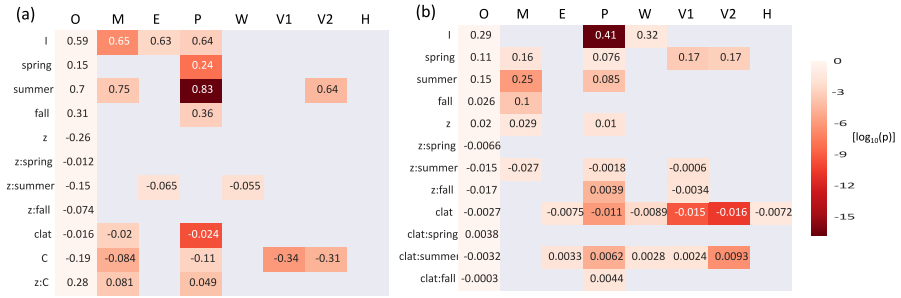

Figure 5.8: Seasonal and geographical dependencies of seasonal humidity (a) and daily clearness index (b) are depicted. The row names are the names of the coefficients, including the intercept (I), of the multiple linear regression model. The regression coefficients of the observational data are shown in the leftmost column of each plot, while the coefficients found for the model estimates are only shown if they are significantly different from those of the observations (using a limit of $p<0.01$ for humidity and $p<0.05$ for CI). Lower p values are indicated with darker colors using a logarithmic color scale (log10(p)). Figure reproduced from Erlandsen et al. (2019).

- (LW↓) The evaluation of LW↓ was partly hindered by a lack of high-quality historical observations. All models except WFDEI showed higher estimates of LW↓ at the stations (Bergen and Trondheim) than the observations. Analysis of the Era-Interim estimates for Bergen using observed cloud cover showed that LW↓ was underestimated in both clear-sky and cloudy conditions. Underestimation LW↓ and overestimation of SW↓ has been a long-standing issue in many reanalyses and in climate models (Katragkou et al. 2015b; Li et al. 2016; Wild et al. 2017). Observational uncertainty might also play in as both of the sensors measuring LW↓ were unshaded from solar radiation.

Paper II further inspected trends in the estimates and observations, where possible. E.g. between 1985 to 1999 many observation stations showed an increase in humidity in April and September. The estimates mostly reproduced the September increase, but not the April increase. More details of these finding are provided in Paper II.

To our knowledge this was the first study comparing more empirically based estimates of humidity and incident radiation with reanalysis-based estimates for a region within Europe. The study may assist impact modelers, and also be relevant for climate change studies. The knowledge of the quality of forcing data is important to know so that model developers do not tune model parameters or parameterizations for the wrong reason. Over-estimations of spring and early summer SW↓ may e.g. influence snow-melt timing and peak runoff.

Future work envisaged in Paper II includes updating the input data to Era5 and a newer version of the SeNorge dataset, and applying the HySN data as forcing data for a hydrological model. Additionally, initial results showed that differences in ground snow conditions between the reanalysis and the observations were significant in predicting the difference between ERA-Interim estimates of SW↓ and the observations. A correction to incident radiation based on surface albedo differences due to e.g. terrain-induced snow-cover variations could be an interesting post-processing option to test in future research.

5.3.4 Paper III : Constraining the HBV model for robust water balance assessments in a cold climate

The aim of the third paper was to produce a more robust and more physically based hydrological model suitable for studies of changes in water balance elements in a non-stationary climate. Paper III directly follows up on the suggested further research suggested in Paper II, of applying the HySN method producing high-resolution reanalysis-based estimates of incident radiation and near-surface humidity to a hydrological model. The HySN method, outlined in Paper II was first updated making use of the Era5 reanalysis (Hersbach et al. 2020) and novel versions of the national, gridded SeNorge precipitation and temperature datasets (Lussana et al. 2019). The validation of the new version of the dataset, HySN5 is summarized in Paper III and Paper III's supplementary material.

The hydrological model used is a gridded version of the conceptually based HBV model described in Beldring et al. (2003). The Beldring et al. (2003) version of the model, from here on called HBV-B03, has a daily resolution and covers mainland Norway with 1 km^2 grid cells. Each grid cell represent up to three land cover classes, and one soil type, and possibly glacial and lake fractions. It has a snow routine and a land cover-dependent evaporation-routine. It has relied on daily temperature, precipitation, and a climatological estimate of potential evaporation as input data.

Six soil parameters are routinely calibrated, and until recently, HBV-B03 included calibrated, often land cover-dependent, parameters for precipitation phase diagnosis, the melting temperature of snow, the snow-melt degree-day factor, and for the temperature-based scaling of monthly climatological potential evaporation providing estimates of evaporation. Recently a more detailed land cover description has been made available for the model, with 19 land cover classes (see Huang et al. 2019). A larger number of land cover classes combined with calibrated land cover dependent parameters for both snow and vegetation processes may potentially cause poorly constrained or confounded parameters (see e.g. Fig. 3.9). This can again make land use and land cover change studies more difficult due to disentanglement problems.

The availability of high-quality input data made way for adding the following physically based updates to the HBV model, (i) an augmented Penman–Monteith based evaporation scheme (see Sec. 2); (ii) a regionally calibrated, radiation-restricted degree-day factor; (iii) a diagnostic temperature- and humidity-based threshold for diagnosing precipitation phase. Additionally, the number of soil classes was reduced from 12 to 5, and the traditional, lognormal SWE-based grid cell tiling was replaced with a simple sigmoidal-function representing grid-cell snow cover fraction.

- (**i: an augmented Penman–Monteith based evaporation scheme:**) In Wong et al. (2011) the HBV-B03 calibrated, temperature-index based evaporation routine was discussed as a large source of uncertainty when analyzing end-of-century changes in summer droughts for Norway. Milly

and Dunne (2011b) found that a temperature-index based evaporation parameterization may simulate considerably larger evaporation changes than net radiation changes might justify. In Huang et al. (2019) a Penman–Monteith based evaporation scheme was implemented in HBV-B03. *In Paper III we optimized the Penman-Monteith evaporation scheme by driving it with HySN5 forcing data, adding a correction to its temporal aggregation, and modifying surface resistance according to Leuning et al. (2008). The Supplementary Material provides an overview of the implemented Penman–Monteith algorithm, which is a based on Eq. 2.12, the Penman-Monteith algorithm for canopy evaporation.*

- (**ii: a regionally calibrated, radiation-restricted degree-day factor**) The degree-day factor, which represents the amount of snow-melt per degree above freezing (see Sec. 3.8), may vary considerably depending on catchment, climate, and time-of-year (Kustas et al. 1994; Merz et al. 2011). A snow-melt routine where the degree-day factor is restricted by a radiative term allows snow-melt to be influenced by land cover class via albedo, without the need of a land cover class-dependent calibration. The radiative term allows for a sensitivity to changes in surface albedo, and incoming shortwave and longwave radiation. Further, the radiative term makes it less likely that an unreasonably large amount of snow remains over the summers, producing artificial 'snow towers' or 'model glaciers'. *In Paper III a radiation-restricted degree-day factor based on Kustas et al. (1994) was implemented. A radiation-based melt rate, in meters per day, obtained by converting net radiation (R_n) to snow-melt rate, was added to the common degree-day factor expression:*

$$M = max(C_{temp}(T2 - T2_{melt}) + C_{rad}\frac{R_n}{\lambda_f \rho_w},\ 0)^2 \tag{5.1}$$

- (**iii: a diagnostic temperature- and humidity-based threshold for diagnosing precipitation phase**) Jennings et al. (2018) and Jennings and Molotch (2019) showed that the accuracy of diagnosing precipitation phase may be increased by including humidity as a predictor, since snowfall is more likely in dryer environments given the same near-surface temperature. *In Paper III we made use of the high quality of the HySN5 humidity data to modify the often calibrated rain/snow criterion to a diagnostic temperature- and humidity-based (in the form of dew point temperature) criterion.*

$$\text{precipitation phase} = \begin{cases} rain, & \text{if } T_2 > 1°C \ \ \& \ \ T_d > 0°C \\ snow, & \text{otherwise} \end{cases} \tag{5.2}$$

[2]M is the melt rate per day in meters, C_{temp} is a calibrated degree-day factor, and $T2_{melt}$ is the minimum near-surface temperature where snow melts, λ_f is the latent heat of fusion, 0.334 $MJkg^{-1}$, R_n is in $MJm^{-2}day^{-1}$, ρ_w is the density of water (1,000 kgm^{-3}), and C_{rad} is a fraction scaling the radiation term (always less than unity, see Supplementary Table S3).

The simulated discharge was evaluated in terms of bias and Kling–Gupta Efficiency (KGE; Gupta et al. (2009)) using measurements from more than 100 catchments, of which 34 were excluded from the calibration. Calibration was conducted over 2000-2010, and as Era5 data from the preceding decades, 1980–1999, model estimates from this period, exempt from calibration, was used as an independent validation period. Keeping in mind that the model often is applied for climate change impact studies we also validated the model's ability to reproduce monthly discharge trends, and maximum winter SWE. The evaporation scheme's output of reference evaporation-like[3] evaporation was compared to the only in-situ measurements of evaporation available for several locations throughout mainland Norway, pan evaporation measurements conducted between 1967-1972 (see also Sec. 4). The model was integrated for the period 1980 to 2014, and the estimated mean water balance was assessed and compared with previous estimates for Norway.

5.3.4.1 Major findings

The model achieved a median KGE of 0.74 during calibration, 0.75 for the independent period, and 0.78 for the 34 independent catchments when evaluated over both the validation and calibration period (1980–2010). The mean bias ranged from -0.1 mm/day for the independent period to -0.8 mm/day for the 34 independent catchments (1980–2010). Simulated SWE showed a Pearson correlation coefficient of 0.78 to SWE observations from around the time of maximum SWE. A positive SWE bias of 6 cm was seen, however, the model grid cell altitude was generally higher than at the locations where SWE measurements were conducted. The model's performance was equally good or better than previous gridded HBV versions applied to the same domain, despite that it contains fewer calibrated parameters.

Simulated evaporation for the land cover class 'Open' gave a May to September evaporation of 272 mm, which was 96% of the measured pan evaporation. A slightly lower reference-type evaporation than pan evaporation is in line with observational studies (e.g. Allen et al. 1998) Overall, the trend patterns in the observations were reproduced by the model; however, there were some regions and times of the year with discrepancies. Both the simulated values and observations show a notable shift in discharge from early summer or late spring to earlier in spring. The quality of the estimated evaporation and interception from, e.g., coniferous forest remains uncertain due to the lack of observations to constrain the estimates (see also the discussion in Sec. 4).

The water balance was assessed. Between 1980 and 2014, the areal mean annual precipitation (P) was 1367 mm, runoff (R) was 1179 mm, evaporation (E) 178 mm, and potential evaporation (Ep) was 210 mm (see Fig. 5.9). The evaporation fraction (E/P) was on average just above one-sixth (0.17); however, in the eastern regions of Norway E/P reached 40%.

[3] see e.g. Allen et al. (1998). We calculated evaporation for the land cover class 'Open', which represents short vegetation (height = 20 cm, leaf area index = 2, see Paper III Supplementary Material, Table S3)

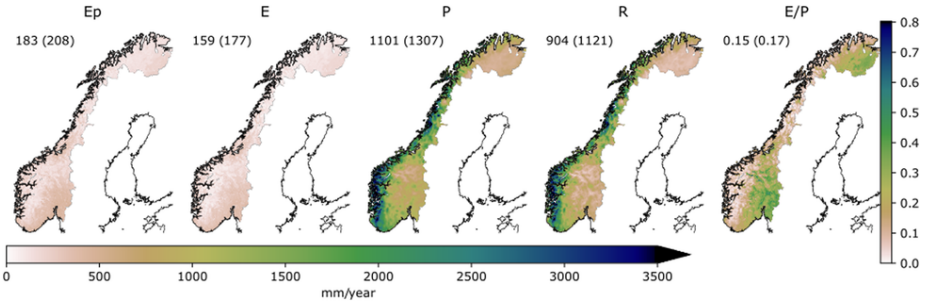

Figure 5.9: 1980-2014 mean annual potential evaporation (E_p), evaporation (E), precipitation (P), runoff (R), and evaporation fraction (E/P). The areal median and mean are denoted in the upper left corner, with the mean in parenthesis. Figure reproduced from Erlandsen et al. (2021)

Comparison with previous estimates of the water balance of mainland Norway (estimates published in 2009, 2017, and 2019), all based on variants of HBV-B03 driven with different forcing data, showed that the runoff estimate is rather similar, 1100-1200 mm, but the evaporation and precipitation estimates vary considerably, with nearly 300 mm. Since precipitation is a variable with a limited horizontal auto-correlation which is incompletely sampled, and since the measurements have some uncertainty, particularly for snowfall (see Sec. 4), correction factors for the precipitation received from the forcing dataset are routinely calibrated within hydrological modeling. In HBV-B03, there are two multiplicative correction factors for precipitation, one for precipitation in general, and one which is only applied (multiplied) when there is snowfall. In Paper III the calibrated precipitation correction factors were small; the model corrected precipitation was just 1.4% larger than in the original precipitation dataset (SeNorge2018, Lussana et al. (2019)). The estimated mean annual evaporation (and thus precipitation) was smaller than that estimated in 2009 (346) and 2017 (500 mm). We conclude that future studies further enhancing the precipitation forcing data, and observational and modeling studies with emphasis on evaporation, and particularly forest interception, are needed to further constrain our estimates on Norway's annual water balance.

5.4 Summary and outlook

The main objective of this thesis is to better our understanding of the surface water and energy balance in Norway in the context of climate change and land cover change. We have worked towards this through three secondary objectives and studies. The key findings are listed here:

- O1: We have, in a regional climate model, identified the sensitivity of the surface water and energy balance to changes in the boreal tree line, snow

cover, and SST in a state-of-the-art regional climate model. The study, Paper I, is published in Erlandsen et al. (2017). The main findings are summarized in the Sec. 5.3.1. Highlights include:

  - (RQ1.1) Annually, heightening the boreal tree line increased net radiation, which was largely balanced out by an increase in latent heat flux. The latter was balanced by an increase in precipitation, leaving annual runoff mostly unchanged. Additionally, the annual surface temperature increased by 0.1°C.
  - (RQ1.2) Increasing ground snow by altering the snowfall/rainfall criterion led to a decrease in net radiation, despite slight increases in both downward shortwave and longwave radiation. The surface temperature was reduced by 0.2°C, however, the annual water balance remained mostly unchanged.
  - (RQ1.3) The 0.4°C SST increase led to more downward and upward longwave radiation in South Norway, raising the annual surface temperature by 0.2°C, on average. Ocean to land moisture advection increased, and with this also both precipitation and runoff (+2.8%).

- 02: In Paper II we have quantified compared, and produced enhanced long-term estimates of atmospheric variables necessary to integrate the surface water and energy balance in offline models. This work is published in Erlandsen et al. (2019). The study's main findings and some directions for future work are summarized in Sec. 5.3.3. Highlights include:

  - ($\mathcal{H}_a$) Altitude is a significant predictor of humidity, SW↓, and LW↓ in Norway.
  - ($\mathcal{H}_b$) The added value of the high horizontal resolution of the more empirically based estimates did not outweigh the added value of relying on estimates from coarser-resolution numerical weather prediction reanalyses. The estimates produced by the method introduced in Paper II produced the overall highest ranking for the humidity estimates and showed similar performance to WFDEI and Era-Interim for the radiation estimates adjusted to the altitude of the observations based on the findings of Paper II ($\mathcal{H}_a$).
  - The study further revealed 1985-1999 trends in humidity and incident radiation, which sometimes varied between observations and estimates.

- O3: Paper III combined physically-based parameterization alterations, a decrease in the number of calibrated parameters, and quality controlled and enhanced forcing data to provide better constrained long-term estimates of Norway's surface water balance. The study is published (Erlandsen et al. 2021). Its main findings and directions for future research are summarized in Sec. 5.3.4. Highlights of the study are:

- More than three decades of model integration showed that the altered model produced equally good or better results than the previous model versions, despite containing fewer calibrated parameters.
- The altered hydrological model mostly reproduced the observed discharge trend patterns (1985–2014) in most months and catchments. Both the simulated values and observations showed a notable shift in discharge from early summer or late spring to earlier in spring.
- The mean annual water balance produced showed lower mean annual evaporation than previous estimates for Norway.

This work has, of course, revealed a number of remaining challenges which may be worked on to better understand and constrain the surface water and energy balance in Norway.

5.4.1 Remaining challenges

Sec. 3.7, 3.8, 3.9, and Chapter 4 highlight that a fair model necessitates a fair description of the model structure, model parameters, and forcing data. In retrospect, we learned that several parts of the land surface configuration (default soil parameters) of the WRF model, used in Paper I and many other studies, likely are suboptimal for Norwegian conditions. Paper III involved working more closely with expert hydrologists. During this work I became familiar with the upper and lower limits for soil parameter values which were considered plausible for Norway. The soil parameterization in an off-the-shelf version of the WRF model would likely provide a too high field capacity (and/or soil depth) in most regions of Norway. Additionally, as touched upon in Sec. 3.7 the parameters describing soil hydraulic conductivity should optimally be calibrated. Establishing soil hydraulic conductivity from pedotransfer functions based on soil texture alone is criticized in Vereecken et al. (2019), since these functions often were developed for point scale and not grid scale, and field scale infiltration experiments have found soil hydraulic conductivity differing in the order of magnitude from those estimated using pedotransfer functions based on e.g. the soil map such as Zobler (1999) (see Fig. 3.7).

Kishné et al. (2017) found that the default soil hydraulic parameters for the Noah land surface model resulted in a strong overestimation of plant available water in their study region (Texas), and suggested revised soil parameters for the land surface model. Zhang et al. (2020) compared the 13 different pedotransfer functions, and found a high variation among 13-pedotransfer functions in estimated field capacity for the Nordic countries (Fig. 2, Zhang et al. (2020)).

Field capacity is an example of a parametric variable linked to soil depth (see e.g. Yang (2004) Eq. 8). An early study (Russell and Miller 1990) comparing observed river discharge and simulated catchment discharge in Model II of Hansen (1983) found that in certain catchments discharge was underestimated even while precipitation was overestimated, likely due to excessively large prescribed soil-water holding capacities which led to exaggerated water storage and evapotranspiration. A more recent model study, Brunke et al. (2016), implemented a

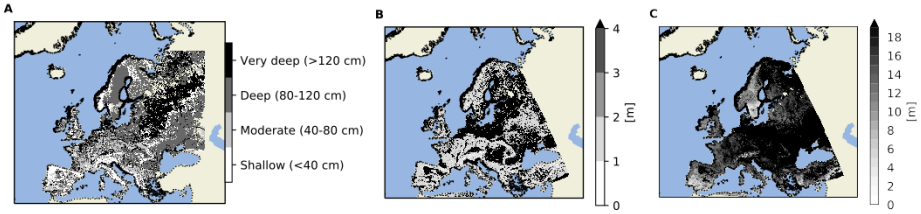

Figure 5.10: **A** depicts 'Depth to rock' according to the European Soil Database distribution v2.0 published by the European Commission and the European Soil Bureau Network in 2006 (Liedekerke et al. 2006), **B** depicts soil, immobile regolith, and sedimentary deposit thicknesses according to Pelletier et al. (2016), while **C** depicts 5 minute resolution absolute depth to bedrock as assessed by Shangguan et al. (2017). Note the different range in grey tones in each map plot.

variable soil depth in the land surface model CLM4.5, the Pelletier et al. (2016) dataset (see Fig. 5.10 B). Compared to the default simulation with 10 soil layers and a uniform soil depth of 3.8 m, the largest impacts of implementing a varying soil depth were found in regions with shallow soil. In these regions impacts included both amplitude and phase changes in annual runoff and amplitude changes in latent heat flux; and further, the inter-annual soil and surface temperature variation increased. These findings may be especially relevant for future studies within Norway. According to estimates from the European Soil Database distribution v2.0 and Pelletier et al. (2016), considerable regions of Norway consist of shallow soil (see Fig. 5.10).

Although the need to better various parts of the soil parameterization in land surface model has been discussed for some time, there are still major issues which might be improved upon in several regions. A recent example is provided in the manuscript Xue et al. (2021), where a first international effort is undertaken to improve the description of spring land surface and subsurface anomalies in high mountain areas so that the properly initialized temperature may feed into subseasonal to seasonal precipitation prediction through land-atmosphere interaction and teleconnections. The initial study (Xue et al. 2021), focusing on the Tibetan Plateau, and found that inadequacies in the land models and reanalysis data hindered the development of the initialized anomalies to the subsequent observed temperature anomalies.

As described above, the soil configuration will have some impact on temperature, how the surface water and energy balance responds to perturbations, and likely impact the strength of land-atmosphere coupling and feedback. In an unpublished study (see the 'List of papers'), we used a land-atmosphere coupling metric to investigate if dry soil conditions exasperated heat during summer droughts in Norway. Using the WRF model, we found little evidence of

this in the model; however, instead using soil and evaporation data input from the HBV model and the SeNorge gridded 2-meter temperature data as input to the software compiling the metric there was ample evidence of land-atmosphere feedback exacerbating the heatwaves. To complicate matters further, changing the metric's input once more, to the estimated variables of the HBV model version developed in Paper III, the land-atmosphere coupling was significant in regions of South Norway, but much less widespread than when the previous version of the HBV model was used. The spatial pattern of the land-atmosphere coupling metric used showed a strong Spearman's rank correlation to the secondary parameter field capacity (linked to the grid cell dominant soil type).

The metric considered if latent heat flux decreased with time while near-surface temperature increased, indicating that the soil had been moved into a state where lack of soil water limited evaporation. In this dryer state, less of the energy received would be converted to a latent (i.e., hidden, see Sec. 2.1) heat flux, leaving more energy to heat the surface and near surface air (via the sensible heat flux). As an experiment, we reran the HBV model of Paper III between 1980 and 2014 with a high field capacity, equivalent to that of the default WRF configuration used e.g. in Paper I, and found that the indication of significant land-atmosphere coupling now was lacking.

Paper II and the subsequent analysis and validation including the recently released reanalysis Era5, provided in the supplementary material of Paper III, pinpointed a number of unresolved issues regarding humidity and incident radiation, variables that force the surface water and energy balance. Apart from the lack of observations of incident radiation, a common issue found was that even the best performing reanalysis datasets considered, such as Era-Interim and Era5, overestimate shortwave and likely underestimate longwave radiation in our study region. The validation conducted in Paper II revealed that the difference in ground snow conditions between the observations and Era-Interim was a significant predictor of the difference between observed and estimated SW↓. An interesting option for future development is to include a snow-cover correction when downscaling of incident shortwave radiation to a finer resolution and orography. The latter finding is in line with the findings in Paper I (RQ1.2), which showed that surface incident shortwave radiation increased with increasing ground snow cover.

While the HBV model used in Paper III included several alterations aiming to make the model more robust under changing climatic conditions, a number of additional enhancements may be considered. The treatment of evaporation, particularly of intercepted precipitation, is uncertain in a model with a daily temporal resolution. However, this is further complicated by the lack of evaporation observations to help constrain the parameters involved in the estimation of evaporation. Additional suggestions for future research are provided in Paper III.

These findings have only come about through cross-disciplinary collaboration, and further cross-disciplinary collaboration is necessary to resolve the remaining challenges we have seen. A future effort should be undertaken to:

1. improve parameters and physiographic fields ingested in land surface models and hydrological models for Norwegian conditions.

    a) This could be done by expert consultation, or by calibration and tuning using e.g. the information available in discharge observations (as is currently done for hydrological models),

    b) the ingestion of better physiographic fields, such as the land cover dataset used in Paper III, or improved depth-to-bedrock information, and

    c) making, or making available, observations of surface turbulent and radiative fluxes, and other variables which are lacking.

The effort involves possibly model calibration, which can be demanding to set-up and computationally expensive to do in more complex land models than, e.g., the HBV model. Improving on the physiographic data involves the gathering and harmonization of physiographic data, e.g., depth to bedrock, gathered by various agencies and institutes within Norway. This would require cross-disciplinary and, perhaps, industry collaboration, since data have been gathered in various forms and units and sometimes with restrictions in usage. These constraints should improve the reliability of output from the models we use for making weather, climate, and hydrological forecasts. Greater gains and impacts still would be seen if the observations or post-processed physiographic fields might be shared with global depositories, to make sure that more realistic physiographic fields are available for global or regional climate and weather forecasting models. Sub-optimal soil configuration in these may likely at least result in poor forecasts or projections of the expected future maximum and minimum temperature.

Additional remaining issues are the lack of observation of several essential variables. While Sweden and Finland have several FLUXNET stations, land modelers wanting to validate latent heat flux or evaporation estimates within mainland Norway have, until very recently, had few or no measurements available. Furthermore, while eddy covariance methods have increased our understanding of biosphere and atmosphere exchange of vapor and CO2, the sensors do not provide accurate readings during precipitation (Allen et al. 2020). Additionally,plot-scale interception loss, particularly that of intercepted snow, is still poorly measured and understood (Allen et al. 2020). Measurements of shortwave radiation are generally more available than longwave radiation, and the latter is lacking to a point where it hinders both model development and validation (e.g. Carrer et al. 2012; Erlandsen et al. 2019). Locally validated satellite products, e.g. skin temperature, may potentially help tune or calibrate land surface models, and are likely underutilized for land model development within our region. Finally, any further improvements regarding precipitation data are helpful to improve land model output and constrain parameters and parameterizations.

Thankfully, there are currently several interdisciplinary projects working to improve on land surface modeling within Norway through both model development and gathering new observations: Land-ATmosphere Interactions in Cold Environments - LATICE (mn.uio.no/geo/english/research/groups/latice/) which

brings a focus on cold-regions exchange processes within Earth System Sciences as an interdisciplinary initiative of collaborative research and education, EMERALD (mn.uio.no/geo/english/research/projects/emerald/), which works to improve the representation of high latitude ecosystems and their climate interactions in The Norwegian Earth System Model (NorESM) by integrating empirical data and knowledge in model development, and last year the project Hydrometeorology to Operations (H2O, met.no/prosjekter/hydrometeorology-to-operations-h20) was initiated at the Norwegian Meteorological Institute with the ambition to develop world leading capacity in regional NWP integrated across the land-atmosphere domain. This recent increase in cross-disciplinary collaborative projects aiming to improve our understanding and ability to simulate land and land-atmosphere processes installs faith that at least parts of these issues will be resolved or improved upon in the coming years.

Bibliography

Abbott, M. B., J. C. Bathurst, J. A. Cunge, P. E. O'Connell, and J. Rasmussen (Oct. 1986). "An introduction to the European Hydrological System - Systeme Hydrologique Europeen, "SHE", 1: History and philosophy of a physically-based, distributed modelling system". In: *Journal of Hydrology* 87.1-2, pp. 45–59. ISSN: 00221694. DOI: 10.1016/0022-1694(86)90114-9.

Abramowitz, G (2012). "Towards a public, standardized, diagnostic benchmarking system for land surface models". In: *Geoscientific Model Development* 5.3, pp. 819–827. ISSN: 1991959X. DOI: 10.5194/gmd-5-819-2012.

Allen, Richard G., L.S. Pereira, D. Raes, and M. Smith (1998). "Crop evapotranspiration: Guidelines for computing crop requirements". In: *Irrigation and Drainage Paper No. 56, FAO*. ISSN: 0254-5284. DOI: 10.1016/j.eja.2010.12.001.

Allen, Scott T., Doug P. Aubrey, Maaike Y. Bader, Miriam Coenders-Gerrits, Jan Friesen, Ethan D. Gutmann, Franccois Guillemette, César Jiménez-Rodríguez, Richard F. Keim, Anna Klamerus-Iwan, Glenda Mendieta-Leiva, Philipp Porada, Robert G. Qualls, Bart Schilperoort, Aron Stubbins, and John T. Van Stan (Jan. 2020). "Key questions on the evaporation and transport of intercepted precipitation". In: *Precipitation Partitioning by Vegetation: A Global Synthesis*. Springer International Publishing, pp. 268–279. ISBN: 9783030297022. DOI: 10.1007/978-3-030-29702-2{_}16.

Anderson, E. A. (Feb. 1968). "Development and testing of snow pack energy balance equations". In: *Water Resources Research* 4.1, pp. 19–37. ISSN: 19447973. DOI: 10.1029/WR004i001p00019.

Appenzeller, Tim (Sept. 2019). "Global warming has made iconic Andean peak unrecognizable". In: *Science*. ISSN: 0036-8075. DOI: 10.1126/science.aaz4542.

Arsenault, Richard, Franccois Brissette, and Jean Luc Martel (2018). "The hazards of split-sample validation in hydrological model calibration". In: *Journal of Hydrology*. ISSN: 00221694. DOI: 10.1016/j.jhydrol.2018.09.027.

Askeland, Kristine, Kristina N. Bozhkova, and Peter Sorknæs (Oct. 2019). "Balancing Europe: Can district heating affect the flexibility potential of Norwegian hydropower resources?" In: *Renewable Energy* 141, pp. 646–656. ISSN: 18790682. DOI: 10.1016/j.renene.2019.03.137.

Badgley, Grayson, Joshua B. Fisher, Carlos Jiménez, Kevin P. Tu, and Raghuveer Vinukollu (Aug. 2015). "On uncertainty in global terrestrial evapotranspiration estimates from choice of input forcing datasets". In: *Journal of Hydrometeorology* 16.4, pp. 1449–1455. ISSN: 15257541. DOI: 10.1175/JHM-D-14-0040.1.

Baldocchi, Dennis, Eva Falge, Lianhong Gu, Richard Olson, David Hollinger, Steve Running, Peter Anthoni, Ch Bernhofer, Kenneth Davis, Robert Evans, Jose Fuentes, Allen Goldstein, Gabriel Katul, Beverly Law, Xuhui Lee, Yadvinder Malhi, Tilden Meyers, William Munger, Walt Oechel, U. K.T. Paw, Kim Pilegaard, H. P. Schmid, Riccardo Valentini, Shashi Verma, Timo Vesala, Kell Wilson, and Steve Wofsy (Nov. 2001). "FLUXNET: A New Tool to Study the Temporal and Spatial Variability of Ecosystem-Scale Carbon Dioxide, Water Vapor, and Energy Flux Densities". In: *Bulletin of the American Meteorological Society* 82.11, pp. 2415–2434. ISSN: 00030007. DOI: 10.1175/1520-0477(2001)082<2415:FANTTS>2.3.CO;2.

Balsamo, G., C. Albergel, A. Beljaars, S. Boussetta, E. Brun, H. Cloke, D. Dee, E. Dutra, J. Muñoz-Sabater, F. Pappenberger, P. de Rosnay, T. Stockdale, and F.

Vitart (Jan. 2015). "ERA-Interim/Land: a global land surface reanalysis data set". In: *Hydrology and Earth System Sciences* 19.1, pp. 389–407. ISSN: 1607-7938. DOI: 10.5194/hess-19-389-2015.

Balsamo, Gianpaolo, Pedro Viterbo, Anton Beijaars, Bart van den Hurk, Martin Hirschi, Alan K. Betts, and Klaus Scipal (June 2009). "A revised hydrology for the ECMWF model: Verification from field site to terrestrial water storage and impact in the integrated forecast system". In: *Journal of Hydrometeorology* 10.3, pp. 623–643. ISSN: 1525755X. DOI: 10.1175/2008JHM1068.1.

Bastidas, Luis A, Hoshin V Gupta, and Soroosh Sorooshian (Jan. 2001). "Bounding the parameters of land-surface schemes using observational data". In: *Land Surface Hydrology, Meteorology, and Climate: Observations and Modeling*. Water Science and Application, pp. 65–76. ISBN: 9781118665589. DOI: 10.1029/WS003p0065.

Batjes, N.H. (May 2016). "Harmonized soil property values for broad-scale modelling (WISE30sec) with estimates of global soil carbon stocks". In: *Geoderma* 269, pp. 61–68. ISSN: 00167061. DOI: 10.1016/j.geoderma.2016.01.034.

Batjes, Niels H., Eloi Ribeiro, and Ad Van Oostrum (Feb. 2020). "Standardised soil profile data to support global mapping and modelling (WoSIS snapshot 2019)". In: *Earth System Science Data* 12.1, pp. 299–320. ISSN: 18663516. DOI: 10.5194/essd-12-299-2020.

Bauer, Peter, Alan Thorpe, and Gilbert Brunet (Sept. 2015). *The quiet revolution of numerical weather prediction*. DOI: 10.1038/nature14956.

Beck, Hylke E., Albert I.J.M. Van Dijk, Ad De Roo, Emanuel Dutra, Gabriel Fink, Rene Orth, and Jaap Schellekens (June 2017a). "Global evaluation of runoff from 10 state-of-the-art hydrological models". In: *Hydrology and Earth System Sciences* 21.6, pp. 2881–2903. ISSN: 16077938. DOI: 10.5194/hess-21-2881-2017.

Beck, Hylke E., Albert I.J.M. Van Dijk, Vincenzo Levizzani, Jaap Schellekens, Diego G. Miralles, Brecht Martens, and Ad De Roo (Jan. 2017b). "MSWEP: 3-hourly 0.25° global gridded precipitation (1979-2015) by merging gauge, satellite, and reanalysis data". In: *Hydrology and Earth System Sciences* 21.1, pp. 589–615. ISSN: 16077938. DOI: 10.5194/hess-21-589-2017.

Beldring, Stein (2002). "Runoff generating processes in boreal forest environments with glacial tills". In: *Nordic Hydrology* 33.5, pp. 347–372. ISSN: 00291277. DOI: 10.2166/nh.2002.0013.

— (2008). *Distributed element water balance model system*. Report no. Norwegian Water Resources and Energy Directorate, p. 42. ISBN: 978-82-410-0670-8.

Beldring, Stein, Kolbjørn Engeland, Lars A. Roald, Nils Roar Sælthun, and Astrid Voksø (2003). "Estimation of parameters in a distributed precipitation-runoff model for Norway". In: *Hydrology and Earth System Sciences* 7.3, pp. 304–316. ISSN: 10275606. DOI: 10.5194/hess-7-304-2003.

Bergström, Sten and Arne Forsman (June 1973). "Development of a Conceptual Deterministic Rainfall-Runoff Model". In: *Hydrology Research* 4.3, pp. 147–170. ISSN: 0029-1277. DOI: 10.2166/nh.1973.0012.

Beven, Keith and Jim Freer (2001). "Equifinality, data assimilation, and uncertainty estimation in mechanistic modelling of complex environmental systems using the GLUE methodology". In: *Journal of Hydrology* 249.1-4, pp. 11–29. ISSN: 00221694. DOI: 10.1016/S0022-1694(01)00421-8.

Bierkens, Marc F. P., Victoria A. Bell, Peter Burek, Nathaniel Chaney, Laura E. Condon, Cédric H. David, Ad de Roo, Petra Döll, Niels Drost, James S. Famiglietti, Martina Flörke, David J. Gochis, Paul Houser, Rolf Hut, Jessica Keune, Stefan Kollet, Reed M. Maxwell, John T. Reager, Luis Samaniego, Edward Sudicky,

Edwin H. Sutanudjaja, Nick van de Giesen, Hessel Winsemius, and Eric F. Wood (Jan. 2015). "Hyper-resolution global hydrological modelling: what is next?" In: *Hydrological Processes* 29.2, pp. 310–320. ISSN: 08856087. DOI: 10.1002/hyp.10391.

Bjerknes, V (1904). "Das problem der wettervorhersage, betrachtet vom standpunkte der mechanik und der physik". In: *Meteor. Z* 21, pp. 1–7.

Bjerknes, Vilhelm (Dec. 2009). "The problem of weather prediction, considered from the viewpoints of mechanics and physics". In: *Meteorologische Zeitschrift* 18.6, pp. 663–667. ISSN: 0941-2948. DOI: 10.1127/0941-2948/2009/416.

Bohn, Theodore J., Ben Livneh, Jared W. Oyler, Steve W. Running, Bart Nijssen, and Dennis P. Lettenmaier (2013). "Global evaluation of MTCLIM and related algorithms for forcing of ecological and hydrological models". In: *Agricultural and Forest Meteorology* 176, pp. 38–49. ISSN: 01681923. DOI: 10.1016/j.agrformet.2013.03.003.

Bonan, Gordon (Feb. 2019). "Terrestrial Biosphere Models". In: *Climate Change and Terrestrial Ecosystem Modeling*. Cambridge University Press, pp. 1–24. DOI: 10.1017/9781107339217.002.

Bosilovich, M et al. (2015). *MERRA-2: Initial evaluation of the climate Technical Report Series on Global Modeling and Data Assimilation*. Tech. rep. NASA/TM–2015-104606.

Bowen, I. S. (June 1926). "The ratio of heat losses by conduction and by evaporation from any water surface". In: *Physical Review* 27.6, pp. 779–787. ISSN: 0031899X. DOI: 10.1103/PhysRev.27.779.

Bright, Ryan M., Stephanie Eisner, Marianne T. Lund, Titta Majasalmi, Gunnar Myhre, and Rasmus Astrup (May 2018). "Inferring Surface Albedo Prediction Error Linked to Forest Structure at High Latitudes". In: *Journal of Geophysical Research: Atmospheres* 123.10, pp. 4910–4925. ISSN: 21698996. DOI: 10.1029/2018JD028293.

Bristow, Keith L. and Gaylon S. Campbell (May 1984). "On the relationship between incoming solar radiation and daily maximum and minimum temperature". In: *Agricultural and Forest Meteorology* 31.2, pp. 159–166. ISSN: 01681923. DOI: 10.1016/0168-1923(84)90017-0.

Brown, Barbara, John Halley Gotway, Randy Bullock, and Eric Gilleland (2009). "THE MODEL EVALUATION TOOLS (MET): COMMUNITY TOOLS FOR FORECAST EVALUATION National Center for Atmospheric Research , Boulder , Colorado". In: *25th Conference on International Interactive Information and Processing Systems (IIPS) for Meteorology, Oceanography, and Hydrology*. Vol. 9, pp. 1–4.

Broxton, Patrick D., Xubin Zeng, and Nicholas Dawson (Nov. 2017). "The impact of a low bias in snow water equivalent initialization on CFS seasonal forecasts". In: *Journal of Climate* 30.21, pp. 8657–8671. ISSN: 08948755. DOI: 10.1175/JCLI-D-17-0072.1.

Broxton, Patrick D., Xubin Zeng, William Scheftic, and Peter A. Troch (Aug. 2014a). "A MODIS-based global 1-km maximum green vegetation fraction dataset". In: *Journal of Applied Meteorology and Climatology* 53.8, pp. 1996–2004. ISSN: 15588432. DOI: 10.1175/JAMC-D-13-0356.1.

Broxton, Patrick D., Xubin Zeng, Damien Sulla-Menashe, and Peter A. Troch (June 2014b). "A global land cover climatology using MODIS data". In: *Journal of Applied Meteorology and Climatology* 53.6, pp. 1593–1605. ISSN: 15588432. DOI: 10.1175/JAMC-D-13-0270.1.

BRSN Webiste (2016). *Baseline Surface Radiation Network: Baseline Surface Radiation Network*.

Brunke, Michael A., Patrick Broxton, Jon Pelletier, David Gochis, Pieter Hazenberg, David M. Lawrence, L. Ruby Leung, Guo Yue Niu, Peter A. Troch, and Xubin Zeng (May 2016). "Implementing and evaluating variable soil thickness in the Community Land Model, version 4.5 (CLM4.5)". In: *Journal of Climate* 29.9, pp. 3441–3461. ISSN: 08948755. DOI: 10.1175/JCLI-D-15-0307.1.

Bryn, Anders (Dec. 2008). "Recent forest limit changes in south-east Norway: Effects of climate change or regrowth after abandoned utilisation?" In: *Norsk Geografisk Tidsskrift* 62.4, pp. 251–270. ISSN: 00291951. DOI: 10.1080/00291950802517551.

Buckland, S. M., J. P. Grime, J. G. Hodgson, and K. Thompson (Dec. 1997). "A Comparison of Plant Responses to the Extreme Drought of 1995 in Northern England". In: *The Journal of Ecology* 85.6, p. 875. ISSN: 00220477. DOI: 10.2307/2960608.

Budyko, M I (1958). *The heat balance of the earth's surface.* Teplovoĭ balans zemnoĭ poverkhnosti.English. Washington: U.S. Dept. of Commerce, Weather Bureau, 259 p.

Camuffo, Dario and Chiara Bertolin (Mar. 2012). "The earliest temperature observations in the world: The Medici Network (1654-1670)". In: *Climatic Change* 111.2, pp. 335–363. ISSN: 01650009. DOI: 10.1007/s10584-011-0142-5.

Carrer, D., S. Lafont, J. L. Roujean, J. C. Calvet, C. Meurey, P. Le Moigne, and I. F. Trigo (Apr. 2012). "Incoming solar and infrared radiation derived from METEOSAT: Impact on the modeled land water and energy budget over France". In: *Journal of Hydrometeorology* 13.2, pp. 504–520. ISSN: 1525755X. DOI: 10.1175/JHM-D-11-059.1.

Cattiaux, Julien, Robert Vautard, and Pascal Yiou (June 2011). "North-Atlantic SST amplified recent wintertime European land temperature extremes and trends". In: *Climate Dynamics* 36.11-12, pp. 2113–2128. ISSN: 09307575. DOI: 10.1007/s00382-010-0869-0.

Charney, Jule, Peter H. Stone, and William J. Quirk (Feb. 1975). "Drought in the Sahara: A biogeophysical feedback mechanism". In: *Science* 187.4175, pp. 434–435. ISSN: 00368075. DOI: 10.1126/science.187.4175.434.

Charney, R. J., R. Fjörtoft, and J. Neumann (Nov. 1950). "Numerical Integration of the Barotropic Vorticity Equation". In: *Tellus* 2.4, pp. 237–254. ISSN: 00402826. DOI: 10.1111/j.2153-3490.1950.tb00336.x.

Chen, Fei, Kevin W. Manning, Margaret A. LeMone, Stanley B. Trier, Joseph G. Alfieri, Rita Roberts, Mukul Tewari, Dev Niyogi, Thomas W. Horst, Steven P. Oncley, Jeffrey B. Basara, and Peter D. Blanken (June 2007). "Description and Evaluation of the Characteristics of the NCAR High-Resolution Land Data Assimilation System". EN. In: *Journal of Applied Meteorology and Climatology* 46.6, pp. 694–713. ISSN: 1558-8424. DOI: 10.1175/JAM2463.1.

Chen, T. H., A. Henderson-Sellers, P. C. D. Milly, A. J. Pitman, A. C. M. Beljaars, J. Polcher, F. Abramopoulos, A. Boone, S. Chang, F. Chen, Y. Dai, C. E. Desborough, R. E. Dickinson, L. Dümenil, M. Ek, J. R. Garratt, N. Gedney, Y. M. Gusev, J. Kim, R. Koster, E. A. Kowalczyk, K. Laval, J. Lean, D. Lettenmaier, X. Liang, J.-F. Mahfouf, H.-T. Mengelkamp, K. Mitchell, O. N. Nasonova, J. Noilhan, A. Robock, C. Rosenzweig, J. Schaake, C. A. Schlosser, J.-P. Schulz, Y. Shao, A. B. Shmakin, D. L. Verseghy, P. Wetzel, E. F. Wood, Y. Xue, Z.-L. Yang, and Q. Zeng (June 1997). "Cabauw Experimental Results from the Project for Intercomparison of Land-Surface Parameterization Schemes". In: *Journal of Climate* 10.6, pp. 1194–1215. ISSN: 0894-8755. DOI: 10.1175/1520-0442(1997)010<1194:CERFTP>2.0.CO;2.

Clapp, Roger B. and George M. Hornberger (Aug. 1978). "Empirical equations for some soil hydraulic properties". In: *Water Resources Research* 14.4, pp. 601–604. ISSN: 00431397. DOI: 10.1029/WR014i004p00601.

Clarke, K. D. (1968). *Application of Stanford watershed model concepts to predict flood peaks for small drainage areas*. Tech. rep. Division of Research Department of Highways Commonwealth of Kentucky.

Clarke, R. T. (May 1973). "A review of some mathematical models used in hydrology, with observations on their calibration and use". In: *Journal of Hydrology* 19.1, pp. 1–20. ISSN: 00221694. DOI: 10.1016/0022-1694(73)90089-9.

Crawford, Norman H and Stephen J Burges (2004). "History of the Stanford watershed model". In: *Water Resour. Impact* 6.2, pp. 1–3.

Crawford, Norman H. and Ray K. Linsley (June 1963). "Estimate of the Hydrologic Results of Rainfall Augmentation". In: *Journal of Applied Meteorology* 2.3, pp. 426–427. ISSN: 0021-8952. DOI: 10.1175/1520-0450(1963)002<0426:EOTHRO>2.0.CO;2.

Cuntz, Matthias, Juliane Mai, Luis Samaniego, Martyn Clark, Volker Wulfmeyer, Oliver Branch, Sabine Attinger, and Stephan Thober (Sept. 2016). "The impact of standard and hard-coded parameters on the hydrologic fluxes in the Noah-MP land surface model". In: *Journal of Geophysical Research* 121.18, pp. 676–10. ISSN: 21562202. DOI: 10.1002/2016JD025097.

Dai, Yongjiu, Wei Shangguan, Nan Wei, Qinchuan Xin, Hua Yuan, Shupeng Zhang, Shaofeng Liu, Xingjie Lu, Dagang Wang, and Fapeng Yan (July 2019). "A review of the global soil property maps for Earth system models". In: *SOIL* 5.2, pp. 137–158. ISSN: 2199398X. DOI: 10.5194/soil-5-137-2019.

Daly, Christopher, David R. Conklin, and Michael H. Unsworth (Oct. 2010). "Local atmospheric decoupling in complex topography alters climate change impacts". In: *International Journal of Climatology* 30.12, pp. 1857–1864. ISSN: 08998418. DOI: 10.1002/joc.2007.

Dask Development Team (2016). *Dask: Library for dynamic task scheduling*.

Dawdy, David R and Terry H Thompson (Jan. 1967). "Digital Computer Simulation in Hydrology". In: *Journal (American Water Works Association)* 59.6, pp. 685–688. ISSN: 0003150X, 15518833.

De Noblet-Ducoudré, Nathalie, Juan Pablo Boisier, Andy Pitman, G. B. Bonan, V. Brovkin, Faye Cruz, C. Delire, V. Gayler, B. J.J.M. Van Den Hurk, P. J. Lawrence, M. K. Van Der Molen, C. Müller, C. H. Reick, B. J. Strengers, and A. Voldoire (May 2012). "Determining robust impacts of land-use-induced land cover changes on surface climate over North America and Eurasia: Results from the first set of LUCID experiments". In: *Journal of Climate* 25.9, pp. 3261–3281. ISSN: 08948755. DOI: 10.1175/JCLI-D-11-00338.1.

De Wit, Heleen A., Anders Bryn, Annika Hofgaard, Jonas Karstensen, Maria M. Kvalevåg, and Glen P. Peters (July 2014). "Climate warming feedback from mountain birch forest expansion: Reduced albedo dominates carbon uptake". In: *Global Change Biology* 20.7, pp. 2344–2355. ISSN: 13652486. DOI: 10.1111/gcb.12483.

Deardorff, J. W. (Apr. 1978). "Efficient prediction of ground surface temperature and moisture, with inclusion of a layer of vegetation". In: *Journal of Geophysical Research* 83.C4, p. 1889. ISSN: 0148-0227. DOI: 10.1029/jc083ic04p01889.

Dee, D. P., S. M. Uppala, A. J. Simmons, P. Berrisford, P. Poli, S. Kobayashi, U. Andrae, M. A. Balmaseda, G. Balsamo, P. Bauer, P. Bechtold, A. C.M. Beljaars, L. van de Berg, J. Bidlot, N. Bormann, C. Delsol, R. Dragani, M. Fuentes, A. J. Geer, L. Haimberger, S. B. Healy, H. Hersbach, E. V. Hólm, L. Isaksen, P. Kållberg, M. Köhler, M. Matricardi, A. P. Mcnally, B. M. Monge-Sanz, J. J. Morcrette,

B. K. Park, C. Peubey, P. de Rosnay, C. Tavolato, J. N. Thépaut, and F. Vitart (Apr. 2011). "The ERA-Interim reanalysis: Configuration and performance of the data assimilation system". In: *Quarterly Journal of the Royal Meteorological Society* 137.656, pp. 553–597. ISSN: 00359009. DOI: 10.1002/qj.828.

Dickinson, R. E., A. Henderson-Sellers, P. J. Kennedy, and M. F. Wilson (1986). *Biosphere-atmosphere Transfer Scheme (BATS) for the NCAR Community Climate Model*. Tech. rep. National Center for Atmospheric Research.

Dickinson, Robert E. (Jan. 1983). "Land surface processes and climate—surface albedos and energy balance". In: *Advances in Geophysics* 25.C, pp. 305–353. ISSN: 00652687. DOI: 10.1016/S0065-2687(08)60176-4.

— (1984). "Modeling evapotranspiration for three-dimensional global climate models". In: *Climate processes and climate sensitivity*. American Geophysical Union; Geophysical Monograph 29, Maurice Ewing vol. 5, pp. 58–72. DOI: 10.1029/GM029p0058.

Doherty, John (2015). *Calibration and uncertainty analysis for complex environmental models*. Watermark Numerical Computing.

Dooge, James C. I. (Aug. 1986). "Looking for hydrologic laws". In: *Water Resources Research* 22.9S, 46S–58S. ISSN: 00431397. DOI: 10.1029/WR022i09Sp0046S.

— (Feb. 1988). "Hydrology in perspective". In: *Hydrological Sciences Journal* 33.1, pp. 61–85. ISSN: 0262-6667. DOI: 10.1080/02626668809491223.

Driemel, Amelie, John Augustine, Klaus Behrens, Sergio Colle, Christopher Cox, Emilio Cuevas-Agulló, Fred M. Denn, Thierry Duprat, Masato Fukuda, Hannes Grobe, Martial Haeffelin, Gary Hodges, Nicole Hyett, Osamu Ijima, Ain Kallis, Wouter Knap, Vasilii Kustov, Charles N. Long, David Longenecker, Angelo Lupi, Marion Maturilli, Mohamed Mimouni, Lucky Ntsangwane, Hiroyuki Ogihara, Xabier Olano, Marc Olefs, Masao Omori, Lance Passamani, Enio Bueno Pereira, Holger Schmithüsen, Stefanie Schumacher, Rainer Sieger, Jonathan Tamlyn, Roland Vogt, Laurent Vuilleumier, Xiangao Xia, Atsumu Ohmura, and Gert König-Langlo (Aug. 2018). "Baseline Surface Radiation Network (BSRN): Structure and data description (1992-2017)". In: *Earth System Science Data* 10.3, pp. 1491–1501. ISSN: 18663516. DOI: 10.5194/essd-10-1491-2018.

Duan, Q., J. Schaake, V. Andréassian, S. Franks, G. Goteti, H. V. Gupta, Y. M. Gusev, F. Habets, A. Hall, L. Hay, T. Hogue, M. Huang, G. Leavesley, X. Liang, O. N. Nasonova, J. Noilhan, L. Oudin, S. Sorooshian, T. Wagener, and E. F. Wood (Mar. 2006). "Model Parameter Estimation Experiment (MOPEX): An overview of science strategy and major results from the second and third workshops". In: *Journal of Hydrology*. Vol. 320. 1-2, pp. 3–17. DOI: 10.1016/j.jhydrol.2005.07.031.

Duan, Qingyun, John Schaake, and Victor Koren (2001). "A Priori Estimation of Land Surface Model Parameters". In: *Land Surface Hydrology, Meteorology, and Climate: Observations and Modeling*. American Geophysical Union (AGU), pp. 77–94. ISBN: 9781118665589. DOI: https://doi.org/10.1029/WS003p0077. eprint: https://agupubs.onlinelibrary.wiley.com/doi/pdf/10.1029/WS003p0077.

Duffy, Christopher J (July 2017). "The terrestrial hydrologic cycle: an historical sense of balance". In: *Wiley Interdisciplinary Reviews: Water* 4.4, e1216. ISSN: 2049-1948. DOI: 10.1002/wat2.1216.

Dy, C. Y. and J. C.H. Fung (Aug. 2016). "Updated global soil map for the Weather Research and Forecasting model and soil moisture initialization for the Noah land surface model". In: *Journal of Geophysical Research* 121.15, pp. 8777–8800. ISSN: 21562202. DOI: 10.1002/2015JD024558.

ECMWF website (n.d.). *ECMWF | Geographical coverage | 2021020106,0,2021020106*.

Ek, M. B., K. E. Mitchell, Y. Lin, E. Rogers, P. Grunmann, V. Koren, G. Gayno, and J. D. Tarpley (Nov. 2003). "Implementation of Noah land surface model advances in the National Centers for Environmental Prediction operational mesoscale Eta model". In: *Journal of Geophysical Research: Atmospheres* 108.22. ISSN: 01480227. DOI: 10.1029/2002jd003296.

Erlandsen, Helene B., Ingjerd Haddeland, Lena M. Tallaksen, and Jørn Kristiansen (Jan. 2017). "The sensitivity of the terrestrial surface energy and water balance estimates in the WRF model to lower surface boundary representations: A South Norway case study". In: *Journal of Hydrometeorology* 18.1, pp. 265–284. ISSN: 15257541. DOI: 10.1175/JHM-D-15-0146.1.

Erlandsen, Helene Birkelund, Stein Beldring, Stephanie Eisner, Hege Hisdal, Shaochun Huang, and Lena Merete Tallaksen (Jan. 2021). "Constraining the HBV model for robust water balance assessments in a cold climate". In: *Hydrology Research*. ISSN: 0029-1277. DOI: 10.2166/nh.2021.132.

Erlandsen, Helene Birkelund, Lena Merete Tallaksen, and Jørn Kristiansen (June 2019). "Merits of novel high-resolution estimates and existing long-term estimates of humidity and incident radiation in a complex domain". In: *Earth System Science Data* 11.2, pp. 797–821. ISSN: 1866-3516. DOI: 10.5194/essd-11-797-2019.

FAO/UNESCO (1974). *UNESCO Soil Map of the World, 1: 5,000,000; 10 Vols.*

Fekete, B. M., Richard D. Robarts, Michio Kumagai, H.-P. Nachtnebel, Eric Odada, and Alexander V. Zhulidov (Aug. 2015). "Time for in situ renaissance". In: *Science* 349.6249, pp. 685–686. ISSN: 0036-8075. DOI: 10.1126/science.aac7358.

Fekete, Balázs M and Charles J Vörösmarty (2007). "The current status of global river discharge monitoring and potential new technologies complementing traditional discharge measurements". In: *Predictions in Ungauged Basins: PUB Kick-off (Proceedings of the PUB Kick-off meeting held in Brasilia,20–22 November 2002), IAHS publication no. 309*.

Findell, Kirsten L., Andrew J. Pitman, Matthew H. England, and Philip J. Pegion (June 2009). "Regional and global impacts of land cover change and sea surface temperature anomalies". In: *Journal of Climate* 22.12, pp. 3248–3269. ISSN: 08948755. DOI: 10.1175/2008JCLI2580.1.

Fisher, Joshua B., Forrest Melton, Elizabeth Middleton, Christopher Hain, Martha Anderson, Richard Allen, Matthew F. McCabe, Simon Hook, Dennis Baldocchi, Philip A. Townsend, Ayse Kilic, Kevin Tu, Diego D. Miralles, Johan Perret, Jean-Pierre Lagouarde, Duane Waliser, Adam J. Purdy, Andrew French, David Schimel, James S. Famiglietti, Graeme Stephens, and Eric F. Wood (Apr. 2017). "The future of evapotranspiration: Global requirements for ecosystem functioning, carbon and climate feedbacks, agricultural management, and water resources". In: *Water Resources Research* 53.4, pp. 2618–2626. ISSN: 00431397. DOI: 10.1002/2016WR020175.

Fladen, Bjørnar Araberg, Gunn Oland, Knut Gakkestad, Svein Kroken, and Inge Harald Vognild (2017). *Overview of Norway's electricity history: information from NVE and Norad, November 2016*. Tech. rep. Oslo, 11 s.

Folse, J. A. (1929). *A new method of estimating stream-flow*. Tech. rep.

Freeze, R. Allan and R. L. Harlan (Nov. 1969). "Blueprint for a physically-based, digitally-simulated hydrologic response model". In: *Journal of Hydrology* 9.3, pp. 237–258. ISSN: 00221694. DOI: 10.1016/0022-1694(69)90020-1.

Friedl, M. A., D. K. McIver, J. C.F. Hodges, X. Y. Zhang, D. Muchoney, A. H. Strahler, C. E. Woodcock, S. Gopal, A. Schneider, A. Cooper, A. Baccini, F. Gao, and C. Schaaf (Nov. 2002). "Global land cover mapping from MODIS: Algorithms

and early results". In: *Remote Sensing of Environment* 83.1-2, pp. 287–302. ISSN: 00344257. DOI: 10.1016/S0034-4257(02)00078-0.

Friedman, Jerome, Trevor Hastie, and Robert Tibshirani (2001). *The Elements of Statistical Learning*. Springer Series in Statistics. Berlin: Springer.

Gochis, David, Wei Yu, and David Yates (2013). *The WRF-Hydro model technical description and user's guide, version 1.0.* NCAR Technical Document. NCAR, p. 120.

Green, W. Heber and G. A. Ampt (May 1911). "Studies on Soil Phyics." In: *The Journal of Agricultural Science* 4.1, pp. 1–24. ISSN: 0021-8596. DOI: 10.1017/S0021859600001441.

Gupta, Hoshin V., Harald Kling, Koray K. Yilmaz, and Guillermo F. Martinez (2009). "Decomposition of the mean squared error and NSE performance criteria: Implications for improving hydrological modelling". In: *Journal of Hydrology* 377.1-2, pp. 80–91. ISSN: 00221694. DOI: 10.1016/j.jhydrol.2009.08.003. arXiv: arXiv:1011.1669v3.

Haddeland, Ingjerd, Douglas B. Clark, Wietse Franssen, Fulco Ludwig, Frank Voß, Nigel W. Arnell, Nathalie Bertrand, Martin Best, Sonja Folwell, Dieter Gerten, Sandra Gomes, Simon N. Gosling, Stefan Hagemann, Naota Hanasaki, Richard Harding, Jens Heinke, Pavel Kabat, Sujan Koirala, Taikan Oki, Jan Polcher, Tobias Stacke, Pedro Viterbo, Graham P. Weedon, and Pat Yeh (2011). "Multimodel estimate of the global terrestrial water balance: Setup and first results". In: *Journal of Hydrometeorology*. ISSN: 1525755X. DOI: 10.1175/2011JHM1324.1.

Halley, Edmond (Jan. 1686). "An account of the circulation of the watry vapours of the sea, and of the cause of springs, presented to the Royal Society". In: *Philosophical Transactions of the Royal Society of London* 17.192, pp. 468–473. ISSN: 0261-0523. DOI: 10.1098/rstl.1686.0084.

Hannah, David M., Siegfried Demuth, Henny A.J. van Lanen, Ulrich Looser, Christel Prudhomme, Gwyn Rees, Kerstin Stahl, and Lena M. Tallaksen (Mar. 2011). "Large-scale river flow archives: Importance, current status and future needs". In: *Hydrological Processes* 25.7, pp. 1191–1200. ISSN: 08856087. DOI: 10.1002/hyp.7794.

Hansen, J. (Apr. 1983). "Efficient three-dimensional global models for climate studies: models I and II." In: *Monthly Weather Review* 111.4, pp. 609–662. ISSN: 00270644. DOI: 10.1175/1520-0493(1983)111<0609:ETDGMF>2.0.CO;2.

Hanssen-Bauer, I., E. J. Førland, I. Haddeland, H. Hisdal, D. Lawrence, S. Mayer, A. Nesje, J. E. Ø. Nilsen, S. Sandven, A. B. Sandø, A. Sorteberg, and B.Ådlandsvik (2017). *Climate in Norway 2100 – a knowledge base for climate adaptation*. Tech. rep. The Norwegian Centre for Climate Services (NCCS).

Henderson-Sellers, A., Z. L. Yang, and R. E. Dickinson (1993). "The project for intercomparison of land surface parameterisation schemes". In: *Bulletin - American Meteorological Society* 74.7, pp. 1335–1349. ISSN: 0003-0007. DOI: 10.1175/1520-0477(1993)074<1335:tpfiol>2.0.co;2.

Hersbach, Hans, Bill Bell, Paul Berrisford, Shoji Hirahara, András Horányi, Joaquín Muñoz-Sabater, Julien Nicolas, Carole Peubey, Raluca Radu, Dinand Schepers, Adrian Simmons, Cornel Soci, Saleh Abdalla, Xavier Abellan, Gianpaolo Balsamo, Peter Bechtold, Gionata Biavati, Jean Bidlot, Massimo Bonavita, Giovanna De Chiara, Per Dahlgren, Dick Dee, Michail Diamantakis, Rossana Dragani, Johannes Flemming, Richard Forbes, Manuel Fuentes, Alan Geer, Leo Haimberger, Sean Healy, Robin J. Hogan, Elías Hólm, Marta Janisková, Sarah Keeley, Patrick Laloyaux, Philippe Lopez, Cristina Lupu, Gabor Radnoti, Patricia de Rosnay, Iryna Rozum, Freja Vamborg, Sebastien Villaume, and Jean Noël Thépaut (July 2020). "The

ERA5 global reanalysis". In: *Quarterly Journal of the Royal Meteorological Society* 146.730, pp. 1999–2049. ISSN: 1477870X. DOI: 10.1002/qj.3803.

Höge, Marvin, Thomas Wöhling, and Wolfgang Nowak (Mar. 2018). "A Primer for Model Selection: The Decisive Role of Model Complexity". In: *Water Resources Research* 54.3, pp. 1688–1715. ISSN: 19447973. DOI: 10.1002/2017WR021902.

Horton, Robert E. (Dec. 1915). "THE MELTING OF SNOW". English. In: *Monthly Weather Review* 43.12, pp. 599–605. ISSN: 0027-0644. DOI: 10.1175/1520-0493(1915)43<599:TMOS>2.0.CO;2.

— (June 1931). "The field, scope, and status of the science of hydrology". In: *Eos, Transactions American Geophysical Union* 12.1, pp. 189–202. ISSN: 23249250. DOI: 10.1029/TR012i001p00189-2.

— (June 1933). "The Rôle of infiltration in the hydrologic cycle". In: *Eos, Transactions American Geophysical Union* 14.1, pp. 446–460. ISSN: 23249250. DOI: 10.1029/TR014i001p00446.

Horvath, Peter, Hui Tang, Rune Halvorsen, Frode Stordal, Lena Merete Tallaksen, Terje Koren Berntsen, and Anders Bryn (Jan. 2021). "Improving the representation of high-latitude vegetation distribution in dynamic global vegetation models". In: *Biogeosciences* 18.1, pp. 95–112. ISSN: 17264189. DOI: 10.5194/bg-18-95-2021.

Hoyer, S. and J. Hamman (2017). "xarray: N-D labeled arrays and datasets in Python". In: *Journal of Open Research Software* 5.1. DOI: 10.5334/jors.148.

Huang, Shaochun, Stephanie Eisner, Jan Olof Magnusson, Cristian Lussana, Xue Yang, and Stein Beldring (Oct. 2019). "Improvements of the spatially distributed hydrological modelling using the HBV model at 1 km resolution for Norway". In: *Journal of Hydrology* 577, p. 123585. ISSN: 00221694. DOI: 10.1016/j.jhydrol.2019.03.051.

Huggins, L. F. and E. J. Monke (June 1968). "A Mathematical Model for Simulating the Hydrologic Response of a Watershed". In: *Water Resources Research* 4.3, pp. 529–539. ISSN: 19447973. DOI: 10.1029/WR004i003p00529.

Humboldt, A von (1807). *Ideen zu einer geographieder pflangen nebat einem naturgemalde der tropenlander*.

Isaacson, W (2017). *Leonardo Da Vinci*. Simon & Schuster UK. ISBN: 9781471166778.

Jaffrés, Jasmine B.D. (Jan. 2019). "GHCN-Daily: a treasure trove of climate data awaiting discovery". In: *Computers and Geosciences* 122, pp. 35–44. ISSN: 00983004. DOI: 10.1016/j.cageo.2018.07.003.

Jarvis, P.G. (Feb. 1976). "The interpretation of the variations in leaf water potential and stomatal conductance found in canopies in the field". In: *Philosophical Transactions of the Royal Society of London. B, Biological Sciences* 273.927, pp. 593–610. ISSN: 0080-4622. DOI: 10.1098/rstb.1976.0035.

Jennings, Keith S. and Noah P. Molotch (Sept. 2019). "The sensitivity of modeled snow accumulation and melt to precipitation phase methods across a climatic gradient". In: *Hydrology and Earth System Sciences* 23.9, pp. 3765–3786. ISSN: 1607-7938. DOI: 10.5194/hess-23-3765-2019.

Jennings, Keith S., Taylor S. Winchell, Ben Livneh, and Noah P. Molotch (Dec. 2018). "Spatial variation of the rain–snow temperature threshold across the Northern Hemisphere". In: *Nature Communications* 9.1, p. 1148. ISSN: 2041-1723. DOI: 10.1038/s41467-018-03629-7.

Kalnay, E., M. Kanamitsu, R. Kistler, W. Collins, D. Deaven, L. Gandin, M. Iredell, S. Saha, G. White, J. Woollen, Y. Zhu, A. Leetmaa, R. Reynolds, M. Chelliah, W. Ebisuzaki, W. Higgins, J. Janowiak, K. C. Mo, C. Ropelewski, J. Wang, Roy Jenne, and Dennis Joseph (Mar. 1996). "The NCEP/NCAR 40-Year Reanalysis

Project". In: *Bulletin of the American Meteorological Society* 77.3, pp. 437–471. ISSN: 0003-0007. DOI: 10.1175/1520-0477(1996)077<0437:TNYRP>2.0.CO;2.

Katragkou, E, M. Garciá-Diéz, R Vautard, S Sobolowski, P Zanis, G Alexandri, R M Cardoso, A Colette, J Fernandez, A Gobiet, K Goergen, T Karacostas, S Knist, S Mayer, P. M.M. Soares, I Pytharoulis, I Tegoulias, A Tsikerdekis, and D Jacob (2015a). "Regional climate hindcast simulations within EURO-CORDEX: Evaluation of a WRF multi-physics ensemble". In: *Geoscientific Model Development* 8.3, pp. 603–618. ISSN: 19919603. DOI: 10.5194/gmd-8-603-2015.

— (2015b). "Regional climate hindcast simulations within EURO-CORDEX: Evaluation of a WRF multi-physics ensemble". In: *Geoscientific Model Development* 8.3, pp. 603–618. ISSN: 19919603. DOI: 10.5194/gmd-8-603-2015.

Kauffeldt, Anna, Sven Halldin, Florian Pappenberger, Fredrik Wetterhall, Chong Yu Xu, and Hannah L. Cloke (June 2015). "Imbalanced land surface water budgets in a numerical weather prediction system". In: *Geophysical Research Letters* 42.11, pp. 4411–4417. ISSN: 19448007. DOI: 10.1002/2015GL064230.

Kay, A. L., V. A. Bell, E. M. Blyth, S. M. Crooks, H. N. Davies, and N. S. Reynard (Sept. 2013). "A hydrological perspective on evaporation: Historical trends and future projections in Britain". In: *Journal of Water and Climate Change* 4.3, pp. 193–208. ISSN: 20402244. DOI: 10.2166/wcc.2013.014.

Keeling, Charles D., Stephen C. Piper, Timothy P. Whorf, and Ralph F. Keeling (Jan. 2011). "Evolution of natural and anthropogenic fluxes of atmospheric CO 2 from 1957 to 2003". In: *Tellus B: Chemical and Physical Meteorology* 63.1, pp. 1–22. ISSN: 1600-0889. DOI: 10.1111/j.1600-0889.2010.00507.x.

Kircher, A (1678). *Athanasii Kircheri ... Mundus subterraneus, in XII libros digestus.* Athanasii Kircheri ... Mundus subterraneus, in XII libros digestus v. 2. Apud Joannem Janssonium à Waesberge & filios.

Kirchner, James W. (Mar. 2006). "Getting the right answers for the right reasons: Linking measurements, analyses, and models to advance the science of hydrology". In: *Water Resources Research* 42.3. ISSN: 00431397. DOI: 10.1029/2005WR004362.

Kishné, Andrea Sz, Yohannes Tadesse Yimam, Cristine L.S. Morgan, and Bright C. Dornblaser (Jan. 2017). "Evaluation and improvement of the default soil hydraulic parameters for the Noah Land Surface Model". In: *Geoderma* 285, pp. 247–259. ISSN: 00167061. DOI: 10.1016/j.geoderma.2016.09.022.

Køltzow, Morten A.Ø. Ø, Trond Iversen, and Jan Erik Haugen (May 2011). "The Importance of Lateral Boundaries, Surface Forcing and Choice of Domain Size for Dynamical Downscaling of Global Climate Simulations". en. In: *Atmosphere* 2.4, pp. 67–95. ISSN: 20734433. DOI: 10.3390/atmos2020067.

Koren, V.I, B.D Finnerty, J.C Schaake, M.B Smith, D.-J Seo, and Q.-Y Duan (Apr. 1999). "Scale dependencies of hydrologic models to spatial variability of precipitation". In: *Journal of Hydrology* 217.3-4, pp. 285–302. ISSN: 00221694. DOI: 10.1016/S0022-1694(98)00231-5.

Koster, Randal D, Taikan Oki, and Max J Suarez (1999). "The Offline Validation of Land Surface Models". In: *Journal of the Meteorological Society of Japan. Ser. II* 77.1B, pp. 257–263. ISSN: 0026-1165. DOI: 10.2151/jmsj1965.77.1B{_}257.

Kotlarski, Sven, Frank Paul, and Daniela Jacob (Mar. 2010). "Forcing a distributed glacier mass balance model with the regional climate model REMO. Part I: climate model evaluation". In: *Journal of Climate* 23.6, pp. 1589–1606. ISSN: 08948755. DOI: 10.1175/2009JCLI2711.1.

Kristiansen, Jørn, Dag Bjørge, John M. Edwards, and Gabriel G. Rooney (Aug. 2012). "Soil Field Model Interoperability: Challenges and Impact on Screen Temperature

Forecast Skill during the Nordic Winter". In: *Journal of Hydrometeorology* 13.4, pp. 1215–1232. ISSN: 1525-755X. DOI: 10.1175/JHM-D-11-095.1.

Kustas, William P., Albert Rango, and Remko Uijlenhoet (1994). "A simple energy budget algorithm for the snowmelt runoff model". In: *Water Resources Research*. ISSN: 19447973. DOI: 10.1029/94WR00152.

Leuning, Ray, Y. Q. Zhang, Amelie Rajaud, Helen Cleugh, and Kevin Tu (2008). "A simple surface conductance model to estimate regional evaporation using MODIS leaf area index and the Penman-Monteith equation". In: *Water Resources Research*. ISSN: 00431397. DOI: 10.1029/2007WR006562.

Lhomme, J.-P. (June 1997). "Towards a rational definition of potential evaporation". In: *Hydrology and Earth System Sciences* 1.2, pp. 257–264. ISSN: 1607-7938. DOI: 10.5194/hess-1-257-1997.

Li, J. L.F., Wei Liang Lee, Jia Yuh Yu, Glynn Hulley, Eric Fetzer, Yi Chun Chen, and Yi Hui Wang (Jan. 2016). "The impacts of precipitating hydrometeors radiative effects on land surface temperature in contemporary GCMS using satellite observations". In: *Journal of Geophysical Research* 121.1, pp. 67–79. ISSN: 21562202. DOI: 10.1002/2015JD023776.

Liedekerke, Marc Van, Arwyn Jones, and Panos Panagos (2006). *ESDBv2 Raster Library - a set of rasters derived from the European Soil Database distribution v2.0*.

Lin, Tzu Shun and Fang Yi Cheng (May 2016). "Impact of soil moisture initialization and soil texture on simulated land-atmosphere interaction in Taiwan". In: *Journal of Hydrometeorology* 17.5, pp. 1337–1355. ISSN: 15257541. DOI: 10.1175/JHM-D-15-0024.1.

Linsley, Ray K and Norman H Crawford (1960). "Computation of a synthetic streamflow record on a digital computer". In: *Int. Ass. sci. Hydrol. Publ. No. 51*, pp. 526–538.

Lussana, Cristian, Ole Einar Tveito, Andreas Dobler, and Ketil Tunheim (2019). "SeNorge_2018, daily precipitation, and temperature datasets over Norway". In: *Earth System Science Data* 11.4, pp. 1531–1551. ISSN: 18663516. DOI: 10.5194/essd-11-1531-2019.

Lynch, Peter (Jan. 1992). "Richardson's barotropic forecast: a reappraisal". In: *Bulletin - American Meteorological Society* 73.1, pp. 35–47. ISSN: 0003-0007. DOI: 10.1175/1520-0477(1992)073<0035:RBFAR>2.0.CO;2.

— (Mar. 2008). "The origins of computer weather prediction and climate modeling". In: *Journal of Computational Physics* 227.7, pp. 3431–3444. ISSN: 10902716. DOI: 10.1016/j.jcp.2007.02.034.

Mahrt, L. and H. Pan (May 1984). "A two-layer model of soil hydrology". In: *Boundary-Layer Meteorology* 29.1, pp. 1–20. ISSN: 00068314. DOI: 10.1007/BF00119116.

Majasalmi, Titta, Stephanie Eisner, Rasmus Astrup, Jonas Fridman, and Ryan M. Bright (Jan. 2018). "An enhanced forest classification scheme for modeling vegetation-climate interactions based on national forest inventory data". In: *Biogeosciences* 15.2, pp. 399–412. ISSN: 17264189. DOI: 10.5194/bg-15-399-2018.

Manabe, S (1982). "Simulation of climate by general circulation models with hydrologic cycle". In: *In "Land Surface Process in Atmospheric General Circulation Model"*. Cambridge Univ. Press London and New York, pp. 19–66.

Manabe, Syukuro (Nov. 1969). "Climate and the Ocean Circulation: 1. The Atmospheric Circulation and the Hydrology of the Earth's Surface". In: *Monthly Weather Review* 97.11, pp. 739–774. ISSN: 0027-0644. DOI: 10.1175/1520-0493(1969)097<0739:CATOC>2.3.CO;2.

Manabe, Syukuro and Robert F. Strickler (July 1964). "Thermal Equilibrium of the Atmosphere with a Convective Adjustment". In: *Journal of the Atmospheric Sciences* 21.4, pp. 361–385. ISSN: 0022-4928. DOI: 10.1175/1520-0469(1964)021<0361:TEOTAW>2.0.CO;2.

Manabe, Syukuro and Richard T. Wetherald (Jan. 1975). "The Effects of Doubling the CO 2 Concentration on the climate of a General Circulation Model". In: *Journal of the Atmospheric Sciences* 32.1, pp. 3–15. ISSN: 0022-4928. DOI: 10.1175/1520-0469(1975)032<0003:TEODTC>2.0.CO;2.

Marty, Christoph (2000). "Surface radiation, cloud forcing and greenhouse effect in the Alps". PhD thesis. ETH Zurich.

Matthews, E. (1983). "Global vegetation and land use: New high-resolution data bases for climate studies". In: *J. Clim. Appl. Meteorol.* 22, pp. 474–487. DOI: {10.1175/1520-0450(1983)022%3C0474%3AGVALUN%3E2.0.CO;2}.

— (1984). *Prescription of Land-Surface Boundary Conditions in GISS GCM II: A Simple Method Based on High-Resolution Vegetation Data Bases*. Washington, D.C.

Mayer, B. and A. Kylling (July 2005). "Technical note: The libRadtran software package for radiative transfer calculations – description and examples of use". In: *Atmospheric Chemistry and Physics Discussions* 5.2, pp. 1319–1381. ISSN: 1680-7375. DOI: 10.5194/acpd-5-1319-2005.

McMahon, T. A., B. L. Finlayson, and M. C. Peel (Nov. 2016). "Historical developments of models for estimating evaporation using standard meteorological data". In: *Wiley Interdisciplinary Reviews: Water* 3.6, pp. 788–818. ISSN: 2049-1948. DOI: 10.1002/wat2.1172.

Meiyappan, Prasanth and Atul K. Jain (July 2012). "Three distinct global estimates of historical land-cover change and land-use conversions for over 200 years". In: *Frontiers of Earth Science* 6.2, pp. 122–139. ISSN: 20950209. DOI: 10.1007/s11707-012-0314-2.

Mendoza, Pablo A., Martyn P. Clark, Michael Barlage, Balaji Rajagopalan, Luis Samaniego, Gab Abramowitz, and Hoshin Gupta (Jan. 2015). "Are we unnecessarily constraining the agility of complex process-based models?" In: *Water Resources Research* 51.1, pp. 716–728. ISSN: 19447973. DOI: 10.1002/2014WR015820.

Merz, Ralf, Juraj Parajka, and Günter Blöschl (Feb. 2011). "Time stability of catchment model parameters: Implications for climate impact analyses". In: *Water Resources Research* 47.2. ISSN: 00431397. DOI: 10.1029/2010WR009505.

Milly, P. C D and Krista A. Dunne (Jan. 2011a). "On the hydrologic adjustment of climate-model projections: The potential pitfall of potential evapotranspiration". In: *Earth Interactions* 15.1, pp. 1–14. ISSN: 10873562. DOI: 10.1175/2010EI363.1.

— (Jan. 2011b). "On the hydrologic adjustment of climate-model projections: The potential pitfall of potential evapotranspiration". In: *Earth Interactions* 15.1, pp. 1–14. ISSN: 10873562. DOI: 10.1175/2010EI363.1.

Milly, P. C.D. and A. B. Shmakin (2002). "Global modeling of land water and energy balances. Part II: Land-characteristic contributions to spatial variability". In: *Journal of Hydrometeorology* 3.3, pp. 301–310. ISSN: 1525755X. DOI: 10.1175/1525-7541(2002)003<0301:GMOLWA>2.0.CO;2.

Miralles, D. G., W. Brutsaert, A. J. Dolman, and J. H. Gash (Nov. 2020). *On the Use of the Term "Evapotranspiration"*. DOI: 10.1029/2020WR028055.

Mitchell, Ken (2001). "The community NOAH land–surface model (LSM)". In: *User, s Guide, Public Release Version* 2.7, p. 1.

Mizukami, Naoki, Martyn P. Clark, Andrew G. Slater, Levi D. Brekke, Marketa M. Elsner, Jeffrey R. Arnold, and Subhrendu Gangopadhyay (Feb. 2014). "Hydrologic

Implications of Different Large-Scale Meteorological Model Forcing Datasets in Mountainous Regions". In: *Journal of Hydrometeorology* 15.1, pp. 474–488. ISSN: 1525-755X. DOI: 10.1175/JHM-D-13-036.1.

Monteith, J. (1985). "Evaporation from land surfaces: progress in analysis and prediction since 1948". In: ASAE publication. American Society of Agricultural Engineers, pp. 4–12. ISBN: 9780916150754.

Monteith, J. L. (1965). *Evaporation and environment.*

— (Jan. 1981). "Evaporation and surface temperature". In: *Quarterly Journal of the Royal Meteorological Society* 107.451, pp. 1–27. ISSN: 1477870X. DOI: 10.1002/qj.49710745102.

Moradkhani, Hamid and Soroosh Sorooshian (July 2008). "General Review of Rainfall-Runoff Modeling: Model Calibration, Data Assimilation, and Uncertainty Analysis". In: *Hydrological Modelling and the Water Cycle*. Springer Berlin Heidelberg, pp. 1–24. DOI: 10.1007/978-3-540-77843-1{_}1.

Mulligan, Joseph F. and H. Gerhard Hertz (Jan. 1997). "An unpublished lecture by Heinrich Hertz: "On the energy balance of the Earth"". In: *American Journal of Physics* 65.1, pp. 36–45. ISSN: 0002-9505. DOI: 10.1119/1.18565.

Nash, J. E. and J. V. Sutcliffe (Apr. 1970). "River flow forecasting through conceptual models part I - A discussion of principles". In: *Journal of Hydrology* 10.3, pp. 282–290. ISSN: 00221694. DOI: 10.1016/0022-1694(70)90255-6.

National Research Council (1991). *Opportunities in the Hydrologic Sciences*. Washington, DC: The National Academies Press. DOI: 10.17226/1543.

Newman, Andrew J., Naoki Mizukami, Martyn P. Clark, Andrew W. Wood, Bart Nijssen, and Grey Nearing (Aug. 2017). "Benchmarking of a physically based hydrologic model". In: *Journal of Hydrometeorology* 18.8, pp. 2215–2225. ISSN: 15257541. DOI: 10.1175/JHM-D-16-0284.1.

Niu, Guo-Yue, Zong-Liang Yang, Kenneth E. Mitchell, Fei Chen, Michael B. Ek, Michael Barlage, Anil Kumar, Kevin Manning, Dev Niyogi, Enrique Rosero, Mukul Tewari, and Youlong Xia (June 2011). "The community Noah land surface model with multiparameterization options (Noah-MP): 1. Model description and evaluation with local-scale measurements". In: *Journal of Geophysical Research* 116.D12, p. D12109. ISSN: 0148-0227. DOI: 10.1029/2010JD015139.

NOAA ESRL website (2020). *Clouds and Climate*.

Ohmura, A. (Apr. 2001). "Physical basis for the temperature-based melt-index method". In: *Journal of Applied Meteorology* 40.4, pp. 753–761. ISSN: 08948763. DOI: 10.1175/1520-0450(2001)040<0753:PBFTTB>2.0.CO;2.

Ohmura, Atsumu (Sept. 2014). "The development and the present status of energy balance climatology". In: *Journal of the Meteorological Society of Japan* 92.4, pp. 245–285. ISSN: 00261165. DOI: 10.2151/jmsj.2014-401.

Oleson, K W, D M Lawrence, G B Bonan, M G Flanner, E Kluzek, P J Lawrence, S Levis, S C Swenson, P E Thornton, and A Dai (2010). "Technical description of version 4.5 of the Community Land Model (CLM), NCAR Tech". In: *Notes (NCAR/TN-478+ STR)*.

Ong, Chin and Colin Black (Dec. 2012). "John Monteith". In: *Agricultural and Forest Meteorology* 166-167, A1–A2. ISSN: 01681923. DOI: 10.1016/j.agrformet.2012.10.012.

Peel, Murray C. and Thomas A. McMahon (Sept. 2020). "Historical development of rainfall-runoff modeling". In: *Wiley Interdisciplinary Reviews: Water* 7.5. ISSN: 20491948. DOI: 10.1002/wat2.1471.

Pelletier, J.D., P.D. Broxton, P. Hazenberg, X. Zeng, P.A. Troch, G. Niu, Z.C. Williams, M.A. Brunke, and D. Gochis (2016). *Global 1-km Gridded Thickness of Soil, Regolith, and Sedimentary Deposit Layers*. en. DOI: 10.3334/ORNLDAAC/1304.

Penman, H. L. (Apr. 1948). "Natural Evaporation from Open Water, Bare Soil and Grass". In: *Proceedings of the Royal Society A: Mathematical, Physical and Engineering Sciences* 193.1032, pp. 120–145. ISSN: 1364-5021. DOI: 10.1098/rspa.1948.0037.

Phillips, Norman A. (Apr. 1956). "The general circulation of the atmosphere: A numerical experiment". In: *Quarterly Journal of the Royal Meteorological Society* 82.352, pp. 123–164. ISSN: 1477870X. DOI: 10.1002/qj.49708235202.

Pitman, A. J. (Apr. 2003). "The evolution of, and revolution in, land surface schemes designed for climate models". In: *International Journal of Climatology* 23.5, pp. 479–510. ISSN: 08998418. DOI: 10.1002/joc.893.

Powers, Jordan G., Joseph B. Klemp, William C. Skamarock, Christopher A. Davis, Jimy Dudhia, David O. Gill, Janice L. Coen, David J. Gochis, Ravan Ahmadov, Steven E. Peckham, Georg A. Grell, John Michalakes, Samuel Trahan, Stanley G. Benjamin, Curtis R. Alexander, Geoffrey J. Dimego, Wei Wang, Craig S. Schwartz, Glen S. Romine, Zhiquan Liu, Chris Snyder, Fei Chen, Michael J. Barlage, Wei Yu, and Michael G. Duda (Aug. 2017). "The weather research and forecasting model: Overview, system efforts, and future directions". In: *Bulletin of the American Meteorological Society* 98.8, pp. 1717–1737. ISSN: 00030007. DOI: 10.1175/BAMS-D-15-00308.1.

Randall, David A., Cecilia M. Bitz, Gokhan Danabasoglu, A. Scott Denning, Peter R. Gent, Andrew Gettelman, Stephen M. Griffies, Peter Lynch, Hugh Morrison, Robert Pincus, and John Thuburn (Jan. 2018). "100 Years of Earth System Model Development". In: *Meteorological Monographs* 59, pp. 1–12. ISSN: 0065-9401. DOI: 10.1175/amsmonographs-d-18-0018.1.

Refsgaard, Jens Christian, Børge Storm, and Thomas Clausen (Oct. 2010). "Système Hydrologique Européen (SHE): Review and perspectives after 30 years development in distributed physically-based hydrological modelling". In: *Hydrology Research* 41.5, pp. 355–377. ISSN: 00291277. DOI: 10.2166/nh.2010.009.

Richards, L. A. (Nov. 1931). "Capillary conduction of liquids through porous mediums". In: *Journal of Applied Physics* 1.5, pp. 318–333. ISSN: 01486349. DOI: 10.1063/1.1745010.

Richardson, L. F. (July 1920). "The supply of energy from and to atmospheric eddies". In: *Proceedings of the Royal Society of London. Series A, Containing Papers of a Mathematical and Physical Character* 97.686, pp. 354–373. ISSN: 0950-1207. DOI: 10.1098/rspa.1920.0039.

Richardson, Lewis F. (2007). *Weather prediction by numerical process, second edition*. ISBN: 9780511618291. DOI: 10.1017/CBO9780511618291.

Richardson, Lewis Fry and Peter Lynch (2007). *Weather Prediction by Numerical Process*. 2nd ed. Cambridge Mathematical Library. Cambridge University Press. DOI: 10.1017/CBO9780511618291.

Rockwood, David M (1968). *Application of Streamflow Synthesis and Reservoir Regulation-" SSARR"-Program to the Lower Mekong River*. Tech. rep. US Army Corps of Engineers.

Rosero, Enrique, Zong-Liang Yang, Thorsten Wagener, Lindsey E. Gulden, Soni Yatheendradas, and Guo-Yue Niu (Feb. 2010). "Quantifying parameter sensitivity, interaction, and transferability in hydrologically enhanced versions of the Noah land surface model over transition zones during the warm season". In: *Journal of Geophysical Research* 115.D3, p. D03106. ISSN: 0148-0227. DOI: 10.1029/2009JD012035.

Russell, Gary L. and James R. Miller (Sept. 1990). "Global river runoff calculated from a global atmospheric general circulation model". In: *Journal of Hydrology* 117.1-4, pp. 241–254. ISSN: 00221694. DOI: 10.1016/0022-1694(90)90095-F.

Sagan, Carl, Owen B. Toon, and James B. Pollack (Dec. 1979). "Anthropogenic albedo changes and the earth's climate". In: *Science* 206.4425, pp. 1363–1368. ISSN: 00368075. DOI: 10.1126/science.206.4425.1363.

Samaniego, Luis, Rohini Kumar, Stephan Thober, Oldrich Rakovec, Matthias Zink, Niko Wanders, Stephanie Eisner, Hannes Müller Schmied, Edwin Sutanudjaja, Kirsten Warrach-Sagi, and Sabine Attinger (Sept. 2017). "Toward seamless hydrologic predictions across spatial scales". In: *Hydrology and Earth System Sciences* 21.9, pp. 4323–4346. ISSN: 16077938. DOI: 10.5194/hess-21-4323-2017.

Schmied, Hannes Müller, Richard Müller, Arturo Sanchez-Lorenzo, Bodo Ahrens, and Martin Wild (Oct. 2016). "Evaluation of radiation components in a global freshwater model with station-based observations". In: *Water (Switzerland)* 8.10, p. 450. ISSN: 20734441. DOI: 10.3390/w8100450.

Selcer, Perrin (2015). "Fabricating Unity: The FAO-UNESCO Soil Map of the World". In: *Historical Social Research / Historische Sozialforschung* 40.2 (152), pp. 174–201. ISSN: 01726404.

Sellers, P. J. (Jan. 1997). "Modeling the Exchanges of Energy, Water, and Carbon Between Continents and the Atmosphere". In: *Science* 275.5299, pp. 502–509. ISSN: 00368075. DOI: 10.1126/science.275.5299.502.

Sellers, P. J., Y. Mintz, Y. C. Sud, and A. Dalcher (Mar. 1986). "A Simple Biosphere Model (SIB) for Use within General Circulation Models". In: *Journal of the Atmospheric Sciences* 43.6, pp. 505–531. ISSN: 0022-4928. DOI: 10.1175/1520-0469(1986)043<0505:ASBMFU>2.0.CO;2.

Shangguan, Wei, Tomislav Hengl, Jorge Mendes de Jesus, Hua Yuan, and Yongjiu Dai (Mar. 2017). "Mapping the global depth to bedrock for land surface modeling". In: *Journal of Advances in Modeling Earth Systems* 9.1, pp. 65–88. ISSN: 19422466. DOI: 10.1002/2016MS000686.

Sheffield, Justin, Gopi Goteti, and Eric F. Wood (July 2006). "Development of a 50-Year High-Resolution Global Dataset of Meteorological Forcings for Land Surface Modeling". EN. In: *Journal of Climate* 19.13, pp. 3088–3111. ISSN: 0894-8755. DOI: 10.1175/JCLI3790.1.

Shukla, J. and Y. Mintz (Mar. 1982). "Influence of land-surface evapotranspiration on the earth's climate". In: *Science* 215.4539, pp. 1498–1501. ISSN: 00368075. DOI: 10.1126/science.215.4539.1498.

Sinclair, TR, CE Murphy, and KR Knoerr (1976). "Development and evaluation of simplified models for simulating canopy photosynthesis and transpiration". In: *Journal of Applied Ecology*, pp. 813–829.

Skamarock, W C, J B Klemp, J Dudhia, D O Gill, D M Barker, M G Duda, X Y Huang, W Wang, and J G Powers (2008). *A description of the Advanced Research WRF version 3*. Tech. rep.

Slater, A. G., T. J. Bohn, J. L. McCreight, M. C. Serreze, and D. P. Lettenmaier (Dec. 2007). "A multimodel simulation of pan-Arctic hydrology". In: *Journal of Geophysical Research: Biogeosciences* 112.4, n/a–n/a. ISSN: 01480227. DOI: 10.1029/2006JG000303.

Snyder, R. L. and Kyaw Tha Paw U (2002). *Penman Monteith Equation Derivation*. URL: http://biomet.ucdavis.edu/Evapotranspiration/PMDerivation/PMD.htm (visited on 10/21/2020).

Staff Hydrologic Research Laboratory (1972). *National Weather Service river forecast system forecast procedures*. Ed. by Hydrologic Research Laboratory (U.S.) and Office of Hydrology United States.

Stephens, Graeme L., Juilin Li, Martin Wild, Carol Anne Clayson, Norman Loeb, Seiji Kato, Tristan L'Ecuyer, Paul W. Stackhouse, Matthew Lebsock, and Timothy Andrews (2012). "An update on Earth's energy balance in light of the latest global observations". In: *Nature Geoscience*. ISSN: 17520894. DOI: 10.1038/ngeo1580.

Taylor, G. I. (Jan. 1915). "Eddy Motion in the Atmosphere". In: *Philosophical Transactions of the Royal Society A: Mathematical, Physical and Engineering Sciences* 215.523-537, pp. 1–26. ISSN: 1364-503X. DOI: 10.1098/rsta.1915.0001.

Thornton, Peter E. and Steven W. Running (1999). "An improved algorithm for estimating incident daily solar radiation from measurements of temperature, humidity, and precipitation". In: *Agricultural and Forest Meteorology* 93.4, pp. 211–228. ISSN: 01681923. DOI: 10.1016/S0168-1923(98)00126-9.

Trenberth, Kevin E., John Fasullo, and Lesley Smith (2005). "Trends and variability in column-integrated atmospheric water vapor". In: *Climate Dynamics*. ISSN: 09307575. DOI: 10.1007/s00382-005-0017-4.

Trenberth, Kevin E., John T. Fasullo, and Jessica Mackaro (2011). "Atmospheric moisture transports from ocean to land and global energy flows in reanalyses". In: *Journal of Climate*. ISSN: 08948755. DOI: 10.1175/2011JCLI4171.1.

UNESCO (1973). *International Classification and Mapping of Vegetation*. UNESCO. ISBN: 92-3-001046-4.

United States Army Corps of Engineers (1956). *Snow hydrology; summary report of the snow investigations*. English. Portland, Or.: North Pacific Division, Corps of Engineers, U.S. Army.

Vereecken, Harry, Lutz Weihermüller, Shmuel Assouline, Jirka Šimůnek, Anne Verhoef, Michael Herbst, Nicole Archer, Binayak Mohanty, Carsten Montzka, Jan Vanderborght, Gianpaolo Balsamo, Michel Bechtold, Aaron Boone, Sarah Chadburn, Matthias Cuntz, Bertrand Decharme, Agnès Ducharne, Michael Ek, Sebastien Garrigues, Klaus Goergen, Joachim Ingwersen, Stefan Kollet, David M. Lawrence, Qian Li, Dani Or, Sean Swenson, Philipp Vrese, Robert Walko, Yihua Wu, and Yongkang Xue (Jan. 2019). "Infiltration from the Pedon to Global Grid Scales: An Overview and Outlook for Land Surface Modeling". In: *Vadose Zone Journal* 18.1, pp. 1–53. ISSN: 1539-1663. DOI: 10.2136/vzj2018.10.0191.

Wang, Chunzai, Liping Zhang, Sang Ki Lee, Lixin Wu, and Carlos R. Mechoso (Feb. 2014). "A global perspective on CMIP5 climate model biases". In: *Nature Climate Change* 4.3, pp. 201–205. ISSN: 17586798. DOI: 10.1038/nclimate2118.

Wang, Jiali, Cheng Wang, Vishwas Rao, Andrew Orr, Eugene Yan, and Rao Kotamarthi (Aug. 2019). "A parallel workflow implementation for PEST version 13.6 in high-performance computing for WRF-Hydro version 5.0: A case study over the midwestern United States". In: *Geoscientific Model Development* 12.8, pp. 3523–3539. ISSN: 19919603. DOI: 10.5194/gmd-12-3523-2019.

Wang, Zhuo, Xubin Zeng, and Mark Decker (Oct. 2010). "Improving snow processes in the Noah land model". In: *Journal of Geophysical Research* 115.D20, p. D20108. ISSN: 0148-0227. DOI: 10.1029/2009JD013761.

Warner, Thomas T. (Dec. 2011). "Quality Assurance in Atmospheric Modeling". In: *Bulletin of the American Meteorological Society* 92.12, pp. 1601–1610. ISSN: 0003-0007. DOI: 10.1175/BAMS-D-11-00054.1.

Washington, Warren M., A. J. Semtner, Gerald A. Meehl, David J. Knight, and Thomas A. Mayer (Dec. 1980). "A general circulation experiment with a coupled atmosphere,

ocean and sea ice model." In: *J. PHYS. OCEANOGR.* 10.12 , Dec. 1980, pp. 1887–1908. ISSN: 00223670. DOI: 10.1175/1520-0485(1980)010<1887:agcewa>2.0.co;2.

Weedon, Graham P., Gianpaolo Balsamo, Nicolas Bellouin, Sandra Gomes, Martin J. Best, and Pedro Viterbo (Sept. 2014). "The WFDEI meteorological forcing data set: WATCH Forcing Data methodology applied to ERA-Interim reanalysis data". In: *Water Resources Research* 50.9, pp. 7505–7514. ISSN: 00431397. DOI: 10.1002/2014WR015638.

Wehn, Sølvi, Gunilla Olsson, and Susanne Hanssen (Feb. 2012). "Forest line changes after 1960 in a Norwegian mountain region -implications for the future". In: *Norsk Geografisk Tidsskrift* 66.1, pp. 2–10. ISSN: 00291951. DOI: 10.1080/00291951.2011.644320.

Wild, Martin (Mar. 2017). *Towards Global Estimates of the Surface Energy Budget*. DOI: 10.1007/s40641-017-0058-x.

Wild, Martin, Atsumu Ohmura, Christoph Schär, Guido Müller, Doris Folini, Matthias Schwarz, Maria Zyta Hakuba, and Arturo Sanchez-Lorenzo (2017). "The Global Energy Balance Archive (GEBA) version 2017: a database for worldwide measured surface energy fluxes". In: *Earth Syst. Sci. Data* 95194, pp. 601–613.

Wilkinson, Mark D., Michel Dumontier, IJsbrand Jan Aalbersberg, Gabrielle Appleton, Myles Axton, Arie Baak, Niklas Blomberg, Jan Willem Boiten, Luiz Bonino da Silva Santos, Philip E. Bourne, Jildau Bouwman, Anthony J. Brookes, Tim Clark, Mercè Crosas, Ingrid Dillo, Olivier Dumon, Scott Edmunds, Chris T. Evelo, Richard Finkers, Alejandra Gonzalez-Beltran, Alasdair J.G. Gray, Paul Groth, Carole Goble, Jeffrey S. Grethe, Jaap Heringa, Peter A.C. t Hoen, Rob Hooft, Tobias Kuhn, Ruben Kok, Joost Kok, Scott J. Lusher, Maryann E. Martone, Albert Mons, Abel L. Packer, Bengt Persson, Philippe Rocca-Serra, Marco Roos, Rene van Schaik, Susanna Assunta Sansone, Erik Schultes, Thierry Sengstag, Ted Slater, George Strawn, Morris A. Swertz, Mark Thompson, Johan Van Der Lei, Erik Van Mulligen, Jan Velterop, Andra Waagmeester, Peter Wittenburg, Katherine Wolstencroft, Jun Zhao, and Barend Mons (Mar. 2016). "Comment: The FAIR Guiding Principles for scientific data management and stewardship". In: *Scientific Data* 3.1, pp. 1–9. ISSN: 20524463. DOI: 10.1038/sdata.2016.18.

Williams, M, A D Richardson, M Reichstein, P C Stoy, P Peylin, H Verbeeck, N Carvalhais, M Jung, D Y Hollinger, J Kattge, R Leuning, Y Luo, E Tomelleri, C M Trudinger, and Y. -P Wang (2009). "Improving land surface models with FLUXNET data". In: *Biogeosciences* 6.7, pp. 1341–1359. ISSN: 17264189. DOI: 10.5194/bg-6-1341-2009.

Wilson, M. F., A. Henderson-Sellers, R. E. Dickinson, and P. J. Kennedy (Mar. 1987a). "Sensitivity of the Biosphere-Atmosphere Transfer Scheme (BATS) to the inclusion of variable soil characteristics". In: *Journal of Climate & Applied Meteorology* 26.3, pp. 341–362. ISSN: 0733-3021. DOI: 10.1175/1520-0450(1987)026<0341:SOTBTS>2.0.CO;2.

Wilson, M. F. and A. Henderson-Sellers (Mar. 1985). "A global archive of land cover and soils data for use in general circulation climate models". In: *Journal of Climatology* 5.2, pp. 119–143. ISSN: 10970088. DOI: 10.1002/joc.3370050202.

Wilson, M. F., A. Henderson-Sellers, R. E. Dickinson, and P. J. Kennedy (July 1987b). "Investigation of the sensitivity of the land-surface parameterization of the NCAR Community Climate Model in regions of tundra vegetation". In: *Journal of Climatology* 7.4, pp. 319–343. ISSN: 10970088. DOI: 10.1002/joc.3370070402.

Wolff, M. A., K. Isaksen, A. Petersen-ØVerleir, K. Ødemark, T. Reitan, and R. Brækkan (Feb. 2015). "Derivation of a new continuous adjustment function for correcting

wind-induced loss of solid precipitation: Results of a Norwegian field study". In: *Hydrology and Earth System Sciences* 19.2, pp. 951–967. ISSN: 16077938. DOI: 10.5194/hess-19-951-2015.

Wong, Wai Kwok, Stein Beldring, Torill Engen-Skaugen, Ingjerd Haddeland, and Hege Hisdal (Dec. 2011). "Climate change effects on spatiotemporal patterns of hydroclimatological summer droughts in Norway". In: *Journal of Hydrometeorology* 12.6, pp. 1205–1220. ISSN: 1525755X. DOI: 10.1175/2011JHM1357.1.

Wood, Eric F., Dennis P. Lettenmaier, and Valerie G. Zartarian (Feb. 1992). "A land-surface hydrology parameterization with subgrid variability for general circulation models". In: *Journal of Geophysical Research* 97.D3, pp. 2717–2728. ISSN: 01480227. DOI: 10.1029/91JD01786.

Xu, C. Y. and V. P. Singh (Feb. 2001). "Evaluation and generalization of temperature-based methods for calculating evaporation". In: *Hydrological Processes* 15.2, pp. 305–319. ISSN: 08856087. DOI: 10.1002/hyp.119.

Xue, Y, P J Sellers, J L Kinter, and J Shukla (Mar. 1991). "A Simplified Biosphere Model for Global Climate Studies". English. In: *Journal of Climate* 4.3, pp. 345–364. ISSN: 0894-8755. DOI: 10.1175/1520-0442(1991)004<0345:ASBMFG>2.0.CO;2.

Xue, Yongkang, Tandong Yao, Aaron Boone, Ismaila Diallo, Ye Liu, Xubin Zeng, William Lau, Shiori Sugimoto, Qi Tang, Xiaoduo Pan, Peter van Oevelen, Daniel Klocke, Myung-Seo Koo, Zhaohui Lin, Yuhei Takaya, Tomonori Sato, Constantin Ardilouze, Subodh Saha, Mei Zhao, Xin-Zhong Liang, Frederic Vitart, Xin Li, Ping Zhao, David Neelin, Weidong Guo, Miao Yu, Yun Qian, Samuel Shen, Yang Zhang, Kun Yang, Ruby Leung, Jing Yang, Yuan Qiu, Michael Brunke, Sin Chan Chou, Michael Ek, Tianyi Fan, Hong Guan, Hai Lin, Shunlin Liang, Stefano Materia, Tetsu Nakamura, Xin Qi, Retish Senan, Chunxiang Shi, Hailan Wang, Helin Wei, Shaocheng Xie, Haoran Xu, Hongliang Zhang, Yanling Zhan, Weiping Li, Xueli Shi, Paulo Nobre, Yi Qin, Jeff Dozier, Craig Ferguson, Gianpaolo Balsamo, Qing Bao, Jinming Feng, Jinkyu Hong, Songyou Hong, Huilin Huang, Duoying Ji, Zhenming Ji, Shichang Kang, Yanluan Lin, Weiguang Liu, Ryan Muncaster, Yan Pan, Daniele Peano, Patricia de Rosnay, Hiroshi Takahashi, Jianping Tang, Guiling Wang, Shuyu Wang, Weicai Wang, Xu Zhou, and Yuejian Zhu (2021). "Impact of Initialized Land Surface Temperature and Snowpack on Subseasonal to Seasonal Prediction Project, Phase I (LS4P-I): Organization and Experimental design". In: *Geoscientific Model Development Discussions*, pp. 1–58. ISSN: 1991-959X. DOI: 10.5194/gmd-2020-329.

Yang, Zong-Liang (Feb. 2004). "MODELING LAND SURFACE PROCESSES IN SHORT-TERM WEATHER AND CLIMATE STUDIES". In: *World Scientific Series on Asia-Pacific Weather and Climate*, pp. 288–313. DOI: 10.1142/9789812791139{_}0014.

Yeh, T-C., R. T. Wetherald, and S. Manabe (Mar. 1984). "The Effect of Soil Moisture on the Short-Term Climate and Hydrology Change—A Numerical Experiment". In: *Monthly Weather Review* 112.3, pp. 474–490. ISSN: 0027-0644. DOI: 10.1175/1520-0493(1984)112<0474:TEOSMO>2.0.CO;2.

Yeh, T. C., R. T. Wetherald, and S. Manabe (May 1983). "A model study of the short-term climatic and hydrologic effects of sudden snow-cover removal." In: *Monthly Weather Review* 111.5, pp. 1013–1024. ISSN: 00270644. DOI: 10.1175/1520-0493(1983)111<1013:AMSOTS>2.0.CO;2.

Zeng, Xubin and Anton Beljaars (July 2005). "A prognostic scheme of sea surface skin temperature for modeling and data assimilation". In: *Geophysical Research Letters* 32.14, n/a–n/a. ISSN: 00948276. DOI: 10.1029/2005GL023030.

Zhang, Yonggen, Marcel G. Schaap, and Zhongwang Wei (Aug. 2020). "Development of Hierarchical Ensemble Model and Estimates of Soil Water Retention With Global Coverage". In: *Geophysical Research Letters* 47.15. ISSN: 19448007. DOI: 10.1029/2020GL088819.

Zhuang, Jiawei (2020). *xESMF: Universal Regridder for Geospatial Data*. DOI: doi.org/10.5281/zenodo.1134365.

Zobler, L. (1999). *Global Soil Types, 1-Degree Grid (Zobler). Data set.* DOI: doi:10.3334/ORNLDAAC/418..

Papers

I. The Sensitivity of the Terrestrial Surface Energy and Water Balance Estimates in the WRF Model to Lower Surface Boundary Representations: A South Norway Case Study.

The Sensitivity of the Terrestrial Surface Energy and Water Balance Estimates in the WRF Model to Lower Surface Boundary Representations: A South Norway Case Study

HELENE B. ERLANDSEN

Norwegian Water Resources and Energy Directorate, and University of Oslo, Oslo, Norway

INGJERD HADDELAND

Norwegian Water Resources and Energy Directorate, Oslo, Norway

LENA M. TALLAKSEN

University of Oslo, Oslo, Norway

JØRN KRISTIANSEN

Norwegian Meteorological Institute, Oslo, Norway

(Manuscript received 17 August 2015, in final form 17 October 2016)

ABSTRACT

A seasonal snow cover, expansive forests, a long coast line, and a mountainous terrain are features of Norway's geography. Forests, ground snow, and sea surface temperature (SST) vary on time scales relevant for weather forecasting and climate projections. The mapping and model parameterization of these features vary in novelty, accuracy, and complexity. This paper investigates how increasing the influence of each of these features affects southern Norway's surface energy and water balance in a regional climate model (WRF). High-resolution (3.7 km) experimental runs have been conducted over two consecutive hydrological years, including 1) heightening the boreal forest line (the Veg experiment), 2) increasing ground snow by altering the snow/rain criterion (the Snow experiment), or 3) increasing the SST (the SST experiment). The Veg experiment led to an increase in annual net radiation R_{net} in the study area (by 3 W m^{-2}), largely balanced out by an increase in latent heat flux. Moisture recycling increased, leaving only a negligible decrease in annual runoff. Surface temperature increased by 0.1°C, and its seasonal variability was dampened. Significant changes were also found outside the area of vegetation change. Snow decreased R_{net} by 1.5 W m^{-2}, despite slight increases in downward shortwave and longwave radiation. Both sensible heat flux and surface temperature decreased (by 1.3 W m^{-2} and 0.2°C, respectively), but the annual water balance remained mostly unchanged. The SST experiment led to increased downward and upward longwave radiation. Surface temperature was raised by 0.2°C. Advected oceanic moisture and thus both precipitation and runoff increased (by 2.5% and 2.8%, respectively).

1. Introduction

The lower surface boundary to the atmosphere moderates roughness, albedo, and emissivity, and can act as a water or heat reservoir, depending on its state. The surface can accordingly modify atmospheric stability, humidity, cloud cover, precipitation, and air temperature, and thus the local and regional surface energy and water balance, through complex interactions.

International studies point to regions where the land surface has a high influence on the local weather and climate, although the strength of the land–atmosphere coupling in southern Norway is still inconclusive. Norway is located in the receiving end of the westerlies that have passed over the North Atlantic. This, combined with a long coast lined with mountains, gives Norway on average nearly 1500 mm of precipitation per year. Evaporation

Corresponding author e-mail: Helene B. Erlandsen, hebe@nve.no

DOI: 10.1175/JHM-D-15-0146.1

from the land surface is on average less than one-fourth of the received precipitation (Hanssen-Bauer et al. 2009). With a predominantly energy-limited evapotranspiration regime, Norway has not stood out in land–atmosphere studies focusing on soil moisture–atmosphere coupling.

Given Norway's high latitude and maritime location, representation of sea surface temperature (SST) and snow cover receives considerable attention in regional weather, climate, and hydrological modeling. Lack of observations; computational restraints on model resolution, parameterizations, assimilation routines, and initialization errors; and model biases in interacting variables introduce uncertainty in modeled SST and ground snow. For instance, historical runs (1900–2005) of the CMIP5 models show cold SST biases in the extratropical North Atlantic (Wang et al. 2014). The same models show historical snowfall rates on ice-free land north of 50°N that are nearly twice the amount estimated in the observation-based Water and Global Change (WATCH; Weedon et al. 2011) dataset (Brutel-Vuilmet et al. 2013). Even recent reanalysis datasets such as ERA-Interim may show biases in snow depth (Balsamo et al. 2015).

Recent studies (Wramneby et al. 2010; Rydsaa et al. 2015) suggest that vegetation change deserves more attention in our region. Previous studies comparing the sensitivity of terrestrial atmospheric variables to SST anomalies and land-cover change have found regional (de Noblet-Ducoudré et al. 2012) and seasonal (Findell et al. 2009) impacts of a similar magnitude. While vegetation change is now included in IPCC climate projections, it is usually not included in statistical or dynamical downscaling of these models for our region. On the other hand, impact assessment studies of hydrological changes due to land surface changes are commonly conducted without coupling to the atmosphere.

This study explores the sensitivity of the surface energy and water balance in southern Norway to three surface representations, namely, vegetation, snow, and SST. This is done within the constrained environment of the Advanced Research version of the Weather Research and Forecasting (WRF) Model (ARW) framework (Skamarock et al. 2008) by 1) increasing the boreal forest line, 2) increasing ground snow by altering the snow/rain criterion in the land surface scheme, and 3) perturbing the SST. The experiments are run with a grid spacing of 3.7 km over two hydrological years, the dry 2009/10 and the wet 2010/11. The experiments shed light on the regional importance of each of these surface features within weather and climate models, such as WRF, and on the expected information loss from using stand-alone land surface and hydrological models.

The WRF Model, its model configuration, and the study area are presented in the following section. Section 3 outlines the design of each of the three experimental runs, and the results are presented in section 4. A discussion and conclusions are offered in sections 5 and 6.

2. The WRF Model, initialization, and forcing

The WRF Model framework is widely used around the world. It is used for weather forecasting, research, and regional downscaling in Norway (e.g., Heikkilä et al. 2011) and Europe (e.g., Katragkou et al. 2015). The WRF Model system is a flexible framework, with two dynamical cores. In this study, ARW, version 3.5.1 (Skamarock et al. 2008), is used.

a. The ARW and configuration

The model was configured as listed in Table 1, with the Yonsei University (YSU) planetary boundary layer (PBL) scheme; the Kain–Fritsch cumulus scheme; the Goddard shortwave, longwave, and microphysics schemes; and the MM5 similarity scheme for the surface layer physics. A version of the Noah land surface model (LSM) was used (Mitchell 2001, and references therein), with enhancements to improve snow processes, as described below. Also tested, but rejected, was the option to include a diurnal SST parameterization (Zeng and Beljaars 2005), as it was found to slightly reduce the daily average SST throughout most of the year. A more detailed description of the Noah LSM is given next, with emphasis on vegetation and snow parameterizations.

b. The Noah LSM

The unified NCEP–NCAR Noah LSM is an open source, community model with a wide range of users. It is a single-column model with four soil layers, a total soil depth of 2 m, with prognostic soil moisture and temperature and freeze/thaw soil physics. Soil thermal and hydraulic parameters like conductivity, field capacity, and wilting point are available as tabulated values according to local soil type. Lookup tables also give the vegetation root depth, stomatal resistance, and maximum snow-covered albedo according to the grid cell's dominating vegetation type (Table 2 for parameter values for evergreen needleleaf forest, wooded tundra, and mixed tundra). Noah has a canopy layer storing water, and snow is stored on the ground in a single, bulk layer. The surface temperature is a single, weighted mean of the temperature of snow-covered ground, canopy, and bare soil, according to their grid-cell fraction. It has a linearized, noniterative surface

TABLE 1. Model configuration with the outer domain values given in parentheses.

Model type	ARW, version 3.5.1
Simulation period	From October 2009 to October 2011
Simulation type	Climate run, initialized once
Horizontal resolution	3.7 km or 0°02′ (18.5 km or 0°10′)
Grid	Lambert, rotated
Mesh	156 × 261 (77 × 160)
Vertical resolution	41 layers (top at 50 hPa)
Time step	20 s (100 s)
Forcing data	ERA-Interim, Δ_t = 6 h
SST update	ERA-Interim, Δ_t = 1 day
Lake temperature	ERA-Interim, mean T_{2m}
Spectral nudging	No
Nesting	One way
Vegetation type	MODIS Boston University and NCEP 20 category with lakes
Vegetation type alterations	Based on Moen et al. (1998)
Green vegetation fraction	MODIS, 1/8° monthly interpolated
Max albedo with snow α_{ms}	Barlage et al. (2005) table values
Land surface scheme	Noah, with University of Arizona physics
Surface scheme	MM5 Monin–Obukhov
PBL scheme	YSU
Cumulus scheme	Kain–Fritsch
Microphysics scheme	Goddard
Longwave scheme	Goddard
Shortwave scheme	Goddard

energy balance, solving for a slab skin temperature after estimating the evapotranspiration using a modified version of the Penman equation (Mahrt and Ek 1984).

c. The University of Arizona Noah alterations

The University of Arizona (UA) snow physics for Noah (Wang et al. 2010) are used in this study. The UA alterations aim to redeem a too early snowmelt, and excess snow sublimation and downward sensible heat flux often found in the Noah model (Wang et al. 2010). The physical processes associated with deep snow in boreal forests in spring were specifically considered, including the effect of vegetation shading on snow, increased (under canopy) aerodynamic resistance under stable atmospheric conditions (increasingly so with more vegetation present), and a revised roughness length for snow-covered vegetation.

d. Vegetation data, forcing data, and spinup

The vegetation types are given by the MODIS Boston University IGBP dataset, with alterations made by NCEP to include tundra and lakes. For this study, all vegetation in the open shrubland class was converted to the mixed tundra class, as the original was a 60°N threshold for the conversion that resulted in a spurious schism through the center of southern Norway. Additionally mixed tundra was changed to wooded tundra below 950 m, representing birch forest, to provide better consistency with a national vegetation map (Moen et al. 1998).

The land surface model was spun up, using the NCAR High-Resolution Land Data Assimilation System (HRLDAS; Chen et al. 2007) forced with ERA-Interim data (Dee et al. 2011), cycling the year preceding the experimental runs, 2008/09.

Apart from ground temperature and moisture fields, which were transferred from HRLDAS, the WRF Model was initialized with fields from the ERA-Interim. The model was run in climate mode, initialized on 1 October 2009, and forced with fields from ERA-Interim (updated every 6 h on the outer domains' lateral boundaries, and every 24 h for SST fields). Spectral nudging was not used in order to allow the model more freedom to react to the changes in surface representation.

e. Study area

This study focuses on South Norway, the southern half of Norway. The integration domains are presented in Fig. 1. The outer domain is the enclosed, outer area of the figure. It consists of 77 × 160 grid boxes, with a grid spacing of about 18.5 km, or 0°10′. The inner domain, shown as a blue rectangle, consists of 156 × 261 grid boxes with a spacing of 3.7 km or 0°02′. In further reference to the study area, only the land area in the inner domain is considered.

A seasonal snow cover is present in most of Norway. The number of days with snow varies considerably, both spatially and from year to year. Normally, it lasts from 0 to 300 days yr^{-1}, with snow water equivalent (SWE) varying from 0 to 3000 mm (Hanssen-Bauer et al. 2009). Norway receives on average nearly 1500 mm of precipitation per year, with large regional differences, as the Scandinavian mountains split South Norway into a rainy western part and a drier eastern part.

f. Study period

Interannual weather variability in Norway is influenced by the North Atlantic Oscillation (NAO), especially in winter. A negative phase of the NAO is usually concurrent with cold and dry conditions in Norway, while a positive NAO phase usually indicates warm and wet conditions. To evaluate to what degree the sensitivities found vary with weather variability, the study is conducted over a time period when the phase of the NAO changed from positive to negative.

TABLE 2. The modified IGBP MODIS Noah vegetation parameters for evergreen needleleaf, wooded tundra, and mixed tundra; that is, the vegetation types that are changed in the Veg experiment. The parameters with a min and max value are scaled according to the spatially and temporally varying green vegetation fraction, as provided by an external, satellite-derived dataset. Parameters Z_{topv} and Z_{botv} are used in the UA subroutines for discriminating vegetation with snow below the canopy and vegetation buried by snow.

		Evergreen needleleaf	Wooded tundra	Mixed tundra
GVF	Green vegetation fraction	0.70	0.60	0.60
Root_n	Rooting soil layer depth	4	3	3
R_s	Stomatal resistance	125.	150.0	200.0
RGL	Radiation stress parameter	30.	100.0	100.0
HS	Vapor pressure deficit parameter	47.35	42.0	42.00
SN_{up}	Parameter scaling snow cover fraction	0.080	0.025	0.025
α_{ms}	Max albedo with snow	34.	62.	72.
LAI_{min}	Min leaf area index	5.00	0.41	0.41
LAI_{max}	Max leaf area index	6.40	3.35	3.35
ε_{min}	Min emissivity	0.950	0.930	0.920
ε_{max}	Max emissivity	0.950	0.930	0.920
α_{min}	Min albedo	0.12	0.15	0.15
α_{max}	Max albedo	0.12	0.20	0.20
$Z0_{\text{min}}$	Min roughness	0.50	0.30	0.15
$Z0_{\text{max}}$	Max roughness	0.50	0.30	0.15
Z_{topv}	Vegetation top	17.0	10.0	5.0
Z_{botv}	Vegetation bottom	8.5	0.1	0.1

A hydrological year is the 12 consecutive months when the hydrological cycle is on average the most in balance. In the Northern Hemisphere, this is usually from October through September. This study spans two hydrological years: from October 2009 to October 2010, which was a particularly cold and dry hydrological year in Norway with the most negative winter (DJF) NAO on record; and from October 2010 to October 2011, which was a warm and wet year during which the NAO switched from negative to positive midwinter. The mean temperature in 2010 was 1°C below the 1961–90 average, and the precipitation was 85% of the 1961–90 average, which is the fifteenth driest since 1900. The year 2011 was one of the warmest and wettest years in Norway; before 2014 it was the warmest and wettest on record. The mean temperature was 1.9°C above the 1961–90 average, and total precipitation was 125% of the 1961–90 average. The winter of 2011 did, however, start out fairly dry and cold.

g. Model performance

The 2-m temperature $T_{2\,\text{m}}$, precipitation, humidity, wind, and snow cover were compared to gridded and synoptic observations. Compared to the SeNorge (Mohr 2008) high-resolution (1 km), spatially interpolated $T_{2\,\text{m}}$ dataset, the model has an average bias of −0.9°C in the study area. The temperature bias is similar in both years, implying little drift in the model. The largest biases are in fall and spring. In winter of 2009/10, a cold bias of −0.8°C occurred, whereas in winter of 2010/11 a warm bias of +1.2°C is evident. Compared to the SeNorge observation-based dataset, the model shows on average 0.2 mm day^{-1} lower precipitation. In 2009/10 slight overestimations are found in all seasons except fall. In 2010/11 slight underestimations are found, which are largest in summer with a bias of −0.4 mm day^{-1}.

Relative humidity was compared to observed humidity from more than 100 meteorological stations for 2010/11 using the Model Evaluation Tools (MET) software (Brown et al. 2009) and observational data from NOAA/NWS/NCEP (2008). The model shows a slight positive bias in specific humidity, by approximately 4%, and a slight exaggeration of the diurnal moisture variability in the warm season. The wind speed was evaluated similarly and shows good performance but has slight underestimations of the highest wind speeds.

The modeled snow depth h_s was compared with daily observations from meteorological stations for the entire simulation period. Following previous snow validation studies conducted for Norway (Dyrrdal 2010; Saloranta 2012), we require, for each station, an elevation difference of less than 100 m to the corresponding model grid point and at least 10 days of observations. This resulted in 100 stations giving in total 23 452 observations. The station-average correlation ρ between observed and modeled h_s is good ($\rho = 0.72$) and the bias is low (+2.0 cm). Using a ground snow cover fraction f_s similar to the LSM, $f_{s,g} = \min(h_s/10\,\text{cm}, 1)$ (assuming a 5:1 ratio between snow depth and SWE), the model shows a fair representation of the seasonal snow cover, with regions of overestimation found inland and regions of underestimation seen near the coast (Fig. 2).

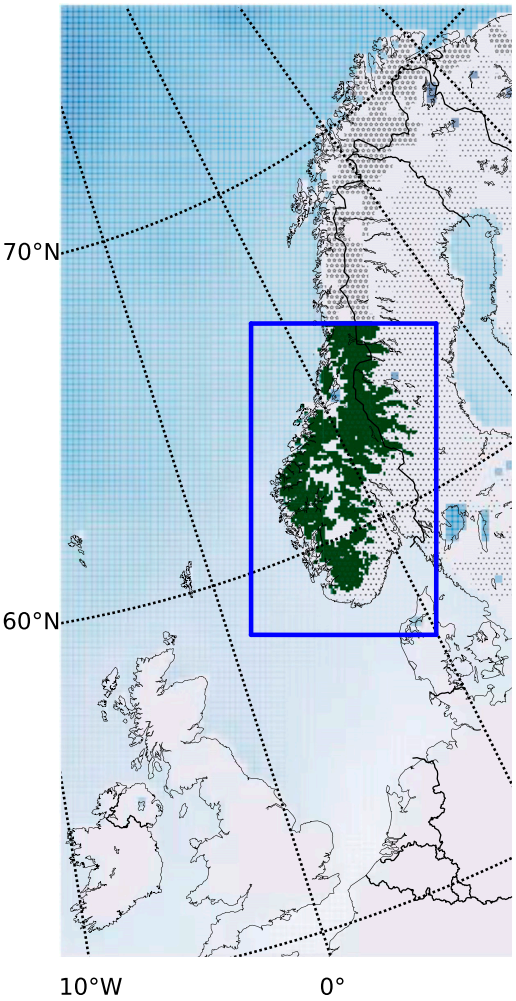

FIG. 1. The outer area of the figure depicts the outer model integration domain. The inner domain, or study area, is within the blue rectangle. Areas originally covered with evergreen needleleaf are marked with dots. Areas where mixed or wooded tundra are replaced by an evergreen needleleaf forest in the Veg experiment are marked with a dark green color (stars) in the inner (outer) domain.

3. Experimental design

After a control run (Cntrl) as described above, three experimental runs were initiated, each perturbing a different surface feature, namely, vegetation, snow, and SST. Table 3 summarizes the three experiments.

a. Increasing the boreal forest line (the Veg experiment)

If global warming continues unabated, the northern extents of boreal forest ecosystems are expected to slowly go through a transition from tundra to open shrubland to woodland to boreal forest (Liess et al. 2012). There is, however, large uncertainty regarding historical, present-day, and future land-cover distribution, and considerably different land-cover inventories and projections are used in weather forecasting and climate model runs (Yucel 2006; Klein Goldewijk et al. 2011; Meiyappan and Jain 2012; Tao et al. 2013; Broxton et al. 2014). Even so, land-use and land-cover (LULC) change were included in CMIP5 because of its importance (e.g., Hurtt et al. 2009; Klein Goldewijk et al. 2011).

Observations by satellites and airplanes and field studies have shown an upward shift in species elevation in Europe (Grytnes et al. 2014) and Norway (Bryn 2008; Wehn et al. 2012). Since 1925, the Norwegian forest volume has tripled (Tomter and Dalen 2014), and in many regions forest lines have expanded to higher altitudes. However, because of historic and current land-use practices, in certain areas the forest line can be as much as 200 m below its present potential (Wehn et al. 2012). Subtle vegetation changes (e.g., vegetation densification or a forest-line advance) are difficult to implement without using a high-resolution model. Feedback effects between warming, snow cover, and vegetation cover may not be adequately addressed in global models unable to resolve the local terrain, and thus temperature gradients, well enough (Giorgi et al. 1997).

To shed light on the sensitivity of the surface energy and water balance to a change in vegetation cover, a simple perturbation of the boreal forest line is implemented in the Veg experimental run. Mixed and barren tundra below 1150 m are replaced with evergreen needleleaf forest, increasing the forest line by about 200 m and changing the vegetation type in about a quarter of the land grid cells (Fig. 1, Table 3).

b. Increasing ground snow (the Snow experiment)

More often than not, models show biases in their snow simulations (Slater et al. 2007; Chen et al. 2014). For instance, in ERA-Interim, forests with snow were given a too low albedo, influencing the timing of spring snowmelt (Balsamo et al. 2015). If such biases significantly affect, for example, modeled precipitation intensity in our region, this needs to be accounted for.

Studies dating back to Yeh et al. (1983) have looked at the effect of ground snow on the following seasons by initializing experimental runs with extra snow. These experiments add moisture to the model. In this study we aim to evaluate and compare the responses of the surface energy and water balance to different changes in surface characteristics. Perturbing the ground snow indirectly by changing the snow/rain criterion for precipitation in the land surface part of the model makes it possible to trace

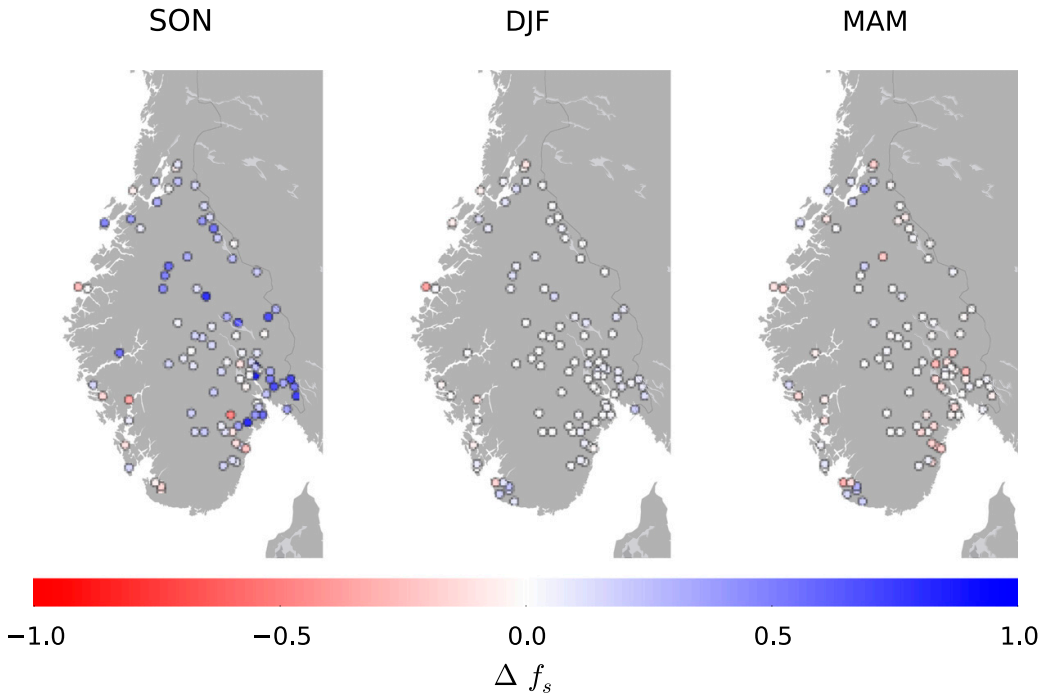

FIG. 2. The difference between simulated and observed snow cover fraction (Cntrl − obs) in fall (SON), winter (DJF), and spring (MAM).

back a response in precipitation to a change in ground snow, rather than having to disentangle it from the effect of extra moisture in the model initialization.

The snow/rain criterion is a feature of the land surface model itself, used to diagnose whether the incoming precipitation should be treated as frozen or liquid (e.g., Yang et al. 1997; Slater et al. 2007; Niu et al. 2011). When Noah LSM is coupled with WRF, by default, the snow/rain criterion relies on the ratio of solid to liquid incoming precipitation as diagnosed in the (atmospheric) microphysical scheme. If this information is not available, the lowest atmospheric model layer temperature with a categorical temperature threshold of 0°C is used.

In the current model configuration, the snow/rain criterion is diagnosed from the ratio of solid to liquid hydrometeors calculated in the Goddard microphysical scheme. Compared to using a categorical temperature threshold of 0°C, the current model setup (using the information from the microphysical scheme) leads to a slightly more snow in coastal areas and slightly less snow in inland areas (not shown).

Snow/rain criteria temperatures in the literature vary from −5° to over 6°C [references within Yang et al. (1997); Wen et al. (2013)]. In the current model configuration, the lowest model layer is at about 27 m above ground; thus, a temperature threshold of 2.5°C is expected to be in the higher end of realistic threshold temperatures for snowfall. In the Snow experiment, a categorical temperature threshold of 2.5°C is used as snow/rain criterion in the land surface model in order to increase ground snow without explicitly adding moisture to the model.

c. *The 0.4°C SST perturbation (the SST experiment)*

A large part of the variability between the models included in CMIP5 can be attributed to differences in the models' representation of snow albedo feedback effect and NAO (Cattiaux et al. 2013). Historical runs (1900–2005) of the CMIP5 models show cold SST biases in the extratropical North Atlantic (Wang et al. 2014). Biases in surface observational and/or model SST data may preclude a hindcast, weather forecast, or climate

TABLE 3. The surface perturbation experiments.

The Veg expt	The Snow expt	The SST expt
Replacing tundra below 1150 m with boreal forest (Fig. 1)	Using a categorical 2.5°C snow/rain criterion to induce more snow	Applying a uniform 0.4°C SST increase (Fig. 1)

TABLE 4. Mean difference ($\overline{\text{exp}} - \overline{\text{Cntrl}}$), averaged over all land grid cells, in 2009/10 and 2010/11 for snow cover, T_s, R_{net}, SH, LH, E, P, and R. For each variable, the two largest differences are marked in boldface. The relative change (%; where a minus sign indicates a decrease and a plus sign indicates an increase) is given below, where applicable, for the single largest change per variable.

Expt	Snow cover (days yr^{-1})	T_s (°C)	R_{net} (W m^{-2})	SH (W m^{-2})	LH (W m^{-2})	E (mm day^{-1})	P (mm day^{-1})	R (mm day^{-1})
Veg 2009/10	6	0.11	**3.6**	0.7	**2.7**	**0.09**	0.07	−0.02
			+10%		+8%	+8%		
Veg 2010/11	4	0.08	**3.1**	0.1	**2.7**	**0.09**	0.08	−0.01
Snow 2009/10	**8**	**−0.24**	−1.5	**−1.3**	−0.7	−0.02	−0.02	−0.01
Snow 2010/11	**13**	**−0.22**	−1.5	**−1.3**	−0.6	−0.02	−0.01	0.01
	+5%			−33%				
SST 2009/10	−2	0.20	0.4	−0.2	0.5	0.02	**0.09**	**0.06**
SST 2010/11	−3	0.19	0.3	−0.3	0.5	0.02	**0.11**	**0.09**
							+2.5%	+2.8%

projection. A hit or miss of the internal variation (for instance of the NAO) in an atmosphere–ocean global circulation model (GCM) providing forcing data for a regional model has the potential to deteriorate the results of a regional study (Laprise 2014).

Previous studies have shown that the implementation of SSTs in a regional climate model (RCM) can influence temperature over the European continent (Cattiaux et al. 2011) and Norway (Køltzow et al. 2011). A North Atlantic SST increase of 0.29°C decade^{-1} for the period 1978–2007 has been observed (Cattiaux et al. 2011). The oceanic warming has been found to have contributed to the European land warming over the same period. Focus in this study is to evaluate the role of feedbacks exerted from changes in the land cover to those from a perturbation in SST. Thus, a uniform SST increase of 0.4°C is implemented in both model domains (Fig. 1). Additional SST sensitivity experiments, such as forcing the model with downscaled SSTs from CMIP5 models, would be of interest but are beyond the scope of this study.

4. Results

Key variables controlling the surface energy and water balance are elaborated on below. The land area of the inner domain (study area) is considered (Fig. 1). Average changes [experimental run (exp) minus control run (Cntrl)] over the study area in ground snow cover, surface temperature T_s, net radiation R_{net}, sensible heat (SH), latent heat (LH), evaporation E, precipitation P, and runoff R are presented in Table 4 for

TABLE 5. The area (%) of significant change in mean value from the control run A and the mean difference ($\overline{\text{exp}} - \overline{\text{Cntrl}}$) within this area M are listed for the 2009/10 and 2010/11 variables. Snow cover changes are listed with areas of significant snow cover fraction changes and mean change in the number of days per year with snow cover within each of these areas. For each variable, the two largest differences are marked in boldface. The relative change (%; where a minus sign indicates a decrease and a plus sign indicates an increase) is given below, where applicable, for the single largest change per variable.

Expt	Snow cover (days yr^{-1})	T_s (°C)	R_{net} (W m^{-2})	SH (W m^{-2})	LH (W m^{-2})	E (mm day^{-1})	P (mm day^{-1})	R (mm day^{-1})
Veg 2009/10 A	70%	46%	**30%**	27%	35%	35%	21%	**67%**
Veg 2009/10 M (days yr^{-1})	6	0.22	**11.7**	**2.4**	**7.6**	**0.26**	0.19	−0.03
			+47%		+31%	+31%		
Veg 2010/11 A	69%	37%	29%	30%	**38%**	**38%**	23%	63%
Veg 2010/11 M (days yr^{-1})	4	0.19	**10.5**	0.5	**7.2**	**0.25**	**0.23**	0.00
Snow 2009/10 A	**98%**	**96%**	**32%**	**47%**	**37%**	**37%**	11%	33%
Snow 2009/10 M (days yr^{-1})	**8**	**−0.25**	−3.4	**−2.7**	−1.3	−0.05	−0.08	−0.03
Snow 2010/11 A	**98%**	92%	27%	**42%**	32%	32%	11%	36%
Snow 2010/11 M (days yr^{-1})	**13**	**−0.24**	−3.9	−2.3	−1.5	−0.04	−0.03	0.01
	+5%							
SST 2009/10 A	76%	96%	10%	16%	21%	21%	**25%**	**67%**
SST 2009/10 M (days yr^{-1})	−4	0.21	1.8	−0.8	1.4	0.05	**0.23**	**0.09**
SST 2010/11 A	69%	**97%**	7%	12%	20%	20%	**27%**	66%
SST 2010/11 M (days yr^{-1})	−4	0.20	1.7	−1.1	1.5	0.05	**0.25**	**0.12**
							+5%	+4%

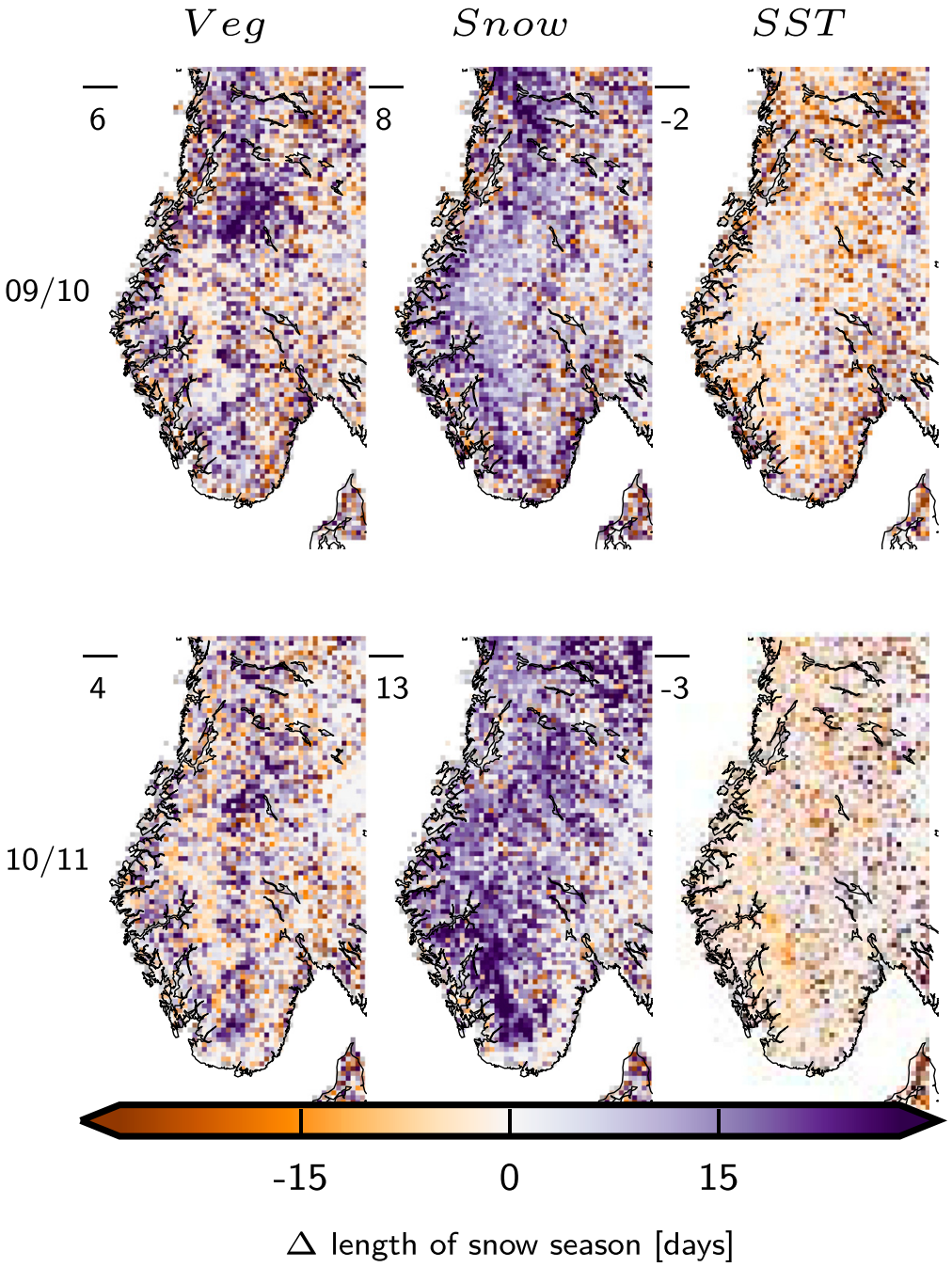

FIG. 3. Change (exp − Cntrl) in the length of the snow season (the number of days with ground snow) in (top) the dry, cold hydrological year 2009/10 and (bottom) the warm, wet hydrological year 2010/11. The study area mean change is denoted in the upper-left corner.

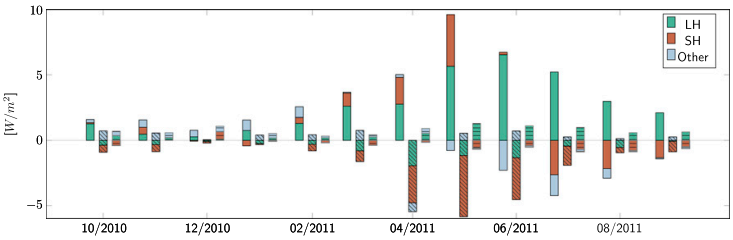

FIG. 4. The 2010/11 study area average monthly change from the control experiment in sensible, latent, and remaining (other) fluxes, for the Veg (first monthly bar), Snow (second monthly bar, marked with diagonal lines), and SST (third monthly bar, marked with horizontal lines) experiments.

each (hydrological) year. The surface temperature rather than the 2-m temperature is discussed, as it is directly related to the surface energy and water balance and is a prognostic rather than diagnostic variable. Overall, the results indicate that the experiments have a modest effect on the surface energy and water balance when averaging over the whole period and entire study area. The results further show minor differences between the relatively cold and dry 2009/10 and the warmer and wetter 2010/11.

Local and seasonal changes were notably larger. Paired sample Student's t tests, using a 95% confidence interval, were performed at each grid cell to determine whether there are significant changes in the annual and seasonal mean values of the control and experimental runs. Table 5 gives, for each variable and year, the mean change averaged over the area of significant change. Percentage land area where significant changes in annual mean values occurred varied from 7% to 98%. For each variable, where applicable, the largest relative change [(exp − Cntrl)/Cntrl] is also presented.

a. Snow cover and energy balance changes

Changes in ground snow cover and the components of the surface energy balance are depicted in Figs. 3–5. Local gridcell changes (exp − Cntrl) in the length of the snow season (the number of days with ground snow) in the two hydrological years are depicted in Fig. 3. Figure 4 depicts 2010/11 monthly change in the surface energy balance induced by each experiment, and Fig. 5 shows the seasonal extent and magnitude of significant changes in mean seasonal T_s.

1) INCREASING THE BOREAL FOREST LINE (THE VEG EXPERIMENT)

The forest-line heightening (the Veg experiment) caused significant changes in ground snow cover fraction in over two-thirds of the study area (Table 5). The average number of days with snow increased by 6 days in 2009/10 and 4 days in 2010/11 (Table 4, Fig. 3), although in certain areas the first snow-free day occurred earlier in 2010/11 (not shown). The experiment caused significant changes in R_{net} and LH in 30%–40% of the land area and also outside the area of vegetation change (24% of the land area). In these areas, the average increase in annual R_{net} was 10–12 W m^{-2}, or nearly 50%, and LH increased by 7–8 W m^{-2}, or 30%. The increase was slightly larger in the colder and drier 2009/10 than in the warmer and wetter 2010/11. The changes in the surface energy balance propagated almost undisturbed to changes in the energy balance at the model's top of the atmosphere (TOA; not shown).

Changes in turbulent fluxes caused by the Veg experiment mainly occurred in the warm season (Fig. 4). Where tundra was converted to evergreen needleleaf forest, a shift toward both higher SH and LH can be seen (Table 5); however, certain locations showed a large increase in LH coinciding with an equivalent decrease in SH (not shown). Where the vegetation remained unaltered, some grid cells showed the opposite pattern, that is, a decrease in LH and a comparable increase in SH.

The colder year, 2009/10, showed a slightly larger increase in T_s, and also significant changes in larger areas than in the warmer year of 2010/11 (Table 5). Seasonally, the highest warming was found in spring, with, on average, a 0.5°C increase in areas of significant change (Fig. 5). In summer, a lower albedo difference (not shown) and increased LH (Fig. 4) resulted in a surface cooling of a similar magnitude as the spring warming (Fig. 5).

2) INCREASING GROUND SNOW (THE SNOW EXPERIMENT)

The parameterization change applied in the Snow experiment clearly increased ground snow cover. Significant changes occurred in nearly the entire study area (Table 5). The largest increase was found near the coast in spring and fall and at higher altitudes in summer (not shown). Averaged over the two hydrological years, the area with ground snow was increased by around 12%, or 40 000 km^2, on

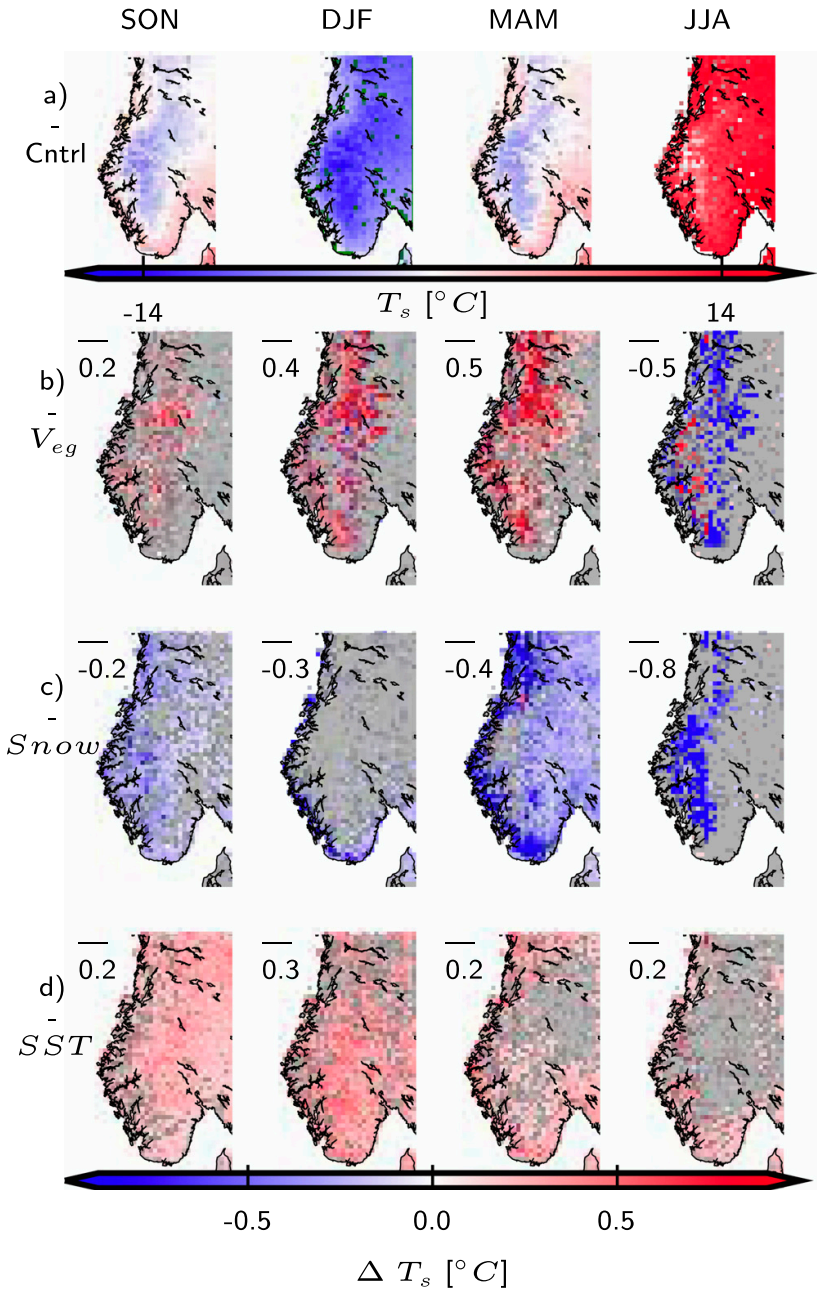

FIG. 5. (a) Mean T_s in the control run during the 2010/11 fall (SON), winter (DJF), spring (MAM), and summer (JJA). Significant changes from the control run in seasonal mean daily temperature for the (b) Veg, (c) Snow, and (d) SST experiments are also shown, with the mean change in the areas of significant change denoted in the upper-left corner. Areas of no significant change are marked in gray.

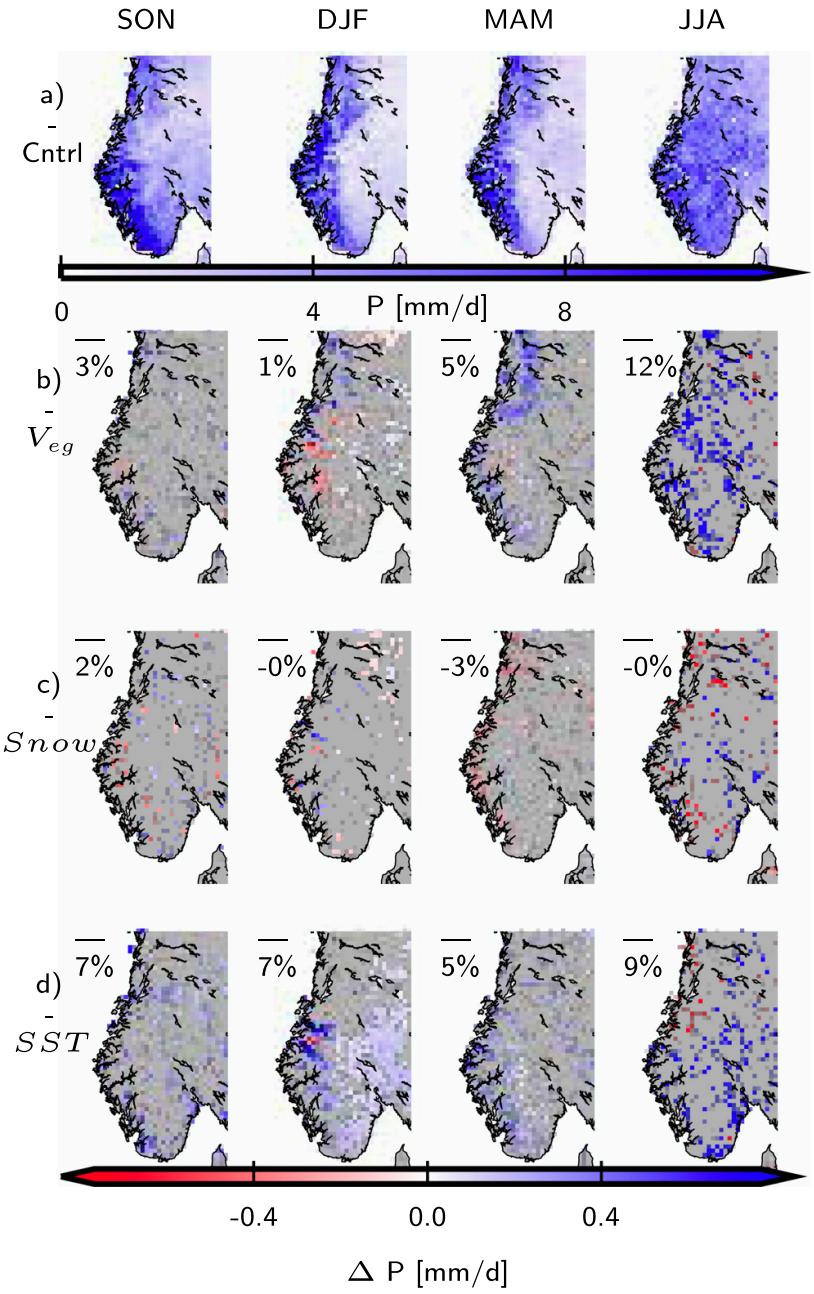

FIG. 6. As in Fig. 5, but for mean daily *P*. Note that here increases are marked in blue tones, while decreases are marked with red tones.

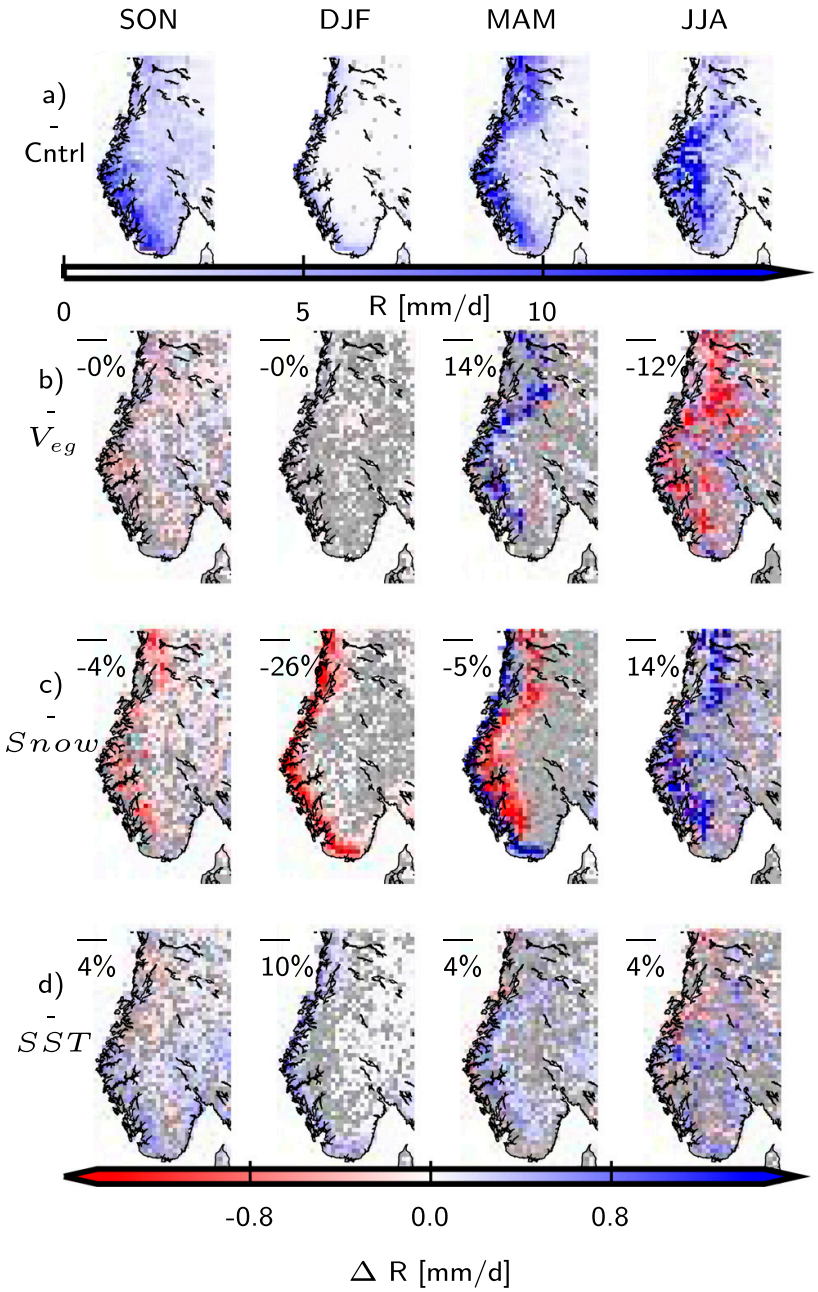

FIG. 7. As in Fig. 5, but for mean daily *R*. Note that here increases are marked in blue tones, while decreases are marked with red tones.

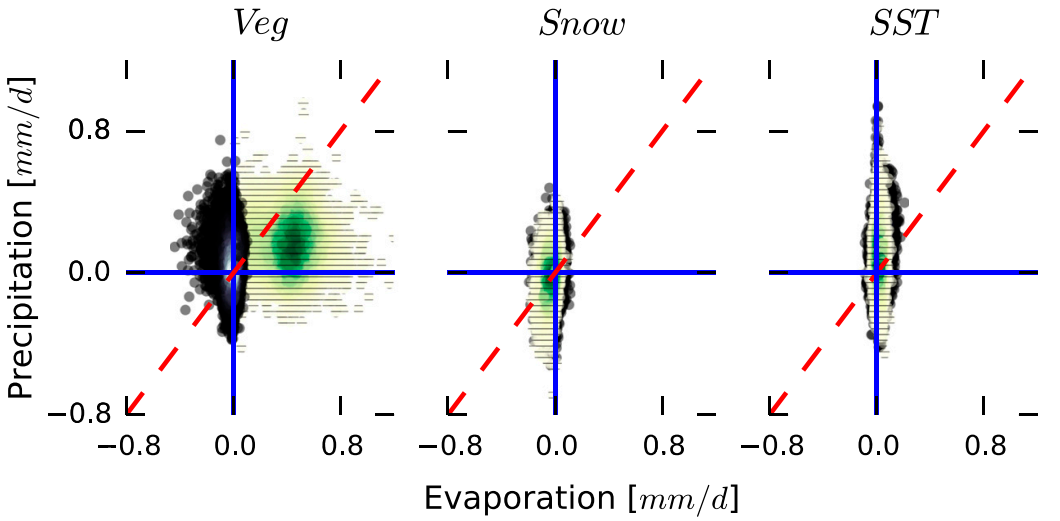

FIG. 8. Scatterplots of the annual mean differences (exp − Cntrl) in E (x axis) and P (y axis). Points originating from areas where the vegetation was changed in the Veg experiment are shown, for reference, for all experiments, with a green, hatched color scheme, with darker colors representing higher densities of points. The remaining points are marked with a black color scheme, with brighter colors representing higher densities of points.

1 November and by around 6%, or 20 000 km^2, on 1 May. In the warmer and wetter 2010/11, the mean number of days with ground snow increased by about 2 weeks, whereas in colder and drier 2009/10, it increased by only 1 week (Fig. 3).

The additional snow increased the reflection of shortwave radiation (albedo) and thus decreased R_{net}. Significant changes in annual R_{net} were found in about 30% of the area, with an average reduction of 3–4 W m^{-2} (Table 5). The increased reflected radiation propagated almost unabated to the models' TOA (not shown). Slight increases in low cloud cover and downward shortwave and longwave radiation were also detected (not shown).

The SH was significantly reduced in nearly half of the area, by 2–3 W m^{-2}, on average. A small decrease in LH was also found. The largest reduction in turbulent fluxes coincided with the months of maximum insolation and snow cover, that is, April–June (Fig. 4). In most months, slight changes in fluxes other than SH and LH are seen (Fig. 4). This is mostly due to changes in the fluxes associated with melting and freezing on the ground. Annual average T_s decreased by about 0.25°C in both years (Table 5). The most extensive, significant changes were found in spring, whereas the largest absolute change was a cooling of 0.8°C at some high-altitude areas in summer (Fig. 5c).

3) THE 0.4°C SST PERTURBATION (THE SST EXPERIMENT)

The SST experiment caused significant changes in ground snow cover in more than 70% of the study area (Table 5). The number of days with ground snow decreased, on average, by 2–3 days (Table 4, Fig. 3). Slight increases in net shortwave radiation were found, but of the three experiments, the SST perturbation had the smallest effect on R_{net}. Meanwhile, both downward and upward longwave radiation increased (not shown). Further, an increase in cloud cover was found in the colder seasons (not shown).

Significant changes in turbulent fluxes were found in less than 21% of the grid cells. The largest changes were found in summer and fall (Fig. 4), when LH increased at the expense of SH. The SST perturbation caused significant changes in annual T_s in almost all of the study area. An average warming of 0.2°C, which is half of the SST increase, was found (Table 5). The largest impact was found in fall and winter (Fig. 5d). The SST perturbation had a smaller effect on T_s in spring and summer, with no significant changes in mean temperature in more inland areas.

b. *Water balance changes*

Changes in the components of the water balance are depicted in Figs. 6–8. The extent and magnitude of the 2010/11 significant changes in mean seasonal precipitation and runoff are presented in Figs. 6 and 7. Gridcell evaporation and precipitation changes are presented, for each experiment, in scatterplots in Fig. 8.

In addition to the surface water balance, the atmospheric water balance is also analyzed. The Lagrangian atmospheric water balance is given by

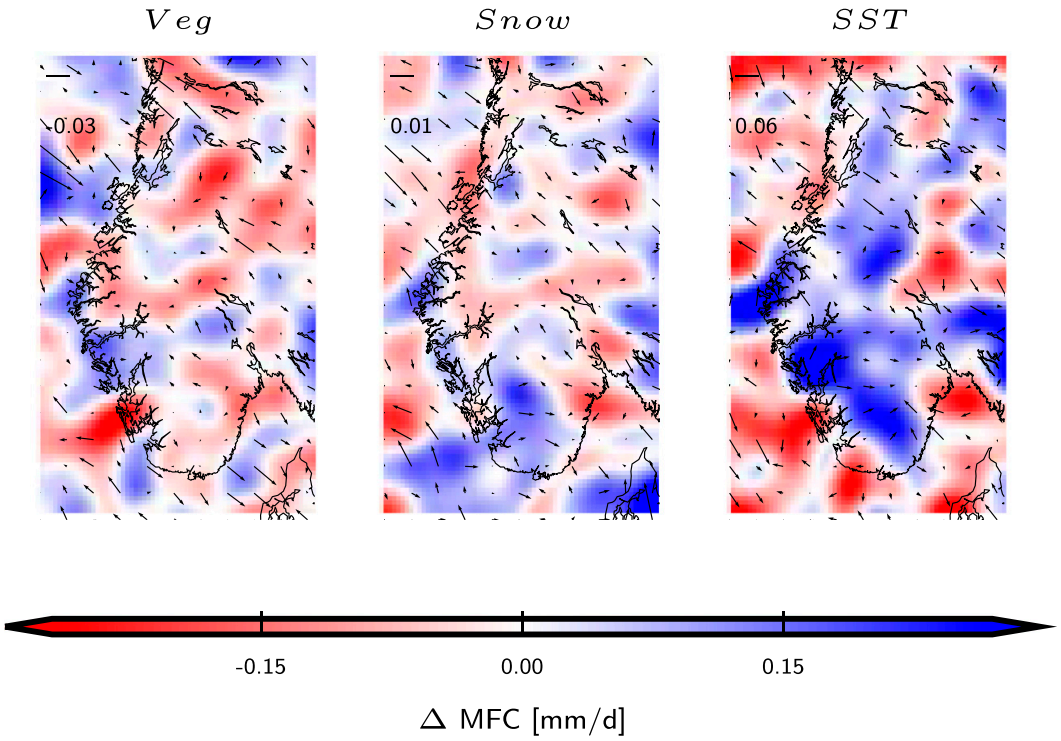

FIG. 9. Annual (2009/10) change in MFC from the control run for each experimental run. The mean change over the study area is given in the upper-left corner. Because of the very high variability of the divergence field, a Gaussian filter has been applied.

$\partial_t q + \mathbf{v} \cdot \nabla q = E - P$, where dt is the local temporal derivative, $\mathbf{v}$ is the wind (vector), and q is the specific humidity (e.g., Banacos and Schultz 2005). Integrating from the first atmospheric level near the surface to about 500 hPa (layer 16 in the model), the second term on the left-hand side of the equation represents the vertically integrated horizontal moisture flux divergence, or the negative of the moisture flux convergence (MFC). From year to year, the temporal change in atmospheric humidity $\partial_t q$ is usually much smaller than the other terms in the equation, simplifying the equation to

$$\overline{P} = \overline{E} + \overline{\mathrm{MFC}}. \quad (1)$$

The annual mean precipitation can thus be sourced from local evaporation or from advected atmospheric moisture (MFC). Figure 9 shows the annual mean change in MFC for each experiment in 2009/10.

1) INCREASING THE BOREAL FOREST LINE (THE VEG EXPERIMENT)

The Veg experiment led to significant changes in precipitation in nearly a quarter of the study area (Table 5). The signal of these changes varied with location and season (Fig. 6b). The most significant change in precipitation was found in summer: an increase of 12% in 15% of the study area. The greatest increase in LH was also found in summer (Fig. 4). Generally, where tundra was replaced with forest, an increase in both evaporation and precipitation is evident (Fig. 8). The scatterplot also shows that in some areas where the vegetation remained unaltered, a slight increase in precipitation in combination with a small decrease in evaporation is found. Indeed, comparing Fig. 6b with Fig. 1 shows that some of the areas where significant changes in precipitation occurred are outside the area of vegetation change.

The annual increase in precipitation was nearly as large as the increase in evaporation, averaged over the study area (Table 4). Compared to the control run, a slight moisture flux divergence occurred in the study area (Fig. 9), that is, part of the humidity increase was transported out of the study area. Only a minor decrease in annual runoff was found. Seasonal runoff variability was, however, affected (Fig. 7b), with more runoff in spring and less runoff in summer in western and central Norway. An increase in precipitation is seen in the same areas in spring (Fig. 6b).

2) INCREASING GROUND SNOW (THE SNOW EXPERIMENT)

The Snow experiment only had a minor effect on the annual water balance (Tables 4, 5), shown as a slight decrease in evaporation throughout the year. The greatest change in precipitation was seen in spring in coastal areas, areas that had more snow cover in the Snow experiment than in the control run. In spring, minor decreases in both convective and nonconvective precipitation were found (not shown), with an average reduction of 3% in 13% of the study area, as well as slight reductions in evaporation. In the other seasons, less than 10% of the study area showed significant changes in mean precipitation. Both decreases and increases in precipitation occurred (Fig. 6). In summer, a slight increase in precipitation is seen in inland areas.

The snow cover experiment directly influenced the partitioning of precipitation between rain and snow and induced rather large seasonal shifts in runoff. Coastal areas experienced less runoff in fall and winter, but more in spring. At higher altitudes more water was stored from spring to summer, delaying runoff (Fig. 7c).

3) THE 0.4°C SST PERTURBATION (THE SST EXPERIMENT)

On average, the SST experiment intensified the water cycle, with increasing precipitation, evaporation, and runoff (Table 4) in all seasons (Fig. 6d). Average absolute land surface evaporation increased by about one-fifth of the precipitation increase. Most of the precipitation increase was due to an increase in atmospheric moisture flux convergence over the study area (an increase of 0.06 mm day^{-1}; Fig. 9). The increase in MFC was due to an increase in west–east (zonal) moisture transport. Annual runoff increased by nearly 3% averaged over the study area.

The SST experiment induced significant precipitation changes in more than a quarter of the study area. The most extensive change was found in winter, when 35% of the land surface experienced, on average, a 7% increase in precipitation (Fig. 6d). A larger mean relative change (an increase of 9%) in precipitation was found in the summer but in fewer areas. The largest relative change in runoff (an increase of 10%) was seen at the coast in winter (Fig. 7d).

5. Discussion

a. Increasing the boreal forest line (the Veg experiment)

The forest-line heightening, that is, the Veg experiment, caused the largest changes in surface R_{net} and LH. The changes in the surface energy balance were driven by increased R_{net} due to the lower albedo of the forest compared to tundra. Significant changes were found also outside areas of vegetation change. As the land surface model is a single-column model with no horizontal advection, these changes were due to atmospheric advection. The new UA subroutines in Noah applied here (section 2c) allow part of the incoming shortwave radiation, in areas where vegetation is protruding over snow, to be absorbed in the canopy instead of in the ground. The energy is then converted to SH input directly to the atmosphere, sidestepping the surface energy balance and thus implying that snow stays longer on the ground. In the Veg experiment, in areas where tundra was changed to evergreen needleleaf forest, the first snow-free day (snow off) was delayed in most areas. However, in the warmer year, 2010/11, snow off occurred earlier in western and coastal areas. Even though forests have a lower albedo than open areas in the presence of snow, forests are generally considered to delay snow off because of vegetation shielding the snow from shortwave radiation (Lundquist et al. 2013; Kremsa et al. 2015). Lundquist et al. (2013) emphasize that whether a specific forest delays or hastens snow off may change in a future climate. Although difficult to parameterize, inclusion of canopy processes is important for correct runoff timing. In high-latitude, boreal regions, the complex interdependencies between vegetation, snow, and temperature changes and their impact on runoff generation may deserve more attention.

The changes in mean temperature, averaged over the study area, were the smallest of the experiments; however, local and seasonal temperature changes were larger than those caused by the SST experiment. Though vegetation shading, as parameterized by the model, delayed the first snow-free day in most areas, snowmelt generally started earlier, and the number of days with a full snow cover on the ground was reduced, allowing the ground to heat up. Warmer T_s values were found in all seasons except summer, when evaporative cooling dominated. Similar studies done with lower-resolution models (Wramneby et al. 2010; Rydsaa et al. 2015) have found an albedo-dominated warming in the colder seasons and an evaporation-dominated cooling in the warmer seasons, even in future climate projections. In areas of significant change, the magnitude of the average annual warming was about 0.2°C. These findings are in line with Bright et al. (2014), who observed a cooling of 0.25°C at a clear-cut site relative to a coniferous site in southeastern Norway, but smaller than a cooling of about 0.95°C observed in open land relative to nearby forested FLUXNET stations at boreal latitudes (<45°N; Zhang et al. 2014). The temperature change was slightly

larger in the colder 2009/10. Previous studies have found that the effect of vegetation change varies with climate (e.g., Pitman et al. 2011; Bright et al. 2014; de Wit et al. 2014). In long climate simulations, the radiative forcing of LULC change is expected to diminish compared to the effects of increased anthropogenic CO_2 emissions (Wramneby et al. 2010; Myhre et al. 2015).

The effect of the Veg experiment was, for the surface water balance, dominated by an evaporation increase, predominantly found in spring and summer. Annual mean precipitation increased by nearly as much as the evaporation increase. Annual runoff was thus barely affected. Snowmelt generally started earlier, shifting a fraction of runoff from summer to spring. If the results are representative of the sensitivity in other models, it justifies a stronger emphasis on vegetation type inventories, vegetation model development and validation, and increased attention to vegetation change in the region, for example, in regional downscaling of climate models or when using the results from climate models that parameterize vegetation changes. Counteracting precipitation changes may need to be considered when modeling evaporation changes in southern Norway in offline land surface or hydrological models. Changes in vegetation properties may also have affected observed temperature and precipitation trends. Further, the large sensitivity of surface and TOA net radiation found here points to the need for high-resolution studies, including biogeochemical effects, on the impact of vegetation change in our region to provide better information for land management.

b. *Increasing ground snow (the Snow experiment)*

The Snow experiment increased the number of days in a year with snow cover by 1–2 weeks. Changes in snowfall diagnosis could not occur when the conditions were so cold that the microphysical scheme, which computed the snowfall fraction in the control run, also diagnosed precipitation as snow (section 3). Thus, the impact of the parameterization change was more pronounced in the warmer 2010/11 than in the colder 2009/10, and on the coast in winter and in the high mountains in summer. Because of the additional precipitation diagnosed as snow, an increase in the flux associated with snow melting on the ground was seen. The Snow experiment induced significant changes in R_{net} and LH in a fraction of the study area similar to the Veg experiment (30%–40%), but the magnitude of changes was considerably lower. However, of the three experiments, the Snow experiment induced the largest changes in SH and T_s. For stand-alone land surface models or hydrological models using an energy balance approach, differences in snow cover between the offline model and models providing forcing data may create temperature gradients that can introduce spurious surface fluxes.

Of the three experimental runs, the Snow experiment had the smallest effect on annual precipitation and runoff. Seasonal runoff changes were found, with peak runoff increasing and being delayed by more than 1 month. Slight reductions in precipitation were seen, predominantly in late spring and early summer. However, in scattered inland areas, slight precipitation increases were seen. Observational (Kasurinen et al. 2014) and modeling (Rydsaa et al. 2015) studies have shown that evapotranspiration in the boreal regions is primarily controlled by the atmospheric vapor pressure deficit and not by soil moisture. In climates and regions, where the evapotranspiration regime is soil moisture limited, an increase in snow cover may lead to increased soil moisture persisting into the warmer seasons when soil moisture normally would be limited, in turn increasing evaporation and precipitation in these months (e.g., Dutra et al. 2012). This was largely not found here. The results suggest that in the study region and for the current climate, slight differences in modeled snow cover in similar, coupled land surface–atmosphere models may be expected to have little impact on modeled evaporation and precipitation rates.

c. *The 0.4°C SST perturbation (the SST experiment)*

The SST experiment resulted in the smallest change in R_{net} and turbulent fluxes among the experiments. However, both incoming and outgoing longwave radiation increased. Significant changes in annual T_s were found in nearly the entire study area, with temperature increasing in these areas, on average, by about 0.2°C, that is, half of the SST increase. The impact on T_s was stronger in the colder seasons, when the sea–air temperature gradient and the westerlies are generally stronger. In summer, significant changes were mostly found on the coast. In certain areas, the SST experiment introduced an increase in LH accompanied by a decrease in SH. This may be connected to the increase in precipitation found in the experiment. While the area affected by a change in snow cover was slightly higher in the colder year, generally, the changes induced by the experiment were similar in the anomalously cold and warm hydrological year.

The annual surface water balance showed a large sensitivity to the rather small SST perturbation. Among the three experimental runs, the SST experiment caused the spatially and temporally most homogeneous changes to the land surface water balance and the largest changes in the annual water balance. Annual terrestrial precipitation rates increased about 5 times more than land evaporation rates, and thus runoff increased. Most of the additional precipitation originated from moisture advected into the

study area. The largest changes were seen in winter. These findings, of a stronger sensitivity in terrestrial precipitation and temperature to SST change in the cold seasons, are in line with previous research (Cattiaux et al. 2011; Køltzow et al. 2011). The findings show that rather small biases in SST data may have significant impacts on the modeled, terrestrial water balance and T_s in the study region, including inland areas.

d. Limitations

The SST experiment was by design simplistic. By applying a uniform SST increase in both model domains throughout the year, it inflicted perturbations of varying size relative to the mean state of the SST in different regions and seasons. The sensitivity to SST perturbations likely depends on the choice of physical parameterization schemes (Table 1), the size of the model integration domain (e.g., Køltzow et al. 2011), and whether or not nudging is applied. In this study nudging has not been used, as more autonomy was sought to allow land–atmosphere coupling effects to develop. Though the lateral boundary conditions of the model's rather modestly sized outer domain are expected to constrain the large-scale circulation, the SST perturbation may have caused circulation changes (e.g., Graff and Lacasce 2014). However, this has not been the topic of this study. Similarly, evaluating possible remote or large-scale effects of the vegetation or snow cover change (e.g., Xu and Dirmeyer 2011; Orsolini et al. 2013) has not been considered within the scope of this study.

The Noah LSM is a land surface model of intermediate complexity, without an explicit canopy layer or multiple snow layers. This may impact the robustness of the results, particularly in winter and at night, since correctly modeling the stable boundary layer is generally a challenge for many models (Masson and Seity 2009; Holtslag et al. 2013). Including a prognostic surface boundary layer with an explicit canopy could alleviate some of these issues (Masson and Seity 2009).

The mechanisms involved resulting in precipitation changes due to the vegetation change, and how sensitive this response is to choice of model and model configuration (e.g., Hagos et al. 2014) needs more exploring. Further, a dedicated study on how changing surface characteristics in a particular LSM influence evaporation and runoff rates in an online versus offline model run is an interesting topic for future work.

The current study does not include biogeochemical processes, which influence the effect vegetation change has on climate. Local biogeochemical effects include, for instance, the interaction between cloud cover and surface organic aerosols (SOAs) from vegetation. This effect may reduce the warming caused by the vegetation change (e.g., Scott et al. 2014). Few observational studies have been conducted on SOAs and biogenic volatile organic compounds (BVOCs) in Norway. A recent study (Yttri et al. 2011) estimated the airmass exposure to marine and terrestrial surface types for four Nordic sites. At the Norwegian site, over 90% of the footprint was marine. The site was, however, located less than 25 km from the coast, so a larger airmass exposure to vegetation can be expected farther inland.

6. Summary and conclusions

The sensitivity of a regional climate model to perturbations of three surface features, namely, the vegetation cover, the snow cover, and the sea surface temperature, has been investigated. The surface perturbations reflect both the effect of model initialization and parameterization choices and of surface forcing biases in similar models. High-resolution (3.7 km) runs have been conducted using the WRF Model coupled to the Noah land surface model. The area of investigation is South Norway. Two consecutive hydrological years are considered, 2009/10 (relatively cold and dry) and 2010/11 (relatively warm and wet).

The vegetation was altered in the Veg experiment by increasing the boreal forest-line height by about 200 m, to 1150 m. This led to an increase in annual evaporation in the study area of 8%. Annual runoff was not much affected, as precipitation increased by nearly the same amount. Significant increases in annual net radiation and surface temperature were found. Significant changes were also found outside the area of the vegetation change. The result justifies more emphasis on vegetation model development and validation and attention to vegetation change in the region. The sensitivity also points to the need to consider counteracting precipitation changes when modeling vegetation change in offline land surface or hydrological models.

In the Snow experiment, the ground snow was increased without adding moisture to the model. This was done by altering the snow/rain criterion, that is, the diagnosis of the snowfall ratio of the precipitation, in the LSM. The number of days with snow increased, on average, by 1–2 weeks per year, spring runoff was delayed, and T_s was reduced by more than 0.2°C. The extra snow cover had little effect on precipitation and evaporation and thus little effect on annual runoff. The results suggest that in the study region and for the current climate, a correct snow cover diagnosis is important for the modeled surface temperature and intra-annual runoff.

In the SST experiment, sea surface temperature was increased with 0.40°C. This remote surface forcing perturbation had the largest effect on runoff of the three

experiments. It induced more precipitation over southern Norway, largely due to an increase in moisture transportation from the ocean, only partially reduced by an increase in evaporation. Land surface temperature increased on average by 0.2°C, and significant changes were also found in inland areas. Modest biases in SST forcing data are thus expected to significantly impact weather and runoff projections.

Acknowledgments. We thank the editor and two anonymous reviewers whose suggestions helped improve and clarify this manuscript. HBE was funded by Grant 81077 from the Norwegian Water Resources and Energy Directorate. HBE was also supported by Grant 230616/E10 from the Research Council of Norway. The work forms a contribution to Land–Atmosphere Interactions in Cold Environments (LATICE), which is a strategic research area funded by the Faculty of Mathematics and Natural Sciences at the University of Oslo. The WRF Model runs were performed on the Abel Cluster, owned by the University of Oslo and the Norwegian Metacenter for Computational Science (NOTUR), and operated by the Department for Research Computing at the University of Oslo's Center for Information Technology [Universitetets senter for informasjonsteknologi (USIT); http://www.hpc.uio.no/].

REFERENCES

Balsamo, G., and Coauthors, 2015: ERA-Interim/Land: A global land surface reanalysis data set. *Hydrol. Earth Syst. Sci.*, **19**, 389–407, doi:10.5194/hess-19-389-2015.

Banacos, P. C., and D. M. Schultz, 2005: The use of moisture flux convergence in forecasting convective initiation: Historical and operational perspectives. *Wea. Forecasting*, **20**, 351–366, doi:10.1175/WAF858.1.

Barlage, M., X. Zeng, H. Wei, and K. E. Mitchell, 2005: A global 0.05° maximum albedo dataset of snow-covered land based on MODIS observations. *Geophys. Res. Lett.*, **32**, L17405, doi:10.1029/2005GL022881.

Bright, R. M., C. Antón-Fernández, R. Astrup, F. Cherubini, M. Kvalevåg, and A. H. Strømman, 2014: Climate change implications of shifting forest management strategy in a boreal forest ecosystem of Norway. *Global Change Biol.*, **20**, 607–621, doi:10.1111/gcb.12451.

Brown, B. G., J. H. Gotway, R. Bullock, E. Gilleland, T. Fowler, D. Ahijevych, and T. Jensen, 2009: The Model Evaluation Tools (MET): Community tools for forecast evaluation. *25th Conf. on Int. Interactive Information and Processing Systems (IIPS) for Meteorology, Oceanography, and Hydrology*, Phoenix, AZ, Amer. Meteor. Soc., 9A.6. [Available online at https://ams.confex.com/ams/89annual/webprogram/Paper151349.html.]

Broxton, P. D., X. Zeng, D. Sulla-Menashe, and P. A. Troch, 2014: A global land cover climatology using MODIS data. *J. Appl. Meteor. Climatol.*, **53**, 1593–1605, doi:10.1175/JAMC-D-13-0270.1.

Brutel-Vuilmet, C., M. Ménégoz, and G. Krinner, 2013: An analysis of present and future seasonal Northern Hemisphere land snow cover simulated by CMIP5 coupled climate models. *Cryosphere*, **7**, 67–80, doi:10.5194/tc-7-67-2013.

Bryn, A., 2008: Recent forest limit changes in south-east Norway: Effects of climate change or regrowth after abandoned utilisation? *Nor. Geogr. Tidsskr.*, **62**, 251–270, doi:10.1080/00291950802517551.

Cattiaux, J., R. Vautard, and P. Yiou, 2011: North-Atlantic SST amplified recent wintertime European land temperature extremes and trends. *Climate Dyn.*, **36**, 2113–2128, doi:10.1007/s00382-010-0869-0.

——, H. Douville, and Y. Peings, 2013: European temperatures in CMIP5: Origins of present-day biases and future uncertainties. *Climate Dyn.*, **41**, 2889–2907, doi:10.1007/s00382-013-1731-y.

Chen, F., and Coauthors, 2007: Description and evaluation of the characteristics of the NCAR high-resolution land data assimilation system. *J. Appl. Meteor. Climatol.*, **46**, 694–713, doi:10.1175/JAM2463.1.

——, C. Liu, J. Dudhia, and M. Chen, 2014: A sensitivity study of high-resolution regional climate simulations to three land surface models over the western United States. *J. Geophys. Res. Atmos.*, **119**, 7271–7291, doi:10.1002/2014JD021827.

Dee, D. P., and Coauthors, 2011: The ERA-Interim reanalysis: Configuration and performance of the data assimilation system. *Quart. J. Roy. Meteor. Soc.*, **137**, 553–597, doi:10.1002/qj.828.

de Noblet-Ducoudré, N., and Coauthors, 2012: Determining robust impacts of land-use-induced land cover changes on surface climate over North America and Eurasia: Results from the first set of LUCID experiments. *J. Climate*, **25**, 3261–3281, doi:10.1175/JCLI-D-11-00338.1.

de Wit, H. A., A. Bryn, A. Hofgaard, J. Karstensen, M. M. Kvalevåg, and G. P. Peters, 2014: Climate warming feedback from mountain birch forest expansion: Reduced albedo dominates carbon uptake. *Global Change Biol.*, **20**, 2344–2355, doi:10.1111/gcb.12483.

Dutra, E., P. Viterbo, P. M. A. Miranda, and G. Balsamo, 2012: Complexity of snow schemes in a climate model and its impact on surface energy and hydrology. *J. Hydrometeor.*, **13**, 521–538, doi:10.1175/JHM-D-11-072.1.

Dyrrdal, A. V., 2010: An evaluation of Norwegian snow maps: simulation results versus observations. *Hydrol. Res.*, **41**, 27–37, doi:10.2166/nh.2010.019.

Findell, K. L., A. J. Pitman, M. H. England, and P. J. Pegion, 2009: Regional and global impacts of land cover change and sea surface temperature anomalies. *J. Climate*, **22**, 3248–3269, doi:10.1175/2008JCLI2580.1.

Giorgi, F., J. W. Hurrell, M. R. Marinucci, and M. Beniston, 1997: Elevation dependency of the surface climate change signal: A model study. *J. Climate*, **10**, 288–296, doi:10.1175/1520-0442(1997)010<0288:EDOTSC>2.0.CO;2.

Graff, L. S., and J. H. Lacasce, 2014: Changes in cyclone characteristics in response to modified SSTs. *J. Climate*, **27**, 4273–4295, doi:10.1175/JCLI-D-13-00353.1.

Grytnes, J.-A., and Coauthors, 2014: Identifying the driving factors behind observed elevational range shifts on European mountains. *Global Ecol. Biogeogr.*, **23**, 876–884, doi:10.1111/geb.12170.

Hagos, S., L. R. Leung, Y. Xue, A. Boone, F. de Sales, N. Neupane, M. Huang, and J.-H. Yoon, 2014: Assessment of uncertainties in the response of the African monsoon precipitation to land use change simulated by a regional model. *Climate Dyn.*, **43**, 2765–2775, doi:10.1007/s00382-014-2092-x.

Hanssen-Bauer, I., and Coauthors, 2009: Klima i Norge 2100: Bakgrunnsmateriale til NOU Klimatilpasning. Norwegian

Climate Centre, 148 pp. [Available online at http://met.no/filestore/klimaiNorge2100_hoyoppl.pdf.]

Heikkilä, U., A. Sandvik, and A. Sorteberg, 2011: Dynamical downscaling of ERA-40 in complex terrain using the WRF regional climate model. *Climate Dyn.*, **37**, 1551–1564, doi:10.1007/s00382-010-0928-6.

Holtslag, A. A. M., and Coauthors, 2013: Stable atmospheric boundary layers and diurnal cycles: Challenges for weather and climate models. *Bull. Amer. Meteor. Soc.*, **94**, 1691–1706, doi:10.1175/BAMS-D-11-00187.1.

Hurtt, G. C., and Coauthors, 2009: Harmonisation of global land-use scenarios for the period 1500–2100 for IPCC-AR5. *iLEAPS Newsletter*, No. 7, Integrated Land Ecosystem–Atmosphere Processes Study (iLEAPS), Walingford, United Kingdom, 6–8. [Available online at http://www.ileaps.org/sites/www.ileaps.org/files/iLEAPS_Newsletter_07_June_2009.pdf.]

Kasurinen, V., and Coauthors, 2014: Latent heat exchange in the boreal and arctic biomes. *Global Change Biol.*, **20**, 3439–3456, doi:10.1111/gcb.12640.

Katragkou, E., and Coauthors, 2015: Regional climate hindcast simulations within EURO-CORDEX: Evaluation of a WRF multi-physics ensemble. *Geosci. Model Dev.*, **8**, 603–618, doi:10.5194/gmd-8-603-2015.

Klein Goldewijk, K., A. Beusen, G. van Drecht, and M. de Vos, 2011: The HYDE 3.1 spatially explicit database of human-induced global land-use change over the past 12,000 years. *Global Ecol. Biogeogr.*, **20**, 73–86, doi:10.1111/j.1466-8238.2010.00587.x.

Køltzow, M. A. Ø., T. Iversen, and J. E. Haugen, 2011: The importance of lateral boundaries, surface forcing and choice of domain size for dynamical downscaling of global climate simulations. *Atmosphere*, **2**, 67–95, doi:10.3390/atmos2020067.

Kremsa, J., J. Keček, and E. Kubin, 2015: Comparing the impacts of mature spruce forests and grasslands on snow melt, water resource recharge, and run-off in the northern boreal environment. *Int. Soil Water Conserv. Res.*, **3**, 50–56, doi:10.1016/j.iswcr.2015.03.005.

Laprise, R., 2014: Comment on ''The added value to global model projections of climate change by dynamical downscaling: A case study over the continental U.S. using the GISS-ModelE2 and WRF models'' by Racherla et al. *J. Geophys. Res. Atmos.*, **119**, 3877–3881, doi:10.1002/2013JD019945.

Liess, S., P. K. Snyder, and K. J. Harding, 2012: The effects of boreal forest expansion on the summer Arctic frontal zone. *Climate Dyn.*, **38**, 1805–1827, doi:10.1007/s00382-011-1064-7.

Lundquist, J. D., S. E. Dickerson-Lange, J. A. Lutz, and N. C. Cristea, 2013: Lower forest density enhances snow retention in regions with warmer winters: A global framework developed from plot-scale observations and modeling. *Water Resour. Res.*, **49**, 6356–6370, doi:10.1002/wrcr.20504.

Mahrt, L., and M. Ek, 1984: The influence of atmospheric stability on potential evaporation. *J. Climate Appl. Meteor.*, **23**, 222–234, doi:10.1175/1520-0450(1984)023<0222:TIOASO>2.0.CO;2.

Masson, V., and Y. Seity, 2009: Including atmospheric layers in vegetation and urban offline surface schemes. *J. Appl. Meteor. Climatol.*, **48**, 1377–1397, doi:10.1175/2009JAMC1866.1.

Meiyappan, P., and A. K. Jain, 2012: Three distinct global estimates of historical land-cover change and land-use conversions for over 200 years. *Front. Earth Sci.*, **6**, 122–139, doi:10.1007/s11707-012-0314-2.

Mitchell, K., 2005: The community Noah land-surface model (LSM) user's guide, version 2.7.1. NOAA/NCEP Doc., 26 pp. [Available online at http://www.ral.ucar.edu/research/land/technology/lsm/noah/Noah_LSM_USERGUIDE_2.7.1.pdf.]

Moen, A., A. Odland, and A. Lillethun, 1998: *Vegetasjon*. Nasjonalatlas for Norge, Statens Kartverk, Hønefoss, 199 pp.

Mohr, M., 2008: New Routines for Gridding of Temperature and Precipitation Observations for "seNorge. no." Met. Note 08/2008, Norwegian Meteorological Institute, 40 pp. [Available online at http://met.no/filestore/NewRoutinesforGriddingofTemperature.pdf.]

Myhre, G., O. Boucher, F.-M. Bréon, P. Forster, and D. Shindell, 2015: Declining uncertainty in transient climate response as CO_2 forcing dominates future climate change. *Nat. Geosci.*, **8**, 181–185, doi:10.1038/ngeo2371.

Niu, G.-Y., and Coauthors, 2011: The community Noah land surface model with multiparameterization options (Noah-MP): 1. Model description and evaluation with local-scale measurements. *J. Geophys. Res.*, **116**, D12109, doi:10.1029/2010JD015139.

NOAA/NWS/NCEP, 2008: NCEP ADP global upper air and surface weather observations (PREPBUFR format), May 1997–continuing (updated daily). NCAR Computational and Information Systems Laboratory Research Data Archive, accessed 5 December 2016. [Available online at http://rda.ucar.edu/datasets/ds337.0/.]

Orsolini, Y. J., R. Senan, G. Balsamo, F. J. Doblas-Reyes, F. Vitart, A. Weisheimer, A. Carrasco, and R. E. Benestad, 2013: Impact of snow initialization on sub-seasonal forecasts. *Climate Dyn.*, **41**, 1969–1982, doi:10.1007/s00382-013-1782-0.

Pitman, A. J., F. B. Avila, G. Abramowitz, Y. P. Wang, S. J. Phipps, and N. de Noblet-Ducoudré, 2011: Importance of background climate in determining impact of land-cover change on regional climate. *Nat. Climate Change*, **1**, 472–475, doi:10.1038/nclimate1294.

Rydsaa, J. H., F. Stordal, and L. M. Tallaksen, 2015: Sensitivity of the regional European boreal climate to changes in surface properties resulting from structural vegetation perturbations. *Biogeosciences*, **12**, 3071–3087, doi:10.5194/bg-12-3071-2015.

Saloranta, T. M., 2012: Simulating snow maps for Norway: Description and statistical evaluation of the seNorge snow model. *Cryosphere*, **6**, 1323–1337, doi:10.5194/tc-6-1323-2012.

Scott, C. E., and Coauthors, 2014: The direct and indirect radiative effects of biogenic secondary organic aerosol. *Atmos. Chem. Phys.*, **14**, 447–470, doi:10.5194/acp-14-447-2014.

Skamarock, W. C., and Coauthors, 2008: A description of the Advanced Research WRF version 3. NCAR Tech. Note NCAR/TN-475+STR, 113 pp., doi:10.5065/D68S4MVH.

Slater, A. G., T. J. Bohn, J. L. McCreight, M. C. Serreze, and D. P. Lettenmaier, 2007: A multimodel simulation of pan-Arctic hydrology. *J. Geophys. Res.*, **112**, G04S45, doi:10.1029/2006JG000303.

Tao, Z., J. A. Santanello, M. Chin, S. Zhou, Q. Tan, E. M. Kemp, and C. D. Peters-Lidard, 2013: Effect of land cover on atmospheric processes and air quality over the continental United States a NASA Unified WRF (NU-WRF) Model study. *Atmos. Chem. Phys.*, **13**, 6207–6226, doi:10.5194/acp-13-6207-2013.

Tomter, S. M., and L. S. Dalen, 2014: Bærekraftig skogbruk i Norge. Tech. Rep. Norsk institutt for skog og landskap, 241 pp. [Available online at http://www.skogoglandskap.no/filearchive/baerekraftig_skogbruk_web.pdf.]

Wang, C., L. Zhang, S.-K. Lee, L. Wu, and C. R. Mechoso, 2014: A global perspective on CMIP5 climate model biases. *Nat. Climate Change*, **4**, 201–205, doi:10.1038/nclimate2118.

Wang, Z., X. Zeng, and M. Decker, 2010: Improving snow processes in the Noah land model. *J. Geophys. Res.*, **115**, D20108, doi:10.1029/2009JD013761.

Weedon, G. P., and Coauthors, 2011: Creation of the WATCH forcing data and its use to assess global and regional reference crop evaporation over land during the twentieth century. *J. Hydrometeor.*, **12**, 823–848, doi:10.1175/2011JHM1369.1.

Wehn, S., G. Olsson, and S. Hanssen, 2012: Forest line changes after 1960 in a Norwegian mountain region implications for the future. *Nor. Geogr. Tidsskr.*, **66**, 2–10, doi:10.1080/00291951.2011.644320.

Wen, L., N. Nagabhatla, S. Lü, and S. Y. Wang, 2013: Impact of rain snow threshold temperature on snow depth simulation in land surface and regional atmospheric models. *Adv. Atmos. Sci.*, **30**, 1449–1460, doi:10.1007/s00376-012-2192-7.

Wramneby, A., B. Smith, and P. Samuelsson, 2010: Hot spots of vegetation–climate feedbacks under future greenhouse forcing in Europe. *J. Geophys. Res.*, **115**, D21119, doi:10.1029/2010JD014307.

Xu, L., and P. Dirmeyer, 2011: Snow–atmosphere coupling strength in a global atmospheric model. *Geophys. Res. Lett.*, **38**, L13401, doi:10.1029/2011GL048049.

Yang, Z.-L., R. E. Dickinson, A. Robock, and K. Y. Vinnikov, 1997: Validation of the snow submodel of the Biosphere–Atmosphere Transfer Scheme with Russian snow cover and meteorological observational data. *J. Climate*, **10**, 353–373, doi:10.1175/1520-0442(1997)010<0353:VOTSSO>2.0.CO;2.

Yeh, T.-C., R. T. Wetherald, and S. Manabe, 1983: A model study of the short-term climatic and hydrologic effects of sudden snow-cover removal. *Mon. Wea. Rev.*, **111**, 1013–1024, doi:10.1175/1520-0493(1983)111<1013:AMSOTS>2.0.CO;2.

Yttri, K. E., and Coauthors, 2011: Source apportionment of the summer time carbonaceous aerosol at Nordic rural background sites. *Atmos. Chem. Phys.*, **11**, 13 339–13 357, doi:10.5194/acp-11-13339-2011.

Yucel, I., 2006: Effects of implementing MODIS land cover and albedo in MM5 at two contrasting U.S. regions. *J. Hydrometeor.*, **7**, 1043–1060, doi:10.1175/JHM536.1.

Zeng, X., and A. Beljaars, 2005: A prognostic scheme of sea surface skin temperature for modeling and data assimilation. *Geophys. Res. Lett.*, **32**, L14605, doi:10.1029/2005GL023030.

Zhang, M., and Coauthors, 2014: Response of surface air temperature to small-scale land clearing across latitudes. *Environ. Res. Lett.*, **9**, 034002, doi:10.1088/1748-9326/9/3/034002.

II

II. Merits of novel high-resolution estimates and existing long-term estimates of humidity and incident radiation in a complex domain

Earth Syst. Sci. Data, 11, 797–821, 2019
https://doi.org/10.5194/essd-11-797-2019

Open Access Earth System Science Data

Merits of novel high-resolution estimates and existing long-term estimates of humidity and incident radiation in a complex domain

Helene Birkelund Erlandsen[1,2,3], **Lena Merete Tallaksen**[2], **and Jørn Kristiansen**[3]

[1]Norwegian Water Resources and Energy Directorate, Hydrology Department, Oslo, Norway
[2]University of Oslo, Department of Geosciences, Oslo, Norway
[3]The Norwegian Meteorological Institute, Development Centre for Weather Forecasting, Oslo, Norway

Correspondence: Helene Birkelund Erlandsen (hebe@nve.no)

Received: 28 September 2018 – Discussion started: 2 January 2019
Revised: 28 March 2019 – Accepted: 17 May 2019 – Published: 12 June 2019

Abstract. To provide better and more robust estimates of evaporation and snowmelt in a changing climate, hydrological and ecological modeling practices are shifting towards solving the surface energy balance. In addition to precipitation and near-surface temperature (T_2), which often are available at high resolution from national providers, high-quality estimates of 2 m humidity and surface incident shortwave (SW↓) and longwave (LW↓) radiation are also required. Novel, gridded estimates of humidity and incident radiation are constructed using a methodology similar to that used in the development of the WATCH forcing data; however, national 1 km × 1 km gridded, observation-based T_2 data are consulted in the downscaling rather than the 0.5° × 0.5° Climatic Research Unit (CRU) T_2 data. The novel data set, HySN, covering 1979 to 2017, is archived in Zenodo (https://doi.org/10.5281/zenodo.1970170). The HySN estimates, existing estimates from reanalysis data, post-processed reanalysis data, and Variable Infiltration Capacity (VIC) type forcing data are compared with observations from the Norwegian mainland from 1982 through 1999. Humidity measurements from 84 stations are used, and, by employing quality control routines and including agricultural stations, SW↓ observations from 10 stations are made available. Meanwhile, only two stations have observations of LW↓. Vertical gradients, differences when compared at common altitudes, daily correlations, sensitivities to air mass type, and, where possible, trends and geographical gradients in seasonal means are assessed. At individual stations, differences in seasonal means from the observations are as large as 7 °C for dew point temperature, 62 W m^{-2} for SW↓, and 24 W m^{-2} for LW↓. Most models overestimate SW↓ and underestimate LW↓. Horizontal resolution is not a predictor of the model's efficiency. Daily correlation is better captured in the products based on newer reanalysis data. Certain model estimates show different dependencies on geographical features, diverging trends, or a different sensitivity to air mass type than the observations.

1 Introduction

Geophysical modeling is advancing, and more and more hydrological, ecological, and land surface models (from here on referred to as land models) are now estimating the surface energy balance (Mueller et al., 2013). Shortwave radiation is the exogenous energy provider to Earth. At middle and higher latitudes, surface downward longwave radiation is an equally important radiative driver at the surface. Estimating the surface energy balance provides a sensible heat flux, as well as a latent heat flux, which in turn can be converted to evaporation or snowmelt, key variables for estimating the surface water balance.

Recent studies have shown the added value of using more forcing data than only precipitation and temperature when modeling evaporation (Milly and Dunne, 2011; Lofgren et al., 2011; Haddeland et al., 2012; Pierce et al., 2013; Stagge et al., 2014) or snow cover

(Raleigh et al., 2016; Harpold et al., 2017). High-quality and robust diagnoses, forecasts, and projections of evaporation- and snowmelt-related processes are essential for flood and hydropower management. Further, gridded data sets of high quality are needed to statistically bias-correct or downscale future climate scenarios (Abatzoglou, 2013), to spin up land surface models (e.g., Rodell et al., 2005; Koster et al., 2004; Kristiansen et al., 2012), and to assist model development.

Considerable effort is used to improve process description in environmental models and compare the results of different models. When land models are run without coupling to an atmospheric model, i.e., in offline or stand-alone mode, meteorological near-surface variables, commonly referred to as forcing data, are required. In practice, different communities use different forcing data estimates, such as the more empirically based estimates from the MTCLIM algorithms (Bristow and Campbell, 1984; Thornton and Running, 1999; Bohn et al., 2013), estimates from numerical weather and climate models, or a combination of the two (see, e.g., Mizukami et al., 2016). The different approaches used make it more difficult to compare the output across land models and have resulted in dedicated projects where various models are run with similar forcing data in, for example, the Inter-Sectoral Impact Model Intercomparison Project (ISI-MIP; Warszawski et al., 2014).

The Norwegian operational hydrological models have historically been calibrated and adapted to use high-resolution, gridded 2 m temperature and precipitation data as forcing data. For this purpose high-resolution (1 km × 1 km) data sets, which cover the period from 1957 until the present (2019) with a daily resolution have been developed, namely the SeNorge data (Mohr, 2008; Tveito and Førland, 1999; Lussana et al., 2018a, b). In recent times a long-term high-resolution, quantile-mapping-based gridded data set of near-surface wind speed has also been developed at the Norwegian Meteorological Institute (MET Norway, available from http://thredds.met.no/thredds/catalog/metusers/klinogrid/KliNoGrid_16.12/FFMRR-Nor/catalog.html, last access: 10 June 2019). Gridded, observation-based, high-resolution data sets for humidity and incident radiation are, however, lacking.

Previous studies have compared and validated gridded estimates of humidity or incident radiation globally (Bohn et al., 2013; Schmied et al., 2016; Weedon et al., 2011), for regions in the US (Slater, 2016; Mizukami et al., 2014; Pierce et al., 2013; Lapo et al., 2017), coastal Brazil (Almeida and Landsberg, 2003), France (Szczypta et al., 2011), and the pan-Arctic region (Shi et al., 2010). No previous studies have, as far as we know, compared and assessed the quality of high-resolution empirically based and reanalysis-based estimates of humidity and incident radiation for regions within Europe (let alone for Norway specifically). This results in an additional and unnecessary source of uncertainty for land modeling in Norway.

Norway's complex topography and coastline may suggest that high-resolution data sets would perform better. When land models are run the near-surface temperature from the forcing data is usually adjusted to sea level and then to the land model's fine-resolution grid cell elevation that uses a standard atmospheric lapse rate to account for the difference in terrain height in the forcing data model and the land model to be run. A standard atmospheric temperature lapse rate may be unreasonable in winter, at high latitudes (Kotlarski et al., 2010; Brinckmann et al., 2016), and in complex terrain (Mizukami et al., 2014), and a much lower resolution in the forcing data grid compared to the land model may increase these error components. Further, if humidity is not also adjusted for inconsistencies between temperature and humidity will likely result in an unrealistic relative humidity (Haddeland et al., 2006; Weedon et al., 2011). Incident radiation is influenced by variables showing a strong vertical dependence like near-surface temperature and humidity, cloud cover (e.g., Marty, 2000), and local variations in surface components like vegetation and snow cover (Erlandsen et al., 2017; Rydsaa et al., 2017), and thus may likely benefit from vertical adjustment.

While the spatial correlation may improve in a data set with a high spatial resolution, Decker et al. (2012) highlight the need to address temporal correlation on timescales shorter than monthly scales in data constructed from reanalyses for the purposes of forcing land surface models. A high horizontal resolution may lead to a better representation of the average state of a variable but not necessarily to an improved description of the concurrent temporal evolution of the forcing variables on shorter timescales, e.g., during the rapid passage of a low-pressure system with multiple distinct air mass characteristics and precipitation types.

This study addresses the aforementioned sources of uncertainty concerning commonly used estimates of humidity, either in the form of vapor pressure (VP) or converted to dew point temperature (T_d), incident longwave radiation (LW↓), and incident (global) shortwave radiation (SW↓) available for long-term land surface modeling in the region through the following processes.

- The construction of an original data set, HySN (to explore the benefit of utilizing a 1 km × 1 km national data set of 2 m temperature in the post-processing reanalysis data);
- The gathering of global long-term gridded data sets of humidity and incident radiation from two reanalysis data sets, two post-processed reanalysis data sets, and two versions of empirically based estimates compiled for continental Norway;
- The aggregation of available observations of humidity and incident radiation between 1982 and 1999 from a variety of providers, and where necessary, implementing quality control routines;

- The construction of multiple linear regression models to provide vertical gradients in both the observations and the model estimates, so that the variables may be adjusted to a similar altitude before their differences are assessed;
- The correlation of model estimates with observations on a daily timescale is explored by compiling anomaly correlation coefficients;
- The comparison of the model estimates' cumulative distributions; their sensitivity to weather types, continentality, and latitude; and their decadal trend to the observational data.

Additionally, two hypotheses are investigated. $\mathcal{H}_a$ – there are vertical gradients in near-surface humidity and incident radiation in our domain. $\mathcal{H}_b$ – the added value of the high horizontal resolution of the more empirically based estimates outweighs the added value of relying on estimates from coarser-resolution numerical weather prediction reanalyses.

The data sets considered are two global reanalysis data sets, the NASA Modern-Era Retrospective Analysis for Research and Applications version 2 (MERRA2) (Bosilovich et al., 2015, 2017), and ECMWF's ERA-Interim (Dee et al., 2011), two products based on reanalysis data post-processed using higher-resolution gridded observational data, the Princeton Global Meteorological forcing data set, version 2 (PGMFDv2) (Sheffield et al., 2006), the WATCH forcing data methodology applied to ERA-Interim (WFDEI) (Weedon et al., 2014), and two versions of high-resolution empirically based estimates from the preprocessor of the Variable Infiltration Capacity (VIC) model, a macroscale hydrological model (Liang et al., 1994) largely based on the MTCLIM algorithms. Finally, a novel data set, the HySN data set, is compiled for the current study and evaluated. HySN is compiled by employing a similar method as was used in the development of PGMFDv2 and WFDEI; however, in this case ERA-Interim near-surface humidity and incident radiation are post-processed using a national, high-resolution, gridded 2 m temperature data set, SeNorge2 (Lussana et al., 2018b).

2 The gridded humidity and radiation estimates considered

Long-term data sets that are freely available, which can be used to drive hydrological, ecological, and land surface models for the Norwegian domain, include the newer reanalyses: MERRA2 and ERA-Interim. Due to computational constraints, currently available long-term global reanalysis data have horizontal resolutions ranging from $2^\circ \times 2^\circ$ to $0.5^\circ \times 0.66^\circ$. The MERRA2 reanalysis has a resolution of 0.5° latitude $\times 0.66^\circ$ longitude. Around Oslo, Norway, this corresponds to a grid cell height and length of about 56 km × 42 km. The reanalysis data sets are based on global circulation models ingesting large amounts of observational data by making use of complex assimilation techniques. However, substantial biases may still occur in reanalysis data. Heikkilä et al. (2011) found a mean error of +42.9 % in precipitation intensity in ERA-40 over Norway between 1961 and 1990. Bromwich et al. (2016) found a negative bias in ERA-Interim surface LW↓ radiation and precipitation between November 2007 and December 2008 across middle and high latitudes in the Northern Hemisphere.

The coarse resolution of reanalysis data and the knowledge of biases that may be present in them has spurred the development of post-processed reanalysis data sets. The PGMFDv2 and WFDEI are data sets consisting of variables relevant for forcing land surface models. The relevant variables are extracted from reanalysis data and post-processed and downscaled with gridded observational data. Both data sets are global and have horizontal resolutions of $0.5^\circ \times 0.5^\circ$. PGMFDv2 and WFDEI both adjust reanalysis estimates of humidity and LW↓ with the gridded, $0.5^\circ \times 0.5^\circ$ Climatic Research Unit (CRU) T_2 following the methods described in the development of NLDAS (Cosgrove, 2003). Taking a note from these methods, a novel high-resolution product is developed and validated in the current study: Hybrid SeNorge, abbreviated as HySN. HySN is constructed by post-processing ERA-Interim humidity and radiances in a similar manner to PGMFDv2 and WFDEI but utilizing a national data set, the 1 km × 1 km SeNorge2 T_2, rather than the $0.5^\circ \times 0.5^\circ$ CRU T_2.

Another source of near-surface humidity and incident radiation estimates are the MTCLIM algorithms, which combine first principles from atmospheric physics with empirical extrapolation logic. Precipitation and temperature, variables that often are available from a dense network of surface observation stations, are used to estimate shortwave radiation and humidity. Versions of the MTCLIM routines are used to provide forcing data for a large number of hydrological and ecological models; it has, for example, recently been made available for the Mesoscale Hydrological model (MHm v5.9, https://doi.org/10.5281/zenodo.1069202). The variables estimated from MTCLIM are often utilized for impact studies, e.g., the impacts of climate change and forest management on ecosystem services in Europe (Bugmann et al., 2017). The algorithms have also been used to generate several gridded data set products of humidity and radiation for the US (e.g., Livneh et al., 2013) and are used to provide climate change projections of humidity and radiation for the US (Bureau of Reclamation, 2013). However, several recent studies have found regionally inconsistent biases in the MTCLIM algorithms (Shi et al., 2010; Bohn et al., 2013; Pierce et al., 2013; Slater, 2016; Mizukami et al., 2014).

The orography and land masks of the models are presented in Fig. 1. Compared to ERA-Interim orography, the SeNorge grid elevation is on average higher (mean: 37 m, median: 13 m; see the red areas in Fig. 1). The difference in maximum elevation is more than 1000 m. Meanwhile, near the coast and in inland areas the ERA-Interim orography is predominantly

higher (see the blue areas in Fig. 1). The data sets are summarized in Table 1. Further details considering ERA-Interim, MERRA2, WFDEI, PGMFDv2, WFDEI, HySN, and two data sets from the VIC model's preprocessor, largely based on the MTCLIM algorithms, are presented in the following.

2.1 ERA-Interim

The ERA-Interim (Dee et al., 2011) is a reanalysis data set developed by ECMWF, covering the time period from 1979 until the present. It is based on a 2006 release of the ECMWF operational model system (IFS Cy31r2) and has a horizontal resolution of about 80 km. It includes a four-dimensional variational analysis (4D-Var). Surface observations are ingested by optimal interpolation. The variables evaluated in this study are daily means of 2 m temperature and dew point temperature from analysis times (00:00, 06:00, 12:00, and 18:00 UTC) and LW↓ and SW↓ taken between +12 and +24 h into the forecast to allow for spin-up (see, e.g., Weedon et al., 2014).

2.2 Modern-Era Retrospective Analysis for Research and Applications 2 (MERRA2)

MERRA2 is an atmospheric reanalysis data set developed by NASA, available from 1980 until the present, with a horizontal resolution of $0.5° \times 0.625°$(Bosilovich et al., 2015). Mass conservation constraints are imposed so that assimilated observations do not cause large violations of the global water balance. In MERRA2 land surface observations are not assimilated. The data variables used in this study are model orography (Mer, 2015a), pressure, and humidity from atmospheric single level diagnostic (Mer, 2015c), LW↓, and SW↓ (Mer, 2015b).

2.3 Princeton's global meteorological forcing data set version 2 (PGMFDv2)

PGMFDv2 is an updated version of the $0.5° \times 0.5°$ 60-year Princeton global meteorological forcing data set (Sheffield et al., 2006). The updates are described in Schmied et al. (2016). The humidity, LW↓, and SW↓ estimates are based on the National Centers for Environmental Prediction–National Center for Atmospheric Research (NCEP-NCAR) reanalysis but post-processed to comply with the gridded, observation-based time series of precipitation, temperature, and cloud cover, with a horizontal resolution of $0.5° \times 0.5°$ from the Climatic Research Unit (CRU TS 3.2.1) and satellite estimates of LW↓ and SW↓.

2.4 The WATCH forcing data methodology applied to ERA-Interim (WFDEI)

The application of the WATCH forcing data methodology to ERA-Interim reanalysis data, WFDEI, is described in Weedon et al. (2014). The data are available from 1979 to the present and have a horizontal resolution of $0.5° \times 0.5°$. The humidity, LW↓, and SW↓ estimates are based on ERA-Interim data, post-processed to comply with the global gridded, observation-based time series of 2 m temperature, cloud cover, and interannual aerosol loading from CRU TS, using CRU TS 3.2.1 prior to 2009 similar to PGMFDv2.

2.5 Hybrid SeNorge ERA-Interim, HySN (H)

As part of this study, additional estimates of humidity and LW↓ are derived, using methods based on Cosgrove (2003), adjusting ERA-Interim humidity and LW↓ to comply with the newly developed, 1 km × 1 km SeNorge2 T_2 data set (Lussana et al., 2018b). Further, the ERA-Interim SW↓ estimates are adjusted based on the previously adjusted humidity estimates and the 1 km × 1 km orography.

ERA-Interim humidity and longwave radiation are vertically adjusted on a daily basis by consulting the daily SeNorge T_2. The method differs from that used in the construction of the WFDEI and Princeton forcing data, where the reanalysis T_2 is adjusted to sea level and then to the CRU grid elevation using a constant lapse rate, before adjusting it on a monthly basis to fit the monthly mean CRU T_2. The vertical adjustment of humidity makes use of the common approximation that relative humidity remains constant with height (see, e.g., Feld et al., 2013), making it easy to solve for a SeNorge2 compatible dew point temperature T_d based on ERA-Interim relative humidity (RH) and SeNorge2 T_2. Humidity is corrected to saturation if supersaturation occurs. Surface pressure is adjusted using an approximation of the hypsometric equation. The vertical adjustment of longwave radiation is done by scaling an empirical expression for clear-sky LW↓ to the SeNorge T_2 and the previously compiled vertically adjusted humidity estimate. No consistent approach is used in other forcing data sets when vertically adjusting SW↓. Given that SW↓ is very sensitive to near-surface humidity and that the Cosgrove (2003) method used above adjusts humidity, we chose to scale the ERA-Interim SW↓ to the ratio of estimated clear-sky transmissivity calculated using an empirical equation from Thornton and Running (1999), taking into account the difference in altitude and humidity in the two data sets. A clear-sky type correction approach is thus used to adjust both SW↓ and LW↓.

For consistency with SeNorge precipitation and T_2, the variables have a temporal resolution of a day, starting from 06:00 UTC. The data are currently compiled for the time period 1979–2017 and cover the same domain as the SeNorge2 grid. The data compilation is described in detail in the Supplement. The HySN data product is freely available from Zenodo (https://doi.org/10.5281/zenodo.1970170), and the Python code to generate the data is available on GitHub (https://doi.org/10.5281/zenodo.1435555).

Table 1. The following data sets provide estimates of humidity, LW↓, and SW↓, which are then evaluated. Precipitation is denoted as P, 2 m temperature as T_2. The global data sets are retrieved from online repositories, while the data sets with regional coverage are compiled locally based on the stated input data, the VFD data sets using the VIC model's preprocessor, and the HySN data set based on the methods outlined in the current study. Additional references are given elsewhere in the text.

	Product	Resolution	Coverage	Type	Processing methods	Input data	Surface obs.
M	MERRA2	0.5° × 0.66°	Global	Reanalysis			No
E	ERA-Interim	0.66° × 0.66°	Global	Reanalysis			Yes
P	PGMFDv2	0.5° × 0.5°	Global, land only	Post-processed reanalysis	VP, LW↓ re-gridded and adjusted to monthly CRU T_2, method from Cosgrove (2003). SW↓ & LW↓ adjusted to satellite-based data set	NCEP-NCAR (2° × 2°), CRU TS3.1 T_2 & cloud cover, NASA MEaSUREs LW↓ & SW↓	Yes
W	WFDEI	0.5° × 0.5°	Global, land only	Post-processed reanalysis	VP, LW↓ re-gridded and adjusted to monthly CRU T_2, method from Cosgrove (2003). SW↓ re-gridded and adjusted to CRU cloud cover & interannual aerosol loading	ERA-Interim, CRU TS3.1 T_2 (1979–2009), CRU cloud cover and aerosol loading	Yes
H	HySN	1 km×1 km	Regional, locally compiled	Post-processed reanalysis	VP, LW↓ re-gridded and adjusted to daily SeNorge2 T_2, method from Cosgrove (2003). SW↓ re-gridding and adjustment, method from Thornton and Running (1999)	ERA-Interim, SeNorge2 T_2	Yes
V1	VFDv1	1 km×1 km	Regional, locally compiled	Empirical model	The VIC4.0.6 preprocessor: MTCLIMv4.2, & TVA+Bras LW↓	SeNorge P & T_2, Nora10 sub-daily T_2	Yes
V2	VFDv2	1 km×1 km	Regional, locally compiled	Empirical model	The VIC4.2.d preprocessor: MTCLIMv4.3, & Prata+Deadroff LW↓	SeNorge2 P, $T_{2\min}$, & $T_{2\max}$	Yes

2.6 VIC type forcing data, VFDv1, and VFDv2

The humidity and radiation estimates referred to here as VIC type forcing data (VFD) (see, e.g., Bohn et al., 2013; Pierce et al., 2013) are products of the VIC model's preprocessor. The VIC model includes the option to generate gridded humidity and radiation from gridded daily precipitation and maximum and minimum temperature. The VIC model preprocessor includes a slightly modified version of the MTCLIM model and algorithms for estimating longwave radiation. The MTCLIM algorithms included in the VIC preprocessors to estimate humidity use a modified version of the Magnus formula with daily minimum temperature used as a proxy for T_d (Kimball et al., 1997). Shortwave radiation is estimated using the Thornton and Running algorithm (Thornton and Running, 1999). The variables are estimated simultaneously; i.e., the algorithms supply each other with information (Bohn et al., 2013).

Two versions of VFD are evaluated in this study. The first version, from here on called VFDv1, uses daily precipitation and mean temperature from SeNorge version 1.1 (Tveito and Førland, 1999; Mohr, 2008), supported by hourly temperature fields from a regional atmospheric reanalysis data set, NOrwegian ReAnalysis (NORA10, Reistad et al., 2011), with a resolution of about 11 km to compile maximum and minimum temperature using a method similar to Vormoor and Skaugen (2013). The VIC4.0.6 preprocessor is used with default options, i.e., a modified version of MTCLIM4.2, and the TVA clear-sky and Bras full-sky LW↓ algorithm (Bras, 1990).

The second version of VIC type forcing data, from here on called VFDv2, is based on slightly different input data, i.e., precipitation and mean, maximum, and minimum temperature from a newer version of the 1 km by 1 km SeNorge data, SeNorge2 (Lussana et al., 2018a, b). The VIC4.0.6 preprocessor is used with default options, i.e., a modified version of MTCLIMv4.3, and with LW↓ estimates based on the Prata (1996) clear-sky algorithm combined with the Deardorff (1978) full-sky algorithm (for further references see Bohn et al., 2013).

3 Study area

Norway is located in the receiving end of the westerlies that pass over the North Atlantic. This, combined with a long coast lined with mountains provides Norway with 1500 mm of precipitation a year, with distinct regional differences in precipitation amounts received. Although almost 40 % of Norway is covered by forest, evaporation from the land surface is estimated to be less than a fourth of the received precipitation (Hanssen-Bauer et al., 2009). Most of Norway will normally have snow cover in the winter season, with the length of the snow season varying from a few days to 300 d a year (dependent on latitude, elevation, and distance from the coast). Mean temperature (1971–2000) is 1.3 °C, and varies from 7 °C near the coast in southern Norway to −4 °C in the mountains. Between 1976 and 2014 T_2 increased by half a degree Celsius per decade (Hanssen-Bauer et al., 2017).

4 Surface observations

The model estimates and observational data are compared between 1982 through 1999. The observational data include humidity measurements from 84 sites, SW↓ observed at 10 sites, and LW↓ observed at two sites. The comparison of the model estimates of incident radiation with stations data is only made possible by including observations from agricultural stations and applying quality control routines. The observations are gathered from the University of Bergen (UiB, SW↓ and LW↓ measurements), and from the Norwegian Meteorological Institute's repository for observational data, which also includes measurements from agricultural stations conducted by the Norwegian Institute of Bioeconomy Research (NIBIO). The locations of the stations used in the comparison with the model estimates are shown in Fig. 1.

4.1 Humidity

Humidity observations from 84 stations are included in the study (see Fig. 1). A minimum of 5 years of daily data was necessary for the station data to be included; however, most stations have the complete station record (18 years) available. The observations, once converted to vapor pressure, have an uncertainty ranging from around 5 % at 20 °C to 6 % at −20 °C (Gabriel Kielland, personal communication, MET Norway, 2019). The latitude, longitude, altitude, distance to the ocean, and the start and end date of the time series are given for each station in the Supplement (Tables S1 and S2).

4.2 Shortwave radiation

The location of the 10 stations included in the evaluation of modeled SW↓ is displayed in Fig. 1 and covers a latitudinal range from 58.8 to 69.7° N. Seven of the stations are agricultural stations managed by NIBIO. The latitude, longitude, altitude, distance to the ocean, the start and end date of the time series, and the percentage of flagged data are given for each station in the Supplement (Table S3). The number of days of data used in the validation varies from 5.6 years for Gjengedal to more than 17 years for Bergen.

Table 2. An overview of the automatic quality control tests, based on the relative values of the solar zenith angle (SZA), measured ($SW_{raw}\downarrow$), extraterrestrial ($SW_E\downarrow$), and clear-sky ($SW_{CS}\downarrow$) incident global radiation. The table is adapted from Table 4.1.1 in Grini (2015).

Name	Quality requirement	Quality procedure
Offset	$SW_{raw}\downarrow \leq -12\,W\,m^{-2}$	Visual control
	$SW_{raw}\downarrow < 6\,W\,m^{-2}$ if SZA $< 93°$	of flagged data
Upper bound 1	$SW_{raw}\downarrow < SW_E\downarrow$	Flagged as erroneous
Upper bound 2	$SW_{raw}\downarrow \leq 1.1\ SW_{CS}\downarrow$ if SZA $< 88°$	Flagged as erroneous
	$SW_{raw}\downarrow \leq 2\ SW_{CS}\downarrow$ if SZA $\geq 88°$	
Lower bound 1	$\mu\frac{SW_{raw}\downarrow}{SW_E\downarrow} \leq 0.03$	The day flagged as erroneous
Lower bound 2	$SW_{raw}\downarrow \leq 10^{-4}$ (80 SZA) $SW_E\downarrow$ if SZA $\leq 80°$	Flagged as erroneous

Most stations measure global radiation with a Kipp & Zonen CM11 thermoelectric pyranometer. The estimated uncertainty of hourly and daily totals of CM11 may be as low as 3 % in optimal conditions (Grini, 2015). Daily global SW↓ measurements from Bergen station (UiB) are included in the World Radiation Data Centre (WRDC) and are quality-controlled by the data provider (UiB, A. Olseth). The daily estimates have an uncertainty of 3.5 % (Parding et al., 2016). Measurement errors and uncertainty may depend on sensor calibration, placement (e.g., sky-view), the temporal resolution of the measurements, cleaning of the pyranometer, and local weather conditions.

For stations other than Bergen, quality control procedures follow the methodology suggested by Grini (2015) as outlined in Table 2. This procedure involves running rtmrun (Godøy, 2013); a Perl wrapper around Libradtran 1.7 (Mayer and Kylling, 2005); a library for radiative heat transfer to provide solar zenith angle (SZA), extraterrestrial ($SW_E\downarrow$), and clear-sky ($SW_{CS}\downarrow$) incident shortwave radiation for each station location; and the Python scripts developed in Grini (2015) to screen and flag the data based on automatic quality control tests. Measurements exceeding the upper and lower bounds given in Table 2 were flagged. Additionally, all station time series were visually inspected at hourly, daily, and monthly levels in order to flag erroneous data not captured by the automatic routines, with emphasis on data points marked as suspicious due to large hourly increments or very high or low variation in the ratio of observed to extraterrestrial radiation. Figure 2 shows the mean monthly values of SZA, $SW_E\downarrow$, $SW_{CS}\downarrow$, the raw measured values ($SW_{raw}\downarrow$), and values passing the quality control routines ($SW_{QC}\downarrow$) for Løken station.

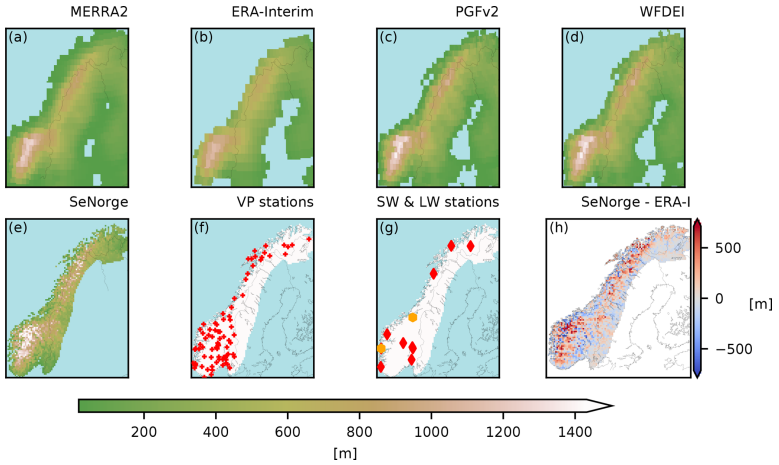

Figure 1. Panels **(a)**–**(e)** show the orography and land mask of MERRA2 **(a)**, ERA-Interim **(b)**, PGMFDv2 **(c)**, WFDEI **(d)**, and SeNorge **(c)**, respectively, visualized on the SeNorge UTM33 grid with a green–brown color scheme. For reference, national borders and the coastline derived from a high-resolution data set are delineated in black. The locations of the 84 VP stations used in the model comparison are denoted with red crosses in **(f)**. The locations of SW↓ and LW↓ stations are marked in **(g)** with red and orange markers, respectively. Note that the southernmost LW↓ station also measures SW↓. The last map **(h)** displays the difference in meters between the SeNorge and ERA-Interim orography in common land areas. Higher elevations in SeNorge are indicated with red, while blue indicates higher elevations in ERA-Interim.

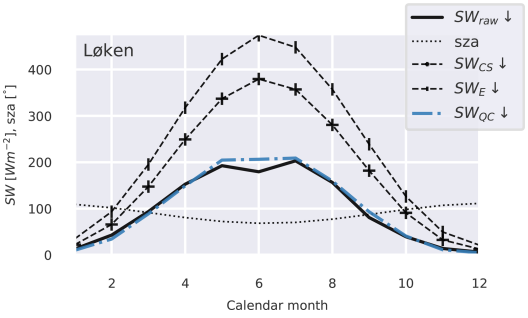

Figure 2. Estimated and measured shortwave radiation ($W\,m^{-2}$) at Løken station (61.1° N, 9.1° E) for the period January 1991 to December 1999. Mean monthly solar zenith angle (SZA), (global) shortwave incident radiation at the top of the atmosphere (SW_E ↓), modeled clear-sky incident shortwave radiation (SW_{CS} ↓), and station measurements of incident shortwave radiation before (SW_{raw} ↓) and after (SW_{QC} ↓) quality control are shown.

In the calculation of daily means, values were flagged as erroneous and subsequently excluded from the validation if more than two hourly data points were flagged or missing during daytime. The number of discarded days varied from 4 % at Kise to 29 % at Tromsø.

4.3 Longwave radiation

Bergen station and Voll station (Trondheim), denoted with orange markers in Fig. 1g, have observations of incident longwave radiation available for the time period considered. The lack of LW↓ measurements is not an uncommon challenge (see, e.g., Carrer et al., 2012). The stations' latitude, longitude, distance to the coast, and the start and end date of the data used are listed in the Supplement (Table S3). Both measurement stations are located within 5 km of the coast (see Fig. 1). The measurements from Bergen are managed and quality-controlled by UiB. In the first part of the period they are from a Schulze radiation balance meter, while later in the period they are from an Eppley pyrgeometer. The sensors are placed on the roof of UiB. The observation station at Voll, Trondheim, was managed by MET Norway from March 1996, until it was shut down. The Trondheim measurements are from a Kipp & Zonen CG 1 pyrgeometer located on the ground. At both stations unshaded sensors were used, possibly leading to slight overestimation due to solar near-infrared radiation contamination (overestimations of 10 % on cloud-free days were found in de Oliveira et al., 2006; Meloni et al., 2012). The data were quality-controlled by visual inspection for spikes and jumps and by comparing the consistency between the two time series. The Stefan–Boltzmann blackbody longwave radiation was set as an upper limit of the measurements, using the air temperature from the station. If more than 2 h were missing or flagged during

a day, observations from that day were omitted in the subsequent validation.

5 Evaluation methods

Daily estimated values are compared to station observations. The nearest model grid cell is selected from the data sets without interpolation, to avoid introducing spatial or temporal smoothing of the meteorological fields (see Hofstra et al., 2010; Gutmann et al., 2012). This study specifically looks into the altitudinal dependence of the humidity and surface incident radiation estimates, and as a starting point the estimates without adjustment to the observation stations' altitudes are used.

5.1 Vertical adjustment to station altitude

Prior to the comparison of the model estimates with the station observations, the observations and model estimates of VP and SW↓ were analyzed using multiple linear regression with geographical features as predictors, in order to find vertical gradients so that the model estimates could be adjusted to station altitude. The geographical predictors used were altitude (either the stations' altitude or, for the models, the altitude of the nearest-neighbor grid cell to the stations), latitude above 57° N, and distance to the coast, which was calculated in Python using the Haversine distance from the station to the coastline, extracted from a coastline data set (Wessel and Smith, 1996) that is available via the Matplotlib Basemap Toolkit, implemented at a coarse resolution to not include large inland lakes. The limited number of SW↓ measurement stations and the varying temporal availability of high-quality observational data made an evaluation of the altitudinal dependence of the SW↓ more demanding. The SW↓ data were first converted to clearness index (CI), which describes the daily incident shortwave radiation fraction of the potential extraterrestrial radiation at the local position and time ($SW\downarrow / SW_E \downarrow$), and then daily data of over 1000 concurrent measurements from eight stations were used in the regression.

The model estimates were adjusted to station altitude by multiplying their grid cell values with the difference in altitude to the observation station and a vertical adjustment gradient. For each model the vertical adjustment gradients were computed as the mean of coefficients found for the model in question and those found for the observational data, linearly interpolated from a seasonal to a daily frequency. A similar regression model was constructed to find vertical gradients in LW↓ using a well-performing data set in lieu of observations due to the limited number of LW↓ observation stations.

5.2 Evaluation metrics

Seasonality and aggregated means are assessed by plotting the mean monthly station values for the observations and models. The differences between the model estimates and observations at individual stations are displayed in heat maps. For each variable a table is provided listing several metrics. The tables list the following variables for each model:

1. $\Delta = \overline{\mu_{\text{station,model}} - \mu_{\text{station,observation}}}$, the mean ($\mu$) of the station differences;
2. $|\Delta| = \overline{|(\mu_{\text{station,model}} - \mu_{\text{station,observation}})|}$, the mean of the station absolute differences;
3. $|\delta|_{\max} = \max(|\mu_{\text{station,model}} - \mu_{\text{station,observation}}|)$, the largest absolute difference at any station;
4. $|\delta^s|_{\max} = \max(|\mu_{\text{season,station,model}} - \mu_{\text{season,station,observation}}|)$, the largest absolute difference found at any station in any season.

Also listed are the mean daily anomaly correlation coefficient (ACC), i.e., the daily Pearson correlation coefficient of the time series where the observed day-of-year mean is subtracted and the number of stations where the cumulative distribution of daily mean estimates passes ($p > 0.001$), and finally the Kolmogrov–Smirnov test of similarity with the cumulative distribution of the observations. The Kolmogrov–Smirnov test returns the probability that the underlying one-dimensional probability distributions are the same (H_0). The similarity between the models and observations on a daily frequency is visualized in Taylor plots, where the normalized standard deviation, the root-mean-square error, and the correlation coefficient of the de-seasonalized time series are displayed. The time series are de-seasonalized by subtracting the observed day-of-year climatology. The correlation coefficient thus corresponds to a non-centered version of the anomaly correlation coefficient (ACC).

5.3 Evaluation of geographical gradients

In order to see if the geographical dependencies of the model estimates of humidity and shortwave radiation differ significantly from those seen in the observational data, similar multiple linear regression models as those previously constructed to find vertical gradients are used. The predictors are the season, altitude (z), latitude above 57° N, and distance to the coast (C). The regression is first performed separately for each model and for the observations. However, a second iteration of regression is performed for each of the models, where the input data are composed of the observational data and model data are appended together with the data sources indicated. The data source is then used as a categorical predictor allowed to interact with any of the model coefficients. Significance of the interaction term, e.g., between latitude and model source, will indicate that the model's latitudinal gradient is significantly different from the gradient seen in the observations.

5.4 Air mass type sensitivity

The differences between the model estimates and observations are also inspected for an air mass type dependence. Bower et al. (2007) found significant decreases in the frequencies of dry moderate and dry polar air mass types at Bergen (Flesland) between 1974 and 2000. If the precision of the model estimates is dependent on air mass type, the derived changes in the variables with time may be less robust if the frequencies of the air mass types also change with time. The spatial, synoptic air mass type classification has been constructed for 48 stations in Europe and 7 stations in Norway (Sola, Flesland, Fornebu, Ørlandet, Bodø, Tromsø, and Slettnes) by Bower et al. (2007), according to the methods developed in Sheridan (2002) and Kalkstein et al. (1996). The categorization is done by using sub-daily surface observations of temperature, dew point, wind, pressure, and cloud cover at individual stations (often airports). The synoptic weather-typing classifies the local air mass conditions into the categories DP (dry polar), DM (dry moderate), DT (dry tropical), MP (moist polar), MM (moist moderate), MT (moist tropical), and TR (transitional). The dry weather types are associated with clearer conditions, while the moist weather types are associated with clouds and higher humidity. TR days are defined by large shifts in the synoptic variables, i.e., days where the weather type is changing. The MT weather type is often found in the warm sectors of cyclones, while the MP and MM type may be found in the vicinity of a front or in air transported inland from a cool ocean.

5.5 Comparison of trends

The year 1985 is considered the start of the SW↓ brightening period in Europe after a period of SW↓ dimming due to aerosol emissions (see, e.g., Wild et al., 2005). For time series of a sufficient length and quality, the observational data and the model data are inspected for trends. Stations that have less than 10 % missing daily data between January 1985 and December 1999 are considered, and trends are calculated for each calendar month using the Mann–Kendall test and by calculating the Sen slope (Hirsch et al., 1982). The analysis is done using the R software and functions within the "trend" package (Pohlert, 2018). A total of 59 humidity stations meet the criteria and are grouped into five geographical regions, southwest (S_W, stations with $< 61.8°$ N, $< 8°$ E), southeast (S_E, stations with $< 61.8°$ N, $> 8°$ E), central (C, $61.8 > °$ N$< 64°$ N), northwest (N_W, $> 64°$ N, $< 20.6°$ E), and northeast (N_E, $> 64°$ N, $> 20.6°$ E) when assessing trends. For SW↓ and LW↓ only the station in Bergen (UiB) meets the criteria. For consistency the humidity observations from Bergen-Florida are inspected for trends as well.

6 Comparison between existing long-term estimates and the new hybrid approach, HySN

Daily estimates of near-surface humidity and SW↓ and LW↓ from MERRA2, ERA-Interim, PGMFDv2, WFDEI, VFDv1, VFDv2, and HySN (see Table 1) from 1982 to 1999 are first inspected for vertical gradients in order to adjust the model estimates to station altitude in the following. Further, the estimates' quality on a multi-annual timescale is assessed by considering their mean and absolute deviations from station measurements. The model estimate's distribution is assessed by comparing their daily cumulative distribution to that of the station observations. The estimate's similarity to the observations on a daily timescale is considered by inspecting the anomaly correlation coefficient, i.e., their daily correlation with the measurements after the seasonal cycle has been subtracted, and by considering if their differences to station measurements show sensitivity to the local daily air mass type, which has been classified for seven Norwegian stations by Bower et al. (2007). For humidity and SW↓, the geographical gradients in the models are compared with those in the observations using multiple linear regression. A separate subsection presents modeled and observed trends in each calendar month from 1985 to 1999. Humidity trends are compared after grouping the observations and model estimates into five regions, while SW↓ and LW↓ are computed for Bergen, the only location where long-term measurements of SW↓ and LW↓ are available within the time period with little missing data.

6.1 Humidity

The model estimates of near-surface humidity are compared against humidity observations from 84 stations. The observation stations used in the validation of humidity are located on average 200 m below the coarse-scale grid cell elevation, i.e., in the fjords and on the coast rather than in the surrounding terrain.

6.1.1 Vertical gradients in humidity

Multiple linear regression of seasonal mean humidity at the location of the humidity stations shows that altitude is a significant predictor of humidity in the observations and all models (see Sect. S2 of the Supplement). The vertical gradient in the observations is close to the moist adiabatic lapse rate but varies considerably with season and distance to the coast (C). On average, dew point temperature decreases by $5.2\,°\mathrm{C\,km^{-1}}$ increase in altitude in summer and freeze point temperature decreases by $4.4\,°\mathrm{C\,km^{-1}}$in winter. Regression based on vapor pressure is found to give smaller relative errors than regression based on dew point temperature. This is because dew point temperature has a higher sensitivity to temperature at low temperatures. The observed vertical gradient in vapor pressure is -0.39 hPa per 100 m in summer

and −0.24 hPa per 100 m in winter, and the vertical gradient is weakened by 0.11 hPa per 100 m every 100 km away from the coast.

The vertical gradients in the humidity data differ depending on the data source; e.g., the estimates from PGMFDv2 and WATCH show a weaker decrease with altitude than the observations and other models. For each model the vertical gradients are computed as the mean of the seasonal coefficients found in the regression analyses of the model in question and the observations, linearly interpolated from a seasonal to a daily frequency. The altitudinal adjustment results in a mean difference in humidity, expressed as dew point temperature (T_d) of about 1 °C for the coarse-scale models and about 0.06 °C for the estimates with a 1 km × 1 km resolution. The largest adjustment is an increase in MERRA2's T_d of 7.3 °C at Tafjord station, where the model's orography is 1154 m above the station altitude.

6.1.2 Differences of humidity estimates to station observations

The seasonal cycle of the observations and models (adjusted to station altitude) is shown in Fig. 3a. The largest deviations are seen in the period of highest humidity, i.e., during summer. The signs of the average deviations are consistent throughout the year. PGMFDv2 (denoted with P), MERRA2 (M), and to some degree ERA-Interim (E) and WFDEI (W) show larger estimates than the observations, whereas VFDv1 (V1) and VFDv2 (V2) generally show lower estimates. The HySN (H) estimates follow the mean monthly values of the observations closely. This is also evident in Table 3, where summary of statistics for the humidity estimates presented, and HySN shows a mean station error in T_d of just 0.1 °C. An aggregated mean similar to the observations does not ensure small deviations from the measurements at individual stations.The VFD estimates have the second smallest deviation in aggregated mean (Δ); however, when considering the average absolute deviation ($|\Delta|$) HySN, WFDEI, and ERA-Interim perform better than VFD.

Differences between the model estimates and the station measurements of humidity, expressed as dew point temperature, are depicted for each station, sorted from south (upper y axis) to north (lower y axis) in Fig. 4. The mean absolute difference ($|\Delta|$ or MAE) varies from 0.7 °C for the HySN estimates to 1.8 °C for the PGMFDv2 estimates. The largest deviation occurs at an inland station, Fagernes, where PGMFDv2 T_d estimates a 5.4 °C higher T_d than observed. The figure suggests a latitudinally dependent bias for certain models, and this is further explored in the following subsection by evaluating the models' geographical gradients.

The humidity estimates are evaluated on a daily basis by de-seasonalizing the time series (subtracting the observed day-of-year mean). Figure 5 shows, for each model, the de-seasonalized time series of humidity, the mean temporal correlation coefficient (now equivalent to the anomaly correlation coefficient, ACC), the mean normalized root-mean-square error, and the mean standard deviation in a Taylor plot. Figure 5a visualizes the mean station metrics for the de-seasonalized time series of humidity. The estimates from ERA-Interim and post-processed ERA-Interim (HySN and WFDEI) are closest to the observations and show similar results. MERRA2 also shows a high ACC. PGMFDv2, which is based on an older reanalysis with lower spatial resolution, and the VIC type estimates show slightly poorer results, with an ACC ranging between 0.5 and 0.7 (see also Table 3).

Table 3. Summary of metrics showing the humidity estimates' similarity to station observations. Differences (Δ) are given in dew point temperature in degrees Celsius. Δ is the mean station difference, $|\Delta|$ is the mean absolute station difference, $|\delta_{max}|$ is the largest absolute difference at any station, while $|\delta^s|_{max}$ is the largest seasonal difference at any station. ACC is the anomaly (de-seasonalized) daily correlation coefficient, while K-S indicates the number of stations where the daily mean cumulative distribution passes the Kolmogrov–Smirnov test of similarity ($p > 0.001$). The best scores are shown in bold.

Model	Δ	$\lvert\Delta\rvert$	$\lvert\delta\rvert_{max}$	$\lvert\delta^s\rvert_{max}$	ACC	K-S
MERRA2	1.4	1.5	4.1	4.7	0.79	0 %
ERA-Interim	0.9	1.0	3.7	4.4	**0.86**	10 %
PGMFDv2	1.7	1.8	5.4	6.2	0.52	0 %
WFDEI	0.7	0.9	3.3	3.9	0.85	**15 %**
VFDv1	−0.7	1.0	−4.2	−6.1	0.58	5 %
VFDv2	−1.0	1.2	−5.3	−7.2	0.66	3 %
HySN	**0.1**	**0.7**	**2.8**	**3.7**	0.83	**15 %**

6.1.3 Evaluation of geographical humidity gradients

Multiple linear regression models are fitted to seasonal mean humidity with the four seasons as categorical predictors, where fall (autumn) is the baseline season in the model. The geographical predictors considered are altitude (z given in kilometers), latitude (above 57° N), and distance to the coast (C, given in per 100 km increments). Further, interactions between altitude and season and between altitude and continentality are included. Each model is paired with the observational data in a common regression model where the data source is included as a categorical predictor.

Figure 6 displays the regression coefficients for the observations and the coefficients for the models if they are significantly different ($p < 0.01$) from those of the observations. Higher significance is marked with a darker color. The HySN estimates have similar coefficients to the observations. The regression shows (Fig. 6) that MERRA2 and PGMFDv2 have significantly higher intercepts (higher fall mean values at the coast of southern Norway) than the observations. MERRA2 further shows a stronger latitudinal gradient and a much weaker decrease in humidity with distance from the coast than the observations. In addition to having a higher intercept than the observations, PGMFDv2 shows a

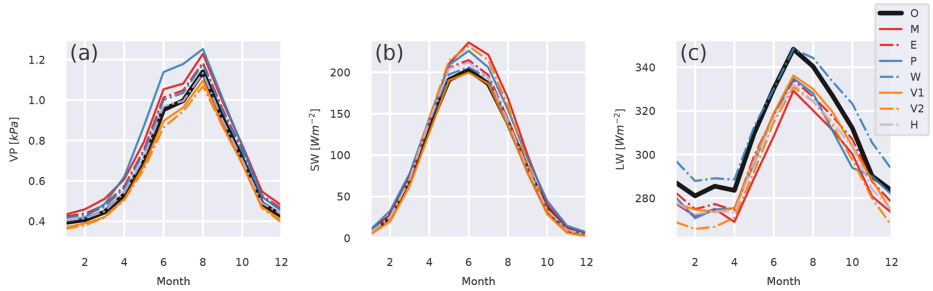

Figure 3. The seasonal cycles of monthly 2 m vapor pressure **(a)**, incident shortwave radiation **(b)**, and incident longwave radiation **(c)**, averaged over the location observations are available. The month of the year is denoted on the horizontal axis. The observations (O) are plotted with a thick, continuous black line. MERRA2 (M, solid) and ERA-Interim (E, dashed) are plotted in red, PGMFDv2 (P, solid) and WFDEI (W, dashed) in blue, VFDv1 (V1, solid) and VFDv2 (V2, dashed) in orange, and HySN (H) with a dashed lilac line.

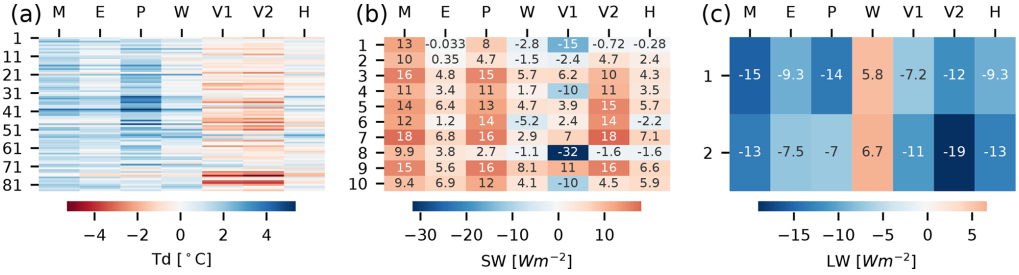

Figure 4. For each station, sorted from south to north (y axis), and each model (x axis) the differences between the modeled and observed station mean dew point temperature **(a)**, incident shortwave radiation **(b)**, and incident longwave radiation **(c)** are shown.

more pronounced seasonal dependency, a weaker continental gradient, and a 50 % stronger latitudinal gradient than the observations. VFDv1 and VFDv2 show a more than 60 % more pronounced decrease in humidity with continentality than the observations. VFDv2 also shows a weaker increase in humidity in summer than the observations.

6.1.4 Air mass type sensitivity of humidity deviations

In Fig. 7a the daily deviations of the humidity estimates are grouped according to the location's daily air mass type classification (SSC type; see Sect. 5). The classification is available for Sola, Fornebu, Flesland, Bodø, Tromsø, and Slettnes stations and the humidity observations considered are from Saerheim, Aas, Bergen, Bodø, Tromsø, and Kirkenes stations. All the estimates are too humid in dry weather types. The PGMFDv2 and VFDv2 estimates show considerable overestimations of humidity in dry weather types and underestimations in moist weather types. The lack of range is consistent with the lower normalized standard deviation seen in the Taylor plot (Fig. 5a). The ERA-Interim, WFDEI, and HySN differences also show a slight sensitivity to air mass type but much less than the VFDv1, VFDv2, MERRA2, and PGMFDv2.

6.2 Incident global shortwave radiation (SW ↓)

SW↓ observations from 10 sites on the Norwegian mainland are considered. At most locations the coarse-scale models' corresponding grid cells have an altitude 300–400 m above station altitudes.

6.2.1 Vertical gradients in clearness index (CI)

Multiple linear regression was used to provide a vertical gradient in SW↓, expressed as clearness index (CI, i.e., the fraction of SW↓ of the extraterrestrial incoming radiation, $SW\downarrow_E$), in order to adjust the estimates to the stations' altitudes. Multiple linear regressions, including both continentality and altitude as predictors resulted in altitudinal coefficients varying in both magnitude and sign for the different models and observations (not shown). This was likely because the correlation between altitude and continentality varies between 0.56 and 0.86 depending on the data source. Excluding continentality from the predictors

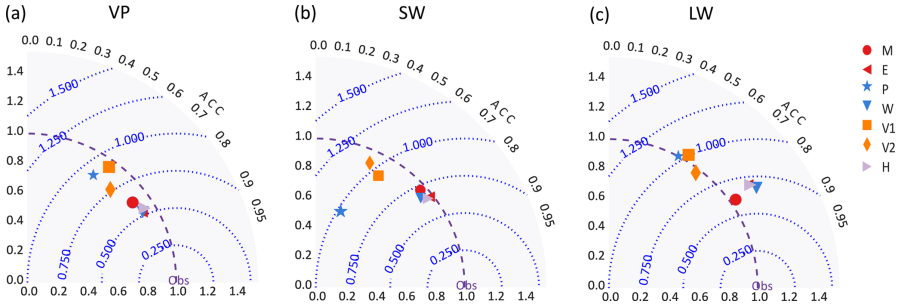

Figure 5. Taylor plots depicting the standard deviation ratio and correlation coefficients (ACCs) for the de-seasonalized time series of vapor pressure **(a)**, incident shortwave radiation **(b)**, and incident longwave radiation **(c)**.

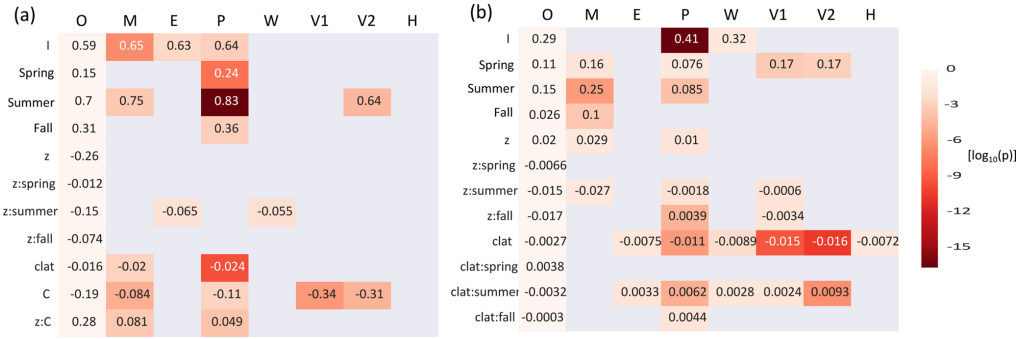

Figure 6. Seasonal and geographical dependencies of seasonal humidity **(a)** and daily clearness index **(b)** are depicted. The row names are the names of the coefficients, including the intercept (I), of the multiple linear regression model. The regression coefficients of the observational data are shown in the leftmost column of each plot, while the coefficients found for the model estimates are only shown if they are significantly different from those of the observations (using a limit of $p < 0.01$ for humidity and $p < 0.05$ for CI). Lower p values are indicated with darker colors using a logarithmic color scale ($\log_{10}(p)$).

provided vertical CI gradients with a consistent sign. The observations show vertical CI gradients of 0.020/100 m in winter, 0.013/100 m in spring, 0.005/100 m in summer and 0.003/100 m in fall (see Fig. 6b). The observed SW↓ thus increases, on average, with altitude in all seasons.

The effect of adjusting the model estimates to station altitude is an average reduction in SW↓ of 0.7–1.5 W m^{-2} for the coarse-scale models (MERRA2, ERA-Interim, PGMFDv2, and WFDEI) and a reduction of merely 0.1–0.3 W m^{-2} for the models with a 1 km×1 km grid (VFDv1, VFDv2, HySN). The largest adjustment is a mean reduction of the PGMFDv2 SW↓ estimate of 4 W m^{-2} at a station in southeastern Norway (Gjengedal).

6.2.2 Differences of SW↓ estimates to station observations

The mean monthly model estimates of SW↓ averaged over all 10 stations, after adjustment to station altitude, are visualized in Fig. 3b. In winter the deviations are small, but in spring and summer all models except VFDv1 overestimate SW↓. The MERRA2 SW↓ is on average 35 W m^{-2} higher than the observations in July, and the VFDv2 SW↓ is 29 W m^{-2} higher than the observations in both June and July. ERA-Interim, WFDEI, and HySN show the largest overestimations in May, a month when solar radiation is high and snow cover is variable.

Figure 4b depicts the mean difference between the model estimate and the observations of SW↓ at individual stations. At half of the stations the mean difference between the WFDEI and HySN and the observations is lower than the measurement uncertainty of newer pyranometers in optimal conditions (Sect. 4). The figure further shows that most models consistently overestimate SW↓. This is not true for VFDv1. While VFDv1 has the second lowest mean monthly deviation (Fig. 3), its mean absolute difference is larger, on average 10 W m^{-2}. This is also evident in Table 4 where summary statistics for the SW↓ estimates are presented.

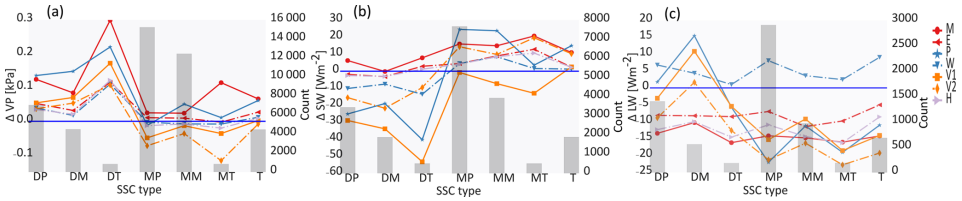

Figure 7. Differences between model estimates and observed values binned according to the daily air mass type, classified for nearby stations within Norway (Bower et al., 2007). The air mass types are dry polar (DP), dry moderate (DM), dry tropical (DT), moist polar (MP), moist moderate (MM), moist tropical (MT), and transitional (T). Panel **(a)** shows the mean difference in vapor pressure for Saerheim, Aas, Bergen, Bodø, Tromsø, and Maze stations. Panel **(b)** shows differences between model estimates and observed incident shortwave radiation at Saerheim (Sola airport), Aas (Fornebu airport), Bergen (Flesland airport), and Trondheim (Ørland airport). Panel **(c)** depicts differences in incident longwave radiation binned according to air mass type in Bergen (Flesland airport) and Trondheim (Ørland airport).

Table 4. As in Table 3 but with metrics listed for SW↓. Except for ACC and K-S, which are dimensionless, the units are given in $\mathrm{W\,m^{-2}}$.

Model	Δ	$\lvert\Delta\rvert$	$\lvert\delta\rvert_{\max}$	$\lvert\delta^{s}\rvert_{\max}$	ACC	K-S
MERRA2	13	13	32	49	0.73	10 %
ERA-Interim	4	**4**	19	20	**0.78**	60 %
PGMFDv2	11	11	19	38	0.31	0 %
WFDEI	**2**	**4**	**8**	**19**	0.76	60 %
VFDv1	−4	10	−23	−62	0.48	10 %
VFDv2	9	10	26	54	0.40	20 %
HySN	3	**4**	9	20	**0.78**	**70** %

Table 4 shows that at individual stations seasonal deviations in model estimates from station observations are as large as $-62\,\mathrm{W\,m^{-2}}$. The large underestimation is found in VFDv1 and not VFDv2 at a coastal station in northern Norway, Bodø. Also listed in the table is the percentage of stations where the daily model estimate, adjusted to station altitude, passes the Kolmogorov–Smirnov test of similarity of their cumulative distribution with the observations, which is zero cases for PGMFDv2 and 70 % for HySN.

The similarity of the model estimates to the observations at a daily frequency is visualized in a Taylor plot (Fig. 5b). As also seen for the humidity estimates, PGMFDv2, VFDv1, and VFDv2 have lower ACCs (31 %–48 %) than the estimates based on newer reanalysis data (73 %–78 %). PGMFDv2 in particular shows a variance at a daily frequency that is considerably smaller than the observations.

6.2.3 Evaluation of geographical gradients in clearness index

Similar to what has been done for humidity, the observations and the corresponding vertically adjusted model estimates of daily CI are compared using multiple linear regression. The seasons, latitude, and altitude are used as predictors, including interaction between season and latitude and between season and altitude. Figure 6b shows the regression coefficients of the observational data in the leftmost column. The coefficients found for the model estimates are only displayed if they are significantly different ($p < 0.05$) from those of the observations. Larger differences ($\log_{10}(p)$) are marked with a darker color.

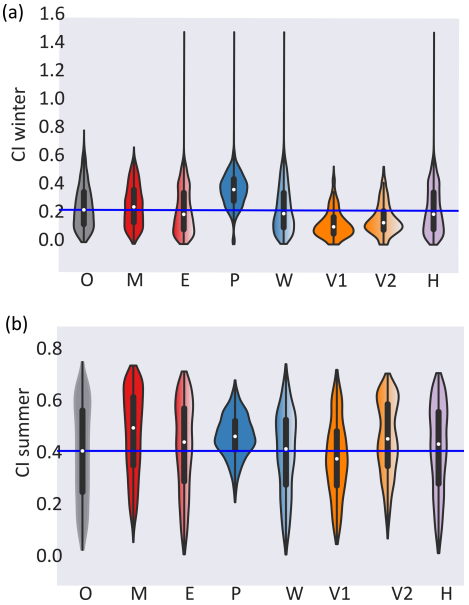

Figure 8. Mean daily clearness index (CI) during winter **(a)** and summer **(b)** is depicted in violin plots, where the kernel density distribution of the observations and each model is shown, mirrored across the y axis. The observed median value is drawn with a blue solid line.

The estimated intercept of PGMFDv2 stands out in the plot. It is 40 % higher than the estimated intercept of the observations. The second most evident difference is the latitudinal gradient in both VFDv1 and VFDv2, which is several times stronger than observed. PGMFDv2 also shows a stronger latitudinal gradient than observed. Other notable differences are the estimated summer CI values of MERRA2, which are considerably higher than those seen in the observations.

6.2.4 Air mass type sensitivity of SW↓ deviations

Figure 7b shows the differences between the models' SW↓ estimates and observations at Aas, Saerheim, Bergen-GFI, Bodø, and Tromsø stations, grouped according to the weather type at nearby weather stations (Fornebu, Sola, Flesland, Bodø, and Tromsø, respectively). All models except VFDv1 show positive SW↓ deviations during weather types classified as moist, which occur most frequently. In the less prevalent dry weather types all models except MERRA2 show slightly lower estimates than observed. The largest underestimations are seen for the VFDv1 estimates. Further, the deviations of PGMFDv2, VFDv1, and VFDv2 show a stronger dependency on weather type than MERRA2, ERA-Interim, WFDEI, and HySN. The MERRA2 SW↓ estimates are, however, overestimated during all weather types. The WFDEI SW↓ estimates show considerable deviations from the ERA-Interim estimates, with larger underestimations found during both dry polar and dry tropical weather types, and considerably lower overestimations found on days classified with a moist tropical weather type. Grouping the clearness index into either dry or moist and transitional weather types shows that the observed CI decreases on average by 0.22 in moist and transitional types. A similar decrease is seen in MERRA2, ERA-Interim, WFDEI, and HySN but not in VFDv1 and VFDv2 (−0.12) or PGMFDv2 (−0.05). The summer and winter distributions of clearness index at the stations considered are depicted in Fig. 8. It is evident that PGMFDv2 spans a much smaller range of transmissivity than observed in both summer and winter and that the VIC type estimates have a bias towards low estimates and show less variability than observed in winter.

Since both WFDEI and HySN are based on ERA-Interim, and ERA-Interim shows overestimations of SW↓ in summer, where observations were available, the differences in estimated SW↓ in ERA-Interim and the observations were inspected for dependencies on differences in modeled and observed cloud cover, near-surface humidity, and snow cover using regression. The results varied with both season and location but for the aggregated data significant dependence on differences in observed and modeled 2 m humidity and snow cover was found (with higher snow cover in the model associated with higher SW↓ estimates in the model), and in the warm season larger overestimations were seen in ERA-Interim when the model produced high clouds.

6.3 Incident longwave radiation (LW↓)

Only two stations have LW↓ observations available during the validation period, Bergen-GFI (western Norway) and Trondheim-Voll (central Norway); both are located near the coast (see Fig. 1 and the Supplement). More than 17 years of daily measurements are available from the Bergen-GFI station, while at Trondheim-Voll only about 2 years of observations are available.

6.3.1 Vertical gradients in LW↓

Since only two stations have longwave observations, no altitudinal gradient can be inferred from the observations; instead altitudinal gradients are taken from ERA-Interim. The previous comparison of altitudinal gradients within the observations and models has shown that ERA-Interim has similar altitudinal gradients to the observations. Further, ERA-Interim has not previously been vertically adjusted. The vertical gradients found ranged from $-4.0\,\mathrm{W\,m^{-2}}$ per 100 m in December to $-0.6\,\mathrm{W\,m^{-2}}$ per 100 m in June, were weakened by $0.20\,\mathrm{W\,m^{-2}}$ per 100 m for every 10 km away from the coast, and strengthened by $0.23\,\mathrm{W\,m^{-2}}$ per 100 m for every latitude north of 57° N. On average the vertical gradients were around $-4.5\,\mathrm{W\,m^{-2}}$ per 100 m in winter and $-1.8\,\mathrm{W\,m^{-2}}$ per 100 m in summer. The gradients were temporally interpolated to day-of-year values and applied to the models in order to adjust the estimates to the altitude of the two observational stations. The largest change in the estimates due to altitudinal adjustment is an average increase of $8.6\,\mathrm{W\,m^{-2}}$ for MERRA2 when adjusted to the 278 m lower altitude of Bergen station compared to MERRA2's grid cell altitude.

6.3.2 Differences of the LW↓ estimates to station observations

Figure 3c depicts the mean monthly LW↓ at the two stations. Summary statistics for the LW↓ estimates after adjustment to station altitude are also presented in Table 5. At the two stations all models except WFDEI estimate lower values than observed in all months. WFDEI, however, estimates on average 10–15 $\mathrm{W\,m^{-2}}$ more LW↓ than is observed from October through January. The largest absolute differences are found in MERRA2, where LW↓ is underestimated at $8\,\mathrm{W\,m^{-2}}$ in winter and at $25\,\mathrm{W\,m^{-2}}$ midsummer. The remaining models estimate 11 to $17\,\mathrm{W\,m^{-2}}$ less LW↓ than observed in summer, and show smaller underestimations in winter.

The skill of the model estimates in capturing the day-to-day variability in LW↓ is visualized in Fig. 5c, indicating the correlation and normalized standard deviation of the de-seasonalized time series. The estimates based on newer reanalysis data, MERRA2, ERA-Interim, WFDEI, and HySN have anomaly correlation coefficients around 0.8, while PGMFDv2, VFDv1, and VFDv2 have lower ACCs (46 %–60 %).

Table 5. As in Table 3 but with metrics listed for LW↓. Except for ACC and KS, which are dimensionless, the units are in $W m^{-2}$.

Model	Δ	$\lvert\Delta\rvert$	$\lvert\delta\rvert_{max}$	$\lvert\delta^s\rvert_{max}$	ACC	K-S
MERRA2	−14	14	−20	−24	0.81	0/2
ERA-Interim	−8	8	−13	−14	0.79	**1/2**
PGMFDv2	−10	10	−12	−16	0.46	0/2
WFDEI	**6**	**6**	**11**	**12**	0.82	**1/2**
VFDv1	−9	9	−11	−15	0.51	0/2
VFDv2	−15	15	−17	−21	0.60	0/2
HySN	−11	11	−15	−17	**0.84**	0/2

6.3.3 Air mass type sensitivity of LW↓ deviations

Figure 7c depicts the differences between the model's LW↓ estimates and the observed values at Bergen and Trondheim stations, grouped according to the daily weather type (classified at Flesland and Ørlandet stations). On days classified with moist or transitional weather types, all models except WFDEI underestimate LW↓. PGMFDv2, VFDv1, and VFDv2 clearly have weather-type-dependent deviations from the observations, with underestimations in moist weather types and smaller underestimations or even overestimations compared to the observations in dry weather types. The MERRA2, ERA-Interim, WFDEI, and HySN estimates largely show similar differences to the observed values in all weather types. An additional comparison of the ERA-Interim estimates at Bergen, where cloud observations are available, showed no difference in average deviation in the estimates of incident longwave radiation on common clear-sky days compared to the remaining days (not shown). The lower estimates of incident longwave radiation in ERA-Interim are thus not likely to be primarily related to differences in cloud properties.

6.4 Modeled and observed trends in near-surface humidity, SW↓, and LW↓ from 1985 to 1999

January 1985 is considered to be the start of the brightening period in Europe after a period of SW↓ dimming due to aerosol emissions (see, e.g., Wild et al., 2005). In the following, where available, observations and co-located model estimates are inspected for trends in near-surface humidity, SW↓, and LW↓ from 1985 to 1999.

After screening the observational time series 59 humidity stations are grouped into five geographical regions (southwest (S_W), southeast (S_E), central (C), northwest (N_W), and northeast (N_E); see Sect. 5). Table 6 lists the results of the trend tests for each calendar month and region, listing only the Sen slope if the Mann–Kendall trend test is significant at a 5 % or 10 % level, with the latter denoted in italics. In all regions except the northeastern part of Norway significant increases in observed T_d occurred in September from 1985 to 1999. The observations further show an increase in T_d in April in southern Norway, an increase July in the northeastern part of Norway, and a decrease in May T_d in central Norway. For southern and central Norway all of the models capture the increase in September T_d. The models reproduce the observed trends in spring and in northern Norway to a lesser degree.

Bergen is the only location in Norway where long-term records of incident shortwave or longwave radiation are available with little missing data within the time range. Between January 1985 and December 1999, observations from the University in Bergen show trends in annual SW↓ of $1.7 W m^{-2}$ per decade ($p < 0.1$), while LW↓ decreases with $-8.4 W m^{-2}$ per decade ($p < 0.001$). At the nearly co-located measurement station of the Norwegian Meteorological Institute, at Bergen-Florida, annual dew point temperature has a trend of 1.2 °C per decade ($p < 0.0001$).

In individual calendar months larger trends were found. Observed August mean SW↓ increased with $51 W m^{-2}$ per decade (Table 7). The observations also show modest, but significant, increases in October and December. Apart from WFDEI and VFDv1, which show no significant SW↓ trends, the models reproduce a significant increase in SW↓ in August, and no models show trends of the opposite sign during the time period considered.

Monthly mean LW↓ in Bergen shows a significant decrease during several months of the year: the largest is found in May, with $-21 W m^{-2}$per decade (Table 8). In August, October, and December, months when concurrent increases in shortwave radiation were found (Table 7), the observations show significant decreases in incident longwave radiation. None of the models show equally strong negative trends in monthly mean LW↓ in their corresponding grid cells. MERRA2 and ERA-Interim show no significant trends during the time period, whereas PGMFDv2, WFDEI, and HySN exhibit one single month with a negative trend. Meanwhile, VFDv1 and VFDv2 show weakly positive trends in September. The increasing trend in incident longwave radiation in September in the VIC type estimates may be related to the concurrent increase in humidity. All the models also show an increasing trend in humidity in the grid cell covering Bergen in September; however, the models generally show weaker trends than observed at Bergen-Florida station (see Table 9).

7 Discussion

Historical estimates of humidity and incident shortwave and longwave radiation have been compared to station observations from mainland Norway from 1982 through 1999. A total of 84 stations provide vapor pressure (VP) observations, 9 stations provided SW↓ observations, while only 2 stations provided LW↓ observations. The estimates evaluated are from two reanalysis data sets, MERRA2 and ERA-Interim; three data sets composed of reanalysis data blended with gridded observational data, PGMFDv2, WFDEI, and HySN; and two versions of the VIC type forcing data, es-

Table 6. Linear, decadal trends in monthly mean T_d (°C) between 1985 and 1999, significant at a 5 % or 10 % (denoted in italics) level in the observations (O) and the model estimates, listed with the month and region denoted on the left (month, region).

	O	M	E	P	W	V	V2	H
Apr, S_W	*1.7*							
Apr, S_E	*2.2*							
May, S_W		*–1.2*		*–1.5*				*–1.1*
May, S_E				−1.8				
May, C	*–1.3*	−1.2	−1.4	−1.3	*–1.3*			−1.5
May, N_E		*–0.9*						
Jul, N_E	1.6							
Aug, S_W		*1.1*				*1.0*		
Aug, S_E						*1.6*		
Sep, S_W	2.7	2.0	2.4	2.3	2.3	2.6	2.4	*2.2*
Sep, S_E	3.0	2.6	3.0	2.3	3.0	3.2	2.9	3.3
Sep, C	2.1	1.9	1.9		1.8	2.3	*1.9*	2.0
Sep, N_W	*1.8*	*1.6*				*1.6*		
Oct, C				*–1.6*				

Table 7. Linear, decadal changes in monthly mean SW↓ ($W m^{-2}$) at Bergen between January 1985 and December 1999, significant at a 5 % or 10 % (denoted in italics) level.

	O	M	E	P	W	V1	V2	H
Jan				1				
Aug	51	26	47	42			*25*	46
Sep			24	*15*				23
Oct	7			7				
Nov			3					
Dec	1	*1*	2			*1*		

Table 8. Linear, decadal changes in monthly mean LW↓ ($W m^{-2}$) at Bergen between January 1985 and December 1999 significant at a 5 % or 10 % (denoted in italics) level.

	O	M	E	P	W	V	V2	H
Apr						8		
May	−21			*–12*				
Aug	−13				−12			*–11*
Sep						*14*	*14*	
Oct	*–17*							
Dec	−17							

timates based on gridded observational data combined with empirical algorithms.

Differences between the estimates and observations are not necessarily due to errors in the estimates, as a vertical adjustment to station altitude is not a sufficient reason to require that the model grid cell estimates should equate to the observed values. The numerical model estimates may still differ from the observations for valid reasons, such as differences in snow cover, differences in land cover type (the observations are from sensors usually located over grass or, in some cases, on top of buildings), and the averaging out of sub-grid variability in the models (see, e.g., Göber et al., 2008). The uncertainty in the observations may also contribute to the differences. However, large differences may suggest biases in the estimates.

Table 9. Linear, decadal changes in monthly mean T_d (°C) for Bergen-Florida station and for the co-located grid cells of the model estimates between January 1985 and December 1999, significant at a 5 % or 10 % (italics) level.

	O	M	E	P	W	V1	V2	H
Apr	2.0					*1.2*	*0.9*	
May		*–1.3*	−1.4					−1.4
Jul	1.7							
Aug	1.9							
Sep	3.2	2.3		2.3	2.1	3.1	2.6	2.2

7.1 Vertical gradients

Significant vertical gradients were found for humidity, incident shortwave, and incident longwave radiation, justifying an altitudinal adjustment to station altitude before comparison of the model estimates with the station observations ($\mathcal{H}_a$). The altitudinal vapor pressure gradients found here were on average −0.25 hPa per 100 m in winter and −0.34 hPa per 100 m in summer. The summer gradient is similar to what Marty (2000) found in the Alps in summer, −0.35 hPa per 100 m; however, the winter gradient is considerably higher than found in the Alps (−0.14 hPa per 100 m). The impact of adjustment to station height was small for the estimates with a finer spatial scale, only a 0.06 °C change in T_d on average, while for the coarser-scale esti-

mates, MERRA2, ERA-Interim, PGMFDv2, and WFDEI, the impact of the vertical adjustment was considerably larger, resulting in an average 1 °C increase in T_d. The WFDEI and PGMFDv2 showed weaker vertical humidity gradients than observed. This may be a result of the interpolation techniques employed in the CRU T_2 data set used to bias-correct and downscale both the ERA-Interim and NCEP-NCAR Reanalysis, or due to the use of a constant temperature lapse rate of 6.5 °C when interpolating the temperature of the two reanalyses to the CRU orography. Notably, the vertical gradients in near-surface humidity in MERRA2, a reanalysis where surface observations are not assimilated (see Table 1), are similar to the vertical gradients found in the observations and those found in ERA-Interim.

Observed SW↓ in the form of clearness index (CI; see Sect. 5) showed the highest altitudinal gradient in winter, a slightly lower gradient in spring, and rather low gradient in summer and fall. The vertical gradients found are larger than the gradient of 0.00295 per 100 m used in the implementation of the Bristow and Campbell (1984) algorithm in historical versions of the VIC preprocessor (MTCLIM versions before 4.2, before the Thornton and Running, 1999, algorithm was implemented). Though the CI gradient is stronger in winter, the considerably smaller amount of SW↓ received leads to a weaker gradient in SW↓. The CI gradients translates to SW↓ gradients of about 0.3 $W m^{-2}$ per 100 m in fall and winter, 1.6 $W m^{-2}$ per 100 m in spring, and 1.2 $W m^{-2}$ per 100 m in summer. Marty (2000) found all-sky gradients in SW↓ in the Alps of 1.1 $W m^{-2}$ per 100 m in winter and 0.7 $W m^{-2}$ per 100 m in summer. The differences between the gradients found here and those given in Marty (2000) may likely be explained by the differences in the received extraterrestrial radiation and differences in cloud and snow cover climatology. The models largely showed similar vertical CI gradients to the observations. The exceptions were PGFMDv2 and VFDv1; PGMFDv2 showed significantly ($p < 0.01$) weaker vertical gradients with a weaker seasonality, and VFDv1 produced a stronger vertical CI gradient in summer than in winter. The adjustment of the coarser-scale estimates resulted, on average, in a 5 times larger change in SW↓ for the coarse-scale estimates than the finer-scale estimates. The regression-based vertical adjustment produced similar SW↓ estimates for ERA-Interim and the HySN estimates.

Since two LW↓ stations located more than 400 km apart could not provide an observation-based vertical gradient in LW↓, ERA-Interim was consulted instead. The gradients were, on average, −4.5 $W m^{-2}$ per 100 m in winter and −1.8 $W m^{-2}$ per 100 m in summer. Marty (2000) found vertical gradients in incident longwave radiation of −2.8 $W m^{-2}$ per 100 m in winter and −3.1 $W m^{-2}$ per 100 m in summer for the Alps and of −4.1 $W m^{-2}$ per 100 m in winter and −2.6 $W m^{-2}$ per 100 m in summer, when considering a subset of observation stations in Switzerland. The different vertical gradients found may be explained by differences in temperature and humidity gradients, different climatological distributions of clouds, and the difference in initial temperature, as LW↓ is a function of temperature to the power of 4. The regression-based vertical adjustment of ERA-Interim LW↓ estimates resulted in a larger correction of LW↓ than the clear-sky adjustment implemented in HySN, alluding to the fact that the clear-sky altitudinal adjustment implemented in similar data products might be too low, especially for locations with a maritime climate, like Bergen.

7.2 Differences to station observations

7.2.1 Humidity estimates

The empirically based model estimates, VFDv1 and VFDv2, show, on average, slightly lower estimates of humidity than observed. Both VFD type estimates are found to show a 50 % stronger decrease in humidity with continentality than the observations (see Sect. 6.1.3). The modified version of the Magnus type formula, based on Kimball et al. (1997), used in MTCLIM to generate the VFD humidity estimates is likely not appropriate for Norway. Previous studies, e.g., in the development of gridded climate variables by New et al. (1999) and in the application of the MTCLIM model over complex terrain in Australia (Thornton et al., 2000) and in the western US (Pierce et al., 2013), found that the Kimball et al. (1997) method did not result in overall improved humidity estimates. Indeed, in Kimball et al. (1997) the method is found to give improved estimates of humidity in locations where the ratio of potential evaporation to annual precipitation is larger than 2.5. In most regions of Norway this ratio is well below unity. The more conventional method of using daily minimum temperature as a proxy for dew point temperature will likely give relatively small overestimations of humidity compared to the underestimations resulting from using the Kimball et al. (1997) method.

The reanalysis-based estimates all overestimate humidity, and the overestimations are generally higher in weather types classified as dry according to the methodology of Bower et al. (2007). MERRA2 and PGFMDv2 particularly overestimate humidity in dry conditions. The same two models also show a significantly stronger decrease in humidity with latitude than observed. MERRA2 also shows a weaker decrease in humidity with continentality. The weaker decrease in humidity with continentality seen in MERRA2 may perhaps be partly explained by the model's coarse resolution and land mask (see Fig. 1), and MERRA2's exaggerated latitudinal gradient in humidity in Norway may perhaps be associated with MERRA2's larger latitudinal gradient in SW↓.

The humidity estimates from HySN match the observations best, considering all metrics except from the anomaly correlation coefficient (ACC). The ACC of ERA-Interim estimates is marginally higher (0.02) than in HySN. This is likely due to the capping of relative humidity at 100 % when applying the SeNorge2 temperature in the development of HySN. Combining the methods outlined in Cosgrove (2003),

which for humidity relies on the assumption of constant relative humidity with altitude, a high-quality reanalysis data set (ERA-Interim), and a high-resolution, national, observation-based temperature data set is found to provide high-quality daily estimates of humidity in the current study region. The coarser, reanalysis-based data sets generally show higher ACCs than the VFD estimates. Numerical weather prediction (NWP) models are skilled at capturing synoptic events, i.e., weather or climatological patterns on a spatial order of 1000 km, and a temporal order of days or weeks, such as cold air outbreaks and the changing sources of air masses during the passage of warm and cold fronts. Though the NWPs may have systematic biases and a much lower spatial resolution than empirically based estimates, it is not surprising that they are useful in representing daily weather variability.

7.2.2 Incident shortwave radiation

Shortwave incident radiation is, on average, overestimated for all model estimates except VFDv1. HySN, ERA-Interim, and WFDEI vary in obtaining the highest ranking depending on the metric considered. For instance, WFDEI shows a slightly lower average deviation from the observations than ERA-Interim and HySN. On the other hand, WFDEI shows larger underestimations in dry weather types than ERA-Interim and HySN (Fig. 7). Overall, the three models provide vertically adjusted estimates of incident SW↓ close to the observations, with average deviations from station measurements below $4\,\mathrm{W\,m^{-2}}$ and ACCs above 0.76.

The average difference between the ERA-Interim estimates and the observations is smaller than in Urraca et al. (2018), where an average overestimation of $12\,\mathrm{W\,m^{-2}}$ was found when comparing ERA-Interim SW↓ estimates to station measurements in Europe between 2010 and 2014. The smaller difference seen in the current study may in part be explained by the relatively small amount of solar radiation reaching Norway, the different time periods considered, and the vertical adjustment included in the current study. Urraca et al. (2018) also found that MERRA2 shows poorer results than ERA-Interim, with average overestimations of $18\,\mathrm{W\,m^{-2}}$. This is consistent with our findings, where MERRA2 has the highest mean deviation from the observations of any of the considered estimates. Overestimations of incident shortwave radiation over land are not only an issue of reanalysis data sets covering Europe but have been a long-standing issue in global (Wild et al., 2015) and regional climate models (Katragkou et al., 2015; Jerez et al., 2015).

Two versions of VIC type forcing data are evaluated in the current study. The two versions differ in their input data and in the version of VIC preprocessor used. The oldest version of the VFD data sets is partly based on a 11 km national reanalysis (NORA10) to provide maximum and minimum temperature. The older version showed large underestimations of incident shortwave radiation at several stations, particularly near the coast in northern Norway (Fig. 4). These findings are in line with Bohn et al. (2013), where the MTCLIM algorithms were found to underestimate incident SW↓ radiation by 26 %, on average, at coastal sites. The MTCLIM algorithms implemented in VFD rely in part on the diurnal temperature range to estimate cloud cover, using a low range as an indication of cloud cover. Near the coast, the diurnal temperature range may be low due to the moderating influence of the nearby ocean, due to its high heat capacity. The more recently compiled version of VFD data, VFDv2, which is based on a newly developed, high-resolution gridded data set of T_{min} and T_{max}, does not show similar underestimations near the coast of northern Norway. The different estimates produced indicate that great care must be taken to make sure the VIC style forcing data have consistent input data and algorithm versions if the data are used in, for example, climate change impact studies.

The newer and higher-resolution input data used in VFDv2 did not result in a lower mean absolute station deviation, as its SW↓ estimates were consistently overestimated. Both VFD versions show a much stronger latitudinal gradient than observed and a too strong altitudinal gradient in summer. The latter finding is in line with Mizukami et al. (2014), where VFD type estimates for the Colorado River basin showed increasing overestimations of SW↓ with increasing altitude. The exaggerated latitudinal gradient in SW↓ may be connected to the use of the diurnal temperature range in the algorithm. Bohn et al. (2013) found that the relationship between cloud cover and the diurnal temperature range breaks down for ranges below 5 °C. Further, New et al. (1999) states that the relationship between diurnal temperature range and cloud cover is weak at around 60° N in winter and, further, becomes positive in the Arctic.

Binning the estimates according to air mass type shows that the PGFv2 and VIC type estimates show less sensitivity to the prevailing weather type than the observations. The observations and the remaining model estimates show a decrease in clearness index of about 0.22 on days classified as moist or transitional weather types rather than dry, while the VIC type estimates and PGFv2 show reductions of 0.12 and 0.05, respectively. On average, the VIC type estimates and PGFv2 underestimate incident radiation in dry weather types (see Fig. 7). The similarity between the PGMFDv2 and VFD estimates of SW↓ may be explained by the fact that the PGMFD SW↓ is bias-corrected based on gridded cloud cover from CRU using the Thornton and Running (1999) relationship between SW↓ and cloud cover, which is also used in VFD. Further, the gridded CRU cloud cover data set is a secondary or derived observational data set, which is, similar to VFD, in part based on regression using diurnal temperature range as a predictor (New et al., 1999). The lower sensitivity to air mass type found in PGMFDv2 and the VIC type forcing data might contribute to the lower ACC found for these estimates.

7.2.3 Incident longwave radiation

The evaluation of incident longwave radiation is compromised by the lack of observational data. Only two sites observe incident longwave radiation in the considered time period. The difference between the annual mean of the model estimates and observations are for the two stations considered larger for incident longwave radiation than for incident shortwave radiation. The annual deviations ranges from -16 to $+7\,\mathrm{W\,m^{-2}}$. Underestimations of monthly means are found throughout the year for all models except WFDEI. The deviations from the station observations for WFDEI, MERRA2, ERA-Interim, and HySN are largely similar in all weather types; i.e., the underestimations are also found on days classified with dry weather types. An additional evaluation of the ERA-Interim LW estimates for Bergen, where cloud observations are available, showed that the deviations from station observations were similar on days where clouds were present in the observations, the model, and the remaining days.

While overestimation of incident shortwave radiation has been a long-standing issue in many climate models and reanalyses, incident longwave radiation is typically underestimated (Katragkou et al., 2015; Li et al., 2016; Zib et al., 2012; Wild et al., 2017). The causes of the underestimation are, however, debated. Li et al. (2016) points to an improper representation of interactions between radiation and suspended frozen water particles in the atmosphere (solid hydrometeors) as a culprit, while Zib et al. (2012) speculate that errors in simulated aerosols, water vapor content, and cloud properties (rather than cloud amounts) are the cause. Local issues such as longwave emissions from nearby terrain may also contribute to the deviations (Rontu et al., 2016). Lastly, observational uncertainty confounds the picture further, particularly given that the two sensors were unshaded.

The anomaly correlation coefficients are, as also seen for humidity and incident shortwave radiation, considerably lower for PGFMDv2 and the VFD estimates than the estimates based on newer reanalysis data (0.46–0.60 vs. 0.79–0.82). This may be caused by the representation of clouds in the models. As discussed for the PGFMDv2 and the VFD SW↓ estimates, the use of diurnal temperature range as a proxy for cloud cover may not be suitable for the current maritime, high-latitude study region.

7.3 Trends

The analysis of observed humidity trends from 1985 to 1999 showed significant increases in April in southern Norway, a decrease in May in central regions of Norway, significant increases in July in the northeastern part of Norway, and increases in all regions except the northeastern part of Norway in September. All the data sets, both the reanalysis-based estimates and the more empirically based VFD estimates, capture the increase in humidity seen in September. The significant increases found in humidity when averaging over the stations in southeastern and southwestern Norway in April are not seen in any of the models. The VFD estimates do, however, capture some of the increases in humidity that were seen in the measurements from Bergen-Florida (Table 9). A recent study by Nilsen et al. (2017) found that changes in large-scale weather patterns can, in part, explain the significant increases in 2 m temperature between 1981 and 2010 seen in Scandinavia in September but not most of the increases seen in April. Another inquiry by Rizzi et al. (2017) found that the increasing temperature trends seen in May in many parts of Norway showed a strong correlation with a concurrent decrease in snow cover. The decline in snow cover in May found in Rizzi et al. (2017) was particularly strong in low-lying areas. If the changes in temperature and humidity are connected to local changes in snow cover, it is possible that the coarser-scale reanalysis data, which often have a mean grid cell altitude above the measurement station elevation, do not capture the measured changes.

Surface incident radiation was inspected for trends from 1985 to 1999 at the one station where measurements are available in the time period with little missing data: Bergen. A hardly significant ($p < 0.1$) annual trend in SW↓ was found in the observations, $1.7\,\mathrm{W\,m^{-2}}$ per decade. However, in individual calendar months larger trends were found. The largest trend, $51\,\mathrm{W\,m^{-2}}$ per decade, was found in the observations in May. The observed August trend was reproduced fairly well in ERA-Interim, PGMFDv2, and HySN, and a weaker but still significant trend was seen in MERRA2 and VFDv2. While ERA-Interim largely reproduces the trend, WFDEI shows no significant trends. For the considered location, the post-processing of ERA-Interim radiances, based on CRU cloud cover and interannual aerosol loading conducted in the production of WFDEI, has a negative effect on its ability to reproduce the observed trend. The clear-sky type post-processing of ERA-Interim implemented in HySN estimates left the trend close to its original value. The two versions of VFD also differed in their ability to capture the SW↓ trend. This might be due to the maritime location of Bergen and coarser VFDv1 input data for T_{min} and T_{max}. A previous study by Parding et al. (2016) showed that circulation type changes could account for a large part of the dimming that was observed in Bergen before around 1980 but a lesser fraction of the subsequent brightening. The fact that ERA-Interim, which does not explicitly account for interannual aerosol changes, picks up the trend while WFDEI, where a correction for interannual aerosol loading has been applied does not, implies that a considerable part of the trend before 2000 must be included in the indirect effects of aerosol changes, which ERA-Interim assimilates, or other factors. On the other hand, MERRA2 accounts for interannual aerosol loading in the time period considered and captures a positive, albeit weaker trend in S_W.

The annual trends in LW↓ during the same period in Bergen were larger in magnitude than those found for SW↓, $-8.4\,\mathrm{W\,m^{-2}}$ per decade. The observed trend in any calen-

dar month was larger for SW↓, while the LW↓ trend showed more consistency throughout the year. More of the models reproduced the SW↓ trend than the LW↓ trend. Both versions of the VIC type forcing data, VFDv1 and VFDv2, simulated a weak increasing trend in September. Given that the VFD estimates did not produce changes in SW↓ in the same month, the increase is likely due to the clear-sky parametrization and the concurrent simulated increase in September T_d. WFDEI and HySN reproduce the decrease in LW↓ seen in August, while ERA-Interim does not. This points to the fact that changes in near-surface temperature, which are used as a scaling factor and to adjust near-surface humidity in WFDEI and HySN, capture the signal that contributes to the decrease in LW↓. A larger sample of stations measuring incident radiation with a high quality is needed to evaluate how well the models capture trends within the region, particularly given the uncertainty in the observational data.

8 Code and data availability

The HySN data product is available archived in Zenodo (https://doi.org/10.5281/zenodo.1970170, Erlandsen, 2018a). The code used to produce the HySN estimates is written in Python and is available at https://github.com/helene-b-e/HySN.git (last access: 10 June 2019). Further, the particular version of the software code used to produce the HySN estimates validated here is archived in Zenodo (https://doi.org/10.5281/zenodo.1435555, Erlandsen, 2018b). The remaining data sets are available from the various named data providers.

9 Conclusions

Hydrological, ecological, and crop modellers seek landscape-scale data. Norway has a long coastline with mountains, fjords, and small islands. Strong land–sea contrast, high mountains, and a seasonal snow cover that is highly dependent on continentality and altitude results in a fine-scale variability difficult for coarse-scale models to represent. A Python script to downscale and consolidate reanalysis data with high-resolution national gridded temperature data has been developed, which, leaning on previously well-tested empirical relationships, provides estimates of humidity and incident radiation on a fine-scale grid. The downscaled humidity ensures that relative humidity is constrained at 100 %, so that, for example, reasonable evaporation estimates can be sought. The new estimates, HySN, provide humidity estimates with the overall highest quality given for the metrics considered here, also surpassing those based on estimating humidity from temperature alone, such as for the VIC type forcing data. The new estimates outperform the VIC type forcing data and the MERRA2 estimates of incident radiation; however, it is not clear that the new estimates have an added value compared to ERA-Interim and WFDEI. The lack of high-quality historical observations, particularly of incident longwave radiation, hinders a proper evaluation of the data sets.

- Additionally, this study has shown that ($\mathcal{H}_a$) altitude is a significant predictor of humidity, SW↓, and LW↓ in the domain. The coarse-scale estimates of T_d increased on average by 1 °C, SW↓ by 0.7–1.5 W m^{-2}, and LW↓ increased by as much as 8.6 W m^{-2}, when adjusted to station altitude.

- Further, the results have shown that a high resolution does not necessarily indicate high-quality estimates. The added value of the high horizontal resolution of the more empirically based estimates does not outweigh the added value of relying on estimates from coarser-resolution numerical weather prediction reanalyses ($\mathcal{H}_b$). Not only is a higher daily temporal correlation (ACC) seen in the estimates based on newer reanalysis data compared to the VIC type forcing data but also a lower mean absolute station bias is seen for several reanalysis-based products (ERA, WFDEI, HySN). VFDv1 and VFDv2 show a 60 % stronger decrease in humidity with distance from the coast than the observations, alluding to the fact that the modified version of the Magnus type formula based on Kimball et al. (1997), implemented in VFD to estimate humidity from daily minimum temperature, is not appropriate for the Norwegian domain. Both VFDv1 and VFDv2 also show a decrease that is several times stronger in solar radiation with latitude than the observations, likely a result of using diurnal temperature range as a proxy for cloud cover, an assumption likely not appropriate in coastal environments and at high latitudes.

To our knowledge reanalysis-based estimates have not been compared with VIC type forcing data for regions within Europe (or Norway specifically). The comparison of model estimates may assist impact modellers that have not yet selected data to use. Some of the findings might help explain persistent errors, for instance found in the timing of snowmelt in a hydrological model. The findings provide emphasis for climate researchers to not only downscale T_2 and precipitation from climate projections, and later use these to estimate humidity and incident radiation, but to utilize the climate model estimates of near-surface humidity and incident radiation. This is already done, for example, in Teklesadik et al. (2017), where the impact of climate change on surface hydrology is examined based on, depending on the hydrological model's structure, bias-corrected climate model output of precipitation, temperature, humidity, and incident radiation from the ISI-MIP project (Hempel et al., 2013). Similarly, we envisage that further work would involve applying the HySN as an input to a hydrological model. Such a model exercise would imply modulating the model's code to accommodate humidity and radiation as input variables.

Once the model includes more physically based parameterizations, the sensitivity in simulated runoff to the choice of forcing data can be assessed, including the impact of errors or perturbations in each of the forcing data variables.

The source code for computing HySN has been made available and may easily be configured to use other reanalysis data or other national data sets as input. The compilation of HySN requires merely half a day on a modern desktop computer. Part of the code might also be implemented in a model preprocessor or in the calculation of various indices, so that the variables do not need to be stored for long time spans. Future work entails calculating indices, such as reference evaporation, and updating the input data to ERA5 and a new version of SeNorge once the full historical time series of the two are available. Additionally, sub-daily estimates, the inclusion of terrain features such as slope and aspect, and adding a correction based on the lack of coupling between the land surface and the atmosphere at times when the differences in the local snow cover and snow cover modeled by the reanalysis are large might be promising, as initial results showed that differences in ground snow conditions between the reanalysis and the observations were significant in predicting the difference between ERA-Interim estimates of SW↓ and the observations.

Supplement. The supplement related to this article is available online at: https://doi.org/10.5194/essd-11-797-2019-supplement.

Author contributions. All authors discussed the results and contributed to the manuscript. HBE derived the HySN data set, acquired and quality-controlled data from external sources, analyzed the results, and drafted the manuscript.

Competing interests. The authors declare that they have no conflict of interest.

Acknowledgements. We would like to thank Sigbjørn Grini for providing the scripts for quality control of the SW↓. We further thank all data providers: MET Norway, NIBIO, UiB (where radiation measurements were provided by Jan Asle Olseth), NASA, and ECMWF. We also thank Ingjerd Haddeland, Jan Magnusson, and Shaochun Huang for compiling the VIC forcing data while working at NVE. The PGMFDv2 was downloaded from the ISI-MIP node of the ESGF server (https://esg.pik-potsdam.de/projects/isimip/, last access: 10 June 2019). The study forms a contribution to LATICE, which is a strategic research area founded by the Faculty of Mathematics and Natural Sciences at the University of Oslo. Helene Birkelund Erlandsen was funded by NVE.

Financial support. This research has been supported by the Norwegian Water Resources and Energy Directorate (grant no. 81077).

Review statement. This paper was edited by Thomas Blunier and reviewed by Graham Weedon and Emma Robinson.

References

Abatzoglou, J. T.: Development of gridded surface meteorological data for ecological applications and modelling, Int. J. Climatol., 33, 121–131, https://doi.org/10.1002/joc.3413, 2013.

Almeida, A. C. and Landsberg, J. J.: Evaluating methods of estimating global radiation and vapor pressure deficit using a dense network of automatic weather stations in coastal Brazil, Agr. Forest Meteorol., 118, 237–250, https://doi.org/10.1016/S0168-1923(03)00122-9, 2003.

Bohn, T. J., Livneh, B., Oyler, J. W., Running, S. W., Nijssen, B., and Lettenmaier, D. P.: Global evaluation of MTCLIM and related algorithms for forcing of ecological and hydrological models, Agr. Forest Meteorol., 176, 38–49, https://doi.org/10.1016/j.agrformet.2013.03.003, 2013.

Bosilovich, M. G., Akella, S., Coy, L., Cullather, R., Draper, C., Gelaro, R., Kovach, R., Liu, Q., Molod, A., Norris, P., Wargan, K., Chao, W., Reichle, R., Takacs, L., Vikhliaev, Y., Bloom, S., Collow, A., Firth, S., Labow, G., Partyka, G., Pawson, S., Reale, O., Schubert, S. D., and Suarez, M.: MERRA-2: Initial evaluation of the climate Technical Report Series on Global Modeling and Data Assimilation, Tech. rep., NASA/TM–2015-104606, 2015.

Bosilovich, M. G., Robertson, F. R., Takacs, L., Molod, A., and Mocko, D.: Atmospheric water balance and variability in the MERRA-2 reanalysis, J. Climate, 30, 1177–1196, https://doi.org/10.1175/JCLI-D-16-0338.1, 2017.

Bower, D., McGregor, G. R., Hannah, D. M., and Sheridan, S. C.: Development of a spatial synoptic classification scheme for western Europe, Int. J. Climatol., 27, 2017–2040, https://doi.org/10.1002/joc.1501, 2007.

Bras, R. L.: Hydrology: an introduction to hydrologic science, Addison Wesley Publishing Company, 1990.

Brinckmann, S., Krähenmann, S., and Bissolli, P.: High-resolution daily gridded data sets of air temperature and wind speed for Europe, Earth Syst. Sci. Data, 8, 491–516, https://doi.org/10.5194/essd-8-491-2016, 2016.

Bristow, K. L. and Campbell, G. S.: On the relationship between incoming solar radiation and daily maximum and minimum temperature, Agr. Forest Meteorol., 31, 159–166, https://doi.org/10.1016/0168-1923(84)90017-0, 1984.

Bromwich, D. H., Wilson, A. B., Bai, L. S., Moore, G. W., and Bauer, P.: A comparison of the regional Arctic System Reanalysis and the global ERA-Interim Reanalysis for the Arctic, Q. J. Roy. Meteor. Soc., 142, 644–658, https://doi.org/10.1002/qj.2527, 2016.

Bugmann, H., Cordonnier, T., Truhetz, H., and Lexer, M. J.: Impacts of business-as-usual management on ecosystem services in European mountain ranges under climate change, Reg. Environ. Change, 17, 3–16, https://doi.org/10.1007/s10113-016-1074-4, 2017.

Bureau of Reclamation: Downscaled CMIP3 an CMIP5 Climate and Hydrology Projections: Release of Downscaled CMIP5 Climate Projections, Comparison with preceding Information, and Summary of User Needs. Prepared by the U.S. Department of the Interior, Bureau of Reclamation, Technic, Tech.

rep., available at: https://gdo-dcp.ucllnl.org/downscaled_cmip_projections/techmemo/BCSD5HydrologyMemo.pdf (last access: 10 June 2019), 2013.

Carrer, D., Lafont, S., Roujean, J.-L., Calvet, J.-C., Meurey, C., Le Moigne, P., and Trigo, I. F.: Incoming Solar and Infrared Radiation Derived from METEOSAT: Impact on the Modeled Land Water and Energy Budget over France, J. Hydrometeorol., 13, 504–520, https://doi.org/10.1175/JHM-D-11-059.1, 2012.

Cosgrove, B. A.: Real-time and retrospective forcing in the North American Land Data Assimilation System (NLDAS) project, J. Geophys. Res., 108, 8842, https://doi.org/10.1029/2002JD003118, 2003.

Deardorff, J. W.: Efficient prediction of ground surface temperature and moisture, with inclusion of a layer of vegetation, J. Geophys. Res., 83, 1889, https://doi.org/10.1029/JC083iC04p01889, 1978.

Decker, M., Brunke, M. A., Wang, Z., Sakaguchi, K., Zeng, X., and Bosilovich, M. G.: Evaluation of the reanalysis products from GSFC, NCEP, and ECMWF using flux tower observations, J. Climate, 25, 1916–1944, https://doi.org/10.1175/JCLI-D-11-00004.1, 2012.

Dee, D. P., Uppala, S. M., Simmons, A. J., Berrisford, P., Poli, P., Kobayashi, S., Andrae, U., Balmaseda, M. A., Balsamo, G., Bauer, P., Bechtold, P., Beljaars, A. C., van de Berg, L., Bidlot, J., Bormann, N., Delsol, C., Dragani, R., Fuentes, M., Geer, A. J., Haimberger, L., Healy, S. B., Hersbach, H., Hólm, E. V., Isaksen, L., Kållberg, P., Köhler, M., Matricardi, M., Mcnally, A. P., Monge-Sanz, B. M., Morcrette, J. J., Park, B. K., Peubey, C., de Rosnay, P., Tavolato, C., Thépaut, J. N., and Vitart, F.: The ERA-Interim reanalysis: Configuration and performance of the data assimilation system, Q. J. Roy. Meteor. Soc., 137, 553–597, https://doi.org/10.1002/qj.828, 2011.

de Oliveira, A. P., Soares, J., Božnar, M. Z., Mlakar, P., and Escobedo, J. F.: An application of neural network technique to correct the dome temperature effects on pyrgeometer measurements, J. Atmos. Ocean. Tech., 23, 80–89, https://doi.org/10.1175/JTECH1829.1, 2006.

Erlandsen, Helene B.: HySN Data set (Version v1.1) [Data set], Zenodo, https://doi.org/10.5281/zenodo.1970170, 2018a.

Erlandsen, Helene B.: helene-b-e/HySN: HySN v1.0 (Version v1.0), Zenodo, https://doi.org/10.5281/zenodo.1435555, 2018b.

Erlandsen, H. B., Haddeland, I., Tallaksen, L. M., and Kristiansen, J.: The Sensitivity of the Terrestrial Surface Energy and Water Balance Estimates in the WRF Model to Lower Surface Boundary Representations: A South Norway Case Study, J. Hydrometeorol., 18, 265–284, https://doi.org/10.1175/JHM-D-15-0146.1, 2017.

Feld, S. I., Cristea, N. C., and Lundquist, J. D.: Representing atmospheric moisture content along mountain slopes: Examination using distributed sensors in the Sierra Nevada, California, Water Resour. Res., 49, 4424–4441, https://doi.org/10.1002/wrcr.20318, 2013.

Göber, M., Zsótér, E., and Richardson, D. S.: Could a perfect model ever satisfy a naïve forecaster? On grid box mean versus point verification, Meteorol. Appl., 15, 359–365, https://doi.org/10.1002/met.78, 2008.

Godøy, Ø.: rtmrun, a Perl wrapper around libRadtran, available at: https://github.com/steingod/rtmrun (last access: 6 June 2019), 2013.

Grini, S.: Quality Control of Global Solar Irradiation Measured at Four Stations in Eastern Norway, PhD thesis, Norwegian University of Life Science, Ås, 2015.

Gutmann, E. D., Rasmussen, R. M., Liu, C., Ikeda, K., Gochis, D. J., Clark, M. P., Dudhia, J., and Thompson, G.: A comparison of statistical and dynamical downscaling of winter precipitation over complex terrain, J. Climate, 25, 262–281, https://doi.org/10.1175/2011JCLI4109.1, 2012.

Haddeland, I., Lettenmaier, D. P., and Skaugen, T.: Reconciling Simulated Moisture Fluxes Resulting from Alternate Hydrologic Model Time Steps and Energy Budget Closure Assumptions, J. Hydrometeorol., 7, 355–370, https://doi.org/10.1175/JHM496.1, 2006.

Haddeland, I., Heinke, J., Voß, F., Eisner, S., Chen, C., Hagemann, S., and Ludwig, F.: Effects of climate model radiation, humidity and wind estimates on hydrological simulations, Hydrol. Earth Syst. Sci., 16, 305–318, https://doi.org/10.5194/hess-16-305-2012, 2012.

Hanssen-Bauer, I., Drange, H., Førland, E., Roald, L. A., Børsheim, K. Y., Hisdal, H., Lawrence, D., Nesje, A., Sandven, S., Sorteberg, A., Sndby, S., Vasskog, K., and Ådlandsvik, B.: Klima i Norge 2100 Bakgrunnsmateriale til NOU Klimatilpasning (Climate in Norway 2100 background material for NOU climate adaptation), p. 148, 2009.

Hanssen-Bauer, I., Førland, E., Haddeland, I., Hisdal, H., Mayer, S., Nesje, A., Nilsen, J., Sandven, S., Sandø, A., Sorteberg, A., and Ådlandsvik, B.: Climate in Norway 2100 – a knowledge base for climate adaptation, Tech. rep., The Norwegian Centre for Climate Services (NCCS), available at: https://www.miljodirektoratet.no/globalassets/publikasjoner/m741/m741.pdf (last access: 10 June 2019), 2017.

Harpold, A. A., Kaplan, M. L., Klos, P. Z., Link, T., McNamara, J. P., Rajagopal, S., Schumer, R., and Steele, C. M.: Rain or snow: hydrologic processes, observations, prediction, and research needs, Hydrol. Earth Syst. Sci., 21, 1–22, https://doi.org/10.5194/hess-21-1-2017, 2017.

Heikkilä, U., Sandvik, A., and Sorteberg, A.: Dynamical downscaling of ERA-40 in complex terrain using the WRF regional climate model, Clim. Dynam., 37, 1551–1564, https://doi.org/10.1007/s00382-010-0928-6, 2011.

Hempel, S., Frieler, K., Warszawski, L., Schewe, J., and Piontek, F.: A trend-preserving bias correction – the ISI-MIP approach, Earth Syst. Dynam., 4, 219–236, https://doi.org/10.5194/esd-4-219-2013, 2013.

Hirsch, R. M., Slack, J. R., and Smith, R. A.: Techniques of trend analysis for monthly water quality data, Water Resour. Res., 18, 107–121, https://doi.org/10.1029/WR018i001p00107, 1982.

Hofstra, N., New, M., and McSweeney, C.: The influence of interpolation and station network density on the distributions and trends of climate variables in gridded daily data, Clim. Dynam., 35, 841–858, https://doi.org/10.1007/s00382-009-0698-1, 2010.

Jerez, S., Thais, F., Tobin, I., Wild, M., Colette, A., Yiou, P., and Vautard, R.: The CLIMIX model: A tool to create and evaluate spatially-resolved scenarios of photovoltaic and wind power development, Renew. Sust. Energ. Rev., 42, 1–15, https://doi.org/10.1016/j.rser.2014.09.041, 2015.

Kalkstein, L. S., Nichols, M. C., David Barthel, C., and Scott Greene, J.: A new spatial synoptic classification: Application to air-mass analysis, Int. J. Clima-

tol., 16, 983–1004, https://doi.org/10.1002/(SICI)1097-0088(199609)16:9<983::AID-JOC61>3.0.CO;2-N, 1996.

Katragkou, E., García-Díez, M., Vautard, R., Sobolowski, S., Zanis, P., Alexandri, G., Cardoso, R. M., Colette, A., Fernandez, J., Gobiet, A., Goergen, K., Karacostas, T., Knist, S., Mayer, S., Soares, P. M. M., Pytharoulis, I., Tegoulias, I., Tsikerdekis, A., and Jacob, D.: Regional climate hindcast simulations within EURO-CORDEX: evaluation of a WRF multi-physics ensemble, Geosci. Model Dev., 8, 603–618, https://doi.org/10.5194/gmd-8-603-2015, 2015.

Kimball, J. S., Running, S. W., and Nemani, R.: An improved method for estimating surface humidity from daily minimum temperature, Agr. Forest Meteorol., 85, 87–98, https://doi.org/10.1016/S0168-1923(96)02366-0, 1997.

Koster, R. D., Suarez, M. J., Liu, P., Jambor, U., Berg, A., Kistler, M., Reichle, R., Rodell, M., and Famiglietti, J.: Realistic Initialization of Land Surface States: Impacts on Subseasonal Forecast Skill, J. Hydrometeorol., 5, 1049–1063, https://doi.org/10.1175/JHM-387.1, 2004.

Kotlarski, S., Paul, F., and Jacob, D.: Forcing a distributed glacier mass balance model with the regional climate model REMO. Part I: climate model evaluation, J. Climate, 23, 1589–1606, https://doi.org/10.1175/2009JCLI2711.1, 2010.

Kristiansen, J., Bjørge, D., Edwards, J. M., and Rooney, G. G.: Soil Field Model Interoperability: Challenges and Impact on Screen Temperature Forecast Skill during the Nordic Winter, J. Hydrometeorol., 13, 1215–1232, https://doi.org/10.1175/JHM-D-11-095.1, 2012.

Lapo, K. E., Hinkelman, L. M., Sumargo, E., Hughes, M., and Lundquist, J. D.: A critical evaluation of modeled solar irradiance over California for hydrologic and land surface modeling, J. Geophys. Res., 122, 299–317, https://doi.org/10.1002/2016JD025527, 2017.

Li, J. L., Lee, W. L., Yu, J. Y., Hulley, G., Fetzer, E., Chen, Y. C., and Wang, Y. H.: The impacts of precipitating hydrometeors radiative effects on land surface temperature in contemporary GCMS using satellite observations, J. Geophys. Res., 121, 67–79, https://doi.org/10.1002/2015JD023776, 2016.

Liang, X., Lettenmaier, D. P., Wood, E. F., and Burges, S. J.: A simple hydrologically based model of land surface water and energy fluxes for general circulation models, J. Geophys. Res., 99, 14415, https://doi.org/10.1029/94JD00483, 1994.

Livneh, B., Rosenberg, E. A., Lin, C., Nijssen, B., Mishra, V., Andreadis, K. M., Maurer, E. P., and Lettenmaier, D. P.: A long-term hydrologically based dataset of land surface fluxes and states for the conterminous United States: Update and extensions, J. Climate, 26, 9384–9392, https://doi.org/10.1175/JCLI-D-12-00508.1, 2013.

Lofgren, B. M., Hunter, T. S., and Wilbarger, J.: Effects of using air temperature as a proxy for potential evapotranspiration in climate change scenarios of Great Lakes basin hydrology, J. Great Lakes Res., 37, 744–752, https://doi.org/10.1016/j.jglr.2011.09.006, 2011.

Lussana, C., Saloranta, T., Skaugen, T., Magnusson, J., Tveito, O. E., and Andersen, J.: seNorge2 daily precipitation, an observational gridded dataset over Norway from 1957 to the present day, Earth Syst. Sci. Data, 10, 235–249, https://doi.org/10.5194/essd-10-235-2018, 2018a.

Lussana, C., Tveito, O. E., and Uboldi, F.: Three-dimensional spatial interpolation of 2 m temperature over Norway, Q. J. Roy. Meteor. Soc., 144, 344–364, https://doi.org/10.1002/qj.3208, 2018b.

Marty, C.: Surface radiation, cloud forcing and greenhouse effect in the Alps, PhD thesis, ETH Zurich, 2000.

Mayer, B. and Kylling, A.: Technical note: The libRadtran software package for radiative transfer calculations – description and examples of use, Atmos. Chem. Phys., 5, 1855–1877, https://doi.org/10.5194/acp-5-1855-2005, 2005.

Meloni, D., Di Biagio, C., Di Sarra, A., Monteleone, F., Pace, G., and Sferlazzo, D. M.: Accounting for the solar radiation influence on downward longwave irradiance measurements by pyrgeometers, J. Atmos. Ocean. Tech., 29, 1629–1643, https://doi.org/10.1175/JTECH-D-11-00216.1, 2012.

MERRA-2 const_2d_ctm_Nx: Constant Model Parameters for Usage by CTM 0.5×0.625 degree V5.12.4, https://doi.org/10.5067/4Z3YUPM81GRJ, 2015a.

MERRA-2 tavg1_2d_rad_Nx: 2d, 1-Hourly, Time-Averaged, Single-Level, Assimilation, Radiation Diagnostics V5.12.4, https://doi.org/10.5067/Q9QMY5PBNV1T, 2015b.

MERRA-2 inst1_2d_asm_Nx: 2d, 1-Hourly, Instantaneous, Single-Level, Assimilation, Single-Level Diagnostics V5.12.4, https://doi.org/10.5067/3Z173KIE2TPD, 2015c.

Milly, P. C. D. and Dunne, K. A.: On the hydrologic adjustment of climate-model projections: The potential pitfall of potential evapotranspiration, Earth Interact., 15, 1–14, https://doi.org/10.1175/2010EI363.1, 2011.

Mizukami, N., Clark, M., Slater, A., Brekke, L., Elsner, M., Arnold, J., and Gangopadhyay, S.: Hydrologic Implications of Different Large-Scale Meteorological Model Forcing Datasets in Mountainous Regions, J. Hydrometeorol., 15, 474–488, https://doi.org/10.1175/JHM-D-13-036.1, 2014.

Mizukami, N., Clark, M. P., Gutmann, E. D., Mendoza, P. A., Newman, A. J., Nijssen, B., Livneh, B., Hay, L. E., Arnold, J. R., and Brekke, L. D.: Implications of the Methodological Choices for Hydrologic Portrayals of Climate Change over the Contiguous United States: Statistically Downscaled Forcing Data and Hydrologic Models, J. Hydrometeorol., 17, 73–98, https://doi.org/10.1175/JHM-D-14-0187.1, 2016.

Mohr, M.: New Routines for Gridding of Temperature and Precipitation Observations for "seNorge.no", Met. no Report, 8, available at: ftp://ftp.met.no/projects/klimagrid/doc/NewRoutinesforGriddingofTemperature.pdf (last access: 10 June 2019), 2008.

Mueller, B., Hirschi, M., Jimenez, C., Ciais, P., Dirmeyer, P. A., Dolman, A. J., Fisher, J. B., Jung, M., Ludwig, F., Maignan, F., Miralles, D. G., McCabe, M. F., Reichstein, M., Sheffield, J., Wang, K., Wood, E. F., Zhang, Y., and Seneviratne, S. I.: Benchmark products for land evapotranspiration: LandFlux-EVAL multi-data set synthesis, Hydrol. Earth Syst. Sci., 17, 3707–3720, https://doi.org/10.5194/hess-17-3707-2013, 2013.

New, M., Hulme, M., and Jones, P.: Representing twentieth-century space-time climate variability. Part I: Development of a 1961–90 mean monthly terrestrial climatology, J. Climate, 12, 829–856, https://doi.org/10.1175/1520-0442(1999)012<0829:RTCSTC>2.0.CO;2, 1999.

Nilsen, I. B., Stagge, J. H., and Tallaksen, L. M.: A probabilistic approach for attributing temperature changes to

synoptic type frequency, Int. J. Climatol., 37, 2990–3002, https://doi.org/10.1002/joc.4894, 2017.

Parding, K., Olseth, J. A., Liepert, B. G., and Dagestad, K.-F.: Influence of atmospheric circulation patterns on local cloud and solar variability in Bergen, Norway, Theor. Appl. Climatol., 125, 625–639, https://doi.org/10.1007/s00704-015-1517-8, 2016.

Pierce, D. W., Westerling, A. L., and Oyler, J.: Future humidity trends over the western United States in the CMIP5 global climate models and variable infiltration capacity hydrological modeling system, Hydrol. Earth Syst. Sci., 17, 1833–1850, https://doi.org/10.5194/hess-17-1833-2013, 2013.

Pohlert, T.: trend: Non-Parametric Trend Tests and Change-Point Detection, available at: https://CRAN.R-project.org/package=trend (last access: 10 June 2019), r package version 1.1.0, 2018.

Prata, A. J.: A new long-wave formula for estimating downward clear-sky radiation at the surface, Q. J. Roy. Meteor. Soc., 122, 1127–1151, https://doi.org/10.1002/qj.49712253306, 1996.

Raleigh, M. S., Livneh, B., Lapo, K., Lundquist, J. D., Raleigh, M. S., Livneh, B., Lapo, K., and Lundquist, J. D.: How Does Availability of Meteorological Forcing Data Impact Physically Based Snowpack Simulations?, J. Hydrometeorol., 17, 99–120, https://doi.org/10.1175/JHM-D-14-0235.1, 2016.

Reistad, M., Breivik, b., Haakenstad, H., Aarnes, O. J., Furevik, B. R., and Bidlot, J.-R.: A high-resolution hindcast of wind and waves for the North Sea, the Norwegian Sea, and the Barents Sea, J. Geophys. Res., 116, C05019, https://doi.org/10.1029/2010JC006402, 2011.

Rizzi, J., Nilsen, I. B., Stagge, J. H., Gisnås, K., and Tallaksen, L. M.: Five decades of warming: impacts on snow cover in Norway, Hydrol. Res., 49, nh2017051, https://doi.org/10.2166/nh.2017.051, 2017.

Rodell, M., Houser, P. R., Berg, A. A., and Famiglietti, J. S.: Evaluation of 10 Methods for Initializing a Land Surface Model, J. Hydrometeorol., 6, 146–155, https://doi.org/10.1175/JHM414.1, 2005.

Rontu, L., Wastl, C., and Niemelä, S.: Influence of the Details of Topography on Weather Forecast – Evaluation of HARMONIE Experiments in the Sochi Olympics Domain over the Caucasian Mountains, Front. Earth Sci., 4, 13 pp., https://doi.org/10.3389/feart.2016.00013, 2016.

Rydsaa, J. H., Stordal, F., Bryn, A., and Tallaksen, L. M.: Effects of shrub and tree cover increase on the near-surface atmosphere in northern Fennoscandia, Biogeosciences, 14, 4209–4227, https://doi.org/10.5194/bg-14-4209-2017, 2017.

Schmied, H. M., Müller, R., Sanchez-Lorenzo, A., Ahrens, B., and Wild, M.: Evaluation of radiation components in a global freshwater model with station-based observations, Water, 8, 450, https://doi.org/10.3390/w8100450, 2016.

Sheffield, J., Goteti, G., and Wood, E. F.: Development of a 50-Year High-Resolution Global Dataset of Meteorological Forcings for Land Surface Modeling, J. Climate, 19, 3088–3111, https://doi.org/10.1175/JCLI3790.1, 2006.

Sheridan, S. C.: The redevelopment of a weather-type classification scheme for North America, Int. J. Climatol., 22, 51–68, https://doi.org/10.1002/joc.709, 2002.

Shi, X., Wild, M., and Lettenmaier, D. P.: Surface radiative fluxes over the pan-Arctic land region: Variability and trends, J. Geophys. Res., 115, D22104, https://doi.org/10.1029/2010JD014402, 2010.

Slater, A. G.: Surface Solar Radiation in North America: A Comparison of Observations, Reanalyses, Satellite, and Derived Products, J. Hydrometeorol., 17, 401–420, https://doi.org/10.1175/JHM-D-15-0087.1, 2016.

Stagge, J. H., Tallaksen, L. M., Xu, C., and Van Lanen, H.: Standardized precipitation-evapotranspiration index (SPEI): Sensitivity to potential evapotranspiration model and parameters, Proceedings of FRIEND-water, 1, 367–373, 2014.

Szczypta, C., Calvet, J.-C., Albergel, C., Balsamo, G., Boussetta, S., Carrer, D., Lafont, S., and Meurey, C.: Verification of the new ECMWF ERA-Interim reanalysis over France, Hydrol. Earth Syst. Sci., 15, 647–666, https://doi.org/10.5194/hess-15-647-2011, 2011.

Teklesadik, A. D., Alemayehu, T., van Griensven, A., Kumar, R., Liersch, S., Eisner, S., Tecklenburg, J., Ewunte, S., and Wang, X.: Inter-model comparison of hydrological impacts of climate change on the Upper Blue Nile basin using ensemble of hydrological models and global climate models, Climatic Change, 141, 517–532, https://doi.org/10.1007/s10584-017-1913-4, 2017.

Thornton, P. E. and Running, S. W.: An improved algorithm for estimating incident daily solar radiation from measurements of temperature, humidity, and precipitation, Agr. Forest Meteorol., 93, 211–228, https://doi.org/10.1016/S0168-1923(98)00126-9, 1999.

Thornton, P. E., Hasenauer, H., and White, M. A.: Simultaneous estimation of daily solar radiation and humidity from observed temperature and precipitation: an application over complex terrain in Austria, Agr. Forest Meteorol., 104, 255–271, https://doi.org/10.1016/S0168-1923(00)00170-2, 2000.

Tveito, O. E. and Førland, E. J.: Mapping temperatures in Norway applying terrain information, geostatistics and GIS, Norsk Geogr. Tidsskr., 53, 202–212, https://doi.org/10.1080/002919599420794, 1999.

Urraca, R., Huld, T., Gracia-Amillo, A., Martinez-de Pison, F. J., Kaspar, F., and Sanz-Garcia, A.: Evaluation of global horizontal irradiance estimates from ERA5 and COSMO-REA6 reanalyses using ground and satellite-based data, Sol. Energy, 164, 339–354, https://doi.org/10.1016/J.SOLENER.2018.02.059, 2018.

Vormoor, K. and Skaugen, T.: Temporal Disaggregation of Daily Temperature and Precipitation Grid Data for Norway, J. Hydrometeorol., 14, 989–999, https://doi.org/10.1175/JHM-D-12-0139.1, 2013.

Warszawski, L., Frieler, K., Huber, V., Piontek, F., Serdeczny, O., and Schewe, J.: The Inter-Sectoral Impact Model Intercomparison Project (ISI–MIP): Project framework, P. Natl. Acad. Sci. USA, 111, 3228–3232, https://doi.org/10.1073/pnas.1312330110, 2014.

Weedon, G. P., Gomes, S., Viterbo, P., Shuttleworth, W. J., Blyth, E., Österle, H., Adam, J. C., Bellouin, N., Boucher, O., and Best, M.: Creation of the WATCH Forcing Data and Its Use to Assess Global and Regional Reference Crop Evaporation over Land during the Twentieth Century, J. Hydrometeorol., 12, 823–848, https://doi.org/10.1175/2011JHM1369.1, 2011.

Weedon, G. P., Balsamo, G., Bellouin, N., Gomes, S., Best, M. J., and Viterbo, P.: The WFDEI meteorological forcing data set: WATCH Forcing Data methodology applied to ERA-Interim reanalysis data, Water Resour. Res., 50, 7505–7514, https://doi.org/10.1002/2014WR015638, 2014.

Wessel, P. and Smith, W. H. F.: A global, self-consistent, hierarchical, high-resolution shoreline database, J. Geophys. Re.-Sol. Ea., 101, 8741–8743, https://doi.org/10.1029/96JB00104, 1996.

Wild, M., Gilgen, H., Roesch, A., Ohmura, A., Long, C. N., Dutton, E. G., Forgan, B., Kallis, A., Russak, V., and Tsvetkov, A.: From dimming to brightening: decadal changes in solar radiation at Earth's surface, Science, 308, 847–850, https://doi.org/10.1126/science.1103215, 2005.

Wild, M., Folini, D., Hakuba, M. Z., Schär, C., Seneviratne, S. I., Kato, S., Rutan, D., Ammann, C., Wood, E. F., and König-Langlo, G.: The energy balance over land and oceans: an assessment based on direct observations and CMIP5 climate models, Clim. Dynam., 44, 3393–3429, https://doi.org/10.1007/s00382-014-2430-z, 2015.

Wild, M., Ohmura, A., Schär, C., Müller, G., Folini, D., Schwarz, M., Hakuba, M. Z., and Sanchez-Lorenzo, A.: The Global Energy Balance Archive (GEBA) version 2017: a database for worldwide measured surface energy fluxes, Earth Syst. Sci. Data, 9, 601–613, https://doi.org/10.5194/essd-9-601-2017, 2017.

Zib, B. J., Dong, X., Xi, B., Kennedy, A., Zib, B. J., Dong, X., Xi, B., and Kennedy, A.: Evaluation and Intercomparison of Cloud Fraction and Radiative Fluxes in Recent Reanalyses over the Arctic Using BSRN Surface Observations, J. Climate, 25, 2291–2305, https://doi.org/10.1175/JCLI-D-11-00147.1, 2012.

Supplement of Earth Syst. Sci. Data, 11, 797–821, 2019
https://doi.org/10.5194/essd-11-797-2019-supplement

Open Access Earth System Science Data

Supplement of

Merits of novel high-resolution estimates and existing long-term estimates of humidity and incident radiation in a complex domain

Helene Birkelund Erlandsen et al.

Correspondence to: Helene Birkelund Erlandsen (hebe@nve.no)

1 Procedure to calculate the HySN data set

Era Interim daily mean 2 meter dew point temperature ($T2d_E$), 2 meter temperature ($T2_E$), surface pressure (ps_E) are taken as the arithmetic mean of the Era-Interim analysis fields, available every 6 hours. Surface incident longwave (LW_E) and shortwave (LW_E) radiation are taken from +12, +18,and +24 hours of the Era-Interim forecasts at 00 and 12 UTC, to reduce the influence spin-up effects have on the fields (see e.g. Weedon et al., 2014; Balsamo et al., 2015). The high resolution gridded observational dataset used in the compilation is the daily SeNorge v2.1 2-meter temperature ($\mathrm{T2_{SN}}$) (Lussana et al., 2018).

The Era-interim data is interpolated to the SeNorge grid in three stages, using bilinear interpolation in most areas, but nearest-neighbour interpolation for SeNorge land areas close to the Era-Interim landmask, and bilinear interpolation for SeNorge land areas outside Era-Interims landmask.

1.1 Vapour pressure [VP] and surface pressure [ps]

The method for downscaling near surface humidity follows Cosgrove (2003), where relative humidity (RH) is assumed constant with height. The assumption of constant relative humidity with elevation is explored in e.g. Feld et al. (2013), and is used in the making of NLDAS, WFD, and PGMFD. RH is given by the ratio of the ambient vapour pressure [VP] (the vapour pressure at dew point [$\mathrm{T_d}$] or frost point [$\mathrm{T_f}$] temperature) divided by the saturation vapour pressure [$\mathrm{VP_s}$] of moist air at the actual air temperature, multiplied by 100:

$$RH = \frac{VP \cdot 100}{VP_s} \tag{S1}$$

The Era-Interim 2-meter RH ($\mathrm{RH_E}$) is calculated using the Era-Interim surface pressure ($\mathrm{ps_E}$), $\mathrm{T2_E}$, and $\mathrm{T2d_E}$, and Equation ew1 in Buck (1981) [Buck81]. The resulting, vertically adjusted HySN dew point or freeze point temperature (for simplicity, denoted $\mathrm{T2d_H}$) is computed (in Celsius) directly from $\mathrm{RH_E}$ (see e.g. Feld et al. (2013)) using the Buck81 equation for water and the AERKi equation in Alduchov and Eskridge (1996) for ice:

$$T2d_H = \frac{c \cdot [ln(RH_E/100) + b(T2_{SN})/(c + T2_{SN})]}{b - ln(RH_E/100) - b(T2_{SN})/(c + T2_{SN})}. \tag{S2}$$

For water b is 17.502 and c is 240.97. For ice b is 22.587 and c is 273.86.

The vapour pressure is then calculated (still using the Buck81 for water and AERKi for ice,) with suggested pressure dependent enhancement factors ($\mathrm{f_e}$) from Alduchov and Eskridge (1996). The HySN surface pressure ($\mathrm{ps_H}$) is estimated by vertically adjusting the Era-Interim surface pressure to SeNorge orography combining the hydrostatic approximation and the ideal gas law equation (Eq. 6 in Cosgrove (2003), similar to the hypsometric equation):

$$ps_H = \frac{ps_E}{e^{(g\Delta z)/(RT2_m)}}, \tag{S3}$$

where $T2_m = \frac{T2_{SN} + T2_E}{2}$ is the estimated mean temperature (in Kelvin) in the atmospheric column between the SeNorge grid elevation and the ERA-Interim grid elevation. Δ z is the difference in elevation between the SeNorge grid and the ERA-Interim grid. Finally the adjusted vapour pressure is calculated:

$$f_e = d \cdot e^{g \cdot ps_H/100.} \tag{S4}$$

$$VP_H = f_e \cdot a \cdot e^{b \cdot T_{dH}/(c + T_{dH})} \tag{S5}$$

For water d is 1.00071 and g is 0.0000045, while for ice d is 0.99882 and g is 0.000008 (Alduchov and Eskridge, 1996). b is 17.502 and c is 240.97 for water [Buck81]. For ice b is 22.587 and c is 273.86 [AERKi]. If supersaturation occurs vapour pressure is calculated for saturation, limiting RH to 100%.

1.2 Longwave incident radiation [LW]

The longwave radiation is adjusted (following Eq. 14 in Cosgrove (2003)) by scaling $\mathrm{LW_E}$ with the ratio of the estimated Stefan-Boltzmann grey body radiation in the SeNorge grid to the estimated Era-Interim Stefan-Boltzmann grey body radiation.

$$LW_H = \frac{\varepsilon_H \, \sigma_{sb}}{\varepsilon_E \, \sigma_{sb}} (\frac{T2_{SN}}{T2_E})^4 \, LW_E. \tag{S6}$$

σ_{sb} is the Stephen-Boltzmann constant, ε_{E} is the Satterlund (1979) estimate of clear sky emissivity given the Era-Interim humidity and temperature: $\varepsilon_E = 1.08(1 - e(-VP_E^{T2E/2016}))$, and ε_{H} is similarly the Satterlund (1979) estimate of clear sky emissivity given the SeNorge temperature and HySN humidity: $\varepsilon_H = 1.08(1 - e(-VP_H^{T2_{SN}/2016}))$.

1.3 Shortwave incident radiation [SW]

No consistent approach is used in other forcing datasets for adjusting SW radiation. Given that SW is very sensitive to near surface humidity, and that the Cosgrove (2003) method used above adjusts VP, we choose to scale the Era-Interim SW based on the estimated clear sky transmissivity for the two datasets; i.e. a method similar to that used to the derive the adjusted LW is used. In Thornton and Running (1999) [TR99] different empirical estimates of the total daily clear sky transmissivity of SW are found, given different input data. Method (z, e) in Table 2 in TR99 predicts the daily clear sky transmissivity based on altitude (z) and VP (denoted with e in TR99):

$$\tau cc = \tau_0^{ps(z)/ps_0} + \alpha VP$$

τ_0 is 0.72 and is an empirical expression of the instantaneous transmittance for a dry atmosphere at reference pressure, $\mathrm{ps}(z)$ is the surface air pressure at grid elevation and ps_0 is the reference surface pressure (e.g. 101300 Pa; it is cancelled out in the calculations). α is $-1.5 \cdot 10^{-5}\mathrm{Pa}^{-1}$ and is a slope parameter relating the influence of water vapour on the transmissivity. The adjusted SW is then calculated by scaling the Era-Interim SW with the ratio of the empirical expression of clear sky SW transmissivity given the difference in grid elevation and VP in the SeNorge and the Era-Interim grid. Since the expression for SW in TR99 is a multiplicative expression of extra-terrestrial (astronomical) radiation scaled by both an all-sky and clear-sky transmissivity, the ratio of the clear-sky transmissivity is squared.

$$SW_H = \left(\frac{\tau_0^{ps_H(z)/ps_0} + \alpha VP_H}{\tau_0^{ps_E(z)/ps_0} + \alpha VP_E}\right)^2 SW_E. \quad \text{(S7)}$$

The HySN data product is freely available from Zenodo (https://doi.org/10.5281/zenodo.1970170), and the Python code to generate the data is available on GitHub (https://doi.org/10.5281/zenodo.1435555).

2 Vertical gradients in vapour pressure

Both the observations and model estimates were analysed for dependence on geographical predictors. In order to derive the coefficients to adjust the model estimates to the station observations linear regression was used on seasonal mean values at the location of the 84 measurement stations (see Table S1 and S2). For brevity the vertical gradients of the annual mean humidity values is show in in Fig. S2. Fig S3 shows the vertical gradient when also latitude (above 57 °N) is included in the regression models, while Fig. S4 shows the vertical gradient when altitude, latitude (above 57 °N), distance to the coast, with interaction allowed between the altitude and distance to the coast. Altitude is a significant predictor of vapour pressure in the observations and models, also when additional geographical predictors are included.

References

Alduchov, O. A. and Eskridge, R. E.: Improved Magnus Form Approximation of Saturation Vapor Pressure, Journal of Applied Meteorology, 35, 601–609, doi:10.1175/1520-0450(1996)035<0601:IMFAOS>2.0.CO;2, 1996.

Balsamo, G., Albergel, C., Beljaars, A., Boussetta, S., Brun, E., Cloke, H., Dee, D., Dutra, E., Muñoz-Sabater, J., Pappenberger, F., de Rosnay, P., Stockdale, T., and Vitart, F.: ERA-Interim/Land: a global land surface reanalysis data set, Hydrology and Earth System Sciences, 19, 389–407, doi:10.5194/hess-19-389-2015, 2015.

Buck, A. L.: New Equations for Computing Vapor Pressure and Enhancement Factor, Journal of Applied Meteorology, 20, 1527–1532, doi:10.1175/1520-0450(1981)020<1527:NEFCVP>2.0.CO;2, 1981.

Cosgrove, B. A.: Real-time and retrospective forcing in the North American Land Data Assimilation System (NLDAS) project, Journal of Geophysical Research, 108, 8842, doi:10.1029/2002JD003118, 2003.

Feld, S. I., Cristea, N. C., and Lundquist, J. D.: Representing atmospheric moisture content along mountain slopes: Examination using distributed sensors in the Sierra Nevada, California, Water Resources Research, 49, 4424–4441, doi:10.1002/wrcr.20318, 2013.

Lussana, C., Tveito, O. E., and Uboldi, F.: Three-dimensional spatial interpolation of 2 m temperature over Norway, Quarterly Journal of the Royal Meteorological Society, 144, 344–364, doi:10.1002/qj.3208, 2018.

Satterlund, D. R.: An improved equation for estimating long-wave radiation from the atmosphere, Water Resources Research, 15, 1649–1650, doi:10.1029/WR015i006p01649, 1979.

Thornton, P. E. and Running, S. W.: An improved algorithm for estimating incident daily solar radiation from measurements of temperature, humidity, and precipitation, Agricultural and Forest Meteorology, 93, 211–228, doi:10.1016/S0168-1923(98)00126-9, 1999.

Weedon, G. P., Balsamo, G., Bellouin, N., Gomes, S., Best, M. J., and Viterbo, P.: The WFDEI meteorological forcing data set: WATCH Forcing Data methodology applied to ERA-Interim reanalysis data, Water Resources Research, 50, 7505–7514, doi:10.1002/2014WR015638, 2014.

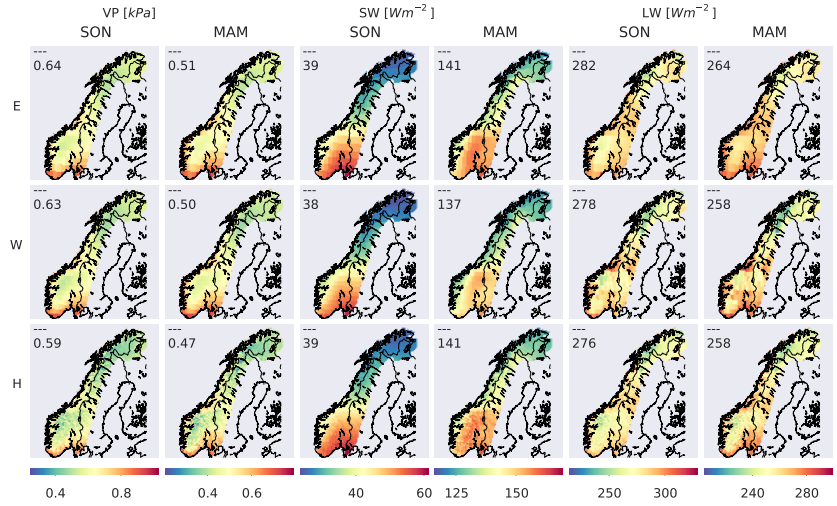

Figure S1. Mean (1982-2000) vapor pressure (VP), incident shortwave (SW ↓) and longwave (LW ↓) radiation estimates in fall (SON) and spring (MAM) of Era-Interim, WFDEI, and HySN. The mean value for the points which are land points for all models are denoted in the upper left corner of each image.

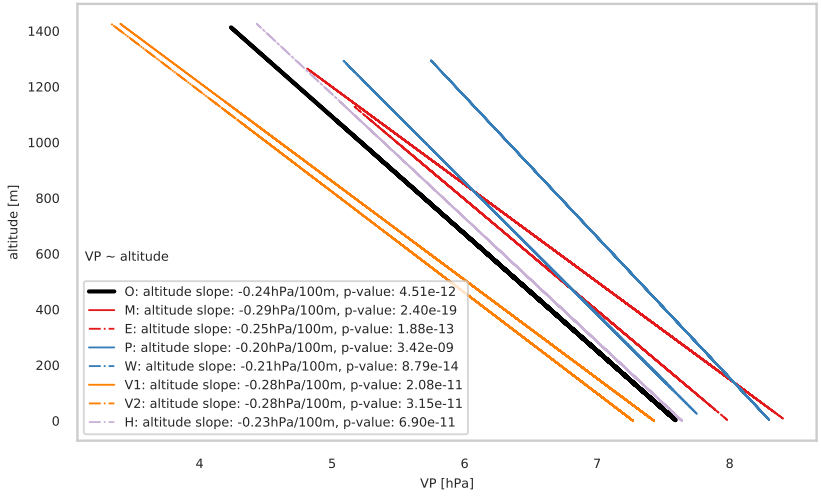

Figure S2. Vapour pressure as a function of altitude based on linear regression using only altitude, with annual means of vapour pressure at or near the location of the 84 measurement stations as predictand.

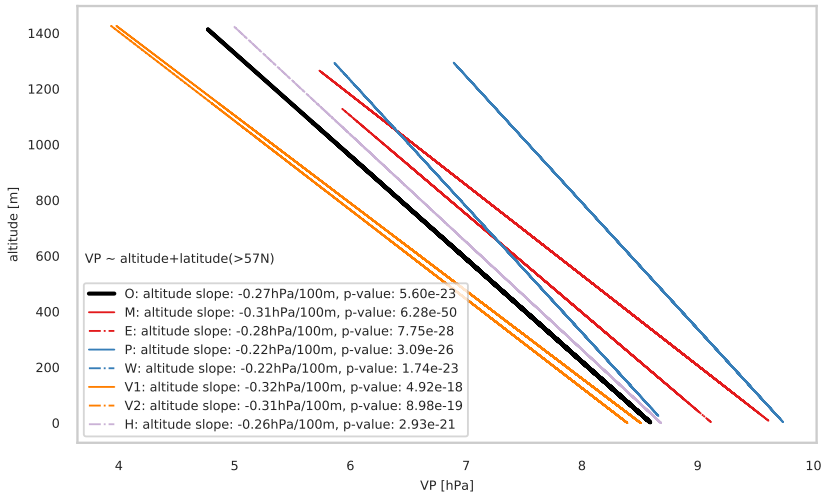

Figure S3. Vapour pressure as a function of altitude based on linear regression using only latitude (above 57 °N) and altitude, for mean annual values of vapour pressure at or near the location of the 84 measurement stations.

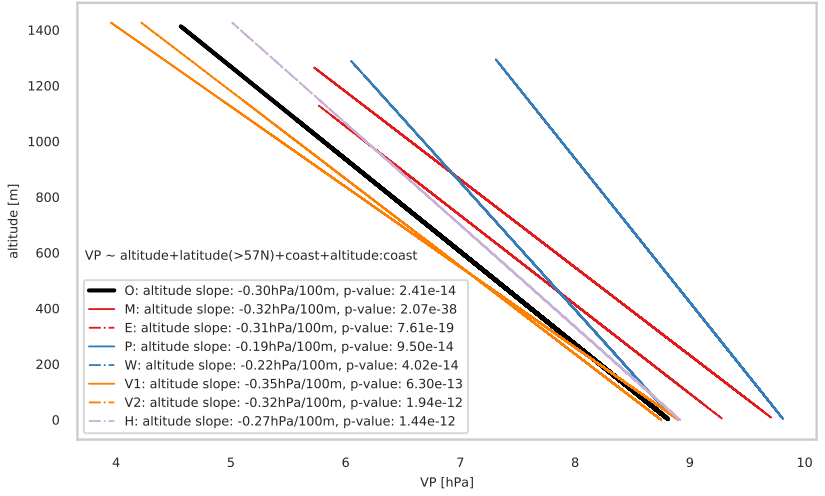

Figure S4. Vapour pressure as a function of altitude alone (excluding the interaction term between distance to the coast and altitude), when based on a linear regression model including latitude (above 57 °N), altitude, distance to the coast, with interaction allowed between the latter predictors. The regression is based on annual mean values of vapour pressure at or near the location of the 84 measurement stations.

: 5

Observation stations

Table S1. Stations observing humidity which are included in the analysis. For each station the name, latitude (lat, [°N]), longitude (lon, [°E]), altitude [m], and distance to the ocean [km] of the station are denoted, as well as the first and last month and year of the time-series included in the study.

Name	Lat	Lon	Altitude [m]	Δ ocean [km]	From	To
MANDALII	58.0	7.4	138	2.3	January 1982	December 1999
LANDVIK	58.3	8.5	10	4.6	January 1982	December 1999
NELAUG	58.7	8.6	142	18.1	January 1982	December 1999
OBRESTADFYR	58.7	5.6	24	0.5	January 1982	December 1999
BYGLANDSFJORD-SOLBAKKEN	58.7	7.8	212	49.7	January 1982	December 1999
SOLA	58.9	5.6	7	1.3	January 1982	December 1999
SIRDAL-TJOERHOM	58.9	6.8	500	21.7	January 1982	December 1999
STAVANGER-VAALAND	59.0	5.7	72	1.0	January 1982	January 1988
PRESTEBAKKE	59.0	11.5	157	16.6	January 1982	December 1999
TVEITSUND	59.0	8.5	252	45.3	January 1982	December 1999
RENNESOEY-GALTA	59.1	5.6	19	11.3	January 1982	December 1999
SKUDENESII	59.1	5.2	2	1.2	November 1992	December 1999
MELSOM	59.2	10.3	26	1.2	January 1982	August 1994
SARPSBORG	59.3	11.1	57	10.1	December 1991	December 1999
RYGGE	59.4	10.8	40	4.9	January 1982	December 1999
GVARV	59.4	9.2	26	34.4	January 1982	July 1989
AAS	59.7	10.8	94	9.4	January 1982	December 1999
KONGSBERGIV	59.7	9.7	168	34.5	January 1982	December 1999
DRAMMEN-MARIENLYST	59.7	10.2	3	18.0	January 1982	December 1999
MOESSTRANDII	59.8	8.2	977	93.0	January 1982	December 1999
MIDTLAEGER	59.8	7.0	1079	33.8	January 1982	December 1999
ASKER	59.9	10.4	163	3.2	January 1983	December 1999
DOENSKI	59.9	10.5	59	2.3	January 1982	December 1999
LYNGDALINUMEDAL	59.9	9.5	288	27.1	January 1982	December 1999
OSLO-BLINDERN	59.9	10.7	94	3.2	January 1982	December 1999
MAGNOR	60.0	12.2	154	35.7	January 1982	December 1999
HAKADAL-BLIKSRUDHAGAN	60.1	10.9	174	21.9	December 1982	December 1999
GARDERMOEN	60.2	11.1	202	22.6	January 1982	December 1999
VINGER	60.2	12.0	175	48.7	January 1982	December 1999
FLESLAND	60.3	5.2	48	1.5	January 1982	December 1999
BERGEN-FLORIDA	60.4	5.3	12	0.96	January 1982	December 1999
KVAMSKOGEN	60.4	5.9	408	8.1	January 1982	December 1999
GEILO-GEILOSTOELEN	60.5	8.2	810	58.1	January 1982	December 1999
NESBYEN-SKOGLUND	60.6	9.1	167	60.7	January 1982	December 1999
VOSS-BOE	60.6	6.5	125	18.2	January 1982	December 1999
GOL-STAKE	60.7	8.9	542	65.3	January 1982	February 1991
KISEPAHEDMARK	60.8	10.8	129	3.1	April 1987	December 1999
MODALENII	60.8	6.0	114	14.5	January 1982	December 1999
AABJOERSBRAATEN	60.9	9.3	639	48.2	January 1982	December 1999

Table S2. Stations observing humidity which are included in the analysis. For each station the name, latitude (lat, [°N]), longitude (lon, [°E]), altitude [m], and distance to the ocean [km] of the station are denoted, as well as the first and last month and year of the time-series included in the study.

Name	lat	lon	altitude [m]	Δ ocean [km]	start	end
FAGERNES	61.0	9.2	358	53.8	July 1982	December 1999
LOEKENIVOLBU	61.1	9.1	521	68.8	January 1982	December 1999
RENA-HAUGEDALEN	61.2	11.4	240	42.5	January 1982	December 1999
EVENSTAD-OEVERENGET	61.4	11.1	255	49.8	January 1982	December 1999
FJAERLAND-SKARESTAD	61.4	6.8	10	2.3	February 1982	December 1999
SKAABU-STORSLAAEN	61.5	9.4	890	71.1	January 1982	December 1999
SOGNEFJELLHYTTA	61.6	8.0	1413	23.2	January 1982	December 1999
VENABU	61.7	10.1	930	61.6	January 1982	December 1999
BJOERKEHAUGIJOSTEDAL	61.7	7.3	305	24.7	January 1982	December 1999
SANDANE	61.8	6.2	51	1.9	January 1982	December 1999
DREVSJOE	61.9	12.0	672	7.7	January 1982	December 1999
KJOEREMSGRENDE	62.1	9.0	626	69.1	January 1982	December 1999
FISKAABYGD	62.1	5.6	41	1.0	January 1982	December 1999
FOKSTUGU	62.1	9.3	973	72.9	January 1982	December 1999
TAFJORD	62.2	7.4	11	0.1	January 1982	December 1999
LESJASKOG	62.2	8.4	621	48.9	January 1982	December 1999
VIGRA	62.6	6.1	22	7.8	January 1982	December 1999
ROEROS	62.6	11.4	628	31.6	January 1982	December 1999
SUNNDALSOERAIII	62.7	8.6	10	1.5	February 1983	December 1999
TINGVOLL-HANEM	62.8	8.3	69	2.2	January 1982	December 1999
ORKDAL-OEYUM	63.2	9.8	22	12.1	January 1982	December 1999
SELBU-STUBBE	63.2	11.1	242	28.0	January 1982	December 1999
VAERNES	63.5	10.9	12	1.8	January 1982	December 1999
OERLANDIII	63.7	9.6	10	2.4	January 1982	December 1999
NAMDALSEID	64.3	11.2	86	6.9	August 1982	November 1999
LEKA	65.1	11.7	47	8.7	January 1982	December 1999
SVENNINGDAL	65.4	13.4	121	24.3	January 1982	June 1987
GLOMFJORD	66.8	14.0	39	1.4	January 1982	December 1999
BODOEVI	67.3	14.4	11	1.0	January 1982	December 1999
FINNOEYIHAMAROEY	68.0	15.6	53	5.0	January 1982	December 1999
NARVIKIII	68.5	17.5	17	1.0	January 1982	December 1999
BOEIVESTERAALENII	68.6	14.5	12	3.0	January 1982	December 1999
SORTLAND-KLEIVA	68.6	15.3	14	2.5	January 1982	August 1991
TENNEVOLL	68.7	17.8	22	1.8	January 1982	December 1999
SIHCCAJAVRI	68.8	23.5	382	122.3	April 1982	December 1999
BORKENES	68.8	16.2	36	3.1	September 1983	December 1999
DIVIDALEN	68.8	19.7	228	48.9	January 1982	December 1999
BARDUFOSS	69.1	18.5	76	15.0	January 1982	December 1999
ANDOEYA	69.3	16.1	10	1.9	June 1982	December 1999
CUOVDDATMOHKKI	69.4	24.4	286	77.5	January 1982	December 1999
KARASJOK	69.5	25.5	155	67.5	January 1982	December 1999
SUOLOVUOPMI	69.6	23.5	377	41.2	March 1982	December 1999
TROMSOE	69.7	18.9	100	3.3	January 1982	December 1999
TROMSOE-LANGNES	69.7	18.9	8	2.0	January 1982	December 1999
KIRKENESLUFTHAVN	69.7	29.9	89	0.9	January 1982	December 1999

Table S3. The stations observing SW ↓ and LW ↓ included in the analysis are listed. For each station the name, latitude (lat, [°N]), longitude (lon, [°E]), altitude [m], and distance to the ocean [km] of the station are denoted, as well as the first and last month and year of the time-series included in the study. The stations with a +-sign are agricultural stations drifted by Bioforsk. The LW observation stations are marked with an asterisk. The percentage of discarded data within the time-series and the total number of days used in the validation are given, for LW data this is given in parenthesis. % flagged data includes missing data within the time-series.

Name	lat.	lon.	altitude	Δ ocean	start	end	% flagged	# Days
+Saerheim	58.8	5.7	90	27.6	April 1987	December 1999	27	3365
+Aas	59.7	10.8	94	9.4	August 1991	December 1999	13	2655
*Bergen-GFI	60.4	5.3	40	3.5	January 1982	December 1999	3(*4)	6357(*6460)
+Apelsvoll	60.7	10.9	262	88.2	March 1987	December 1999	25	3494
+Kise	60.8	10.8	129	96.1	April 1987	December 1999	4	4455
Loeken	61.1	9.1	527	73.4	January 1991	December 1999	15	2778
Gjengedal	61.7	6.0	355	24.6	July 1989	June 1996	18	2062
+*Trondheim	63.4	10.5	127	4.1	September 1996	December 1999	(23)	(675)
+Bodoe	67.3	14.5	26	6.5	April 1987	December 1999	15	4002
Maze	69.5	23.7	277	59.0	August 1982	January 1990	13	2408
+Tromsoe	69.7	18.9	12	3.5	June 1987	December 1999	29	3468

III

III. Constraining the HBV model for robust water balance assessments in a cold climate

 Hydrology Research | in press | 2021

Constraining the HBV model for robust water balance assessments in a cold climate

Helene Birkelund Erlandsen, Stein Beldring, Stephanie Eisner, Hege Hisdal, Shaochun Huang and Lena Merete Tallaksen

ABSTRACT

Robust projections of changes in the hydrological cycle in a non-stationary climate rely on trustworthy estimates of the water balance elements. Additional drivers than precipitation and temperature, namely wind, radiation, and humidity are known to have a significant influence on processes such as evaporation, snow accumulation, and snow-melt. A gridded version of the rainfall-runoff HBV model is run at a 1×1 km scale for mainland Norway for the period 1980–2014, with the following alterations: (i) the implementation of a physically based evaporation scheme; (ii) a net radiation-restricted degree-day factor for snow-melt, and (iii) a diagnostic precipitation phase threshold based on temperature and humidity. The combination of improved forcing data and model alterations allowed for a regional calibration with fewer calibrated parameters. Concurrently, modeled discharge showed equally good or better validation results than previous gridded model versions constructed for the same domain; and discharge trend patterns, snow water equivalent, and potential evaporation compared fairly to observations. Compared with previous studies, lower precipitation and evaporation values for mainland Norway were found. The results suggest that a more robust and more physically based model for climate change studies has been obtained, although additional studies will be needed to further constrain evaporation estimates.

Key words | climate, evaporation, HBV, Norway, snow-melt

HIGHLIGHTS

- The distributed HBV model is updated with physically based parameterizations.
- High-quality forcing data are included to enhance estimates evaporation, precipitation phase, and snow-melt.
- More than 100 discharge measurements are used for calibration and validation.
- The updates help constrain the long-term water balance for Norway.
- Additional work is called for to better constrain the evaporation estimates.

Helene Birkelund Erlandsen (corresponding author)
Stein Beldring
Hege Hisdal
Shaochun Huang
Norwegian Water Resources and Energy Directorate,
Oslo,
Norway
E-mail: *helenebe@met.no*

Helene Birkelund Erlandsen
Lena Merete Tallaksen
University of Oslo,
Oslo,
Norway

Stephanie Eisner
Norwegian Institute of Bioeconomy Research (NIBIO),
Ås,
Norway

doi: 10.2166/nh.2021.132

GRAPHICAL ABSTRACT

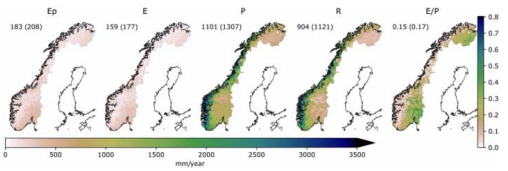

INTRODUCTION

Many hydrological models were developed for operational water resources management and have accordingly been built to rely only on input data that is commonly available, and to be easy to use. Any increase in model complexity should be justified by an increase in model performance, often measured according to the ability of the model to reproduce daily or monthly catchment runoff (Nash & Sutcliffe 1970; Lindström *et al.* 1997; Ferguson 1999). Today, gridded input data are becoming more widely available, either from numerical weather prediction models, reanalysis data such as Era5 (Hersbach *et al.* 2018), gridded observational data, e.g. SeNorge2018 (Lussana *et al.* 2019), or hybrid products such as HySN (Erlandsen *et al.* 2019) and WFDEI (Weedon *et al.* 2014). Further, the non-stationarity of the current climate calls for hydrological models with a stronger physical basis and a higher robustness in a wide range of climates (Ferguson 1999; Clark *et al.* 2015).

Hydrological models range from the simplest, data-driven, lumped, and conceptually based water balance models, to those akin to land surface models, where the surface energy balance is solved numerically (see e.g. Kauffeldt *et al.* 2016). The different modeling strategies have complimenting merits (Hrachowitz & Clark 2017). For example, numerically solving the surface energy balance requires an increase in input data requiring higher storage and pre-processing capacity, as well as an increase in model integration time; however, it allows the computation of surface temperature, and imposing a closed surface energy balance, which further constrains the latent heat flux or evaporation estimates. In this paper, the term evaporation encompasses water loss from soil, leaves, lakes, and plant stomata (transpiration).

A large number of hydrological modeling studies involve replacing a rather simple conceptual process description with a more physically based one and comparing the results (Bruland *et al.* 2001; Zappa *et al.* 2003; Hegdahl *et al.* 2016), while other studies compare models of different complexities (e.g. Magnusson *et al.* 2015). In cases where a more physically based model was compared with a more conceptually based model and an increase in model performance was not found, it is difficult to say whether this was due to an ill-stated empirical equation or parameter being included, over-parameterization, or that the more physically based process description relied on input variables that were poorly estimated. Thus, an important question raised in Clark *et al.* (2015) is 'to what extent is additional model complexity supported by the available information on geophysical attributes (topography, vegetation, soils, geology, and fine-scale meteorological data)?'.

A particular challenge for using conceptual, calibrated models for hydrological impact assessment is that parameter values can be overfitted to the climate conditions in the calibration period. Merz *et al.* (2011) found that calibrated parameters representing snow and soil moisture processes were sensitive to the choice of the calibration period. Milly & Dunne (2011) found that a temperature-index based evaporation parameterization may simulate considerably larger evaporation changes than net radiation changes might justify. Any change in vapor pressure deficit with climate change, or plant physiological mechanisms for preserving water, are also not accounted for in temperature-index based evaporation parameterizations. Besides evaporation-related calibrated parameters, other often calibrated parameters which potentially might be omitted

from calibration, or considerably restricted in range, are the precipitation phase threshold temperature and the commonly used degree-day factors for calculating snow-melt. Precipitation phase may be diagnosed using near-surface temperature and humidity (Jennings *et al.* 2018). The degree-day factor, which represents the amount of snow-melt per degree above freezing, may vary considerably depending on catchment, climate, and time-of-year (Kustas *et al.* 1994; Merz *et al.* 2011). Indirectly, it reflects biases in accumulated snowfall, sublimation and deposition processes not accounted for, spatial and temporal variation in incident longwave and shortwave radiation, vegetation shading, longwave radiation emitted by vegetation, and variation in surface albedo, to name a few. Accordingly, in climate change studies, for some processes in particular, there is a need to move from a simple and conceptually based description to a more robust, physically based one.

In Norway, a gridded version of the conceptual HBV rainfall-runoff model (Beldring *et al.* 2003, from here on referred to as HBV-B03) has been used to study the effect of climate change on hydrology (see e.g. Hanssen-Bauer *et al.* 2017). Until recently HBV-B03 included calibrated, land cover-dependent parameters for precipitation phase diagnosis, the melting temperature of snow, the snow-melt degree-day factor, and for the temperature-based scaling of monthly climatological potential evaporation to provide estimates of evaporation. In Wong *et al.* (2011), the existing evaporation routine was discussed as a large source of uncertainty when analyzing end-of-century changes in summer droughts for Norway. Further, the lack of an in-line computation of potential evaporation may be particularly unsuitable in cold climates – since potential evaporation is limited by the received incident radiation, which is bound to increase in a warmer climate with reduced snow cover and thus albedo.

There has been a recent effort to improve the physical basis of evaporation estimates in HBV-B03 by implementing a Penman–Monteith (Monteith 1965) potential evaporation routine. Simultaneously, the number of land cover classes represented by the model was increased from 7 to 19 to allow for more spatial heterogeneity related to natural vegetation cover and land use activity. These alterations are described in Huang *et al.* (2019), from here on this version of the model is referred to as HBV-H19. The inclusion of a more detailed land cover description combined with land use dependent, calibrated parameters controlling processes such as snow accumulation and ablation may lead to confounded or poorly constrained parameters, and thus disentanglement problems if the model were to be applied to study the effect of a perturbed land cover. Kustas *et al.* (1994) suggested an enhanced degree-day factor parameterization, where the degree-day factor is restricted by an additive term relating snow-melt to net radiation. A snow-melt routine where the degree-day factor is restricted by a radiative term allows snow-melt to be influenced by land cover class via albedo, without the need of a land cover class-dependent calibration.

The implementation of more physically based process descriptions as described above is here facilitated by a newly established hybrid method, HySN, for producing gridded estimates of near-surface vapor pressure and incident radiation. HySN was derived by merging reanalysis data with the 1×1 km SeNorge data and showed high fidelity when compared with station observations (Erlandsen *et al.* 2019).

In this study, we aim at obtaining a robust and more physically based model for studies of changes in water balance elements in a non-stationary climate. The HySN method for deriving estimates of evaporation and incident radiation was paired with an improved version of the SeNorge temperature and precipitation fields, SeNorge2018 (Lussana *et al.* 2019) and used as forcing data for a modified version of HBV-H19. The availability of high-quality input data made way for adding the following physically based updates to the HBV model:

i. an augmented Penman–Monteith based evaporation scheme;
ii. a regionally calibrated, radiation-restricted degree-day factor;
iii. a diagnostic temperature- and humidity-based threshold for diagnosing precipitation phase.

Simulated discharge was evaluated in terms of bias and Kling–Gupta Efficiency (KGE; Gupta *et al.* 2009) using measurements from more than 100 catchments, of which 34 were independent, i.e. not used for calibration. Calibration was conducted for the period 2000–2010. In addition, an independent validation time period, 1980–1999,

was identified. The model's suitability for climate studies was assessed by evaluating its ability to reproduce monthly discharge trends, simulated maximum winter snow water equivalent (SWE), and by comparing estimated potential evaporation with pan evaporation measurements. The model was run from 1980 to 2014. Its simulated mean water balance was assessed and compared with previous water balance estimates for Norway.

STUDY AREA AND DATA

Study area

Mainland Norway stretches several latitudes, from 58° to 71° North, on the western coast of northern Europe (see Figure 1). Its coastline is lined with fjords, while further inland the Scandinavian Mountains divide the country's western and eastern regions. Norway's location on the eastern end of the North Atlantic and its prevailing westerly winds, together with the Scandinavian Mountains, leads to a high annual precipitation on its western coast, with distinctly lower precipitation rates received leeward of the mountain range. Around a third of precipitation falls as snow. About 38% of the land area is forest covered, while the land surface is dominated by bare rock and shallow deposits (see e.g. Figure 17.1, replication of the Geological Survey of Norway (NGU) sediment map in Weynants *et al.* (2013)). Relatively shallow soils with a low water storage capacity in large parts of the country make way for a rapid runoff response to precipitation (e.g. Beldring 2002), but also for moisture stressed conditions in periods of meteorological drought (Buckland *et al.* 1997).

Forcing data

The model is forced with gridded daily temperature and precipitation fields from SeNorge2018, and with surface incident shortwave radiation, surface net longwave radiation, and vapor pressure deficit derived following the HySN method, and with a 1×1 km resolution wind data set from the Norwegian Meteorological Institute (MET Norway). Details of the forcing data are given below.

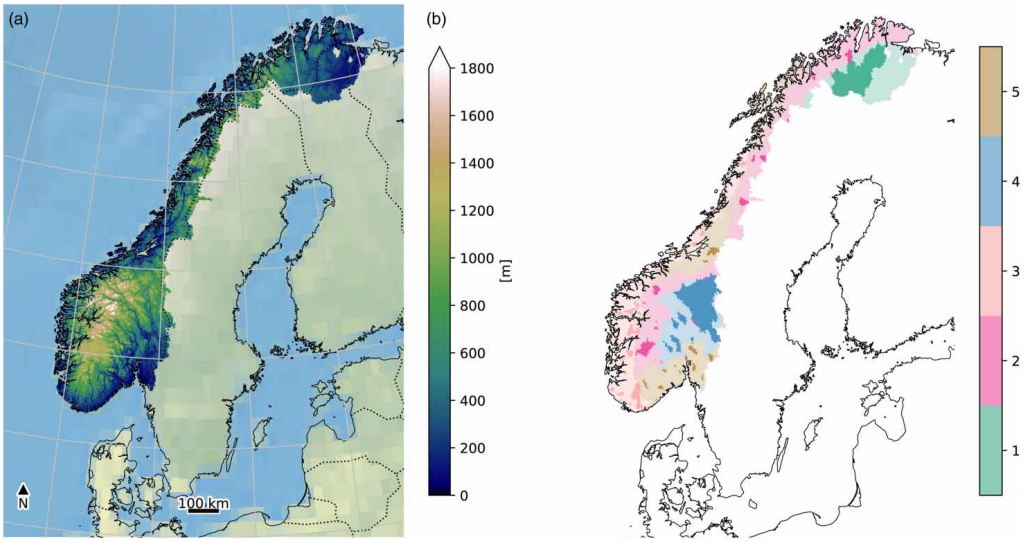

Figure 1 | The study region, Norway, with catchment areas outside Norway which drain into Norway included. (a) The orography and (b) the five regions used in the model calibration, with catchments used for calibration shown with a more opaque color. Please refer to the online version of this paper to see this figure in color: https://doi.org/10.2166/nh.2021.132.

SeNorge2018

SeNorge2018 version 18.12 is the newest version of the 1 × 1 km gridded data sets of 2-meter temperature (T2) and precipitation (P) based on observations from surface meteorological stations, developed by MET Norway. The data have a daily resolution and cover the period 1957 until the present. SeNorge2018 includes several innovations compared with the previous SeNorge version, such as the inclusion of a wind-induced undercatch correction for precipitation based on Wolff *et al.* (2015), and the use of climatological background fields from a convection-permitting dynamical downscaling of the global reanalysis ERA-Interim (Dee *et al.* 2011) instead of observational gridded data. For the model integration period, 1980–2014, SeNorge2018 shows an annual mean precipitation of 1,348 mm for Norway, while the previous version, SeNorge2.1 (Lussana *et al.* 2018), which did not include precipitation undercatch corrections, shows 1,068 mm, i.e. 280 mm less (see Supplementary Figure S1).

Klinogrid wind

The wind data set used to force HBV is a high-resolution, quantile-mapping-based gridded data set of near-surface wind speed developed at MET Norway. The daily wind data is available for October 1957 until May 2015 from http://thredds.met.no/thredds/catalog/metusers/klinogrid/KliNoGrid_16.12/FFMRR-Nor/catalog.html (accessed 13 December 2019).

HySN5

HySN5 is a modified version of HySN, a high-resolution HYbrid SeNorge data set of daily near-surface humidity, surface incident shortwave and longwave radiation, and surface pressure. The data have the same temporal frequency and projection as the SeNorge data sets. It is described and compared with surface observations and other data sets in Erlandsen *et al.* (2019). The downscaling procedure used to produce HySN5 is unchanged from Erlandsen *et al.* (2019); however, Era5 has replaced Era-Interim and SeNorge2018 has replaced SeNorge2. The assumptions and methods used to downscale humidity and longwave radiation are similar to those used in the WATCH and WFDEI data sets (Weedon *et al.* 2014), PGMFD (Sheffield *et al.* 2006), and NLDAS-1 (Cosgrove 2003).

HySN5 is compared with surface observations for the same time period as used in Erlandsen *et al.* (2019) (1982–1999), including 84 stations where measurements of 2-meter humidity are available, and 10 (2) stations where incident shortwave (longwave) radiation are observed. The comparison shows that HySN5 vapor pressure has a similar mean daily correlation with station measurements, 0.95, and a slightly lower mean absolute station bias than HySN, 31 kPa rather than 35 kPa (see Supplementary Figure S2). The incident shortwave radiation of HySN5 shows a slightly higher daily correlation with observations (0.95) than HySN (0.94, see Supplementary Figure S3); however, it also shows a larger mean difference to the station observations (7.9 W m^{-2}) than HySN (3.2 W m^{-2}). A proper validation of incident longwave radiation is difficult since only two stations are available, both situated near the coast; nevertheless, at the two stations, HySN5 shows a higher daily correlation with observations than HySN, 0.94 rather than 0.91; however, also here HySN5 shows a higher average difference to the observations (Supplementary Figure S4).

Vapor pressure deficit was estimated by calculating vapor pressure at saturation using SeNorge2018 T2. Net longwave radiation was calculated assuming a surface emissivity of 0.96 and that surface temperature can be approximated by T2. These two derived variables are available on request. At present, HySN5 is available from Zenodo from 1979 through 2000 (https://doi.org/10.5281/zenodo.3351430) and from 2001 through 2017 (https://doi.org/10.5281/zenodo.3516560).

Calibration and validation data

Discharge observations, quality controlled and available from The Norwegian Water Resources and Energy Directorate (NVE), for 119 catchments across Norway, were used for calibration and validation. Additional evaluation data includes 24,148 observations from 1,181 measurement sites of SWE. SWE was derived from snow depth and

density, which are routinely measured, predominantly measured in the mountainous regions of southern Norway, by hydropower companies (Saloranta 2012), usually once a year, around the time of maximum SWE.

Few measurements of evaporation are available for Norway as compared with other Nordic countries. Pan evaporation was measured in the summer season, May through September, between 1967 and 1972. Table 7.5 in Hetager & Lystad (1974) lists the mean monthly Pan evaporation, covering 3–5 years, for 42 stations (reproduced in the Supplementary Material). The measurements were retrieved by a Thorsrud 2500 evaporimeter, composed of a 50 cm deep sunken pan with a diameter of 56 cm, filled with water.

METHODS

The gridded HBV model

HBV-B03

HBV-B03 (Beldring *et al.* 2003) has a daily resolution and covers mainland Norway with 1 km^2 grid cells. The model performs water balance calculations for square grid cells characterized by their elevation, land use, and soil type. Each grid cell includes glacial and lake fractions, and up to three land cover classes, and one soil type. It has a snow routine with components for accumulation, and sub-grid scale distribution and ablation of snow. It also includes glacier melt. The evaporation routine includes a land cover-dependent evaporation, lake evaporation, and interception storage. Soil moisture and discharge are simulated including a sub-grid scale distribution of soil moisture storage, groundwater storage, and runoff response. Six soil parameters are routinely calibrated: field capacity (FC), an exponent controlling the fraction of infiltration that percolates to the upper zone (beta), a parameter controlling the percolation to the lower zone (perc), the upper (kuz) and lower (klz) zones' runoff response coefficients, and the upper zone recession parameter (alpha). The model further includes a routing module; however, routing has not been included in either of the model implementations discussed in this study.

HBV-H19

In HBV-H19 (Huang *et al.* 2019), HBV-B03 was modified by replacing its simple, temperature-based scaling of potential evaporation (E_p) with a Penman–Monteith big leaf approximation for estimating daily E_p. E_p parameters were set as fixed parameters based on the literature or physical empirical relationships in a look-up table; however, maximum interception storage was for most land cover classes calibrated according to the region and land cover class. The precipitation phase threshold temperature was set to 0 °C, while the threshold temperature for snow-melt and the degree-day factor were calibrated according to the region and land cover class. The minimum and maximum degree–day factor allowed during calibration was 0.0001 and 0.01 m $°C^{-1}$, respectively (Table 1 in Huang *et al.* (2019)). The land cover class was diagnosed based on the high-resolution National Land Resource Map (Ahlström *et al.* 2014) combined with a structural forest classification map provided by Majasalmi *et al.* (2018). Forests were classified into three species groups (spruce, pine, and deciduous) with four structure classes, each reflecting a low (class 1) to high (class 4) biomass density, among other attributes. The number of land cover and soil types represented by the model was increased to 19 and 12, respectively (see Huang *et al.* 2019). The model domain was divided into five calibration regions (see Figure 1(b)), which resulted from *k*-means clustering of two temperature and two precipitation indices.

HBV-E20

The model version used in this study, HBV-E20, builds upon HBV-B03 and HBV-H19. The land cover and soil type classification are based on the same data sets as in HBV-H19; however, the resulting classification is slightly modified for land cover, while the soil type classification was simplified, allowing a total of seven classes for all of Norway. Figure 2 depicts the dominant land cover class and soil type in each grid cell.

The evaporation scheme is similar to that described in HBV-H19. The Supplementary Material provides an overview of the implemented Penman–Monteith algorithm (Equation S3). In HBV-E20, surface resistance (r_s) is

Table 1 | Summary statistics comparing model simulated discharge and observations for the calibrated catchments in the calibration period and the independent period, and for independent basins

	Number of catchments	KGE (–)	Mean bias (simulated – observed) (mm/day)	Mean observed discharge (mm/day)	Relative bias (%)
Calibration period (2000–2010)	79	0.71 (0.74)	−0.3	17.2	−1.9
Independent period (1980–1999)	76	0.70 (0.75)	−0.1	13.6	−0.7
Independent basins (1980–2010)	34	0.74 (0.78)	−0.8	17.0	−4.8

modified from HBV-H19. The new approach describes r_s as a function of humidity deficit, visible radiation at the top of the canopy, and leaf area index, according to Leuning *et al.* (2008). Standard parameters are used, as recommended by Leuning *et al.* (2008), with maximum stomatal conductance given as a function of land cover class, and based on literature recommendations (Schulze *et al.* 1994; Kelliher *et al.* 1995; Körner 1995). Additionally, the surface resistance formula in Leuning *et al.* (2008) is modified to include a temperature constraint, as described in Mu *et al.* (2011). Look-up table values with parameters related to the 19 land cover types are provided in Supplementary Table S3.

HBV-E20 further includes changes to the model's snowmelt routine. We implement a radiation-restricted degree-day factor based on Kustas *et al.* (1994). A radiation-based melt rate, in meters per day, obtained by converting the R_n to snow-melt rate, is added to the common degree-day factor expression:

$$M = \max\left(C_{\text{temp}}(T2 - T2_{\text{melt}}) + C_{\text{rad}}\frac{R_n}{\lambda_f \rho_w}, 0\right) \quad (1)$$

where M is the melt rate per day in meters, C_{temp} is a calibrated degree-day factor, and $T2_{\text{melt}}$ is the melt temperature of snow, λ_f is the latent heat of fusion, 0.334 MJ kg^{-1}, R_n is

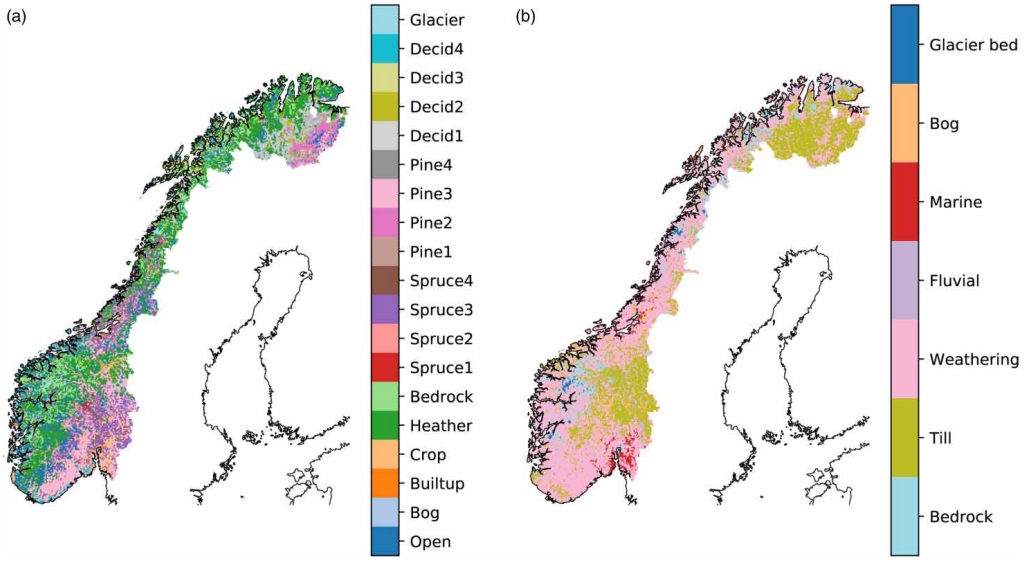

Figure 2 | The dominant land cover class within each grid cell is shown in (a), while (b) shows the soil type. Please refer to the online version of this paper to see this figure in color: https://doi.org/10.2166/nh.2021.132.

in MJ m^{-2} day^{-1}, ρ_w is the density of water (1,000 kg m^{-3}), and C_{rad} is a fraction scaling the radiation term, which is always less than unity (see Supplementary Table S3). C_{temp} is allowed to vary between 0.0014 and 0.0030 m °C^{-1} during the calibration, a considerably smaller range than allowed in e.g. HBV-H19 (0.0001 – 0.01 m °C^{-1}). The inclusion of a radiative term makes it possible for the simulated snow cover to respond to changes in incoming shortwave and longwave radiation, as well as surface albedo. Further, adding a radiative term makes it less likely that an unreasonably large amount of snow remains over the summers, ultimately building up so-called 'snow towers' (see e.g. Figure 6 in Skaugen & Weltzien (2016)). The adjustment makes it possible to run the model over consecutive years without zeroing out snow at the beginning of the hydrological year, which has been a common procedure to get rid of 'snow towers' in similar models (Skaugen & Weltzien 2016). The Supplementary Material includes an example of aggregated SWE in a simplified snow module when a traditional degree-day factor, with a constant melt rate of 2.5 mm °C^{-1} day^{-1} is employed, and when the new, radiation-restricted degree-day factor is used (Equation (1)).

The snow module of the HBV model is further modified. The former versions of the model decompose grid cells where ground snow is present into 1–9 sub-grid tiles, depending on the total grid cell SWE, where each tile represents similar snow depths within the grid cell; and further, the numerical snow scheme is applied separately to each of the tiles. In conjunction with adding a radiation-restricted snow-melt routine, the traditional, log-normal SWE-based grid cell tiling is replaced with a simple sigmoidal tanh-function representing grid cell snow cover fraction ($f_s = \tanh(75\,\mathrm{SWE})$, similar to e.g. Roesch *et al.* (2001). Omitting tiling simplifies the model structure, which, following the implementation of the radiation-restricted degree-day factor, would also have needed a tile-area-based discretization of net radiation. Furthermore, the previously used tiling approach was also associated with the build-up of 'snow towers' (Frey & Holzmann 2015).

A final, physically based model enhancement was implemented, which has its base in the availability of high-quality humidity estimates. The traditionally, often calibrated, precipitation phase threshold temperature was replaced with a diagnostic criteria where precipitation is set as snowfall if T2 is below 1 °C and the 2-meter dew point temperature is below 0 °C, and as rain otherwise. Recent studies (Jennings *et al.* 2018; Jennings & Molotch 2019) have shown that including humidity as a predictor of precipitation phase increases its accuracy, as snowfall is more likely in drier rather than more humid environments given the same T2.

Calibration and validation

The model was calibrated with the aim to minimize the regional mean catchment bias in discharge (simulated – observed daily discharge) and to maximize the regional mean KGE. KGE is related to the Nash–Sutcliffe efficiency (NSE), but avoid two caveats embedded within NSE, namely (i) that in order to reach a maximum NSE, variability has to be underestimated, and (ii) within NSE, bias is scaled by the observed temporal standard deviation, which may inflate scores in watersheds with a high seasonal component. The KGE version used is from Gupta *et al.* (2009):

$$\mathrm{KGE} = 1 - \sqrt{(r-1)^2 + (\sigma_s/\sigma_o - 1)^2 + (\mu_s/\mu_o - 1)^2} \qquad (2)$$

where r is the Pearson correlation coefficient, σ_s and σ_o are the simulated and observed standard deviation, and μ_s and μ_o are the simulated and observed mean. The optimal KGE, and highest possible value, is unity, while it has no lower limit. The KGE is a relative bias measure, so the two optimization goals used in model calibration are not entirely independent.

The model was jointly calibrated for catchments within each of the five calibration regions. The regions following HBV-H19 and are shown in Figure 1(b). Observed daily discharge during the period 2000–2010 from 85 catchments located across mainland Norway was used in the calibration, and discharge observations from 34 independent stations were used for validation. At all calibrated stations, the model was additionally validated for an independent period, 1980 through 1999.

For each of the five regions, only three above-ground parameters were calibrated: a multiplicative correction factor for precipitation, an additional multiplicative

undercatch correction factor in case of snowfall, and the snow-melt degree-day factor (C_{temp}). The six soil parameters described in HBV-B03, FC, beta, perc, kuz, klz, and alpha were individually calibrated for each soil class, except for the glacier and till class, which were merged. Thus, the parameters of a maximum of six soil classes were calibrated for each region, depending on the number of soil classes represented within a region. Lower zone lake runoff response (klz) was set according to that of soil class bog. The regional calibration was conducted using PEST: Model-Independent Parameter Estimation and Uncertainty Analysis (Doherty 2015).

Model evaluation

In order to assess the HBV-E20 model's ability to simulate relevant hydrological states, fluxes and temporal dynamics, results were evaluated against a variety of observational data sets: (i) Simulated SWE was compared with 24,148 SWE observations from 1,181 unique locations from around the time of maximum SWE. (ii) The routine for estimating potential evaporation (E_p), including surface resistance, was evaluated by comparing to May–September mean monthly pan evaporation observations (1967–1972). E_p was calculated for the land cover class 'Open', which represents short vegetation (height = 20 cm, leaf area index = 2, see Supplementary Table S3). The estimated E_p was obtained for the five closest years for which the HBV forcing data is available, i.e. 1979–1984. (iii) The model's ability to reproduce observed trends in monthly discharge was evaluated using a modified Mann–Kendall test including a trend free pre-whitening method (Yue & Wang 2002), as implemented in pyMannKendall (Hussain & Mahmud 2019). For the trend test to be applied 29 out of 30 complete years of daily observations were required, following in-filling of up to two consecutive days of missing data by linear interpolation.

RESULTS

The model was calibrated and validated in terms of regional mean KGE and bias of its daily discharge estimates. The calibrated model parameters are presented in the Supplementary Material. The calibrated parameters were either derived for each calibration region or for each soil class within a calibration region. The calibration provided values for the full study domain except for parameters for the soil class 'marine' within region 1 and 2. These were given calibrated parameters from the soil class 'fluvial'. The model calibration resulted in minor correction factors for rain and snowfall, with the product of the two correction factors amounting to an average increase of 3%. The model corrected precipitation was just 1.4% larger than the SeNorge2018 precipitation between 1980 and 2014 (see Supplementary Material). The model's ability to reproduce potential evaporation, winter maximum SWE, and discharge trends are evaluated below. Finally, the physically enhanced HBV model is applied to provide a mean water balance for the period 1980–2014.

Daily discharge, potential evaporation, maximum SWE, and monthly discharge trends

Daily discharge

The results of the model calibration and validation are given in Table 1, including only catchments where at least 5 years of observations are available. Daily mean and median KGE, with the median given within brackets, mean bias, mean observed discharge, and relative bias are provided. The calibration resulted in a median KGE of 0.74. A KGE above 0.6 was achieved in 86% of the catchments, values above 0.7 in 66% of the catchments, while a KGE score above 0.8 was achieved in 22% of the catchments. In five catchments, the KGE score was above 0.85. The mean bias was −0.3 mm/day or −1.9% of mean discharge. When the model was run for an independent time period, 1980–1999, the median KGE for the catchments was 0.75, while the mean bias was −0.1 mm/day or −0.7% of the mean observed discharge. The model was further evaluated for 34 independent catchments not included in calibration. For these catchments, the median KGE was 0.78, and the mean bias −0.8 mm/day, or −4.8% of observed discharge, for the period 1980–2010. The distribution of KGE and mean bias for the calibration and independent catchments, and for the calibration period and the independent time period is displayed in Supplementary Figure S10. Depending

on the metric considered HBV-E20 show equally good or better performance than previous gridded HBV versions applied for the same domain (see Huang *et al.* 2019 and references therein).

Winter maximum SWE

SWE observations from around the time of maximum SWE are in Figure 3 compared with the model's simulated SWE. The observations and model estimates show a Pearson correlation coefficient of 0.78 (Figure 3(a)). The model's simulated maximum SWE is on average 6 cm higher than the observations; however, as seen in Figure 3(b), there is a strongly significant, positive correlation ($p < 0.000$) between SWE bias and the difference between model grid cell and measurement altitude.

Potential evaporation

The new scheme to calculate potential evaporation, E_p, is compared with pan evaporation in the growing season from May through September in Figure 4. The maps (upper row) and box plots (lower row) compare mean monthly simulated E_p for the land cover class 'Open' (1979–1984) to the pan measurements (1967–1972). A reasonable agreement is found; however, the simulated E_p tends to show higher values than the pan measurements in July, but lower values in September. Overall, the pan measurements show a May to September evaporation of 284 mm, while the simulated values give 272 mm, i.e. 96% of the measured values.

Discharge trends

Trends in observed and simulated monthly discharge for the period 1985–2014 at various measurement stations are shown as a heat map in Figure 5, where a blue color indicates an increasing trend and a red color indicates a decreasing trend. The trends' significance is evaluated using a Mann–Kendall test, and significant trends (low *p*-values) are marked with one or more asterisks in the plot. At most of the stations, a notable shift in discharge can be seen from early summer or late spring to earlier in spring. This is evident in both the model simulations and observations; the largest monthly change in both is an increase in discharge of around 1.6% in April. The single, largest observed change is an increase of 5.2% at the

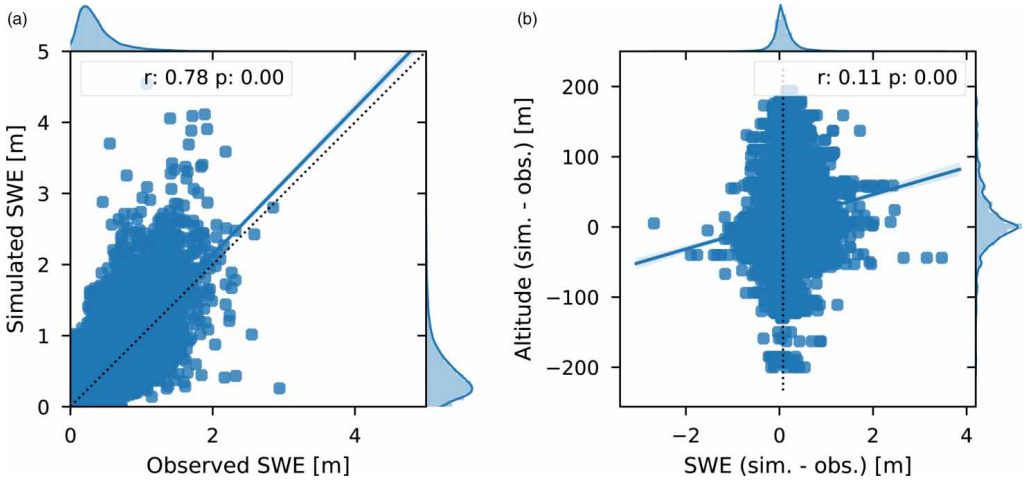

Figure 3 | Observed (*x*) and simulated (*y*) SWE around the time of maximum SWE (a), and difference between simulated and observed SWE (*x*) plotted against difference in altitude between the model grid cell and observation (*y*) (b). The Pearson correlation and its significance are denoted near the top of each plot.

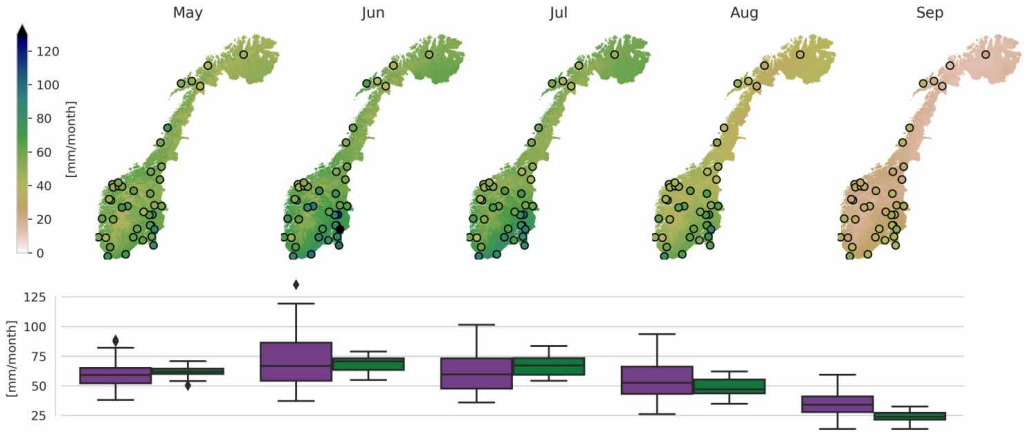

Figure 4 | Mean monthly pan evaporation measured at 42 sites across Norway (1967–1972) shown within black circles overlaid the simulated E_p for the land cover class 'Open' (1979–1984). The lower box plots show the pan measurements in purple and the simulated E_p for collocated grid cells in green. Please refer to the online version of this paper to see this figure in color: https://doi.org/10.2166/nh.2021.132.

station Sundbyfoss, where the model shows a corresponding 3.3% increase. Overall, the trend patterns in the observations are reproduced by the model; however, there are some regions and times of the year with discrepancies, e.g. an observed increase in winter discharge at several stations in Finnmark and Nordland and at Bjoreio (50.13, Hardanger county), which are not reproduced by the model.

1980–2014 water balance

The September 1980 to August 2014 simulated mean annual E_p, evaporation (E), precipitation (P), runoff (R), and the evaporation fraction of precipitation, i.e. E/P, are depicted in Figure 6. There are large regional variations in the water balance elements, with the coastal regions receiving the most precipitation and producing the highest runoff, while more continental regions show the highest potential and actual evaporation. Areal median (mean) annual P is 1,168 (1,367) mm, while R is 975 (1,179) mm, E 157 (178) mm, and E_p 182 (210) mm. The evaporation fraction is 0.17, i.e. just above one-sixth; however, in southeastern and northeastern parts of Norway, annual evaporation reach 40% of precipitation.

DISCUSSION

Model calibration and validation

The herein alterations to the gridded HBV model code implemented in HBV-E20, including a modified physically based potential evaporation routine, a radiation-restricted degree-day factor for snow-melt, and the introduction of humidity as a predictor of precipitation phase led to fewer calibrated parameters. A reduction in the number of parameters reduces the dimensions in parameter space and with that parameter uncertainty, contributing to a more robust model in general, and for climate change impact assessment in particular.

The model achieved a median KGE between 0.74 and 0.78, and a mean bias between −0.1 and −0.8 mm/day, depending on the period and catchments considered. Though the primary goal of the alterations was to increase the physical robustness of the model under climate change, we find that the HBV-E20 model's performance in simulating daily discharge is equally good or better than previous gridded HBV versions applied for the same domain (see Huang *et al.* 2019 and references therein). Additionally, the model showed a fair amount of skill in reproducing observed annual maximum SWE, with a correlation of 0.78 and a

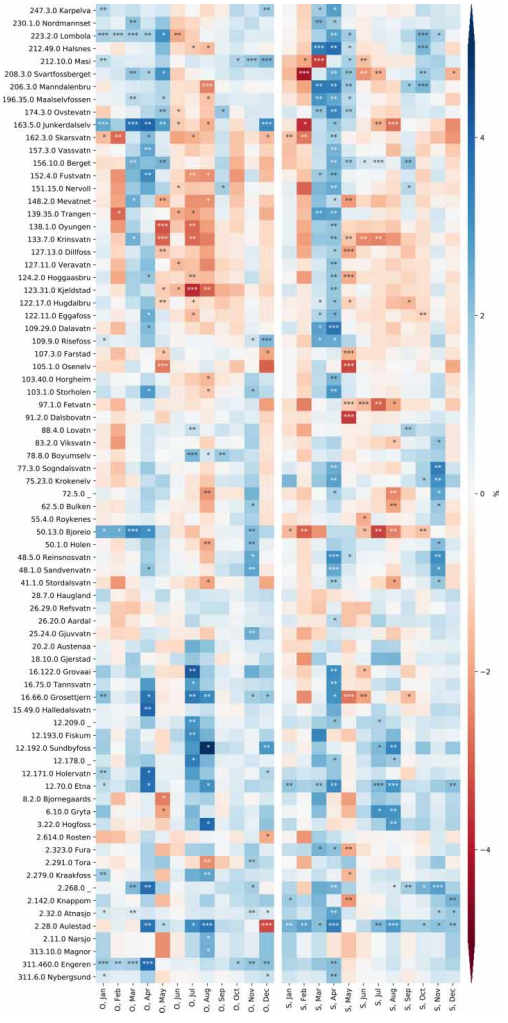

Figure 5 | Observed (left panel) and simulated (right panel) monthly trends in discharge (%) between 1985 and 2014 for individual catchments, sorted from north (upper rows) to south (lower rows). *$p < 0.1$, **$p < 0.05$, ***$p < 0.01$. Please refer to the online version of this paper to see this figure in color: https://doi.org/10.2166/nh.2021.132.

mean difference of 6 cm to the point observations. The improved availability of high-quality forcing data facilitated the implementation of model alterations and thus likely contributed to the improved model performance.

A reasonable agreement was seen between pan evaporation measurements (1967–1972) and E_p calculated for the land cover class 'Open' (representing short vegetation) (1979–1984), with the latter amounting to 95% of the former. The pan evaporation measurements show higher regional variability than the estimates. This may, in part, be explained by the fact that the measurements represent points in the terrain with a varying degree of exposure (Hetager & Lystad 1974), while the estimates are provided for 1×1 km grid cell averages. The pan measurements showed relatively higher values in September, whereas the calculated E_p showed relatively higher values in July. Evaporation rates from pans are on average above that of larger, natural water bodies, since pans are surrounded by drier areas, leaving the air less saturated (the oasis effect), and because the pan itself can absorb heat and sunlight, ultimately increasing evaporation. According to Allen *et al.* (1998), reference crop evaporation may be 0.5–1.1 of that measured from a pan, depending on the wind speed, humidity, fetch, and surrounding vegetation. The calculated E_p for the 'Open' land cover class should, similarly to reference crop evaporation, show lower values than the pan measurements. While the variation in the time periods considered may influence the differences seen in observed and simulated E_p, it is possible that the HySN5 incident shortwave radiation, which shows slight overestimations compared with surface observations, contributes to the slightly larger calculated E_p than the pan observations mid-summer. However, the lack of surface observations of incident longwave radiation limits a comprehensive validation of the forcing data estimates, and it is thus difficult to say if the total incident radiation is overestimated or not. A likely larger impact on the calculated E_p is the choice of E_p parameter values for the land cover class 'Open'. The values chosen for the current implementation in HBV should, however, be reasonable, given the close agreement found with the pan measurements. It should be noted that the veracity of estimated E_p for other vegetation types, and the estimates of evaporation from the coniferous forest, where interception loss plays a significant part, remains uncertain due to the lack of observations to constrain the estimates.

A comparison of monthly discharge trends revealed an overall good agreement of the trend; however, for some catchments and calendar months, the simulated and

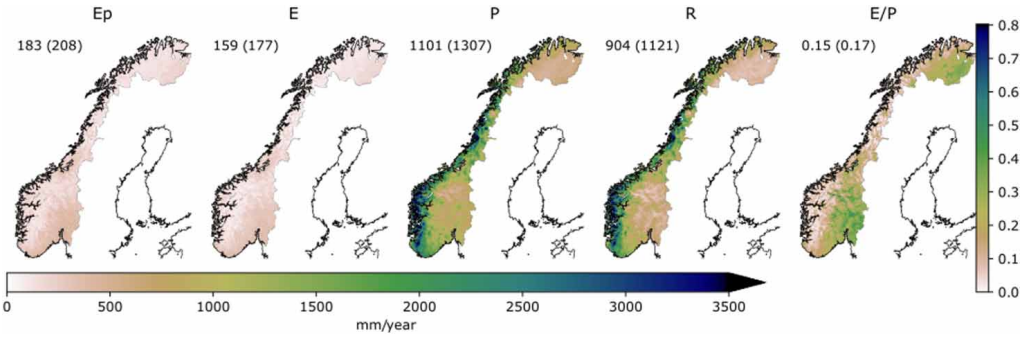

Figure 6 | The 1980–2014 mean annual potential evaporation (E_p), evaporation (E), precipitation (P), runoff (R), and E/P, in mm/year. The areal median and mean are denoted in the upper left corner, with the mean in parenthesis. Please refer to the online version of this paper to see this figure in color: https://doi.org/10.2166/nh.2021.132.

observed trends did not agree. These discrepancies, where present, might be explained by deficiencies in the model, e.g. in its diagnosis of precipitation phase, melting temperature, or perhaps its lack of representation of land use change (e.g. Erlandsen *et al.* 2017). The lack of precipitation observations in some regions, particularly in the mountains, and the variation in the station network feeding into the SeNorge precipitation data set with time, likely limits the ability of the HBV model to reproduce observed discharge trends. Work is currently in progress to resolve the latter issue; a gridded precipitation data set where the observation network is consistent with time (see e.g. Masson & Frei 2016) is under construction (pers. comm. C. Lussana, MET Norway).

The model calibration resulted in very small correction factors for rain and snowfall; model corrected P was just 1.4% larger than the SeNorge2018 precipitation. Allowed ranges of precipitation and snow correction factors under calibration typically vary from around 0.5, i.e. a halving, to 2–3, that is doubling or tripling the precipitation amount (e.g. Table 1 within Huang *et al.* (2019)). The small correction factors of the current study can likely largely be attributed to the high quality of the SeNorge2018 forcing data, which, unlike its predecessor, SeNorge2, includes a correction for precipitation undercatch. The mean annual P for Norway is about 280 mm or 26% higher in SeNorge2018 than its predecessor, SeNorge2. The physically based E_p estimates, being considerably smaller than those estimated in previous versions of the HBV model (see the discussion below), also contribute to smaller precipitation correction factors.

1980–2014 water balance

Averaged over continental Norway, HBV-E20 produced a September 1980 to August 2014 mean annual water balance of 1,367 mm P, E of 178 mm, and 1,179 mm R. Previous water balance estimates for Norway vary considerably (see Table 2). HBV-H19 gives 1983–2012 average annual water balance elements of about 1,333 mm P, 221 mm E, and 1,121 mm R. The climate synthesis report for Norway (Hanssen-Bauer *et al.* 2009, in Norwegian) states that 1961–1990 areal average P is 1,486 mm, E 346 mm, and R 1,140 mm; while the similar, updated climate report published in 2017 (Hanssen-Bauer *et al.* 2017) states that 1971–2000 average P is 1,600 mm, E slightly less than 500 mm, and R 1,100 mm.

Table 2 | Estimates of the annual surface water balance, provided for annual precipitation (P, mm), evaporation (E, mm), and runoff (R, mm), over continental Norway

Source	Period	*P*	*E*	*R*
HBV-E20	1980–2014	1,367	178	1,179
Huang *et al.* (2019) HBV-H19	1983–2012	1,333	221	1,112
Hanssen-Bauer *et al.* (2017) HBV-B03	1971–2000	1,600	500	1,100
Hanssen-Bauer *et al.* (2009) HBV-B03	1961–1990	1,486	346	1,140

It should be noted that the estimates provided in the two climate synthesis reports were based on a simple, temperature-dependent E approximation (as outlined in HBV-B03), and that the estimates are for different reference periods. Furthermore, the precipitation estimates have different sources. The estimates provided in Hanssen-Bauer *et al.* (2009) were based on stations measurements that were interpolated and given correction factors within the gridded hydrological model. The estimates in Hanssen-Bauer *et al.* (2017) were based on a previous version of the national, gridded, observation-based precipitation estimates (SeNorge), and precipitation correction factors added during calibration. The SeNorge data set likely overestimated precipitation (Saloranta 2012). The P estimate of HBV-H19 was based on SeNorge2, after precipitation correction factors had been added.

While the various R estimates are similar, likely since this estimate is constrained by discharge measurements, the estimates of P and E vary considerably. New and improved observational data, particularly of evaporation, incident longwave radiation, and high-altitude precipitation, would help constrain the water balance estimates. Furthermore, future studies regarding the treatment of intercepted precipitation, particularly given that the model is run with a daily resolution, are needed to reduce uncertainty regarding Norway's mean water balance (Tallaksen *et al.* 1996; Haddeland *et al.* 2006). Examples of physically based model enhancements that could help constrain long-term water balance estimates include, e.g.: (i) a sub-daily temporal resolution, which could make way for an improved representation of rain- and snowfall interception; (ii) improved description of sublimation processes; and (iii) inline computation of surface net longwave radiation, possibly based on the inclusion of snow-pack thermal inertia (cold content).

CONCLUSIONS

With the availability of updated and improved forcing data, a gridded version of the HBV model has been enhanced to include a physically based evaporation scheme, a net radiation-restricted degree-day factor approach for snow-melt, and a prescribed precipitation phase threshold based on 2-meter temperature and humidity. The improved forcing data combined with more physically based parameterizations allowed for the model to be calibrated for mainland Norway with fewer free parameters, i.e. only three calibrated above-soil parameters for each of five calibration regions. The model calibration resulted in relatively small correction factors for rain and snowfall, increasing precipitation with just 1.4% compared with the original field. The model showed equally good or better results than previous gridded versions constructed for the same domain. Furthermore, annual maximum SWE, E_p, and discharge trends were satisfactorily represented by the model when compared with observations. The model's mean annual water balance showed lower P and E values for mainland Norway than previous estimates. Additional modeling studies and more observational data are needed to get higher confidence in current and recent estimates of Norway's water balance.

These are the first steps among several that might be undertaken to improve process representation in the model providing more robust long-term water balance estimates in a changing climate. Additional constraints, which might further improve and constrain the physical process description and calibration of the model, include enhanced gridded precipitation data sets, further improved representation and parameterization of the land surface (soil, bedrock, and vegetation), and additional physically based model enhancements.

ACKNOWLEDGEMENTS

The authors would like to thank Tumo Saloranta at NVE for providing SWE data. S.B., S.E., and S.H. were supported by the Norwegian Research Council under grant no. 243803/E10 (I:CAN – Impacts: Climate, Anthroposphere and Nature) and grant no. 295128/E10 (The human imprint on land-atmosphere exchange in high latitudes). The study has further been supported by the Norwegian Centre for Climate Services. This work is a contribution to the Strategic Research Initiative 'Land Atmosphere Interaction in Cold Environments' (LATICE) of the University of Oslo. We also thank two anonymous reviewers for helpful comments on the manuscript.

DATA AVAILABILITY STATEMENT

Data cannot be made publicly available. Readers should contact the corresponding author for details.

REFERENCES

Ahlström, A., Bjørkelo, K. & Frydenlund, J. 2014 AR5 klassifikasjonssystem - Klassifikasjon av arealressurser Rapport fra skog og landskap (06/14).

Allen, R. G., Pereira, L. S., Raes, D. & Smith, M. 1998 Crop evapotranspiration: Guidelines for computing crop requirements. Irrigation and Drainage Paper No. 56, FAO. https://doi.org/10.1016/j.eja.2010.12.001.

Beldring, S. 2002 Runoff generating processes in boreal forest environments with glacial tills. *Nordic Hydrology*. https://doi.org/10.2166/nh.2002.0013.

Beldring, S., Engeland, K., Roald, L. A., Sælthun, N. R. & Voksø, A. 2003 Estimation of parameters in a distributed precipitation-runoff model for Norway. *Hydrology and Earth System Sciences* **7** (3), 304–316. https://doi.org/10.5194/hess-7-304-2003.

Bruland, O., Sand, K. & Killingtveit, Å. 2001 Snow distribution at a high arctic site at Svalbard. *Nordic Hydrology*. https://doi.org/10.2166/nh.2001.0001.

Buckland, S. M., Grime, J. P., Hodgson, J. G. & Thompson, K. 1997 A comparison of plant responses to the extreme drought of 1995 in Northern England. *The Journal of Ecology*. https://doi.org/10.2307/2960608.

Clark, M. P., Fan, Y., Lawrence, D. M., Adam, J. C., Bolster, D., Gochis, D. J., Hooper, R. P., Kumar, M., Leung, L. R., Mackay, D. S., Maxwell, R. M., Shen, C., Swenson, S. C. & Zeng, X. 2015 Improving the representation of hydrologic processes in Earth System Models. *Water Resources Research* **51** (8), 5929–5956. https://doi.org/10.1002/2015WR017096.

Cosgrove, B. A. 2003 Real-time and retrospective forcing in the North American Land Data Assimilation System (NLDAS) project. *Journal of Geophysical Research* **108** (D22), 8842. https://doi.org/10.1029/2002JD003118.

Dee, D. P., Uppala, S. M., Simmons, A. J., Berrisford, P., Poli, P., Kobayashi, S., Andrae, U., Balmaseda, M. A., Balsamo, G., Bauer, P., Bechtold, P., Beljaars, A. C. M., van de Berg, L., Bidlot, J., Bormann, N., Delsol, C., Dragani, R., Fuentes, M., Geer, A. J. & Vitart, F. 2011 The ERA-Interim reanalysis: configuration and performance of the data assimilation system. *Quarterly Journal of the Royal Meteorological Society* **137** (656), 553–597. https://doi.org/10.1002/qj.828.

Doherty, J. 2015 *Calibration and Uncertainty Analysis for Complex Environmental Models*. Watermark Numerical Computing, Brisbane, Australia.

Erlandsen, H. B., Haddeland, I., Tallaksen, L. M. & Kristiansen, J. 2017 The sensitivity of the terrestrial surface energy and water balance estimates in the WRF model to lower surface boundary representations: a South Norway case study. *Journal of Hydrometeorology* **18** (1), 265–284. https://doi.org/10.1175/JHM-D-15-0146.1.

Erlandsen, H. B., Tallaksen, L. M. & Kristiansen, J. 2019 Merits of novel high-resolution estimates and existing long-term estimates of humidity and incident radiation in a complex domain. *Earth System Science Data* **11** (2), 797–821. https://doi.org/10.5194/essd-11-797-2019.

Ferguson, R. I. 1999 Snowmelt runoff models. *Progress in Physical Geography: Earth and Environment* **23** (2), 205–227. https://doi.org/10.1177/030913339902300203.

Frey, S. & Holzmann, H. 2015 A conceptual, distributed snow redistribution model. *Hydrology and Earth System Sciences* **19** (11), 4517–4530. https://doi.org/10.5194/hess-19-4517-2015.

Gupta, H. V., Kling, H., Yilmaz, K. K. & Martinez, G. F. 2009 Decomposition of the mean squared error and NSE performance criteria: implications for improving hydrological modelling. *Journal of Hydrology* **377** (1–2), 80–91. https://doi.org/10.1016/j.jhydrol.2009.08.003.

Haddeland, I., Lettenmaier, D. P. & Skaugen, T. 2006 Reconciling simulated moisture fluxes resulting from alternate hydrologic model time steps and energy budget closure assumptions. *Journal of Hydrometeorology* **7** (3), 355–370. https://doi.org/10.1175/JHM496.1.

Hanssen-Bauer, I., Drange, H., Førland, E., Roald, L. A., Børsheim, K. Y., Hisdal, H., Lawrence, D., Nesje, A., Sandven, S., Sorteberg, A., Sndby, S., Vasskog, K. & Ådlandsvik, B. 2009 *Klima i Norge 2100 Bakgrunnsmateriale til NOU Klimatilpasning (Climate in Norway 2100 Background Material for NOU Climate Adaptation)*, p. 148.

Hanssen-Bauer, I., Førland, E. J., Haddeland, I., Hisdal, H., Lawrence, D., Mayer, S., Nesje, A., Nilsen, J. E. Ø., Sandven, S., Sandø, A. B., Sorteberg, A. & Ådlandsvik, B. 2017 Climate in Norway 2100 – a knowledge base for climate adaptation. Norwegian Environment Agency (Miljødirektoratet).

Hegdahl, T. J., Tallaksen, L. M., Engeland, K., Burkhart, J. F. & Xu, C. Y. 2016 Discharge sensitivity to snowmelt parameterization: a case study for Upper Beas basin in Himachal Pradesh, India. *Hydrology Research*. https://doi.org/10.2166/nh.2016.047.

Hersbach, H., Rosnay, P. d., Bell, B., Schepers, D., Simmons, A., Soci, C., Abdalla, S., Alonso-Balmaseda, M., Balsamo, G., Bechtold, P., Berrisford, P., Bidlot, J.-R., de Boisséson, E., Bonavita, M., Browne, P., Buizza, R., Dahlgren, P., Dee, D., Dragani, R. & Zuo, H. 2018 *Operational Global Reanalysis: Progress, Future Directions and Synergies with NWP*. ERA Report Series (ERA Report).

Hetager, S. E. & Lystad, S. L. 1974 *Fordampning fra fri vannflate: verdier basert på målinger i perioden 1967–1972*. Den Norske komité for Den internasjonale hydrologiske dekade.

Hrachowitz, M. & Clark, M. P. 2017 HESS opinions: the complementary merits of competing modelling philosophies

in hydrology. *Hydrology and Earth System Sciences*. https://doi.org/10.5194/hess-21-3953-2017

Huang, S., Eisner, S., Magnusson, J. O., Lussana, C., Yang, X. & Beldring, S. 2019 Improvements of the spatially distributed hydrological modelling using the HBV model at 1 km resolution for Norway. *Journal of Hydrology* **577**, 123585. https://doi.org/10.1016/J.JHYDROL.2019.03.051.

Hussain, M. & Mahmud, I. 2019 pyMannKendall: a python package for non parametric Mann Kendall family of trend tests. *Journal of Open Source Software* **4** (39), 1556. https://doi.org/10.21105/joss.01556.

Jennings, K. S. & Molotch, N. P. 2019 The sensitivity of modeled snow accumulation and melt to precipitation phase methods across a climatic gradient. *Hydrology and Earth System Sciences* **23** (9), 3765–3786. https://doi.org/10.5194/hess-23-3765-2019.

Jennings, K. S., Winchell, T. S., Livneh, B. & Molotch, N. P. 2018 Spatial variation of the rain-snow temperature threshold across the Northern Hemisphere. *Nature Communications* **9** (1), 1148. https://doi.org/10.1038/s41467-018-03629-7.

Kauffeldt, A., Wetterhall, F., Pappenberger, F., Salamon, P. & Thielen, J. 2016 Technical review of large-scale hydrological models for implementation in operational flood forecasting schemes on continental level. *Environmental Modelling and Software*. https://doi.org/10.1016/j.envsoft.2015.09.009.

Kelliher, F. M., Leuning, R., Raupach, M. R. & Schulze, E. D. 1995 Maximum conductances for evaporation from global vegetation types. *Agricultural and Forest Meteorology*. https://doi.org/10.1016/0168-1923(94)02178-M.

Körner, C. 1995 Leaf diffusive conductances in the major vegetation types of the globe. *Ecophysiology of Photosynthesis*. https://doi.org/10.1007/978-3-642-79354-7_22.

Kustas, W. P., Rango, A. & Uijlenhoet, R. 1994 A simple energy budget algorithm for the snowmelt runoff model. *Water Resources Research*. https://doi.org/10.1029/94WR00152.

Leuning, R., Zhang, Y. Q., Rajaud, A., Cleugh, H. & Tu, K. 2008 A simple surface conductance model to estimate regional evaporation using MODIS leaf area index and the Penman-Monteith equation. *Water Resources Research*. https://doi.org/10.1029/2007WR006562.

Lindström, G., Johansson, B., Persson, M., Gardelin, M. & Bergström, S. 1997 Development and test of the distributed HBV-96 hydrological model. *Journal of Hydrology* **201** (1–4), 272–288. https://doi.org/10.1016/S0022-1694(97)00041-3.

Lussana, C., Tveito, O. E. & Uboldi, F. 2018 Three-dimensional spatial interpolation of 2 m temperature over Norway. *Quarterly Journal of the Royal Meteorological Society* **144** (711), 344–364. https://doi.org/10.1002/qj.3208.

Lussana, C., Tveito, O. E., Dobler, A. & Tunheim, K. 2019 seNorge_2018, daily precipitation, and temperature datasets over Norway. *Earth System Science Data* **11** (4), 1531–1551. https://doi.org/10.5194/essd-11-1531-2019.

Magnusson, J., Wever, N., Essery, R., Helbig, N., Winstral, A. & Jonas, T. 2015 Evaluating snow models with varying process representations for hydrological applications. *Water Resources Research*. https://doi.org/10.1002/2014WR016498.

Majasalmi, T., Eisner, S., Astrup, R., Fridman, J. & Bright, R. M. 2018 An enhanced forest classification scheme for modeling vegetation–climate interactions based on national forest inventory data. *Biogeosciences* **15** (2), 399–412. https://doi.org/10.5194/bg-15-399-2018.

Masson, D. & Frei, C. 2016 Long-term variations and trends of mesoscale precipitation in the Alps: recalculation and update for 1901–2008. *International Journal of Climatology* **36** (1), 492–500. https://doi.org/10.1002/joc.4343.

Merz, R., Parajka, J. & Blöschl, G. 2011 Time stability of catchment model parameters: implications for climate impact analyses. *Water Resources Research* **47** (2). https://doi.org/10.1029/2010WR009505.

Milly, P. C. D. & Dunne, K. A. 2011 On the hydrologic adjustment of climate-model projections: the potential pitfall of potential evapotranspiration. *Earth Interactions* **15** (1), 1–14. https://doi.org/10.1175/2010EI363.1.

Monteith, J. L. 1965 Evaporation and environment. In *Symposia of the Society for Experimental Biology*, Vol. 19. Cambridge University Press (CUP), Cambridge, pp. 205–234.

Mu, Q., Zhao, M. & Running, S. W. 2011 Improvements to a MODIS global terrestrial evapotranspiration algorithm. *Remote Sensing of Environment* **115** (8), 1781–1800. https://doi.org/10.1016/j.rse.2011.02.019.

Nash, J. E. & Sutcliffe, J. V. 1970 River flow forecasting through conceptual models: part I – a discussion of principles. *Journal of Hydrology* **10** (3), 282–290. https://doi.org/10.1016/0022-1694(70)90255-6

Roesch, A., Wild, M., Gilgen, H. & Ohmura, A. 2001 A new snow cover fraction parameterization for the ECHAM4 GCM. *Climate Dynamics* **17** (12), 933–946. https://doi.org/10.1007/s003820100153.

Saloranta, T. M. 2012 Simulating snow maps for Norway: description and statistical evaluation of the seNorge snow model. *The Cryosphere* **6** (6), 1323–1337. https://doi.org/10.5194/tc-6-1323-2012.

Schulze, E. D., Kelliher, F. M., Korner, C., Lloyd, J. & Leuning, R. 1994 Relationships among maximum stomatal conductance, ecosystem surface conductance, carbon assimilation rate, and plant nitrogen nutrition: a global ecology scaling exercise. *Annual Review of Ecology and Systematics*. https://doi.org/10.1146/annurev.es.25.110194.003213.

Sheffield, J., Goteti, G. & Wood, E. F. 2006 Development of a 50-year high-resolution global dataset of meteorological forcings for land surface modeling. *Journal of Climate* **19** (13), 3088–3111. https://doi.org/10.1175/JCLI3790.1.

Skaugen, T. & Weltzien, I. H. 2016 A model for the spatial distribution of snow water equivalent parameterized from the spatial variability of precipitation. *Cryosphere* **10** (5), 1947–1963. https://doi.org/10.5194/tc-10-1947-2016.

Tallaksen, L. M., Schunselaar, S. & Van Veen, R. 1996 Comparative model estimates of interception loss in a

coniferous forest stand. *Nordic Hydrology* **27** (3), 143–160. https://doi.org/10.2166/nh.1996.0001.

Weedon, G. P., Balsamo, G., Bellouin, N., Gomes, S., Best, M. J. & Viterbo, P. 2014 The WFDEI meteorological forcing data set: WATCH forcing data methodology applied to ERA-Interim reanalysis data. *Water Resources Research* **50** (9), 7505–7514. https://doi.org/10.1002/2014WR015638.

Weynants, M., Montanarella, L. & Tóth, G. 2013 European HYdropedological Data Inventory (EU-HYDI). In: *European Commission Joint Research Centre Institute for Environment and Sustainability*. https://doi.org/10.2788/5936.

Wolff, M. A., Isaksen, K., Petersen-ØVerleir, A., Ødemark, K., Reitan, T. & Brækkan, R. 2015 Derivation of a new continuous adjustment function for correcting wind-induced loss of solid precipitation: results of a Norwegian field study. *Hydrology and Earth System Sciences* **19** (2), 951–967. https://doi.org/10.5194/hess-19-951-2015.

Wong, W. K., Beldring, S., Engen-Skaugen, T., Haddeland, I. & Hisdal, H. 2011 Climate change effects on spatiotemporal patterns of hydroclimatological summer droughts in Norway. *Journal of Hydrometeorology*. https://doi.org/10.1175/2011JHM1357.1.

Yue, S. & Wang, C. Y. 2002 Applicability of prewhitening to eliminate the influence of serial correlation on the Mann-Kendall test. *Water Resources Research*. https://doi.org/10.1029/2001wr000861.

Zappa, M., Pos, F., Strasser, U., Warmerdam, P. & Gurtz, J. 2003 Seasonal water balance of an alpine catchment as evaluated by different methods for spatially distributed snowmelt modelling. *Nordic Hydrology*. https://doi.org/10.2166/nh.2003.0003.

First received 5 September 2020; accepted in revised form 11 December 2020. Available online 19 January 2021

S1 Data and methods

S1.1 Forcing data

S1.1.1 SeNorge2018

Annual mean precipitation (1980-2014) over mainland Norway of SeNorge2.1, SeNorge2018, and the difference between the two (SeNorge2018 - SeNorge2.1) are shown in Figure S1.

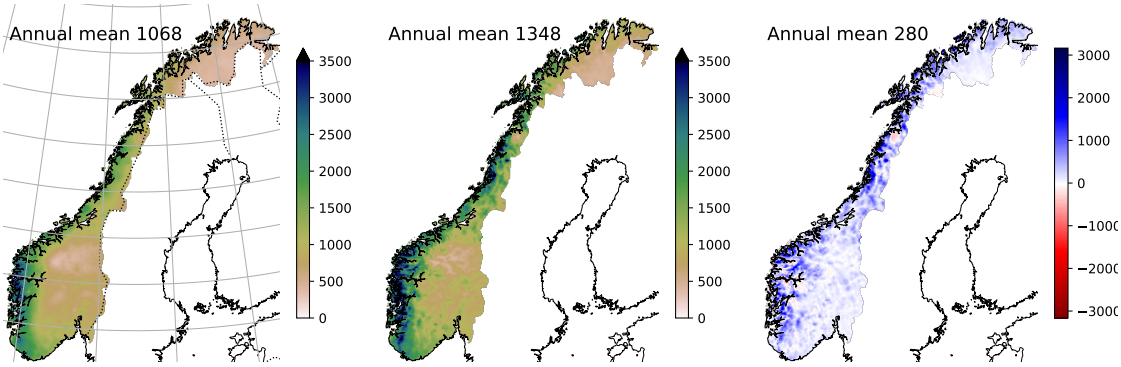

Figure S1: The annual mean precipitation (1980-2014) of SeNorge2.1 (left hand side), SeNorge2018 (center), and SeNorge2018 - SeNorge2.1 (r.h.s) in mainland Norway.

S1.1.2 HySN5

HySN5 ingests reanalysis variables from Era5, which means that the data-set may be extended back in time to cover the full SeNorge historic period once Era5 covers these periods. HySN5 estimates between 1982 and 2000 of vapour pressure (VP), incident shortwave (SW) and incident longwave (LW) radiation are compared to surface observations. The results are listed in Figure S2, S3, and S4, for VP, SW, and LW, respectively. The daily Pearson correlation coefficient and the mean difference to the station observations, after adjustment to station altitude (using the same method as stated in Erlandsen et al. (2019)) are shown for each station in heatmap plots. Correlations and differences for other estimates of VP, SW, and LW are also shown, for comparison. Table S1 gives an overview of the various data sources compared.

Table S1: The data set estimates of vapour pressure (VP), $LW\downarrow$, and $SW\downarrow$ which, are compared to observations are listed. Precipitation is denoted as P, 2-meter temperature as T_2. The table is a modified version of Table 1 in Erlandsen et al. (2019). References are available in Erlandsen et al. (2019) for all sources except Era5 (Hersbach et al. (2019), *Copernicus Climate Change Service (C3S) (2017): ERA5: Fifth generation of ECMWF atmospheric reanalyses of the global climate.* (2017)).

	Product	Resolution	Coverage	About	Input data.
M	MERRA2	1/2° x 2/3°	Global	Reanalysis	
E	ERA-Interim	2/3° x 2/3°	Global	Reanalysis	
E5	Era5	1/4° x 1/4°	Global	Reanalysis	
P	PGMFDv2	1/2° x 1/2°	Global, land only	Post-processed reanalysis, VP $LW\downarrow$ re-gridded and adjusted to monthly CRU T_2, method from Cosgrove (2003). $SW\downarrow$ & $LW\downarrow$ adjusted to satellite-based data set	NCEP-NCAR (2° x 2°), CRU TS3.1 T_2 CRU TS3.1 cloud cover, NASA MEaSUREs $LW\downarrow$ & $SW\downarrow$
W	WFDEI	1/2° x 1/2°	Global, land only	Post-processed reanalyis, VP, $LW\downarrow$ re-gridded and adjusted to monthly CRU T_2, method from Cosgrove (2003). $SW\downarrow$ re-gridded and adjusted to CRU cloud cover & inter-annual aerosol loading	ERA-Interim, CRU TS3.1 T_2 (1979-2009), CRU cloud cover and aerosol loading
V1	VFDv1	1 x 1 km	Regional, locally compiled	Empirical model, The VIC4.0.6 pre-processor: MTCLIMv4.2 & TVA+Bras $LW\downarrow$	SeNorge2 P & T_2, Nora10 sub-daily T_2
V2	VFDv2	1 x 1 km	Regional, locally compiled	Empirical model, The VIC4.2.d pre-processor: MTCLIMv4.3 & Prata+Deadroff $LW\downarrow$	P, SeNorge2 T_{2min}, SeNorge2 T_{2max}
H	HySN	1 x 1 km	Regional locally compiled	Post-processed reanalyis, VP, $LW\downarrow$ re-gridded and adjusted to daily SeNorge2 T_2, method from Cosgrove (2003). $SW\downarrow$ re-gridding and adjustment, method from Thornton and Running (1999)	ERA-Interim, SeNorge2 T_2
H5	HySN5	1 x 1 km	Regional locally compiled	Post-processed reanalyis, VP, $LW\downarrow$ re-gridded and adjusted to daily SeNorge2018 T_2, method from Cosgrove (2003). $SW\downarrow$ re-gridding and adjustment, method from Thornton and Running (1999)	Era5, SeNorge2018 T_2

190

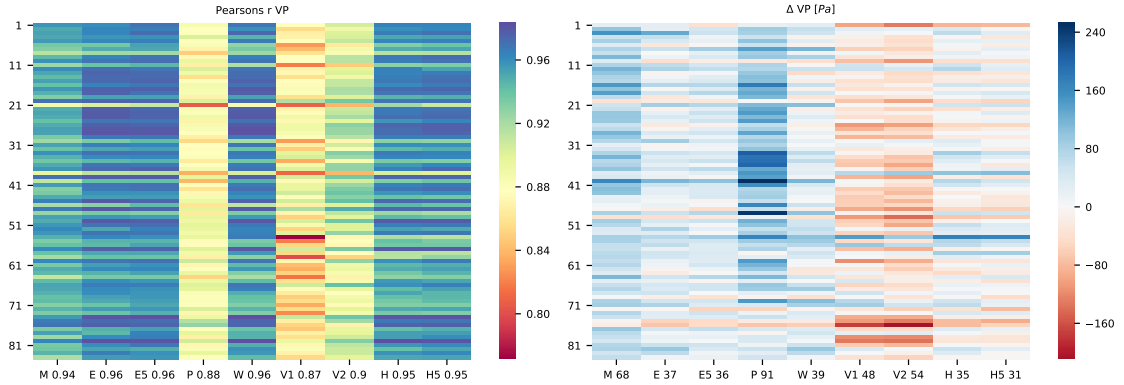

Figure S2: VP estimates, from the sources listed in Table S1, compared with surface observations, sorted from South to North (y-axis). The leftmost panel shows, in each column, the Pearson correlation coefficient of daily VP estimates and observed values, with the mean correlation denoted below each column. The rightmost panel shows the mean bias at each station for each VP estimate (columns), with the mean absolute station bias denoted below each column.

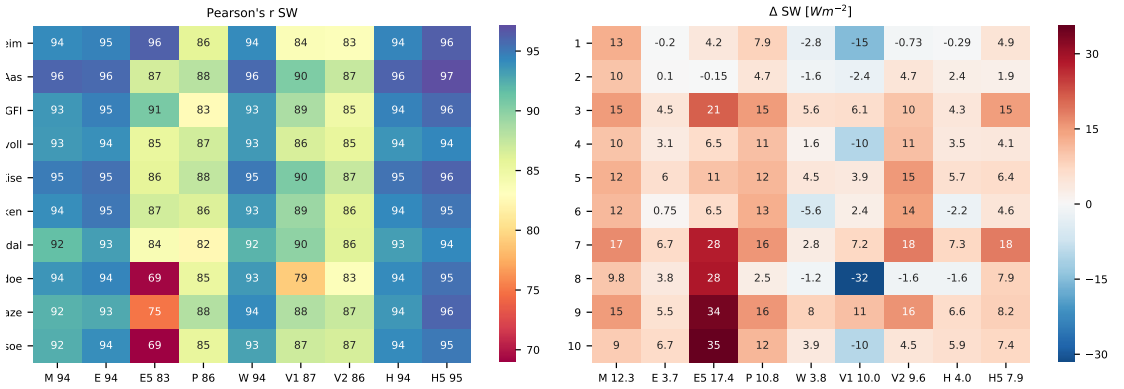

Figure S3: As in Fig. S2, but for $SW \downarrow$.

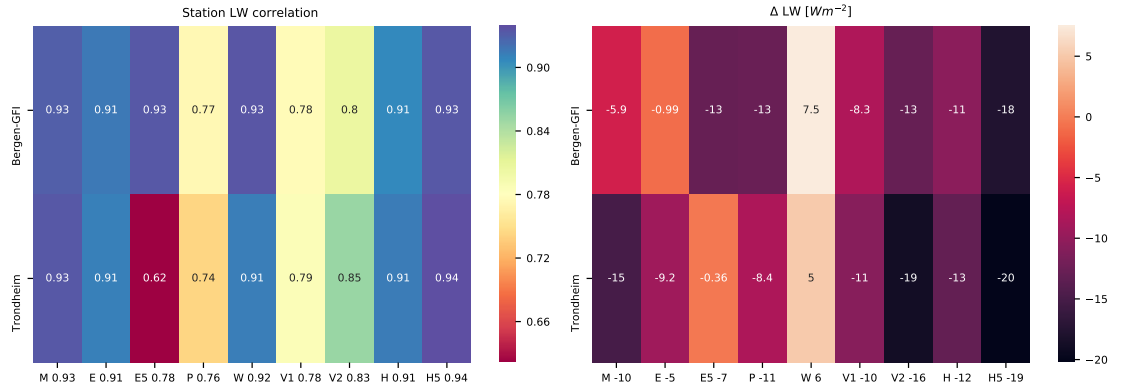

Figure S4: As in Fig. S2, but for $LW \downarrow$.

191

S1.2 Calibration and validation data

Table S2 is a replication of Table 7-5 within Hetager and Lystad (1974), with added station coordinates, displaying mean May to September pan evaporation sum measured between 1967 and 1972. The table list the station number (Num.) ,the name of the station (station), the stations latitude (lat.) and longitude (lon.), the station altitude (m.a.s.l.), the number of years the monthly average is based on (n years), and finally the mean monthly values and sum.

192

Table S2: Replication of Table 7-5 within Hetager and Lystad (1974), with added station coordinates.

Num.	station	lat.	lon.	m.a.s.l.	n years	May	June	July	Aug.	Sept.	sum
12	Avdal	62.03	10.78	485	6	61.60	76.00	73.40	66.70	36.80	314.30
34	Lesja	62.13	8.72	572	4	63.10	80.30	67.80	64.50	33.80	309.50
53	Varden	61.18	8.15	1012	4	66.90	95.10	61.60	66.40	37.00	327.00
66	Loesset	61.37	11.38	262	6	52.20	62.40	58.00	49.40	28.10	250.10
68	Trysil	61.33	12.25	356	6	57.30	67.00	60.00	67.10	48.00	299.30
70	Bjørke	60.80	11.20	200	5	80.00	119.50	100.70	85.10	43.20	428.40
72	Kise	60.77	10.82	128	4	66.20	91.50	81.50	70.10	47.20	356.40
86	Aust Torpa	60.93	10.13	495	6	44.60	62.90	60.80	55.00	31.80	255.00
900	Furusmo	60.17	11.12	200	5	87.50	107.80	101.70	93.80	59.50	450.30
901	østby	60.17	11.00	170	5	65.00	82.60	81.00	67.70	41.20	337.60
112	Blindern	59.93	11.53	94	6	88.90	135.60	95.00	89.00	53.60	462.10
148	Lyngdal	59.90	9.53	190	5	60.60	73.10	67.90	62.10	40.00	303.50
164	Stokke	59.25	10.28	76	5	63.80	83.00	69.60	56.30	38.20	311.00
180	Eidsberg	59.50	11.28	141	6	61.10	87.10	83.00	75.50	42.40	349.00
197	Prestebakke	58.98	11.53	189	6	82.40	98.10	84.40	64.80	42.40	372.20
204	Gvarv	59.38	9.18	24	6	64.30	86.60	87.00	65.10	34.20	337.20
233	Landvik	58.33	8.52	6	6	73.70	97.50	83.20	67.60	41.90	363.90
268	Lista	58.10	6.57	13	6	78.20	88.00	93.30	81.50	55.80	396.70
272	Tonstad	58.67	6.70	57	3	65.20	67.70	59.70	60.00	40.60	293.20
296	Fister	59.18	6.07	1	6	42.60	46.80	40.10	34.80	27.60	191.90
304	Skudesnes	59.15	5.25	7	4	57.30	66.90	59.20	46.90	31.70	264.00
324	Ullensvang	60.32	6.65	12	6	56.60	66.10	52.80	47.40	32.10	255.10
350	Stend	60.27	5.35	50	4	62.90	76.80	68.10	65.30	45.10	318.20
372	Fjærland	61.42	6.07	10	6	50.30	51.70	46.60	47.30	25.30	221.20
376	Laerdal	61.07	7.52	36	6	73.20	87.20	69.20	63.60	33.30	326.60
396	Førde	61.47	5.85	43	6	48.90	55.00	45.30	45.20	26.80	221.10
417	Hareid	62.37	5.98	25	3	51.70	50.60	47.80	44.80	36.30	231.20
418	Orstavik	62.20	6.15	35	6	47.60	45.00	44.60	42.70	32.40	212.40
419	Stranda	62.30	6.80	84	4	52.20	47.20	45.70	35.90	15.00	196.00
421	Valldal	62.30	7.23	50	4	59.30	57.10	55.50	50.80	30.40	253.00
422	Skodje	62.50	6.68	30	5	58.00	53.90	51.20	43.30	31.10	237.60
454	Smøla	63.43	6.68	30	6	79.00	75.00	66.50	53.00	30.00	303.40
478	Øvre Gjervan	63.33	10.65	176	4	57.70	54.50	42.50	41.90	28.00	224.60
486	Stugusjø II	62.90	11.88	616	3	59.90	60.50	41.50	37.80	23.00	222.70
496	Sulstua	63.67	12.02	251	6	54.10	61.40	52.20	47.50	29.70	245.00
528	Leka	65.10	11.70	50	6	57.70	54.60	57.70	52.80	38.40	261.20
545	Sandnessjøen	65.98	12.58	75	4	74.40	60.20	59.80	39.70	35.80	270.00
596	Narvik	68.47	17.50	32	6	40.50	37.40	36.20	26.30	16.60	157.00
640	Bø	68.63	14.47	11	5	56.50	67.20	59.70	47.50	38.20	269.10
642	Borkenes	68.77	16.20	36	6	50.20	40.30	40.80	37.70	20.60	189.60
680	Tromsø	69.65	18.97	102	6	38.30	42.10	44.00	29.60	13.70	167.80
714	Brennelv	70.07	25.12	34	6	43.00	51.60	47.80	36.00	21.70	200.00

S1.3 The gridded HBV model

S1.3.1 HBV-E20

Figure S5 shows an example of the evolution of mean snow melt equivalent (SWE) from September 1979 to 1999 for the study area, in a simplified snow accumulation and snow melt model implemented in Python, without precipitation correction factors, tiling of snow, or refreezing of melted snow. The melt temperature of snow ($T2_{melt}$), used in the degree-day factor expression, is set to 0 $°C$. The degree-day factor, C_{temp}, provides the melt rate in meters for every degree Celsius the daily mean 2-meter temperature ($T2$) is above $T2_{melt}$. A blue, stippled line shows SWE when snow melt (M) is given by a traditional degree-day factor expression:

$$M = max(C_{temp}(T2 - T2_{melt}), 0) \tag{S1}$$

where the degree-day factor, C_{temp}, is 0.0025 $m/°C$. In HBV-E20 the degree day factor expression is modified by adding a radiative term to the traditional equation. Figure S5 shows, in orange and green stippled lines, an example of the evolution of mean SWE for a radiation-restricted degree day factor:

$$M = max(C_{temp}(T2 - T2_{melt}) + C_{rad}\frac{R_n}{\lambda_f \rho_w}, 0), \tag{S2}$$

where C_{rad} is a fraction scaling the radiative term which is added to the degree-day factor, set to 0.82 , λ_f is the latent heat of fusion, 0.334 $MJkg^{-1}$, R_n is net surface incident radiation in $MJm^{-2}day^{-1}$, while ρ_w is the density of water (1000 kgm^{-3}). The net incident shortwave radiation was calculated as a weighted mean according to the grid cell snow cover fraction (fs) and the albedos (one for snow free conditions and one for snow covered conditions) provided in the look-up table (Table S3) for the grid cell dominant land cover class. The orange stippled line shows SWE when fs is expressed as $fs = 0.95 \cdot tanh(100 \cdot SWE)$, as in Eq. 6, Roesch et al. (2001) while the green stippled line shows SWE when f_s is expressed as $fs = tanh(75 \cdot SWE)$. $fs = tanh(75 \cdot SWE)$ is used in HBV-E20. Figure S5 shows that with C_{temp} given as 2.5 $mm/°C$, the simplified snow model shows a build-up of SWE over summer when the traditional degree-day factor expression (Eq. S1) is used to describe snow-melt, while snow moslty does not build-up over time when the radiation restricted degree factor expressions (Eq. S2) are used.

Table S3 list various land use type dependent parameters. Other parameters related to vegetation and snow include the degree day melt rate for ice, C_{ice}, which is set to 1.2 mm/day, the melt temperature for snow (0.0$°C$, the amount of melt water which may refreeze (0.05 mm), and maximum interception capacity (in meters) is calculated as one fifth of the the land use type' s LAI.

The Penman-Monteith equation for E_p, in millimeters per day, is implemented as follows:

$$E_p = \frac{t_d}{\lambda}\frac{\Delta \cdot R_n + \frac{\rho_a c_p VP_d}{r_a}}{\Delta + \gamma(1 + r_s/r_a)} \tag{S3}$$

Here t_d is the seconds in a day ($s\ day^{-1}$), λ is the latent heat of vaporization ($\simeq 2.4510^6\ Jkg^{-1}$), Δ is the slope of the saturation vapour pressure ($\Delta = b \cdot c \cdot es(T)/(c + T)^2$ in $kPaK^{-1}$) and is calculated with the constants a, b, c taken from Buck (1981) to be consistent with the formulas used to derive vapour pressure. R_n is surface net radiation (Wm^{-2}), ρ_a air density (kgm^{-3}). c_p is the specific heat capacity of water (1013 $Jkg^{-1}K^{-1}$); VP_d is the vapour pressure deficit (kPa), while γ is the psychrometric constant (K^{-1}), given by $\gamma = c_p/\varepsilon p_s/\lambda$, where ε is the ratio of the molecular weight of water vapor to dry air, 0.622, and p_s is surface pressure. r_a (sm^{-1}) is the aerodynamic surface resistance, and r_s (sm^{-1}) is the surface resistance. Surface net radiation, Rn, is calculated from HySN5 LWn(estimated from HySN5 LW and SeNorge2018 T2) and SW , and surface albedo (α), which is calculated as a weighted average of land cover class albedo with and without snow, according to the snow cover fraction.

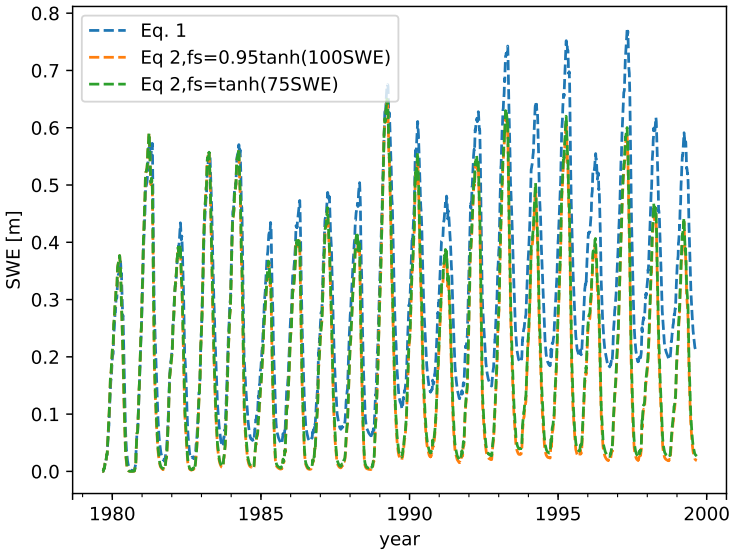

Figure S5: Evolution of SWE for the study area between September 1979 and September 1999 in a simplified snow accumulation and ablation mondel implemented in Python, where snow melt is given by Eq. 1 (blue. stapled line), or by Eq. 2 (orange and green stapled lines), including two grid cell snow cover fraction parameterizations: $fs = 0.95 \cdot tanh(100 \cdot SWE)$ (orange line), and $fs = tanh(75 \cdot SWE)$ (green line).

Table S3: Look-up table providing parametric values for vegetation related parameters used in HBV-E20

Land use type	no.	C_{rad} [−]	α [−]	α_s [−]	height $[m]$	LAI [−]	$T2_{open}$ $[°C]$	$T2_{close}$ $[°C]$	$z0_g$ $[m]$	gs_{max} $[sm^{-1}]$
Open	0	0.85	0.14	0.57	0.2	2.0	12.02	-8.0	0.001	0.0060
Bog	1	0.85	0.13	0.58	0.5	2.0	8.80	-8.0	0.010	0.0066
Built-up	2	0.75	0.13	0.14	10.0	4.0	12.02	-8.0	0.020	0.0060
Crop	3	0.75	0.15	0.32	2.0	5.0	12.02	-8.0	0.010	0.0110
Heather	4	0.85	0.15	0.64	0.3	1.0	8.80	-8.0	0.020	0.0060
Bedrock	5	0.95	0.12	0.60	0.1	0.0	12.02	-8.0	0.001	0.0090
Spruce 1	6	0.75	0.13	0.36	7.5	1.4	8.31	-8.0	0.020	0.0057
Spruce 2	7	0.75	0.12	0.32	12.3	4.3	8.31	-8.0	0.020	0.0057
Spruce 3	8	0.75	0.10	0.18	16.8	6.7	8.31	-8.0	0.020	0.0057
Spruce 4	9	0.75	0.09	0.13	22.0	9.1	8.31	-8.0	0.020	0.0057
Pine 1	10	0.75	0.12	0.40	7.5	0.9	8.31	-8.0	0.020	0.0057
Pine 2	11	0.75	0.10	0.30	11.6	2.4	8.31	-8.0	0.020	0.0057
Pine 3	12	0.75	0.10	0.24	17.0	2.3	8.31	-8.0	0.020	0.0057
Pine 4	13	0.75	0.10	0.17	17.2	4.4	8.31	-8.0	0.020	0.0057
Deciduous 1	14	0.75	0.13	0.57	4.9	0.5	9.09	-6.0	0.020	0.0046
Deciduous 2	15	0.75	0.13	0.46	8.4	1.8	9.09	-6.0	0.020	0.0046
Deciduous 3	16	0.75	0.14	0.42	12.2	3.9	9.09	-6.0	0.020	0.0046
Deciduous 4	17	0.75	0.12	0.24	18.3	7.0	9.09	-6.0	0.020	0.0046
Glacier	20	0.95	0.50	0.50	0.1	0.0	12.02	-8.0	0.001	0.0093

S1.4 Calibration

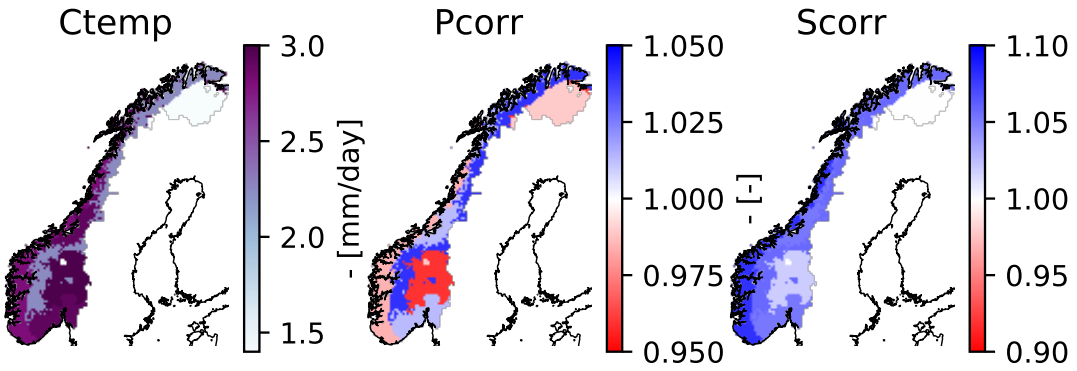

Figure S6: The three above soil parameters calibrated for each of the five climatic zones, the degree day factor (C_{tmep}), a multiplicative correction factor for all precipitation (Pcorr), and an additional one only applied for snowfall (Scorr).

Table S4: Calibrated above-soil parameters each of the five climatic zones (rows), the degree day factor (C_{tmep}), a multiplicative correction factor for all precipitation (Pcorr), and an additional one only applied for snowfall (Scorr).

Zone	C_{tmep} $[mm\ day^{-1}]$	Pcorr [–]	Scorr [–]
1	1.40	0.99	1.00
2	2.25	1.04	1.06
3	2.81	0.98	1.08
4	3.00	0.96	1.02
5	2.92	1.01	1.05

196

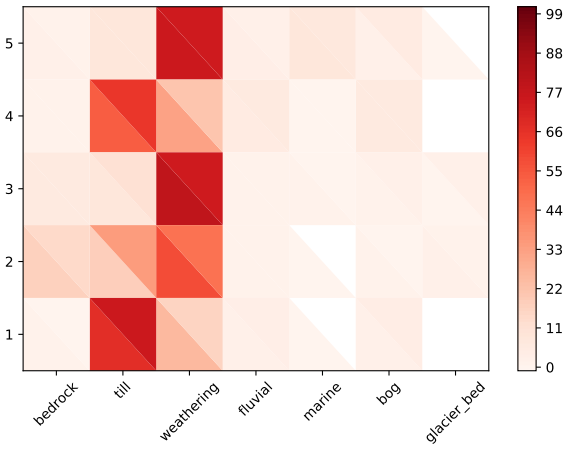

Figure S7: Percentage of soil types (columns) within each calibration zone (rows). The lower diagonal indicates the percentage within the full calibration zone, while the upper diagonal indicates the percentage within the calibration catchments within the zone. A white indicates no presence of the soil type.

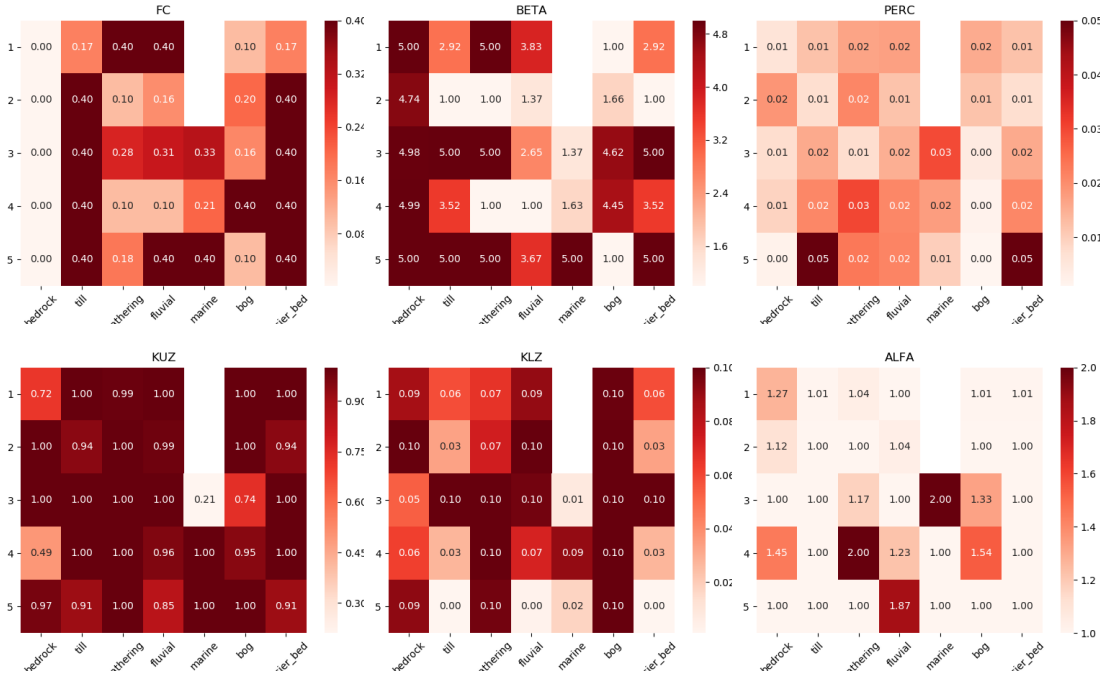

Figure S8: Calibrated parameter values for field capacity (FC), β (BETA), percolation to the lower zone (PERC), the upper (KUZ) and lower (KLZ) zones runoff response coefficients, and the upper zone recession parameter (ALFA), for the five soil types (columns) for each calibration zone (rows).

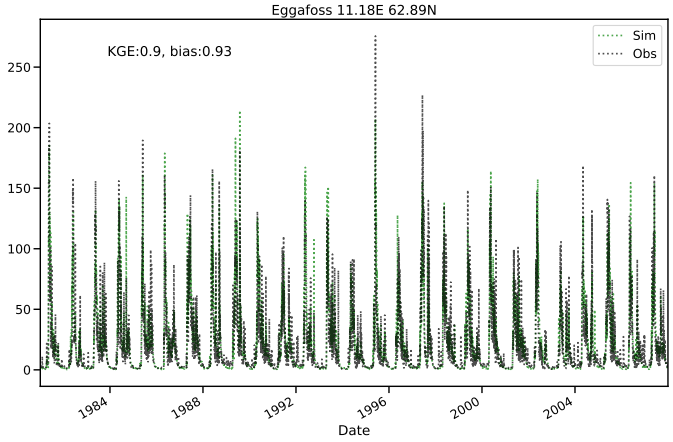

Figure S9: Time-series of simulated (green line) and observed (black line) discharge at Eggafoss catchment in central Norway.

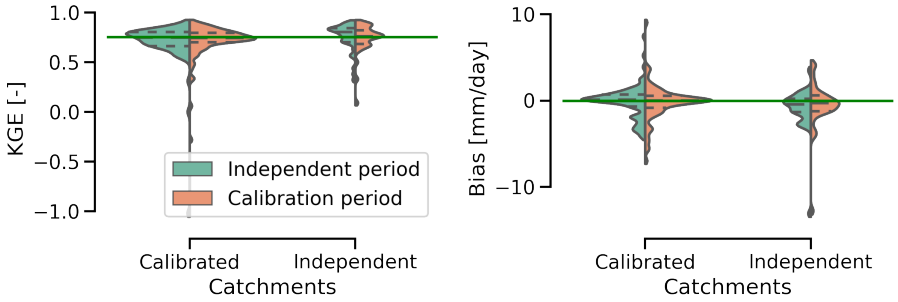

Figure S10: Catchment KGE scores, depicted in violin plots, are displayed in the left panel, for calibration (left) and independent (right) catchments, for the calibration period (2000-2010, orange color) and an independent time period (1980-1999, green color). The right panel shows similar violin plots for catchment bias.

S2 Results

S2.1 Validation

The model calibration resulted in high KGE values for many catchments, as exemplified in Figure S9, where a close fit between observed and simulated runoff at Eggafoss, a validation catchment in the Trøndelag region of Norway, is displayed. The distribution of KGE and mean bias for the calibration and independent catchments, and for the calibration period and the independent time period is further provided (Fig. S10).

198

References

Buck, A. L. 1981. "New Equations for Computing Vapor Pressure and Enhancement Factor." *Journal of Applied Meteorology* 20, no. 12 (): 1527–1532. ISSN: 0021-8952. doi:10.1175/1520-0450(1981)020<1527:NEFCVP>2.0.CO;2.

Copernicus Climate Change Service (C3S) (2017): ERA5: Fifth generation of ECMWF atmospheric reanalyses of the global climate. 2017. Copernicus Climate Change Service Climate Data Store (CDS), https://cds.climate.copernicus.eu/cdsapp#!/home. ECMWF. doi:10.5067/4Z3YUPM81GRJ.

Cosgrove, B. A. 2003. "Real-time and retrospective forcing in the North American Land Data Assimilation System (NLDAS) project." *Journal of Geophysical Research* 108 (D22): 8842. ISSN: 0148-0227. doi:10.1029/2002JD003118.

Erlandsen, H. B., L. M. Tallaksen, and J. Kristiansen. 2019. "Merits of novel high-resolution estimates and existing long-term estimates of humidity and incident radiation in a complex domain." *Earth System Science Data* 11 (2): 797–821. doi:10.5194/essd-11-797-2019.

Hersbach, H., W. Bell, P. Berrisford, A. Horányi, M. J., J. Nicolas, R. Radu, D. Schepers, A. Simmons, C. Soci, and D. Dee. 2019. "Global reanalysis: goodbye ERA-Interim, hello ERA5" (159): 17–24. doi:10.21957/vf291hehd7.

Hetager, S. E., and S. L. Lystad. 1974. *Fordampning fra fri vannflate: verdier basert på målinger i perioden 1967-1972.* Tech. rep. Oslo.

Roesch, A., M. Wild, H. Gilgen, and A. Ohmura. 2001. "A new snow cover fraction parameterization for the ECHAM4 GCM." *Climate Dynamics* 17, no. 12 (): 933–946. ISSN: 09307575. doi:10.1007/s003820100153.

Thornton, P. E., and S. W. Running. 1999. "An improved algorithm for estimating incident daily solar radiation from measurements of temperature, humidity, and precipitation." *Agricultural and Forest Meteorology* 93 (4): 211–228. ISSN: 01681923. doi:10.1016/S0168-1923(98)00126-9.

Appendices

A. Derivation of the Penman-Monteith equation for plant and canopy evaporation

The original Penman-48 equation (Eq. 2.10) may be written :

$$LE = \lambda E = \frac{\Delta R_n + \frac{\rho_a c_p}{r_{SH}}(e_s(T) - e(T))}{\Delta + \gamma}$$

The Penman-Monteith expression may be derived by expressing both turbulent fluxes in terms of the resistance to sensible heat transfer (r_{SH}), by defining a modified psychometric constant (γ), $\gamma^* == \gamma(r_{LE}/r_{SH})$. The sensible and latent heat fluxes may then be given by by the following two expressions:

$$SH = \frac{\rho c_p}{r_{SH}}(T_s - T) = -\frac{\rho c_p}{r_{SH}}(T - T_s),$$

$$LE = \frac{\lambda\rho\varepsilon}{r_{LE}p_s}(e_s(T_s) - e(T)) = \frac{\rho c_p}{\gamma r_{LE}}(e_s(T_s) - e(T)) = \frac{\rho c_p}{\gamma^* r_{SH}}(e_s(T_s) - e(T)),$$

.

Assuming, as Penman did, that $e_s(T_s) = e_s(T) - \Delta(T - T_s)$, and inserting this into the expression for latent heat above gives:

$$LE = \frac{\rho c_p}{\gamma^* r_{SH}}(e_s(T) - \Delta(T - T_s) - e(T)).$$

T_0 may be removed by using the expression for sensible heat:

$$LE = \frac{\rho c_p}{\gamma^* r_{SH}}(e_s(T) - \Delta(-(SH\frac{r_{SH}}{\rho c_p})) - e(T)) = \frac{\rho c_p}{\gamma^* r_{SH}}(e_s(T) - e(T)) + \frac{\Delta}{\gamma^*}SH.$$

SH can be expressed as $SH = R_n - LE$ (with ground heat flux omitted here for brevity):

$$LE = \frac{\rho c_p}{\gamma^* r_{SH}}(e_s(T) - e(T)) + \frac{\Delta}{\gamma^*}R_n - \frac{\Delta}{\gamma^*}LE.$$

Rearranging LE to the left hand side provides:

$$(1 + \frac{\Delta}{\gamma^*})LE = (\frac{\gamma^* + \Delta}{\gamma^*})LE = \frac{\rho c_p}{\gamma^* r_{SH}}(e_s(T) - e(T)) + \frac{\Delta}{\gamma^*}R_n,$$

which finally gives:

$$LE = \frac{\frac{\rho c_p}{\gamma^* r_{SH}}(e_s(T) - e(T)) + \frac{\Delta}{\gamma^*}R_n}{\frac{\gamma^* + \Delta}{\gamma^*}} = \frac{\Delta R_n + \frac{\rho c_p}{r_{SH}}(e_s(T) - e(T))}{\gamma^* + \Delta} \qquad \text{(A.1)}$$

Often the above equation is used with r_{LE}, the resistance to vapor transfer, replaced with two resistances, one component describing the plant specific resistance to vapor exchange from the plant to some level above the canopy surface (r_s), and another component describing the aerodynamic resistance (r_a) from that level and on wards: $r_{LE} = r_s + r_a$. If one further assumes that the aerodynamic resistance for heat and vapor transfer is the same ($r_{SH} = r_a$), $\gamma^* = \gamma(r_{LE}/r_{SH}) = \gamma((r_s + r_{SH})/r_{SH}) = \gamma(r_s/r_a + 1)$, the Penman-Monteith expression for canopy evaporation is:

$$LE = \frac{\Delta R_n + \frac{\rho c_p}{r_a}(e_s(T) - e(T))}{\Delta + \gamma(1 + \frac{r_s}{r_a})} \tag{A.2}$$

B. Source code written for Paper III

B.1 The Python script which compiles the HySN5 dataset

The Python script to compile the HySN5 dataset, and vapor pressure deficit and estimated net incident longwave radiation, used in Paper III as input to the HBV model:

```
#!/usr/bin/env python
# -*- coding: utf-8 -*-
# author: Helene B. Erlandsen
# date 09.01.2019
# updating for Era5 and SeNorge2018 use

import sys, os, glob
import os.path
from datetime import date
today = str(date.today())
import numpy as np
import bokeh
import dask
import pandas as pd
import xarray as xr
import xarray.ufuncs as xu
from dask.diagnostics import ProgressBar
from dask.distributed import Client, LocalCluster, TimeoutError
import gc #garbage collector
#from pyproj import Proj
#The interpolation could be done with scipy interp,
#Basemap interp or xarray interp
#choosing to use xesmf cause saves weights, needs pip install
import xesmf as xe #pip install
#pip install --upgrade git+https://github.com/JiaweiZhuang/xESMF.
    git@masking
#(https://github.com/JiaweiZhuang/xESMF/issues/22)
# Follows SCRIP convention where 1 is unmasked and 0 is masked.
# See https://github.com/NCPP/ocgis/blob/61
    d88c60e9070215f28c1317221c2e074f8fb145/src/ocgis/regrid/base.py#
    L391-L404
# extrapMethod=extrap_method,
# ESMF ESMC_EXTRAPMETHOD_NEAREST_IDAVG
# :param ExtrapMethod extrap_method: Specify which extrapolation method
    to use on unmapped destination points after regridding.ESMF.api.
    regrid.Regrid ESMF_FieldRegrid() ~/*conda*/lib/pythonN.N/site-
    packages/ESMF/api/regrid.py
#conda install -c nesii -c conda-forge esmpy=7.1.0r
#conda create -n esmpy -c nesii -c conda-forge esmpy=7.1.0r
# esmpy=7.1.0r or higher includes extrap_method



from pyproj import Proj
#if you want to print run time of script
#import cProfile
#pr = cProfile.Profile()

import matplotlib.pyplot as plt


def convert_bytes(num):
    """
    this function will convert bytes to MB.... GB... etc
    """
```

```
    for x in ['bytes', 'KB', 'MB', 'GB', 'TB']:
        if num < 1024.0:
            return "%3.1f %s" % (num, x)
        num /= 1024.0


if __name__ == '__main__':
    try:
        cluster = LocalCluster(processes=False,memory_limit='25GB',
    n_workers=2, threads_per_worker=4,scheduler_port=8780,
    dashboard_address=9787)
        # processes vs threds pool https://github.com/pydata/xarray/
    issues/2417
        client = Client(cluster)

    except TimeoutError:

        pass
    with dask.config.set({'temporary_directory': '/home/helenebe/storah/
    HySN/script/dtmp'}):
        pass
    client
    print(client)
    print(client.scheduler_info())
    os.system("export HDF5_USE_FILE_LOCKING=FALSE")
    #os.system("export OMP_NUM_THREADS=4")

    chnkt=10 #'auto' #chunk for time
    datadir="../data/"
    E5path=datadir+'Era5/'
    savedir=datadir+"HySN5/"

    startyr=1979
    endyr=2000
    #Make precip_24hours_means ie 06 UTC to 06 UTC set RRday to True
    RRday=True

    if RRday==True:
        dayshh=6
        lab='right'
    else:
        dayshh=0
        lab='left'

    #Constants

    T0NVE=273.1
    #-------------------------------------------------------
    #          EC constants from IFS manual and mars wiki
    #          Double check that same is true for Era5
    #          Td is calculated for saturation above water
    ecg=9.80665 #gravitational constant
    T0=273.16 #K
    Rd=287.0597 #JK
    Rv=461.5250 #JK
    eps=Rd/Rv
    R=287.# J/kg/K

    #Buck(1981) used to calculate Td in Era-interim
    aw=611.21
    bw=17.502
    cw=240.97
    #-------------------------------------------------------
    #AERKi to calculate Tf (freeze point temperature)
    ai=aw
    bi=22.587
    ci=273.86

```

```
    # SW regridding
    tau=0.720
    alpha=-1.5E-5

    # LW net
    sigma=5.670373E-8 # Wm-2 K-4
    epsgr=0.96 #https://journals.ametsoc.org/doi/full/10.1175/JCLI3720.1


    #SeNorge initialization ----------------------------
    SeNorgegeo='http://thredds.met.no/thredds/dodsC/senorge/geoinfo/seNorge2_dem_UTM33.nc'
    dx=1000.
    SeNorge2018p='https://thredds.met.no/thredds/dodsC/senorge/seNorge_2018/Archive/seNorge2018_'
    SeNyear=2000 # random
    SeNorge2018pd='https://thredds.met.no/thredds/dodsC/senorge/seNorge_2018/Archive/seNorge2018_'
    SeN=xr.open_dataset(SeNorge2018pd+str(SeNyear)+'.nc',cache=False) #
    projs=SeN['UTM_Zone_33'].proj4
    myP=Proj(projs)

    #maybe make def below ------------------------------------------
    Xcorners=np.arange(SeN['X'].data[0]-dx/2., SeN['X'].data[-1]+3*dx/2., dx)
    Ycorners=np.flipud(np.arange(SeN['Y'].data[-1]-dx/2., SeN['Y'].data[0]+3*dx/2., dx))
    Lon2, Lat2 = myP(*np.meshgrid(SeN['X'].data,SeN['Y'].data),inverse=True)
    Lon2b, Lat2b = myP(*np.meshgrid(Xcorners,Ycorners),inverse=True) #

    lons=np.asarray(Lon2)
    lats=np.asarray(Lat2)
    SeN.coords['lat'] = (('Y','X'),Lat2)
    SeN.coords['lon'] = (('Y','X'),Lon2)
    SeN.set_coords(['lat','lon'])

    SeN.coords['Xb'] = (Xcorners)
    SeN.coords['Yb'] = (Ycorners)
    SeN.set_coords(['Xb','Yb'])

    SeN.coords['lat_b'] = (('Yb','Xb'),Lat2b)
    SeN.coords['lon_b'] = (('Yb','Xb'),Lon2b)
    SeN.set_coords(['lat_b','lon_b'])

    write_to_file=False
    if write_to_file:
        mapSN=SeN.drop('tg')#][0,:,:]
        mapSN=mapSN.drop('rr')
        mapSN=mapSN.drop('time')
        mapSN.set_coords(['lat_b','lon_b'])
        mapSN.to_netcdf('SeN_UTM33_with_crns_4_HySN.nc', mode='w', format='NETCDF4',
                        group=None, engine='netcdf4',encoding={'lon': {'_FillValue':False},
                                                               'lat': {'_FillValue':False},
                                                               'lon_b': {'_FillValue':False},
                                                               'lat_b': {'_FillValue':False}})
    #-------------

    SeNoro=xr.open_dataset(SeNorgegeo)
    SeNorge_oro=SeNoro['elevation']
    SeNorgemask=SeNorge_oro.isnull() #True/1 for water, False/0 for land
    SeNorgelsm=SeNorge_oro.notnull()*1.0 #0. for water, 1. for land
    SeN.coords['mask'] = (('Y', 'X'), SeNorgelsm)
```

```
171     SeN['orography'] = (('Y', 'X'), SeNorge_oro)
172
173     #SeNorge is indexed as precip days with the stamp reflecting
174     #the accumulated 24 hour precip until the date at 06 hours
175
176
177     #Era-5 orography
178     Era_oro = xr.open_dataset(E5path+'Era5_land_sea_mask_oro_region.nc')
179     # Era-5 grid
180     eclat=Era_oro['latitude'][:]
181     eclon=Era_oro['longitude'][:]
182     dl=abs(eclat.diff('latitude').data[0])
183     lonc=np.arange(eclon.data[0]-dl/2., eclon.data[-1]+3*dl/2., dl)
184     latc=np.flipud(np.arange(eclat.data[-1]-dl/2., eclat.data[0]+3*dl
        /2., dl))
185
186     def fixcoords(var):
187         var=var.rename({'longitude': 'lon', 'latitude': 'lat'})
188         var.coords['lat_b'] = (latc)
189         var.coords['lon_b'] = (lonc)
190         var.set_coords(['lat_b','lon_b'])
191         return var
192
193     Era_oro=fixcoords(Era_oro)
194     ecsgeo=Era_oro['z'][0]
195     ecmaskbf=Era_oro['lsm'][0] # 0 for water , fractional
196     ecmaskb=ecmaskbf.where(ecmaskbf==0.,1) #
197     ecnamask=ecmaskbf.where(ecmaskbf==0.,np.nan)
198     ## Land-sea mask values
199     '''When interpolating the land-sea mask field, MIR returns
        fractional values greater than or equal to 0 and less than or equal
         to 1 whereas EMOSLIB returns only 0s and 1s.  Users should regard
        land-sea mask values greater than or equal to 0.5 as representing
        land points and those less than 0.5 as representing sea points. (
        https://confluence.ecmwf.int/display/UDOC/MARS+interpolation+with+
        MIR)'''
200     ecmask=ecnamask.notnull()
201     ECoro=ecsgeo/ecg
202     ECoro.attrs['units'] = 'meters'
203     ECoro.name='orography'
204
205     Era_oro.coords['mask'] = (('lat', 'lon'), ecmaskb)
206     Era_oro['orography']=(['lat', 'lon'], ECoro.data, ECoro.attrs)
207     savEra=False
208     if savEra:
209         Era_oro.to_netcdf('Era5_with_crns0_5lsm.nc',encoding={'lon': {'
        _FillValue':False},'lat': {'_FillValue':False},'lon_b': {'
        _FillValue':False},'lat_b': {'_FillValue':False}})
210
211
212     #Era-5 -hourly SW and LW files
213     Era5_rad= xr.open_dataset(E5path+'ssrd_slrd_Era5_1979_t2000RRok.nc',
        cache=False)
214
215     #Era-5 2-meter temperature (T2) and 2-meter dew point temperature,
        from analysis fields
216     Era5_termo_a =  xr.open_dataset(E5path+'
        t2m_d2m_ps_Era5_1979_tom2000RRday06stamp.nc',cache=False)
217
218     Era5_rad=fixcoords(Era5_rad)
219     Era5_termo_a=fixcoords(Era5_termo_a)
220
221     T2E=Era5_termo_a['t2m']
222     T2dE=Era5_termo_a['d2m']
223     psE=Era5_termo_a['sp']
224     SW=Era5_rad['msdwswrf']
225     LW=Era5_rad['msdwlwrf']
226
```

```
227     # shoud be enough
228     SW,T2E=xr.align(SW,T2E, join='inner')
229     LW,T2dE=xr.align(LW,T2dE, join='inner')
230     LW,psE=xr.align(LW,psE, join='inner')
231
232     #Era-Interim Vapour pressure
233     e2w=aw*np.exp(bw*(T2dE-T0)/(T2dE-T0 +cw))#/1000. #for water, ref ifs
          copernicus knowledge base
234
235     #Era-Interim saturation vapour pressure
236     e2si=ai*np.exp(bi*(T2E-T0)/(T2E-T0 +ci))
237     e2sw=aw*np.exp(bw*(T2E-T0)/(T2E-T0 +cw))
238
239     #do not need to use enhancement factors because they are cancelled
        for RH
240     RHEw=e2w/e2sw*100.
241     RHEi=e2w/e2si*100.
242     #check RH not more than 100%
243     RHEi=RHEi.where(RHEi<100.,100.)
244     RHEw=RHEw.where(RHEw<100.,100.)
245
246
247     #Regridding this is based on
248     #pip install --upgrade git+https://github.com/JiaweiZhuang/xESMF.
        git@masking
249     #(https://github.com/JiaweiZhuang/xESMF/issues/22)
250
251     regridder=xe.Regridder(Era_oro, SeN, 'bilinear',reuse_weights=True)
252
253     regridder_s2d = xe.Regridder(Era_oro, SeN, 'nearest_s2d',
        reuse_weights=True)
254
255     dr_mask_bil=regridder(Era_oro['mask'])
256     extrapolate=dr_mask_bil.where(dr_mask_bil!=0,-99999)
257     dr_mask=regridder_s2d(Era_oro['mask'])
258
259     #look to check
260     #dr_mask_bil_f_IDV=regridder(T2E.isel(time=0))
261     #dr_mask_NN=regridder_s2d(T2E.isel(time=0))
262     #plt.imshow(dr_mask_bil_f_IDV);plt.colorbar();plt.title('oro w/IDW
        ?');plt.figure(); plt.imshow(SeN['mask']);plt.colorbar();plt.title
        ('SeN mask');plt.figure(); plt.imshow(dr_mask_NN);plt.colorbar();
        plt.title('oro NN'); plt.show()
263     #dr_mask_bil_f_IDV_NN=dr_mask_bil_f_IDV.where(extrapolate != -99999,
          dr_mask_NN)
264     #plt.imshow(dr_mask_bil_f_IDV);plt.colorbar();plt.figure(); plt.
        imshow(SeN['mask']);plt.colorbar();plt.figure(); plt.imshow(
        dr_mask_bil_f_IDV_NN);plt.colorbar(); plt.show()
265
266     #dr_mask_bil1=regridder(Era_oro['mask']*ecnamask)
267     #sav=dr_mask_bil1.isnull()
268     #plt.imshow(SeN['mask']);plt.colorbar();plt.show()
269
270     def regrid2step(data):
271         dr_out_bil=regridder(data)
272         #dr_out_cons_norm=regridder_consnorm(data)
273         dr_outs2d=regridder_s2d(data)
274         #outside mapped places nearest s2d (nearest neighbour; IDW not
        supp yet):
275         dr_out=dr_out_bil.where(extrapolate != -99999, dr_outs2d)
276         #add coords
277         dr_out.coords['X'] = (SeN['X'].data)
278         dr_out.coords['Y'] = (SeN['Y'].data)
279         dr_out.coords['lon'] = (('Y','X'),Lat2)
280         dr_out.coords['lat'] = (('Y','X'),Lon2)
281         dr_out.coords['mask']=SeN['mask'].astype('i2')
282         dr_out.name=data.name
283         dr_out=dr_out.astype('f4')
```

```
284             return dr_out
285
286         E5mask=regrid2step(Era_oro['mask'])
287         #after much thought using bilinear on all except near coast for
            consistency
288         #1:since reanalysis is already bil-interp from original grid
289         #2:since going from 0.25deg to 1km --> difference mostly small
290         #3:on all vars and params for consistency:
291         #i.e. if Eras T2 is bilinearly interp and then oro or LW is not,
292         # the ds will be somewhat inconsistent. eg T2=b+lapse*z
293
294         dr_oro=regrid2step(Era_oro['orography'])
295
296         #--DZ--------
297         dz=SeN['orography']-dr_oro #
298         #dz.plot();plt.show()
299         Commask=(dr_mask_bil.data>0.999) & (SeNorgelsm.data==1)
300         dzmask=dz.where(Commask, np.nan) #masked to common land points
301         print('mean elevation diff (SeNorge2018-Era5):', np.nanmean(dzmask))
302
303
304
305         def writetotmp_nc(data,pn):
306             filname='tmp/'+data.name+pn+'.nc'
307             data.to_netcdf(filname, format='NETCDF4',encoding={data.name:{'
            dtype': 'f4', '_FillValue': -9999.}})
308             #data.close()
309             #faster IO w/o zlib, but takes much more space
310
311         # To work with pc memory, and due to issues with dask+opendap or
            thredds bug?
312         # the data is sliced in time
313         # Three bolks a year ['p1', 'p2','p3']
314         #p1ul='<120'; p2ll='>=120'; p2ul='<140'; p3ll='>=140'
315         littlemem=True
316         if littlemem:
317             loweri = {}; upperi={}
318             loweri['p1']=0
319             loweri['p2']=120
320             loweri['p3']=240
321             upperi['p1']=120
322             upperi['p2']=240
323             upperi['p3']=None
324             partslist=['p1', 'p2','p3']
325         else:
326             partslist=['pu']
327             loweri = {}; upperi={}
328             loweri['pu']=0
329             upperi['pu']=None
330
331         if not os.path.exists('tmp'):
332             os.makedirs('tmp')
333
334
335
336         Epsn=psE.name
337         ET2n=T2E.name
338         ERHwn='RHw'
339         ERHin='RHi'
340         ESWn=SW.name
341         ELWn=LW.name
342         Ee2n='e2'
343         SNTn='tg'
344         yr=2000
345
346
347         for yr in np.arange(startyr,endyr+1): #make loop
348             print('year loop top')
```

```
349         if not os.path.isfile('tmp/'+'tgp3'+str(yr)+'.nc'):
350             for filename in glob.glob('tmp/*') :
351                 os.remove( filename )
352             SeNTd=xr.open_dataset(SeNorge2018pd+str(yr)+'.nc',chunks={'
    time': chnkt})
353             print('starting '+ str(yr))
354             for pn in partslist:
355                 SeNTu=SeNTd['tg'][loweri[pn]:upperi[pn],:,:]
356                 SeNTu,SWp=xr.align(SeNTu,SW, join='inner',copy=False)
357                 SeNTu,LWp=xr.align(SeNTu,LW, join='inner',copy=False)
358                 SeNTu,psp=xr.align(SeNTu,psE, join='inner',copy=False)
359                 SeNTu,RHwp=xr.align(SeNTu,RHEw, join='inner',copy=False)
360                 RHwp.name='RHw'
361                 SeNTu,RHip=xr.align(SeNTu,RHEi, join='inner',copy=False)
362                 RHip.name='RHi'
363                 SeNTu,T2p=xr.align(SeNTu,T2E, join='inner',copy=False)
364                 SeNTu,e2p=xr.align(SeNTu,e2w, join='inner',copy=False)
365                 e2p.name='e2'
366
367
368                 #--Regridding some variables----------
369                 print('regridding '+pn)
370                 Mps=regrid2step(psp)
371                 writetotmp_nc(Mps,pn=pn+str(yr))
372
373                 del Mps
374                 MT2=regrid2step(T2p)
375                 writetotmp_nc(MT2,pn=pn+str(yr))
376
377                 del MT2
378                 MRHw=regrid2step(RHwp)
379                 writetotmp_nc(MRHw,pn=pn+str(yr))
380
381                 del MRHw
382                 gc.collect()
383                 MRHi=regrid2step(RHip)
384                 writetotmp_nc(MRHi,pn=pn+str(yr))
385
386                 del MRHi
387                 MSW=regrid2step(SWp)
388                 writetotmp_nc(MSW,pn=pn+str(yr))
389
390                 del MSW
391                 MLW=regrid2step(LWp)
392                 writetotmp_nc(MLW,pn=pn+str(yr))
393
394                 del MLW
395                 Me2=regrid2step(e2p)
396                 writetotmp_nc(Me2,pn=pn+str(yr))
397
398                 del Me2
399                 writetotmp_nc(SeNTu,pn=pn+str(yr))
400
401                 print('regridded '+pn+' '+str(yr))
402                 gc.collect()
403
404             SeNTd.close()
405
406
407         # START
    ----------------------------------------------------------------
408         print('Starting downscaling')
409
410         SeNT=xr.open_mfdataset('tmp/tg*.nc',chunks={'time': chnkt},
    combine='by_coords')
411         SeNT.close()
412         SeNTr=SeNT['tg']
413         SeNTr.attrs={}
```

```
414
415         EraT=xr.open_mfdataset('tmp/t2m*.nc',chunks={'time': chnkt},
    combine='by_coords')
416         EraTr=EraT['t2m']
417
418         #calculating hypso adjusted pressure
419         Eps=xr.open_mfdataset('tmp/sp*.nc',chunks={'time': chnkt},
    combine='by_coords')
420         Epsr=Eps['sp']
421
422         if not os.path.isfile(savedir+'HySN5_Surface_Pressure_'+str(yr)+
    '.nc'):
423             pSN=Epsr/xu.exp(ecg*dz/(Rd*((SeNTr+T0NVE)+EraTr)/2.)) #
    Kelvin
424             pSN.attrs['longname']='surface pressure'
425             pSN.attrs['unit']='Pa'
426             pSN.name='sp'
427             pSN.attrs['notes']='Instantaneous, average of the last 24
    hours, sampled every six hours.'
428             pSNd=pSN.to_dataset(dim=None, name='sp')
429
430
431             #Make DataArray to nice dataset
432             pSNd.attrs['date_created'] = today
433             pSNd.attrs['license'] = 'Norwegian Licence for Open
    Government Data (NLOD), https://data.norge.no/nlod/en/1.0'
434             pSNd.attrs['creator_name'] = 'Helene B. Erlandsen'
435             pSNd.attrs['proj4']=projs
436
437             delayed_obj=pSNd.to_netcdf(savedir+'HySN5_Surface_Pressure_'
    +str(yr)+'.nc',
438                                        compute=False,unlimited_dims=
    None,
439                                        encoding={'sp':{'dtype': 'f8','
    _FillValue': -9999.,
440                                                        '
    least_significant_digit':1,'zlib':True},
441                                                  'lon': {'_FillValue':
    False},
442                                                  'lat': {'_FillValue':
    False},
443                                                  'X': {'_FillValue':
    False},
444                                                  'Y': {'_FillValue':
    False},
445                                                  'mask':{'_FillValue':
    -9999}})
446
447             print('Writing downscaled surface pressure for year '+str(yr
    ) +' to file:'+
448                   savedir+'HySN5_Surface_Pressure_'+str(yr)+'.nc')
449             with ProgressBar():
450                 results = delayed_obj.compute()
451
452             gc.collect()
453             EraT.close();Eps.close();pSNd.close();del pSN
454             print('Finished:'+ savedir+'HySN5_Surface_Pressure_'+str(yr)
    +'.nc')
455         else:
456             print('Found:'+ savedir+'HySN5_Surface_Pressure_'+str(yr)+'.
    nc, assuming finished')
457             file_info = os.stat(savedir+'HySN5_Surface_Pressure_'+str(yr
    )+'.nc')
458             size= convert_bytes(file_info.st_size)
459             print('Size is :' + size)
460
461         #
    #-------------------------------------------------------------------
```

```
462         #Calculating adjusted vapour pressure assuming constant RH with
    height
463         ERHw=xr.open_mfdataset('tmp/RHw*.nc',chunks={'time': chnkt},
    combine='by_coords')
464         ERHwr=ERHw['RHw']
465         ERHi=xr.open_mfdataset('tmp/RHi*.nc',chunks={'time': chnkt},
    combine='by_coords')
466         ERHir=ERHi['RHi']
467 
468         #in Celsius:
469         TdH0w=cw*(xu.log(ERHwr/100.) + bw*SeNTr/(cw+SeNTr))/(bw-xu.log(
    ERHwr/100.)-bw*SeNTr/(cw+SeNTr))
470         TdH0i=ci*(xu.log(ERHir/100.) + bi*SeNTr/(ci+SeNTr))/(bi-xu.log(
    ERHir/100.)-bi*SeNTr/(ci+SeNTr))
471 
472         PS=xr.open_dataset(savedir+'HySN5_Surface_Pressure_'+str(yr)+'.
    nc',chunks={'time': chnkt})
473         pSN=PS['sp']
474         fw=(1.00071*xu.exp(0.0000045*pSN/100.)) #Ald Esk 1996 eq 17
475         fi=(0.99882*xu.exp(0.000008*pSN/100.)) #Ald Esk 1996 eq 18
476 
477         eHw=fw*aw*xu.exp(bw*TdH0w/(cw+TdH0w))# Buck
478         eHi=fi*ai*xu.exp(bi*TdH0i/(ci+TdH0i))# AERK ice eq 24 want temp
    in C, p in hPa
479         if not os.path.isfile(savedir+'HySN5_Vapour_Pressure_'+str(yr)+'
    .nc'):
480 
481             eH=eHi.where(SeNTr<0, eHw)/1000. #test if tmean is lower
    than zero. making it kPa
482             eH.attrs['longname']='Vapour Pressure'
483             eH.attrs['unit']='kPa'
484             eH.attrs['notes']='Average of the last 24 hours, based on
    SeNorge2018 T2 and Era5 Td and T2'
485             eH.name='e2'
486             eH.coords['lon'] = (('Y','X'),Lat2)
487             eH.coords['lat'] = (('Y','X'),Lon2)
488             eHd=eH.to_dataset(dim=None, name='e2')
489             eHd.attrs['date_created'] = today
490             eHd.attrs['license'] = 'Norwegian Licence for Open
    Government Data (NLOD), https://data.norge.no/nlod/en/1.0'
491             eHd.attrs['creator_name'] = 'Helene B. Erlandsen'
492             eHd.attrs['proj4']=projs
493             delayed_obj = eHd.to_netcdf(savedir+'HySN5_Vapour_Pressure_'
    +str(yr)+'.nc',
494                                         compute=False,unlimited_dims=None
    ,
495                                         encoding={'e2':{'dtype': 'f8','
    _FillValue': -9999.,
496                                                         '
    least_significant_digit':3,'zlib':True},
497                                                   'lon': {'_FillValue':
    False},
498                                                   'lat': {'_FillValue':
    False},
499                                                   'X': {'_FillValue':
    False},
500                                                   'Y': {'_FillValue':
    False},
501                                                   'mask':{'_FillValue': -
    9999}})
502 
503             print('Writing downscaled vapour pressure for year '+str(yr)
    +' to file:'
504                   +savedir+'HySN5_Vapour_Pressure_'+str(yr)+'.nc')
505             with ProgressBar():
506                   results = delayed_obj.compute()
507             eHd.close()
```

```
508                 del eH;
509                 gc.collect()
510                 print('Finished: ' +savedir+'HySN5_Vapour_Pressure_'+str(yr)
        +'.nc')
511             else:
512                 print('Found:'+ savedir+'HySN5_Vapour_Pressure_'+str(yr)+'.
        nc, assuming finished')
513                 file_info = os.stat(savedir+'HySN5_Vapour_Pressure_'+str(yr)
        +'.nc')
514                 size= convert_bytes(file_info.st_size)
515                 print('Size is :' + size)
516
517
518             #VPD=esSN-eH
519             if not os.path.isfile(savedir+'
        HySN5_Near_Surface_Vapur_Pressure_Deficit_'+str(yr)+'.nc'):
520                 VPDw=eHw*(100./ERHwr -1.)/1000.
521                 VPDi=eHi*(100./ERHir -1.)/1000.
522                 VPD=VPDi.where(SeNTr<0, VPDw)
523                 #qH=eps*eH/(pSN-(1-eps)*eH) #are all in Pa
524                 VPD.attrs['longname']='Vapour Pressure Deficit'
525                 VPD.attrs[ 'unit']='kPa'
526                 VPD.attrs['notes']='Average of the last 24 hours, based on
        SeNorge2018 T2 and Era5 Td and T2'
527                 VPD.name='VPD'
528                 VPD.coords['lon'] = (('Y','X'),Lat2)
529                 VPD.coords['lat'] = (('Y','X'),Lon2)
530                 VPD=VPD.to_dataset(dim=None, name='VPD')
531                 VPD.attrs['date_created'] = today
532                 VPD.attrs['license'] = 'Norwegian Licence for Open
        Government Data (NLOD), https://data.norge.no/nlod/en/1.0'
533                 VPD.attrs['creator_name'] = 'Helene B. Erlandsen'
534                 VPD.attrs['proj4']=projs
535                 #,writer=xarray_api.ArrayWriter()
536                 delayed_obj = VPD.to_netcdf(savedir+'
        HySN5_Near_Surface_Vapur_Pressure_Deficit_'+str(yr)+'.nc',
537                                             compute=False,unlimited_dims=None
        ,
538                                             encoding={'VPD':{'dtype': 'f8','
        _FillValue': -9999.,
539                                                              '
        least_significant_digit':3,'zlib':True},
540                                                       'lon': {'_FillValue':
        False},
541                                                       'lat': {'_FillValue':
        False},
542                                                       'X': {'_FillValue':
        False},
543                                                       'Y': {'_FillValue':
        False},
544                                                       'mask':{'_FillValue': -
        9999}})
545
546                 print('Writing downscaled vapour pressure '+str(yr) +' to
        file:'
547                       +savedir+'HySN5_Near_Surface_Vapur_Pressure_Deficit_'+
        str(yr)+'.nc')
548                 with ProgressBar():
549                       results = delayed_obj.compute()
550
551
552                 ERHw.close()
553                 ERHi.close()
554                 #VPD.close()
555                 PS.close()
556                 gc.collect()
557                 print('Finished: ' +savedir+'
        HySN5_Near_Surface_Vapur_Pressure_Deficit_'+str(yr)+'.nc')
```

```
558             else:
559                 print('Found:'+ savedir+'
    HySN5_Near_Surface_Vapur_Pressure_Deficit_'+str(yr)+'.nc, assuming
    finished')
560                 file_info = os.stat(savedir+'
    HySN5_Near_Surface_Vapur_Pressure_Deficit_'+str(yr)+'.nc')
561                 size= convert_bytes(file_info.st_size)
562                 print('Size is :' + size)
563 
564             #Longwave clear sky scaling
565             Ee=xr.open_mfdataset('tmp/'+Ee2n+'*.nc',chunks={'time': chnkt},
    combine='by_coords')
566             Eer=Ee[Ee2n]
567             ELW=xr.open_mfdataset('tmp/'+ELWn+'*.nc',chunks={'time': chnkt},
    combine='by_coords')
568             ELWr=ELW[ELWn]
569             SeNTt=xr.open_mfdataset('tmp/tg*.nc',chunks={'time':  chnkt},
    combine='by_coords')
570             SeNTr=SeNTt['tg']
571             SeNTr.attrs={}
572 
573             EraT=xr.open_mfdataset('tmp/t2m*.nc',chunks={'time': chnkt},
    combine='by_coords')
574             EraTr=EraT['t2m']
575 
576             eHn=xr.open_dataset(savedir+'HySN5_Vapour_Pressure_'+str(yr)+'.
    nc',chunks={'time': chnkt})
577             eHr=eHn['e2'] #is kPa
578 
579             #check power in dask xr
580             epsE=1.08*(1-xu.exp(-((Eer/100.)**(EraTr/2016.))))#hpa correct
581             epsH=1.08*(1-xu.exp(-((eHr*10.)**((SeNTr+T0NVE)/2016.)))) #
    satterlund 1969  #eH already div by 1000. and is kPa. kPa*10 = hPa
582             sca=(epsH/epsE)*((SeNTr+T0NVE)/EraTr)**4
583             LWSN=sca*ELWr
584             LWSN.name='rlds'
585             LWSN.coords['lon'] = (('Y','X'),Lat2)
586             LWSN.coords['lat'] = (('Y','X'),Lon2)
587             LWSN.attrs['longname']='Surface Downwelling Longwave Radiation'
588             LWSN.attrs['standard_name']='
    surface_downwelling_longwave_flux_in_air'
589             LWSN.attrs['unit']='W m-2'
590             LWSN.attrs['notes']='Average over the last 24 hours. Positive
    downwards'
591 
592             if not os.path.isfile(savedir+'
    HySN5_Surface_Downwelling_Longwave_Radiation_'+str(yr)+'.nc'):
593                 LWSNd=LWSN.to_dataset(dim=None, name='rlds')
594                 #LWSN=LWSN.to_dataset(dim=None, name='rlds') already
595                 LWSNd.attrs['date_created'] = today
596                 LWSNd.attrs['license'] = 'Norwegian Licence for Open
    Government Data (NLOD), https://data.norge.no/nlod/en/1.0'
597                 LWSNd.attrs['creator_name'] = 'Helene B. Erlandsen'
598                 LWSNd.attrs['proj4']=projs
599 
600                 delayed_obj = LWSNd.to_netcdf(savedir+'
    HySN5_Surface_Downwelling_Longwave_Radiation_'+str(yr)+'.nc',
601                                               compute=False,unlimited_dims=
    None,
602                                               encoding={'rlds':{'dtype': 'f8'
    ,'_FillValue': -9999.,
603                                                                 '
    least_significant_digit':2,'zlib':True},
604                                                         'lon': {'_FillValue':
    False},
605                                                         'lat': {'_FillValue':
    False},
606                                                         'X': {'_FillValue':
```

```
        False},
607                                                     'Y': {'_FillValue':
        False},
608                                                     'mask':{'_FillValue':
         -9999}})
609
610             print('Writing downscaled longwave radiation for year '+str(
        yr) +
611                   ' to file:'+savedir+'
        HySN5_Surface_Downwelling_Longwave_Radiation_'+str(yr)+'.nc')
612             with ProgressBar():
613                   results = delayed_obj.compute()
614             print('Finished: '+savedir+'
        HySN5_Surface_Downwelling_Longwave_Radiation_'+str(yr)+'.nc')
615         else:
616             print('Found:'+ savedir+'
        HySN5_Surface_Downwelling_Longwave_Radiation_'+str(yr)+'.nc,
        assuming finished')
617             file_info = os.stat(savedir+'
        HySN5_Surface_Downwelling_Longwave_Radiation_'+str(yr)+'.nc')
618             size= convert_bytes(file_info.st_size)
619             print('Size is :' + size)
620         #sigma=5.670373E-8 # Wm-2 K-4
621         #epsgr=0.96 #LWnet_g=recieved-emitted=epsgr*LWdown-BB*epsgr #
        Kirchoffs law abs \simeq em
622
623         if not os.path.isfile(savedir+'
        HySN5_Surface_Net_Downwelling_Longwave_Radiation_'+str(yr)+'.nc'):
624             LWnet=epsgr*LWSN-epsgr*sigma*(SeNTr+T0NVE)**4
625             LWnet.coords['lon'] = (('Y','X'),Lat2)
626             LWnet.coords['lat'] = (('Y','X'),Lon2)
627             LWnet=LWnet.to_dataset(dim=None, name='rls')
628             LWnet['rls'].attrs['longname']='Surface Net Downwelling
        Longwave Radiation'
629             LWnet['rls'].attrs['standard_name']='
        surface_net_downward_longwave_flux'
630             LWnet['rls'].attrs['unit']='W m-2'
631             LWnet['rls'].attrs['notes']='Average over the last 24 hours.
         Positive downwards. Ground emmissivity assumed to be 0.96, and
        with tskin=t2m'
632
633             #LWnet=LWnet.to_dataset(dim=None, name='rlds') already
634             LWnet.attrs['date_created'] = today
635             LWnet.attrs['license'] = 'Norwegian Licence for Open
        Government Data (NLOD), https://data.norge.no/nlod/en/1.0'
636             LWnet.attrs['creator_name'] = 'Helene B. Erlandsen'
637             LWnet.attrs['proj4']=projs
638
639             delayed_obj = LWnet.to_netcdf(savedir+'
        HySN5_Surface_Net_Downwelling_Longwave_Radiation_'+str(yr)+'.nc',
640                                           compute=False,unlimited_dims=
        None,
641                                           encoding={'rls':{'dtype': 'f8',
        '_FillValue': -9999.,
642                                                            '
        least_significant_digit':2,'zlib':True},
643                                                     'lon': {'_FillValue':
        False},
644                                                     'lat': {'_FillValue':
        False},
645                                                     'X': {'_FillValue':
        False},
646                                                     'Y': {'_FillValue':
        False},
647                                                     'mask':{'_FillValue':
         -9999}})
648
649             print('Writing downscaled longwave radiation for year '+str(
```

```
        yr) +
650                     ' to file:'+savedir+'
        HySN5_Surface_Net_Longwave_Radiation_'+str(yr)+'.nc')
651             with ProgressBar():
652                     results = delayed_obj.compute()
653             SeNTt.close();EraT.close(); Ee.close();ELW.close();LWnet.
        close()
654             gc.collect()
655             print('Finished: '+savedir+'
        HySN5_Surface_Net_Downwelling_Longwave_Radiation_'+str(yr)+'.nc')
656         else:
657             print('Found:'+savedir+'
        HySN5_Surface_Net_Downwelling_Longwave_Radiation_'+str(yr)+'.nc,
        assuming finished')
658             file_info = os.stat(savedir+'
        HySN5_Surface_Net_Downwelling_Longwave_Radiation_'+str(yr)+'.nc')
659             size= convert_bytes(file_info.st_size)
660             print('Size is :' + size)
661         #
        ##-------------------------------------------------------------------
662         ### Cosgrove end
        ------------------------------------------------

663
664         if not os.path.isfile(savedir+'
        HySN5_Surface_Downwelling_Shortwave_Radiation_'+str(yr)+'.nc'):
665             # SW clear sky scaling T&R
        ---------------------------------------

666
667             #tau_H=np.power(tau,pSN/101300.)+alpha*eH
668             PS=xr.open_dataset(savedir+'HySN5_Surface_Pressure_'+str(yr)
        +'.nc',chunks={'time': chnkt})
669             pSN=PS['sp']
670             eHn=xr.open_dataset(savedir+'HySN5_Vapour_Pressure_'+str(yr)
        +'.nc',chunks={'time': chnkt})
671             eHr=eHn['e2']*1000. #divided by 1000. above to make kPa, now
         in Pa
672             Ee=xr.open_mfdataset('tmp/'+Ee2n+'*.nc',chunks={'time':
        chnkt},combine='by_coords')
673             Eer=Ee[Ee2n]
674             Eps=xr.open_mfdataset('tmp/sp*.nc',chunks={'time': chnkt},
        combine='by_coords')
675             Epsr=Eps['sp']
676             tau_H=tau**(pSN/101300.)+alpha*eHr
677             tau_E=tau**(Epsr/101300.)+alpha*Eer
678             Taut_ratio=tau_H/tau_E
679
680             ESW=xr.open_mfdataset('tmp/'+ESWn+'*.nc',chunks={'time':
        chnkt},combine='by_coords')
681             ESWr=ESW[ESWn]
682
683             SWSN=(Taut_ratio**2)*ESWr
684             SWSN.attrs['longname']='Surface Downwelling Shortwave
        Radiation'
685             SWSN.attrs['standard_name']='
        surface_downwelling_shortwave_flux_in_air'
686             SWSN.attrs['unit']='W m-2'
687             SWSN.attrs['notes']='Average over the last 24 hours.
        Positive downwards'
688             SWSN.name='rsds'
689             SWSN.coords['lon'] = (('Y','X'),Lat2)
690             SWSN.coords['lat'] = (('Y','X'),Lon2)
691             SWSN=SWSN.to_dataset(dim=None, name='rsds')
692
693             SWSN.attrs['date_created'] = today
694             SWSN.attrs['license'] = 'Norwegian Licence for Open
        Government Data (NLOD),https://data.norge.no/nlod/en/1.0'
695             SWSN.attrs['creator_name'] = 'Helene B. Erlandsen'
696             SWSN.attrs['proj4']=projs
```

```
697             #SWSN.attrs['creator_email'] = 'hebe@nve.no'
698             #ncfile.Proj4_string=
699
700
701             delayed_obj=SWSN.to_netcdf(savedir+'
    HySN5_Surface_Downwelling_Shortwave_Radiation_'+str(yr)+'.nc',
702                                        compute=False,unlimited_dims=None
    ,
703                                        encoding={'rsds':{'dtype': 'f8','
    _FillValue': -9999.,
704                                                  '
    least_significant_digit':1,'zlib':True},
705                                                  'lon': {'_FillValue':
    False},
706                                                  'lat': {'_FillValue':
    False},
707                                                  'X': {'_FillValue':
    False},
708                                                  'Y': {'_FillValue':
    False},
709                                                  'mask':{'_FillValue': -
    9999}})
710
711             print('Writing downscaled shortwave radiation for year '+str
    (yr) +
712                   ' to file:'+savedir+'
    HySN5_Surface_Downwelling_Shortwave_Radiation_'+str(yr)+'.nc')
713             with ProgressBar():
714                   results = delayed_obj.compute()
715
716             Ee.close(); eHn.close(); ESW.close(); EraT.close(); Eps.
    close(); PS.close(); SWSN.close()
717             print('Finished: '+savedir+'
    HySN5_Surface_Downwelling_Shortwave_Radiation_'+str(yr)+'.nc')
718         else:
719             print('Found:'+savedir+'
    HySN5_Surface_Downwelling_Shortwave_Radiation_'+str(yr)+'.nc,
    assuming finished')
720             file_info = os.stat(savedir+'
    HySN5_Surface_Downwelling_Shortwave_Radiation_'+str(yr)+'.nc')
721             size= convert_bytes(file_info.st_size)
722             print('Size is :' + size)
723
724         #for filename in glob.glob('tmp/*') :
725         #    os.remove( filename )
726         print('finished '+ str(yr))
727
728
729
730     print('done all')
731     #client.stop_worker(w)
732
733     client.close()
```